Baotang Shen
Ove Stephansson
Mikael Rinne

# Modelling Rock Fracturing Processes

## A Fracture Mechanics Approach Using FRACOD


Springer

# Modelling Rock Fracturing Processes

Baotang Shen • Ove Stephansson • Mikael Rinne

# Modelling Rock Fracturing Processes

## A Fracture Mechanics Approach Using FRACOD

Springer

Baotang Shen
CSIRO Earth Science and Resource Engineering
Brisbane, QLD, Australia

Mikael Rinne
School of Engineering
Department of Civil and Environmental Engineering, Geoengineering
Aalto University
Espoo, Finland

Ove Stephansson
Helmholtz Centre Potsdam
GFZ German Research Centre for Geosciences
Potsdam, Germany

Additional material can be downloaded from http://extras.springer.com

ISBN 978-94-007-6903-8 ISBN 978-94-007-6904-5 (eBook)
DOI 10.1007/978-94-007-6904-5
Springer Dordrecht Heidelberg New York London

Library of Congress Control Number: 2013944753



*Cover illustration*: This figure shows a typical case of hydraulic fracturing simulated using FRACOD. A borehole is drilled in a rock mass with several isolated pre-existing fractures. A high fluid pressure is then applied in the borehole which causes fracture initiation at the borehole wall, followed by fracture propagation toward the pre-existing fractures. The hydraulically driven fractures eventually coalesce with the pre-existing fractures. The pre-existing fractures then propagate under the influence of high fluid pressure. The figure is a plot of vertical displacement contour in the vicinity of the injection hole and the new and pre-existing fractures. Figure created by the authors.

Printed on acid-free paper

Springer is part of Springer Science+Business Media (www.springer.com)

# Foreword

This carefully written and expert text on fracturing of rock, reflecting deep theoretical understanding and second to none modelling abilities, has been written by three well-known authors. They combine theoretical brilliance and creativity, a long life of expert insight, professorship, and authorship in many rock mechanics problems, and expert application in several current nuclear waste repository studies. All three are well known to the reviewer, who has been persuaded to provide an opinion on this interesting text, despite an altogether simpler background in practical rock engineering. Their theoretical and applied fracture mechanics text, which of course is written for experts, is presented in such an ordered manner that it is digestible, even if the theory and extensive matrices required have to be accepted as the production of an unusually talented main author, whose exceptional mathematical abilities have never been in doubt.

The usefulness of FRACOD, the boundary element – displacement discontinuity method (DDM) of modelling of fracturing in over-stressed rock, which is developed, validated, and demonstrated during the 200 pages of this book, has several times been appreciated by the reviewer, in specific deep tunnelling and over-stressed shallow cavern scenarios in the past 7 or 8 years. In the first case, the predicted deeply penetrating stress-induced rock-bursting damage, with and without additional jointing, caused by in situ principal stresses as high as 60 MPa, was not believed by the contractor, but was severe enough to later damage the TBM, and required completion of the tunnel by drill-and-blast, an approach suggested many years before completion, due to the severe FRACOD-related results. In the second case, the predicted fracturing of weather-weakened rock beneath the elephant-footing foundations of overloaded lattice girders was observed in practice (due to post-collapse excavation), and was undoubtedly a triggering factor in the collapse of the large cavern at shallow depth, with the severe overloading due to an undiscovered ridge of rock high above the cavern arch. Various load, rock strength, and modulus variations were tested, and the modelled results could be ‘seen’ in practice, at the overloaded side of the cavern.

Chapters 2 and 3 of this book on the modelling of rock fracturing processes, lay a foundation for a thorough understanding of fracture mechanics, and its modelling

using DDM. Fracture initiation, and development with time, including sub-critical crack growth, and sliding on pre-existing joints is modelled by FRACOD. Coupled thermo-mechanical effects, coupled hydro-mechanical effects, and a particularly realistic looking hydraulic fracturing development in a (2D) rock mass with some pre-existing jointing, follow in later chapters, but are preceded by their theoretical description and possibility of development in FRACOD.

The authors have taken care to explain and then give examples of the input data needed for FRACOD and describe how it can be obtained from laboratory testing. They then validate FRACOD by comparing the numerical solutions, using a range of element sizes, with problems that have analytical solutions. This is done of course for tensile fracturing and shear fracturing, followed by modelling of creep (in the form of sub-critical crack growth), and ends with the coupled processes caused by heating or fluid pressure, and the different styles of fracturing they induce. The hydraulic fracturing development causes some wing cracks to form at the tips of the closest pre-existing jointing, on either side of the injection borehole.

The final chapter gives numerous cases of application of FRACOD, where the major emphasis is probably on the field of high-level nuclear waste isolation and also geothermal energy access boreholes. Particular concern is with the excavation disturbed zone, or EDZ, which can have important consequences both for well stability and for repository construction. The latter may be in different orientations with respect to, e.g., the major horizontal stress, where optimal disposal tunnel orientation may not be optimal for access tunnel excavation. Subsequent canister placement in large diameter holes and the subsequent thermal loading phase have been tested at large scale by Sweden's SKB in Äspö, and here these have been modelled with FRACOD.

For those who desire greater insight and understanding of fracture mechanics, coupled process modelling, and the application and capabilities of the code FRACOD, this book is of course 'a must have' item. It is an impressive accomplishment, and congratulations to all the authors for their unique and essential contributions to its success.

Oslo, Norway Nick Barton
August 2012

# Preface

This book describes a unique approach using the principles of rock fracture mechanics to investigate the behaviour of fractured rock masses for rock engineering purposes.

Rock fracture mechanics, a promising outgrowth of rock mechanics and fracture mechanics, has developed rapidly in recent years, driven by the need for in-depth understanding of rock mass failure processes in both fundamental research and rock engineering designs.

Today, as rock engineering extends into many more challenging fields (like mining at depth, radioactive waste disposal, geothermal energy, and deep and large underground spaces), it requires knowledge of rock masses, complex coupled thermal–hydraulic–chemical–mechanical processes. Rock fracture mechanics play a crucial role in these complex coupled processes simply because rock fractures are the principal carrier and common interface.

To date, the demand for rock fracture mechanics–based design tools has outstripped the very limited number of numerical tools available. Most of those tools were developed for civil engineering and material sciences and deal with substances such as steel, ceramic, glass, ice, and concrete which differ markedly from rocks in their fracturing behaviour.

To address this need, in 1990 the authors began the work of developing a practical numerical approach using fracture mechanics principles to predict rock mass failure processes. It started with a Ph.D. thesis by the first author suggesting a new fracture criterion that predicts both tensile and shear fracture propagations, overcoming the shortcomings of traditional fracture criteria that predict only tensile failure. This approach has proved very effective in simulating the behaviour of multiple fractures in rock-like materials in laboratory tests.

The development of this modelling approach with a view to engineering application was initially driven by proposals for radioactive waste disposal in Sweden and Finland, where fracture propagation in the hard bedrock (due to thermal loading and glaciations) is considered a major risk factor. During this period, an earlier version of the code FRACOD was developed, capable of simulating fracture propagation, fracture initiation, and acoustic emission. This code capability was then expanded to

include time-dependent rock behaviour and subcritical crack growth through a Ph.D. study in 2008 by the third author. In the course of this development process, many application case studies were conducted using FRACOD, including the well-known Äspö Hard Rock Laboratory's Pillar Spalling Experiments (APSE) in Sweden, the DECOVALEX International Collaboration Project, and the Mizunami Underground Research Laboratory (MIU) Investigations in Japan.

This fracture mechanics approach was further expanded to other application fields of rock engineering such as tunnelling and geothermal energy. In an attempt to investigate the stability of a tunnel under high horizontal stresses, FRACOD successfully predicted the same "log-spiral" type of fracturing pattern around the tunnel that was observed in the laboratory (Barton 2007). When applied to back-analysis of in situ stresses in a 4.4 km deep geothermal well in Australia, this approach was shown to realistically simulate the borehole breakout, thereby accurately predicting the rock mass stress state.

Recent surges in fossil fuel (e.g., oil and coal) prices and concerns about global warming have significantly increased worldwide interest in alternative energy sources and storage methods. Thus, accurate prediction of the coupled behaviour of rock fracturing, fluid flow and thermal processes is now a vital scientific endeavour. FRACOD seeks to address the complex design issues facing various emerging developments in energy-related industries including geothermal energy, LNG underground storage, and $CO_2$ geosequestration.

Since 2007, the focus of FRACOD development has shifted to the coupling between rock fracturing, fluid flow, and thermal loading thanks to the establishment of an international collaboration project with participants from Australia, Europe, and South Korea. Coupling functions of T-M (thermal-mechanical) processes and H-M (hydro-mechanical) processes have been developed in FRACOD. Several application case studies related to hydraulic fracturing and LNG underground storage have been conducted.

Development and application of the fracture mechanics approach using FRACOD has not stopped – and it will continue. Currently, the full three-way coupling of M-T-H is being developed in the two-dimensional FRACOD code to address industry needs. A three-dimensional version of FRACOD is also under development for modelling true 3D problems.

It is our wish that this book will familiarize readers with the concepts and basic principles of using a fracture mechanics approach to solve rock engineering problems. We also hope this book will stimulate more research and development in this area, eventually providing the rock mechanics and rock engineering society with an alternative, robust, and unique tool for rock engineering design.

Brisbane
July 2012

# Acknowledgements

The development and first rock engineering applications of FRACOD 2D can be traced back to 1992 when the first and second authors started up the activities at the Division of Engineering Geology of the Royal Institute of Technology, KTH, in Stockholm, Sweden. Sometime later, the third author, Mikael Rinne, joined the group at KTH and added to the further development of the code. We gratefully acknowledge the encouragement and support provided by KTH during the period 1992–2001.

The first applications of the code to rock engineering problems were done in close co-operation with the Swedish Nuclear Power Inspectorate, SKI, in Stockholm. The code was applied to stability problems of tunnels and deposition holes of the early versions of the KBS-3 system for disposal of spent nuclear fuel. We are thankful to Dr. Johan Andersson and Dr. Fritz Kautsky at SKI for providing challenging problems and stimulating discussions and SKI for the support of the code development.

The international contact network in the field of management of spent nuclear fuel led us to a close co-operation with Hazama Corporation in Japan. We are grateful to Hazama for the many years of support for developing the code and to Dr. Kiyoshi Amemyia for supporting new developments of FRACOD to interesting nuclear waste handling problems in Japan. We would also like to thank Christer Svemar and Rolf Christiansson at the Swedish Nuclear Fuel and Waste Management Company, SKB, Stockholm for stimulating discussions and project support.

During the last two decades The Finnish Funding Agency for Technology and Innovation, TEKES, has supported the code development through funding the FRACOD code owner FRACOM Oy in Finland. We gratefully acknowledge the support by TEKES and our contact persons Lasse Pöyhönen and Arto Kotipelto. Support from the Finnish nuclear waste management company, Posiva Oy, in many phases of the code development is also highly appreciated. Special thanks go to Juhani Vira, Kimmo Kemppainen, and Topias Siren at Posiva.

Since 2004, several studies were conducted using FRACOD for geothermal energy development in Australia and they were supported by Geodynamics Ltd, Green Rock Energy Ltd, and the Commonwealth Scientific and Industrial Research Organisation (CSIRO). We are very grateful for the support and close involvement in these studies by Dr. Doone Wyborn of Geodynamics Ltd, Adrian Larking and Gary Meyer of Green Rock Energy Ltd, and Dr. Rob Jeffrey of CSIRO.

We would like to express our most sincere appreciation to Dr. Nick Barton who, over many years, has been one of the strongest advocators of FRACOD development. With his strong support and guidance, FRACOD has continued its improvement, in particular for applications to underground tunneling.

Since 2007, two international collaboration projects were established to develop an advanced numerical package based on FRACOD that predicts the effect of coupled explicit fracturing/fluid flow/thermal processes. The projects were led and supported by CSIRO Earth Science and Resource Engineering, Australia, and several international organisations participated in them. We are thankful to the following participants of the project and their organisations: Drs. Hyung Mok Kim and Eui Seob Park, Korea Institute of Geoscience and Mineral Resources; Drs. Taek Kon Kim, Jin Moo Lee, Hee Suk Lee, Tae Young Ko, and Julie Kim, SK Engineering and Construction, South Korea; Drs. Manfred Wutke, Ralf Junker, and Christian Bönneman, Leibniz Institute for Applied Geophysics, Hannover, Germany; Drs. Tobias Backers and Tobias Meier, geomecon GmbH, Potsdam, Germany; Topias Siren and Matti Hakala, Posiva Oy, Finland; Dr. Doone Wyborn, Geodynamics Ltd, Australia; Prof. Ki-Bok Min, National University of Seoul, South Korea; Prof. Simon Loew, Federal Institute of Technology ETH Zurich, Switzerland.

The later development in FRACOD and the writing of this book could not have been possible without the strong support from CSIRO Earth Science and Resource Engineering, Australia. We would like to thank Dr. Hua Guo for his strong support and scientific contribution to the international collaboration projects. We are very grateful to Dr. Binzhong Zhou for the development of the pre- and postprocessors to FRACOD, Dr. Jingyu Shi for the development of the first parts of the three-dimensional version of the code.

The second author is thankful to Dr. Reinhard Hüttle, Prof. Georg Dresen, and Dr. Gottfried Grünthal of GFZ German Research Centre for Geosciences, Potsdam, Germany, for providing a stimulating environment and for supporting this work. The FRACOD code needs elastic input parameters, rock fracture mechanics, and thermal data. For providing all this, we appreciate the close co-operation of Dr, Tobias Backers at geomecon GmbH (previously GeoFrames GmbH) which has been of value in the development of FRACOD.

The third author wishes to thank Helsinki University of Technology, which is today part of the Aalto University in Finland. Special thanks go to Prof. Pekka Särkkä and his laboratory personnel at Aalto. Rock testing to verify the new features in the code has been an essential part in the code development.

We very much appreciate the expertise and skill of Andreas Hendrich, GFZ, who, with great patience, redrew all the viewgraphs. Also, we like to thank Jeoung Seok Yoon, Section 2.6, GFZ, for his useful comments to the manuscript from a Postdoc's point of view. The English editing of the final version of the manuscript was done by Michelle Burgess and she is gratefully acknowledged. Finally, we acknowledge the support by Petra D. Van Steenbergen and Hermine Vloemans, Springer, SBM NL, for their help with the publishing of this book.

Finally, we would like to thank our families for the patience and support in completing this book.

# Contents

# Chapter 1
# Introduction

**Abstract** Understanding the long-term behaviour of a rock mass and the coupled hydro-thermal-mechanical processes is crucial for geological radioactive waste disposal, geothermal, mining, LNG underground storage, and $CO_2$ geosequestration. Rock fracture initiation and propagation are the key mechanism for rock mass instability.

The ability to predict and realistically reproduce rock mass behaviour using a numerical model is a pivotal step in solving many rock engineering problems. Although several existing numerical codes can model the behaviour of jointed or fractured rock mass, most do not consider the explicit fracture initiation and propagation—a dominant mechanism, particularly in hard rocks.

The *FRA*cture propagation *COD*e (FRACOD) presented here is a two-dimensional computer code designed to simulate fracture initiation and propagation in elastic and isotropic rock mediums. This book focuses on the theories and numerical principles behind FRACOD, providing examples where the numerical method is applied to solve practical problems.

Rock mass is increasingly employed as the host medium for a vast array of human activities. Facilities like storage areas, wells, tunnels, underground power stations are located in a variety of rock types and under different rock mechanical conditions. Excavation stability is imperative for all such constructions, in both the short and long term.

Understanding the long-term behaviour of a rock mass is crucial for safety and performance assessments of geological radioactive waste disposal. Hydro-thermal-mechanical couplings of the ongoing processes around these repositories are particularly important. The understanding of fracturing of rock masses has also become a critical endeavour for energy extraction and storage. Small-scale breakouts around single wells in petroleum engineering can devastate the oil and gas extraction from source rock. The large-scale fracturing of rock formations for improved oil, gas and heat extraction is an essential field of development in the

B. Shen et al., *Modelling Rock Fracturing Processes: A Fracture Mechanics Approach Using FRACOD*, DOI 10.1007/978-94-007-6904-5_1,

petroleum and geothermal industries. $CO_2$ geosequestration is a complex new field of rock engineering where fracturing of the overburden rock during pressurization must be prevented while fracturing of the storage formation might be needed. All these intricate design tasks require powerful prediction and modelling tools.

Failure of brittle rock is often associated with a rapid and violent event, as detected in short-term loading strength laboratory tests. From these test results, the mechanical properties of rock including fracture mechanics parameters are obtained. When rock is stressed close to its short-term strength, slow crack growth (also called subcritical crack propagation), occurs. With time, this slow fracturing process may generate critical stress concentrations that lead to a sudden unstable failure event. Slow subcritical crack growth (SCG) is thought to play an important role in long-term rock stability at all scales and for all kinds of rocks, ranging from laboratory samples to earthquake-generated faults. When sudden rock movement occurs in nature or around excavations the consequences can be serious.

The ability to predict and realistically reproduce rock mass behaviour using a numerical model is a pivotal step in solving many rock engineering problems. Numerical modelling can improve our understanding of the complicated failure processes in rock and the many factors affecting the behaviour of fractured rock. When our models manage to better capture the fundamental failure mechanisms observed in the laboratory, our ability to generate reliable large-scale models improves, as does our ability to predict the short and long-term behaviour of rock masses in situ. Our ability to identify conditions where time is an important variable for the stability and long-term behaviour of rock excavations is likewise enhanced.

Several different types of numerical methods have been developed for various geomechanical problems (Jing 2003). Since every method and code has its advantages and disadvantages, the choice of a suitable code should be carefully assessed for each rock-engineering problem. Code suitability depends on the character of the problem and the goal of the study. The mechanical behaviour of the rock mass is largely influenced by the presence of natural discontinuities. Hence, numerical methods that allow the introduction of displacement discontinuities into the continuous medium are often required in solving rock engineering problems.

Numerical methods can be subdivided into "Continuum methods" and "Discontinuum methods". Continuum methods (or continuum approaches) do not take into account the presence of distinct discontinuities. If natural discontinuities are numerous, then the substitution, at a certain scale, of a discontinuous medium with a continuous one is required. The mechanical characteristics of the continuous medium must be such that its behaviour is equivalent from a mechanical point of view to that of the discontinuous medium. The effects of fractures are smoothed out and the heavily jointed rock mass is considered as an equivalent continuous medium.

The Discontinuum methods (or "Explicit joint approaches") allow one to incorporate discrete discontinuities in the displacement field, that is, individual joints in the rock mass can be modelled explicitly. Discontinuum methods may describe the fracture process using fracture mechanics principles.

Although several existing numerical codes can model the behaviour of jointed or fractured rock mass, most do not consider the explicit fracture initiation and

propagation—a dominant mechanism, particularly in hard rocks. A very limited number of codes can model the fracture propagation but are not designed for application at engineering scales. Using fracture mechanics principles, this book aims to introduce unique numerical approaches to complex rock failure problems.

The *FRA*cture propagation *COD*e (FRACOD) presented here is a two-dimensional computer code designed to simulate fracture initiation and propagation in elastic and isotropic rock mediums. The code employs Displacement Discontinuity Method (DDM) principles and a fracture propagation criterion for detecting the possibility and path of fracture propagation, Shen and Stephansson (1993).

This book focuses on the theories and numerical principles behind FRACOD, providing examples where the numerical method is applied to solve practical problems involving rock fracture initiation and propagation in rock masses subjected to various loads (including in situ stress, thermal stress and hydraulic pressure).

We begin with the fundamental theory of fracture mechanics and the Displacement Discontinuity Method in Chaps. 2 and 3. In Chaps. 4, 5, 6, 7 and 8, we describe the methodology and principles of using FRACOD to simulate joint behaviour, time-dependency, multiple region systems, gravitational problems, and sequential excavations. In Chap. 9, the development of a thermal–mechanical coupling function in FRACOD is described. In Chap. 10, the newly developed hydro-mechanical coupling function is introduced. Chapter 11 presents the function for modelling anisotropic problems. Chapter 12 outlines the rock properties needed for modelling with FRACOD. Chapter 13 gives numerous verification cases of the code. Finally, Chap. 14 describes several real case studies, applying FRACOD to practical problems.

For those wishing to try the numerical code FRACOD, the demonstration version of FRACOD is provided and can be downloaded from http://extras.springer.com.

## References

Jing L (2003) A review of techniques, advances and outstanding issues in numerical modelling for rock mechanics and rock engineering. Int J Rock Mech Min Sci 40:283–353

Shen B, Stephansson O (1993) Modification of the G-criterion of crack propagation in compression. Int J Eng Fract Mech 47(2):177–189

# Chapter 2
# Introduction to Rock Fracture Mechanics

**Abstract** This chapter provides the basic theories and principles behind rock fracture mechanics. It starts with introducing the Griffith flaws and energy balance theory, which is the foundation of the modern fracture mechanics. Then the concept of stress intensity factor for linear elastic fracture mechanics is introduced, followed by a description of the criteria for fracture propagation. Also described in this chapter is the subcritical crack growth which dominates the time-dependent long term stability of a fractured medium.

In rock mechanics, failure mechanisms generally refer to the overall processes of failure in a continuous sense, i.e. when a rock mass suffers damage permanently affecting its load-bearing ability. Failure criteria such as the well-known Mohr-Coulomb or Hoek and Brown criteria predict the failure conditions by applying the ultimate strength value of the rock matrix but do not account for any localised stresses caused by the discontinuities always inherent in the rock mass.

Bieniawski (1967) distinguishes between a phenomenological failure criterion and a genetic failure mechanism. A *phenomenological failure criterion* simply provides a formula enabling the prediction of the strength values for all states of a multi-axial stress from a critical quantity that may be determined in one type of test, e.g. the uniaxial tensile or compression test. A *genetic failure criterion* describes the physical processes occurring in the material over the course of loading, eventually leading to failure.

The failure of most rock materials is essentially a process of crack initiation and propagation. Therefore the phenomenological failure criteria, although widely used as a good approximation of overall rock behaviour, may not be adequate to describe the failure in detail. The Griffith theory (1920), which led to the evolution of modern *fracture mechanics*, assumes that the propagation of the inherent flaws in the fabric is the source of failure of loaded brittle material. This approach provides a description of the transformation of an unbroken structural component into a fractured one by crack growth. Fracture mechanics assesses the *strength* of

B. Shen et al., *Modelling Rock Fracturing Processes: A Fracture Mechanics Approach Using FRACOD*, DOI 10.1007/978-94-007-6904-5_2,

a stressed structure through the relationship between the loading conditions, the geometry of the crack and the resistance to crack propagation in terms of *critical stress energy release rate* ($G_C$). Irwin proposed modification of Griffith's theory (1957). He described the stress distribution around the crack tip and introduced the concept of the *stress intensity factor* ($K$). Irwin also showed the equivalence of strain energy release rate ($G$) and stress intensity factor ($K$).

Irwin's concept assumes that a fracture tip that has a *stress intensity* ($K$) equal to the material's fracture toughness ($K_C$ – critical stress intensity factor) will accelerate to speeds approaching a terminal velocity that is governed by the speed of the elastic waves in the brittle medium. If the fracture propagation criterion is not met, i.e. if $K < K_C$, then the fracture remains stable. In terms of the Griffith approach, a crack is stable when $G < G_C$, where $G_C$ is the *critical strain energy release rate*. For a wide range of materials, it was determined experimentally that significant crack growth rates can occur at values of $K$ or $G$ often far below the critical values of these parameters. This phenomenon of subcritical crack growth (SCG) is one of the key mechanisms in the time dependent failure behaviour of rocks (Atkinson 1984).

In this book *crack initiation* is the failure process by which one or more cracks are formed through micro-mechanical processes in previously crack-free material. Sometimes the crack initiation is referred to as the threshold stress value of the registered acoustic emission (AE) events $\sigma_{ci}$(AE) for a structure under increasing load. The term *crack initiation* sometimes refers to the stress level where the volume of a test specimen in compression starts to increase after initial compaction.

The term *fracture propagation* or *crack propagation* is defined as the failure process by which a pre-existing single crack or cracks extend or grow after fracture initiation. A distinction can be made between two types of crack propagation, namely 'stable' and 'unstable'. Stable crack propagation is the process of fracture propagation in which the crack extension is a function of loading and can be controlled accordingly. Unstable crack propagation is the process where the crack extension is also governed by factors other than loading.

A *rupture* is the failure process by which a structure (e.g. rock specimen) disintegrates into two or more pieces. A *brittle fracture* is defined as a fracture process exhibiting little or no permanent (plastic) deformation.

*Fracture initiation* indicates the formation of a new fracture from intact rock. *Fracture propagation* represents the process of crack extension from the crack tips to a new position, which may eventually lead to failure of a rock volume. This is referred to as a global failure process or rupture.

In rock material under tension loading, fracture initiation, unstable fracture propagation and crack coalescence occur almost simultaneously. Crack coalescence describes when individual cracks merge and form a continuous fracture. Under compression, the failure process in rock is far more complex. The rupture of the rock material results primarily from stable and unstable fracture propagation and crack coalescence rather than directly from fracture initiation.

Rock materials are inhomogeneous and discontinuous at all scales. At the micro-scale, defects causing stress concentrations include micro-cracks, grain boundaries,

pores, and bedding planes. At the macro-scale, geological fractures are referred to as joints (open or closed) and faults (having signs of shearing) based on their genesis. The term 'crack' is reserved for short discontinuities of the grain size. A 'fracture' has a length several times the grain size and refers to a crack that has extended into the matrix. Although a fracture usually shows a more irregular trace compared with a short crack, from a modelling standpoint, cracks and fractures can be considered equivalent.

## 2.1 Griffith Flaws and Energy Balance Theory

Given that the tensile strength of a material is generally much lower than theoretically predicted, Griffith (1920) postulated that typical brittle materials inevitably contain numerous randomly distributed sub-microscopic flaws, micro-cracks or other discontinuities. These discontinuities serve as stress concentrators and they are often referred to as Griffith flaws or cracks. Griffith established a relationship between critical stress and crack size, now known as the Griffith energy balance approach. It is the starting point for the development of modern fracture mechanics.

Griffith explained how failure is caused by the extension of flaws or cracks. The creation of a new crack surface absorbs energy that is supplied from the work done by the external force. Release of the stored strain energy in the solid promotes the crack propagation and failure.

Two requirements for failure are sufficient stress and sufficient energy. The stress requirement states that the local stress must be high enough to overcome the molecular cohesive strength. This can be achieved by stress concentrations due to the presence of discontinuities such as pre-existing micro-cracks. The energy requirement states that sufficient potential energy must be released to overcome the resistance to crack propagation. This can also be achieved through increasing the work done by external forces. The more energy a solid absorbs, the greater is its resistance to crack propagation.

In pure tension, the total energy $U$ of an infinite cracked plate (Fig. 2.1a) can be expressed in the following energy components (Whittaker et al. 1992):

$$U = U_t + U_c - W + U_s \tag{2.1}$$

$U$ = Total energy of the infinite cracked plate
$U_t$ = Total initial elastic strain energy of the stressed but un-cracked plate
$U_c$ = Total elastic strain energy release caused by the introduction of a crack of length $2a$ and the relaxation of material above and below the crack
$W$ = Work done by the external forces
$U_s$ = Change in the elastic surface energy due to the formation of new crack surfaces (irreversible).

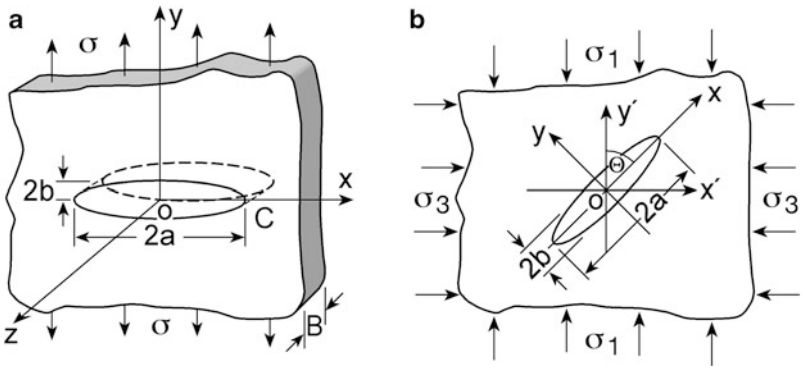


**Fig. 2.1** A crack with the length 2a and width 2b subjected to (**a**) uniform tension; (**b**) biaxial compression (After Whittaker et al. 1992)

The energy components can be obtained separately from the Theory of elasticity:

$$U = \frac{\sigma^2 A}{2E'} \pm \frac{\pi\sigma^2 a^2}{E'} - \frac{\sigma\varepsilon A}{2} + 4a\gamma_s \tag{2.2}$$

$\sigma$ = Tensile stress
$a$ = Half-crack length
$E'$ = Effective Young's modulus: $E' = E$ for plane stress and $E' = E/(1-\nu^2)$ for plane strain
$\nu$ = Poisson's ratio
$A$ = The infinite area of the thin plate of unit thickness ($B = 1$)
$\varepsilon$ = Average axial strain in the plate
$\gamma_S$ = Specific surface energy, i.e. energy required to create a unit area of new crack surface as the crack increases in length.

Two extreme loading conditions can be considered (Fig. 2.2):

(a) Constant displacement (fixed-gripped loading) where the applied loading system suffers zero displacement as the crack extends;
(b) Constant load (dead-weight loading) where the applied force remains constant as the crack extends. In the first case there is no work done by the external force $P$. Therefore, $U_c$ should be negative in Eq. (2.2). In the second case, the work done by the applied load $P$ increases the elastic strain energy release and accordingly $U_c$ should be positive. Boundary conditions in real loading situations are generally somewhere between case (a) and (b).

Note that $W$ must be subtracted from the reversible energy terms, since it does not form part of the plate's potential energy ($U_p = U_t + U_c - W$). The mechanical energy released during incremental crack propagation is also independent of the loading configuration.

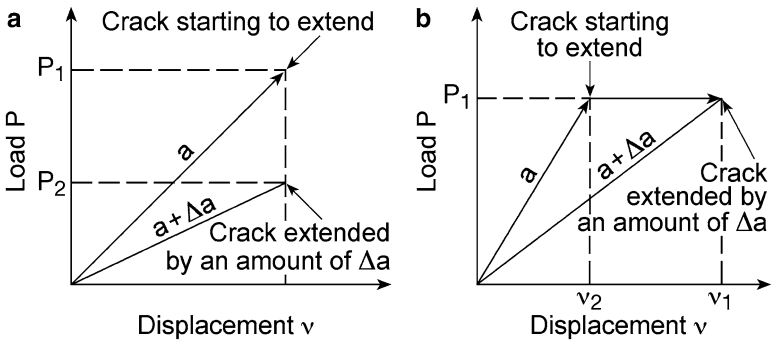


**Fig. 2.2** Load–displacement illustration for crack propagation: (**a**) constant displacement; (**b**) constant load (After Whittaker et al. 1992)

Griffith's idea implies that the critical equilibrium for fracture initiation occurs when:

$$\frac{\partial U}{\partial a} = 0, \tag{2.3}$$

leading to:

$$\sigma\sqrt{\pi \cdot a} = \sqrt{2E' \cdot \gamma_s} \tag{2.4}$$

Equation (2.4) indicates that fracture initiation in ideally brittle solids is governed by the product of an applied far-field stress and the square root of the crack length and by the material properties characterized by Young's modulus $E'$, Poisson's ratio $\nu$ and the specific surface energy $\gamma_s$.

Rearrangement of Eq. (2.4) gives:

$$\frac{\pi\sigma^2 a}{E'} = 2\gamma_s \tag{2.5}$$

The left-hand side of the equation represents the elastic energy per unit crack surface. This energy is available for crack propagation and it defines an important parameter called the strain energy release rate, denoted by $G$ in honour of Griffith. Thus, an expression for the strain energy release rate $G$ can be given as:

$$G = \frac{\pi\sigma^2 a}{E'} \tag{2.6}$$

Griffith's theory for the critical condition for fracture initiation becomes:

$$G = G_C \tag{2.7}$$

where $G_C$ is the critical strain energy released per unit length of crack extension. More generally, G is defined as the derivative of the elastic strain energy release with respect to crack area rather than crack length.

The above formulation describes the simple case of a flat and open elliptical crack subjected perpendicularly to a uniaxial tensile load, assuming that the crack propagates along its own plane. As indicated, the strain energy release rate is the governing parameter for fracture propagation, which is accordingly referred to as the energy balance approach. With his flaw hypothesis and energy balance concept Griffith laid a solid foundation for a general theory of fracture. He further improved his concept known as the 'fracture stress approach' to consider more complicated stress fields involving compression (Fig. 2.1b).

The energy change of crack formation can be considered as entire crack formation from the initially intact rock body, as presented above, or as an incremental extension of an existing crack. In Fig. 2.1a the boundary conditions were obtained as uniform far-field tensile stresses. In practical applications it is often useful to describe crack extension in terms of an external force (point load P), a cross-section of the new crack surface ($d_c$) and elastic compliance ($\lambda$), defined as the load-point displacement ($u_0$) per unit load (e.g. Lawn 1993). Parameter G can be evaluated with respect to new crack area rather than the crack length at equilibrium for crack initiation (Eq. 2.3).

## 2.2 Loading Modes and Associated Displacements

The flat crack tip in an ideally linear elastic brittle material can be subjected to a normal stress $\sigma$, an in-plane shear stress $\tau_i$, an out-of-plane (or anti-plane) shear stress $\tau_o$, or any combination of these. Figure 2.3 illustrates the crack tip coordinates and stress state in terms of both Cartesian and polar coordinates. Different loading configurations at the crack tips lead to different modes of crack tip surface displacements. Three basic loading configurations form the fracture modes of crack tip deformation: Mode I, II and III, as illustrated in Fig. 2.4.

**Mode I** is the opening (or tensional) mode. The crack tip is subjected to a stress $\sigma$ normal to the crack plane and crack faces separate at the crack front so that the displacements of the crack surfaces are perpendicular to the crack plane.

**Mode II** is the edge-sliding mode (or in-plane shearing) where the crack tip is subjected to an in-plane shear stress $\tau_i$ and crack faces slide relative to each other so that the displacements of the crack surfaces are on the crack plane **and** perpendicular to the crack front.

**Mode III** is the tearing (or out-of plane shearing) mode. The crack tip is subjected to an anti-plane shear stress $\tau_o$. The crack faces move relative to each other so that the displacement of the crack surfaces are in the crack plane but parallel to the crack front.

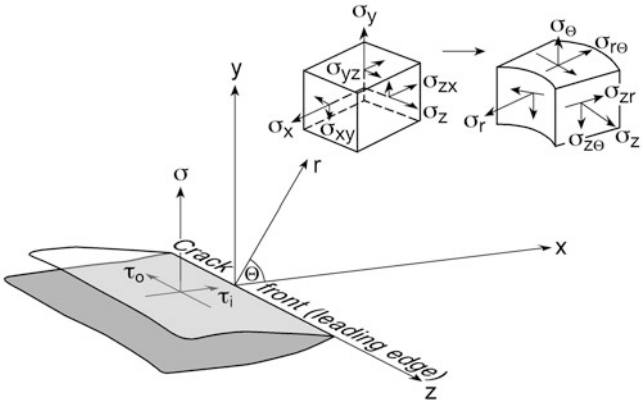


**Fig. 2.3** Crack tip coordinates and stress state in Cartesian and polar coordinate systems (After Whittaker et al. 1992)

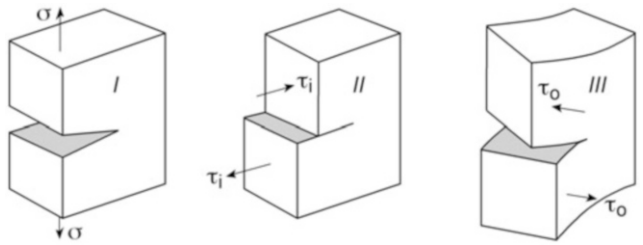


**Fig. 2.4** The three basic modes of loading for a crack and the corresponding crack surface displacements (After Whittaker et al. 1992)

**Mixed-mode loading** is a combination of any of the three loading modes. For example, a combination of Mode I and Mode II loading forms a Mixed-mode I-II loading.

## 2.3 Stress Intensity Approach

Griffith's energy balance approach formed a solid basis for Irwin's (1957) widely applied 'stress intensity factor approach'. This is based on the crack tip characteristic parameter, called the stress intensity factor $K$, which uniquely governs the crack tip stress and displacement fields. For a given cracked body under a certain type and magnitude of loading, $K$ is known and the stresses and displacements can be determined accordingly.

The three stress intensity factors ($K_I$, $K_{II}$, $K_{III}$) each correspond to a loading mode (Fig. 2.4), and each is associated with a unique stress distribution near the fracture

tip. A detailed stress state for an infinite plate containing a central crack of length $2a$ under uniaxial tension, σ, as shown in Fig. 2.1a (Mode I) is given:

$$\begin{bmatrix} \sigma_x \\ \sigma_y \\ \sigma_{xy} \end{bmatrix} = \frac{K_I}{\sqrt{2\pi \cdot r}} cos\frac{\theta}{2} \begin{bmatrix} 1 - sin\frac{\theta}{2} sin\frac{3\theta}{2} \\ 1 + sin\frac{\theta}{2} sin\frac{3\theta}{2} \\ sin\frac{\theta}{2} cos\frac{3\theta}{2} \end{bmatrix} \tag{2.8}$$

Where

$$K_I = \sigma\sqrt{\pi \cdot a} \tag{2.9}$$

and $r$ is the distance from crack tip, $\sigma_z = v(\sigma_x + \sigma_y)$ for plane strain and $\sigma_z = \sigma_{xz} = \sigma_{yz} = 0$ for plane stress. The crack tip stress components are often expressed in terms of polar coordinates in 2D:

$$\begin{bmatrix} \sigma_r \\ \sigma_\theta \\ \sigma_{r\theta} \end{bmatrix} = \frac{K_I}{\sqrt{2\pi \cdot r}} cos\frac{\theta}{2} \begin{bmatrix} 1 + sin^2\frac{\theta}{2} \\ cos^2\frac{\theta}{2} \\ sin\frac{\theta}{2} cos\frac{3\theta}{2} \end{bmatrix} \tag{2.10}$$

where $\sigma_z = v(\sigma_r + \sigma_\theta)$ for plane strain and $\sigma_z = \sigma_{rz} = \sigma_{\theta z} = 0$ for plane stress.

The stress intensity factors $K$ for Mode II and Mode III can be similarly defined as follows:

$$K_{II} = \tau_i\sqrt{\pi \cdot a} \tag{2.11}$$

and

$$K_{III} = \tau_0\sqrt{\pi \cdot a} \tag{2.12}$$

where $\tau_i$ is the far-field in-plane shear stress and $\tau_o$ is the far-field anti-plane shear stress (Fig. 2.5).

The stress intensity factors ($K_{I, II, III}$) are dependent on the magnitude of the far-field stress, the crack size and the loading conditions. In this sense, stress intensity factors can be physically regarded as fracture parameters reflecting the distribution of the stress in a cracked brittle body. Consequently, for any specific mode, with knowledge of the stress intensity factor, the crack tip stresses and displacements can be determined. The derivation of crack tip displacements follows the crack tip stresses using Hooke's law. According to the superposition principle, crack tip stress and displacement components for a Mixed-mode I-II loading can be obtained by superimposing those resulting from pure Mode I and pure Mode II loadings, and likewise for other loading combinations.

Closed-form solutions of the stress and displacement functions can be found for simple loading configurations in fracture mechanics handbooks (Whittaker et al.

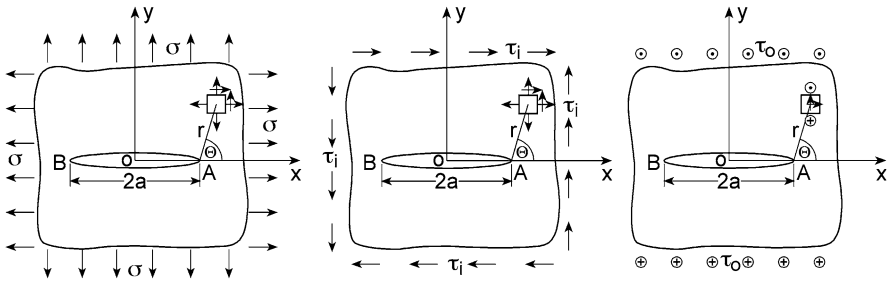


**Fig. 2.5** An infinite plate containing a crack under biaxial tension, in-plane shear and anti-plane shear (After Whittaker et al. 1992)

1992; Lawn 1993). In practice, the geometries of cracked bodies and loading conditions are usually complicated, so closed-form solutions are not generally obtainable. For a cracked body of finite dimensions, numerical methods are usually needed to calculate the stress and displacement distributions. The problem is further compounded when fracture criteria are used to study crack initiation and propagation under compression because the crack faces tend to close and frictional forces must be considered.

According to Eqs. (2.8) and (2.10), the stress approaches infinity (singular) at the tip of a crack (when $r \rightarrow 0$). However, this is practically impossible since no material can bear infinite stress. When the stresses near the crack tip exceed the yield strength $\sigma_{ys}$ the material yields until the stresses drop below $\sigma_{ys}$. Accordingly, a small region around the crack tip is formed in which the material behaves plastically rather than elastically as is usually assumed for the treatment of fracture mechanics problems. This small region has many names depending on the material. For brittle rock, this region is called the 'crack tip micro-cracking zone', the 'crack tip inelastic zone' or the 'Fracture Process Zone (FPZ)'. The presence of this inelastic zone ahead of the crack tip affects the fracture behaviour of the material.

The application of an elastic analysis to a real cracked body depends on the extent of the FPZ. If the FPZ is sufficiently small compared with the geometry of the crack and any other characteristic dimensions of the specimen, then it can be assumed that the linear elastic behaviour prior to failure prevails. If the inelastic zone satisfies the requirement, it is referred to as small-scale yielding (SSY) and the elastic analysis of such a cracked body is termed Linear Elastic Fracture Mechanics (LEFM). In general, conditions for SSY can be met for a number of materials like brittle rocks, glasses and ceramics.

In contrast, if the non-linear elastic deformation is a dominant preceding failure and the non-linear elastic zone is substantial, i.e. large-scale yielding (LSY), then such an analysis is termed Non-Linear Elastic Fracture Mechanics (NEFM). In such analyses, $K$ can no longer characterise the crack tip stress, strain and displacements, since prior to failure the crack tip has become very blunted due to the formation of a yielded region in metals or micro-cracking in rocks. The R-curve concept,

developed from the Griffith energy balance theory, can be used to address fracture problems involving the crack tip non-linear region. J-integral and crack opening displacement approaches can treat fracture problems involving relative large crack tip non-linear zones.

## 2.4 Relationship Between G and K

Irwin (1957) showed the relation between the global energy parameter, the strain energy release rate $G$, and the local crack tip parameter, the stress intensity factor $K$:

$$G_I = \frac{K_I^2}{E'} \tag{2.13}$$

$$G_{II} = \frac{K_{II}^2}{E'} \tag{2.14}$$

$$G_{III} = \frac{K_{III}^2}{2\mu} \tag{2.15}$$

where $G_I$, $G_{II}$ and $G_{III}$ are the strain energy release rates for Mode I, Mode II and Mode III, respectively, E′ is the effective Young's modulus (see Eq. 2.2) and μ is the shear modulus.

$$\mu = \frac{\mathrm{E}}{2(1+\nu)} \tag{2.16}$$

The above relationships between $G$ and $K$ for different modes of loading are obtained by assuming that the crack extends along its own plane. If a crack extends at an angle with respect to the crack plane, the relation between $G$ and $K$ is more complex. When a crack is exposed to a Mixed-mode I-II loading, the overall strain energy release rate, $G$, is a summation of the Mode I strain energy release rate, $G_I$, and that of Mode II, $G_{II}$, which indicates that the strain energy release rates for various loading modes are additive and that the superposition principle applies not only to the same mode but also to different modes. This is similar to the crack tip stress and displacement fields, but unlike the stress intensity factors that are additive only for the same mode (Whittaker et al. 1992). The equivalence of $G$ and $K$ is important and forms the basis for the development of other branches of fracture mechanics involving LEFM, NEFM, dynamic fracture mechanics, statistical fracture mechanics, composite fracture mechanics etc.

## 2.5 Stress Intensity Factor K and the Critical Value $K_C$

If the fracture initiation is expressed for Mode I loading in terms of the stress intensity factor, then crack initiation occurs when the stress intensity factor reaches its critical value called the Mode I plane strain fracture toughness, $K_{IC}$:

$$K_I = K_{IC} \tag{2.17}$$

Similarly, in Mode II, when the crack tip stress intensity factor, $K_{II}$, reaches the Mode II plane strain fracture toughness, $K_{IIC}$, cracking will initiate. Fracture toughness is basically a property of the material reflecting its resistance to physical macroscopic separation through crack propagation. Conceptually, $K_C$ is a constant, and since $K_C$ can be obtained by laboratory testing with specified methods and using specimens with known corresponding stress intensity factors, this approach has gained popularity.

Analyses related to Mixed-mode loading conditions are common. For example, for an angled crack subjected to a uniform far-field compressive stress, both $K_I$ and $K_{II}$ at the crack tip must be considered (Fig. 2.1b). According to the superposition principle, the crack tip stress and displacement components can be obtained by superimposing those resulting from pure Mode I and pure Mode II loadings.

Crack propagation will occur when a certain combination of $K_I$ and $K_{II}$, f($K_I$, $K_{II}$), reaches a critical value, f($K_I$, $K_{II}$)$_C$. The quantity f($K_I$, $K_{II}$)$_C$ is known as the Mixed-mode I-II fracture toughness envelope or the $K_I$–$K_{II}$ envelope. The question is: what is the exact $K_I$−$K_{II}$ envelope as a criterion for Mixed-mode I-II cracking? The development of a fracture criterion to predict the initiation and propagation of individual cracks in rock subjected to arbitrary loading conditions is of tremendous importance for rock engineering. With the assumption that crack propagation is governed by a specific parameter, various fracture criteria have been established.

The three fundamental fracture criteria appear to be the most frequently cited approaches in the literature: maximum tangential stress, maximum energy release rate and minimum strain energy density. These criteria can all predict the propagation and direction of crack initial extension under Mixed-mode I-II loading. Descriptions of a number of Mixed-mode fracture criteria and comparisons of predicted results are presented in Whittaker et al. (1992), Shen (1993) and Rao (1999). Shen and Stephansson (1993a) suggest a criterion for fracture propagation under Mixed-mode I-II loading based on the maximum energy release rate. This criterion is further explained in Sect. 3.3.

## 2.6 Stress Intensity Factor and Crack Velocity

The time dependency of crack growth is due to rate-controlled processes acting at the tips of cracks where stress concentration exists. Propagation velocities can vary

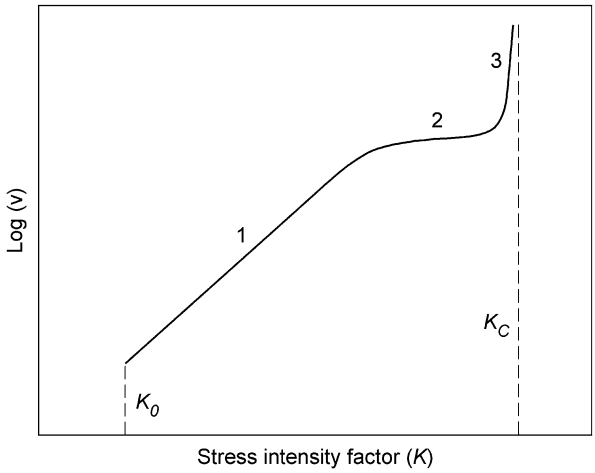


**Fig. 2.6** Schematic stress intensity factor/crack velocity diagram for subcritical tensile crack on glass (After Atkinson 1984)

over many orders of magnitude as a function of the stress intensity. Experimental studies on rocks have been made at crack velocities down to $10^{-9}$ m/s and $K$ values less than $0.5\,K_C$ (Atkinson and Meredith 1987).

Slow crack velocity is due to subcritical crack growth, SCG. Subcritical crack growth can be caused by several competing mechanisms, such as stress corrosion, diffusion, dissolution, ion exchange and micro-plasticity. One particular mechanism will be dominant under specific ranges of environmental and material conditions. In its most elementary form, the theory of stress corrosion postulates that for crystalline silicates and for silicate glasses the strained Si-O bonds at crack tips can react more readily with environmental agents than can unstrained bonds, because of a strain-induced reduction in the overlap of atomic orbital.

SCG velocity increases as ($G$ or $K$) is increased. The exact form of the relationship is

$$v = \mathrm{f}\,(G \text{ or } K) \tag{2.18}$$

and it depends on the crack growth mechanisms, until the critical value $(G \text{ or } K)_c$ is achieved. At this critical level, the crack propagates rapidly accelerating to speeds approaching a terminal velocity that is governed by the speed of the elastic waves.

Figure 2.6 shows the three regions of behaviour from SCG studies on glass. The SCG mechanisms and the interaction between the environment and the microstructure of the solid will control the details of the stress intensity factor/crack velocity curve. The schematic figure is presented merely as a starting point and its shape varies considerably when the effective factors such as temperature, pore pressure, pH, etc., are changed (Atkinson 1984).

The behaviour in Region 1 is controlled by the rate of stress corrosion reactions at the crack tips. Region 2 is controlled by the rate of transport of reactive species to the crack tips. In Region 3, crack growth is mainly controlled by mechanical rupture and is relatively insensitive to chemical environment. Most experimental data on subcritical tensile crack propagation in geological materials appear to be in Region 1 or Region 3 of the schematic stress intensity factor/crack velocity curve. Region 2 is observed infrequently in rocks, although apparently it was found in tests on black gabbro in water (Atkinson 1984).

It is assumed that a threshold exists below which no significant crack propagation can occur through stress corrosion ($K_0$, stress corrosion limit). The value of this parameter is a function of the material's fracture properties and environment. It is likely that $K_0$ is a small fraction of $K_C$, about 10–20 %. However, experiments have not yet confirmed the existence of a stress corrosion limit in ceramics and rocks (Atkinson 1984).

## 2.7 Charles' Law

Charles explored the delayed failure of glass in relation to its sensitivity to atmospheric corrosion (1958). His study investigated the rate of corrosion layer formation of lime glass rods treated in saturated water vapour. An analysis of the failure process was presented based on the concept that inherent surface flaws grow by corrosive mechanisms to critical dimensions through a reaction between atmospheric water vapour and the components of glass. The rate of this reaction is determined by local stress conditions and by the temperature, pressure and composition of the surrounding atmosphere. Experimental work shows a close relationship between the temperature dependence of the failure process and that of the self-diffusion of sodium ions in bulk glass. It is concluded that the alkali content is responsible for the very low long-term strengths of most inorganic glasses.

Charles assumed a stress power relationship to describe the crack velocity controlled by the rate of stress corrosion reactions at the crack tip:

$$v(T) = k'(\sigma_m)^n + k \tag{2.19}$$

where

$v$ = Penetration velocity of crack tip
$T$ = Temperature
$\sigma_m$ = Tensile stress at crack tip
$k$ = Corrosion rate of the material under zero stress, and
$k'$ and $n$ are constants.

For stress-activated corrosion, Charles further assumed that the temperature dependence of the flaw growth process takes the form of an Arrhenius-type

relationship. Bearing in mind that the stress at the crack tip is related to crack size and geometry, he suggested the following crack growth relationship:

$$v \approx C\left(\frac{x}{x_{cr}}\right)^{n/2} e^{-A/RT} \tag{2.20}$$

where

$C =$ Constant
$x$, $x_{cr} =$ Crack size and critical crack size
$A =$ Activation energy term, and
$R =$ Gas constant.

A variety of mathematical functions can be fitted to the laboratory data when describing the stress intensity as a function of subcritical crack velocity. Subcritical crack growth data can be expressed with the power law, exponential and hyperbolic functions.

## References

Atkinson BK (1984) Subcritical crack growth in geological materials. J Geophys Res 89: 4077–4114

Atkinson BK, Meredith PG (1987) The theory of subcritical crack growth with applications to minerals and rock. In: Atkinson BK (ed) Fracture mechanics of rock. Academic Press, London, pp 111–162

Bieniawski ZT (1967) Mechanics of brittle fracture of rock. Part I, II and III. Int J Rock Mech Min Sci 4(3):95–430

Charles RJ (1958) Static fatigue of glass. J Appl Phys 1958(29):1549–1560

Griffith AA (1920) The phenomena of rupture and flow in solids. Phil Trans R Soc Lond Ser A 221:163–198

Irwin GR (1957) Analysis of stresses and strains near the end of a crack. J Appl Mech 24:361–364

Lawn B (1993) Fracture of brittle solids, 2nd edn. Cambridge University Press, Cambridge

Rao Q (1999) Pure shear fracture of brittle rock – a theoretical and laboratory study. Ph.D. thesis 1999:08, Lulea University of Technology

Shen B (1993) Mechanics of fractures and intervening brisges in hard rocks. Doctorate thesis, Royal Institute of Technology, ISBN 91-7170-140-0

Shen B, Stephansson O (1993a) Modification of the G-criterion of crack propagation in compression. Int J Eng Fract Mech 47(2):177–189

Whittaker BN, Singh RN, Sun G (1992) Rock fracture mechanics: principles, design and applications, vol 71, Developments in geotechnical engineering. Elsevier, Amsterdam

# Chapter 3
# Numerical Method

**Abstract** The FRACOD code is based on Boundary Element Method principles. It utilizes the Displacement Discontinuity Method (DDM), one of the three commonly used boundary element methods. In the FRACOD code, a fracture criterion, the F-criterion, is incorporated into the numerical method for simulating fracture propagation. This chapter describes the numerical method DDM, the F-criterion and modelling the initiation and propagation of fractures.

## 3.1 Displacement Discontinuity Method (DDM)

A crack or fracture always has two surfaces or boundaries, one effectively coinciding with the other. Conventional boundary element methods, such as the Direct Integration Method, will treat the two surfaces separately and use two elements for each segment of the crack. The Displacement Discontinuity Method (DDM) considers the two sides of a crack surface as one crack element, or DD element, and hence is much more efficient in representing fracture problems. The Displacement Discontinuity Method (DDM) was developed by Crouch (1976) to deal with problems of discontinuities. The DDM is based on the analytical solution to the problem of a constant discontinuity in displacement over a finite line segment in the x, y plane of an infinite and elastic solid. Physically, one may imagine a displacement discontinuity as a line crack whose opposing surfaces have been displaced relative to one another (see Fig. 3.1).

### *3.1.1 DDM in an Infinite Solid*

The problem of a constant displacement discontinuity over a finite line segment in the x, y plane of an infinite elastic solid is specified by the condition that the

B. Shen et al., *Modelling Rock Fracturing Processes: A Fracture Mechanics Approach Using FRACOD*, DOI 10.1007/978-94-007-6904-5_3,

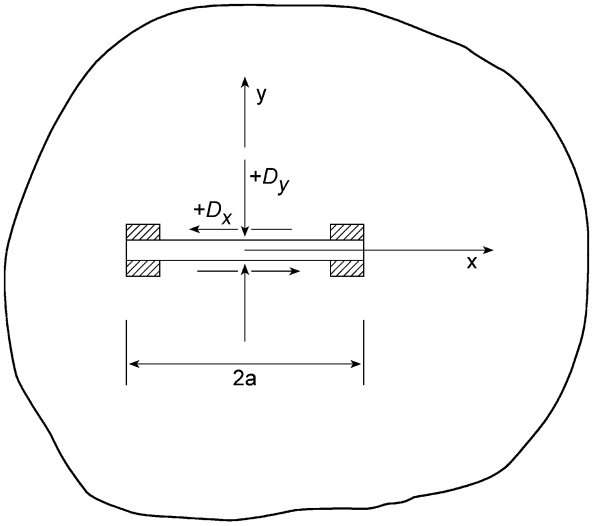


**Fig. 3.1** Constant displacement discontinuity components $D_x$ and $D_y$ of a fracture with the length 2a in DDM

displacements be continuous everywhere except over the line segment in question. The line segment may be chosen to occupy a certain portion of the x-axis, say the portion $|x| \leq a$, $y = 0$. If we consider this segment to be a line crack, we can distinguish its two surfaces by saying that one surface is on the **positive** side of $y = 0$, denoted $y = 0_+$, and the other is on the **negative** side, denoted $y = 0_-$. In crossing from one side of the line segment to the other, the displacement undergoes a constant specified change in value $D_i = (D_x, D_y)$.

We will define the displacement discontinuity $D_i$ as the difference in displacement between the two sides of the segment as follows:

$$\begin{aligned} D_x &= u_x(x, 0_-) - u_x(x, 0_+) \\ D_y &= u_y(x, 0_-) - u_y(x, 0_+) \end{aligned} \tag{3.1}$$

Because $u_x$ and $u_y$ are positive in positive $x$ and $y$ coordinate direction, it follows that the $D_x$ and $D_y$ are positive as illustrated in Fig. 3.1.

The solution is given by Crouch (1976), and Crouch and Starfield (1983). The displacement and stresses can be written as:

$$\begin{aligned} u_x &= D_x \lfloor 2(1-\nu) f_{,y} - y f_{,xx} \rfloor + D_y \lfloor -(1-2\nu) f_{,x} - y f_{,xy} \rfloor \\ u_y &= D_x \lfloor (1-2\nu) f_{,x} - y f_{,xy} \rfloor + D_y \lfloor 2(1-\nu) f_{,y} - y f_{,yy} \rfloor \end{aligned} \tag{3.2}$$

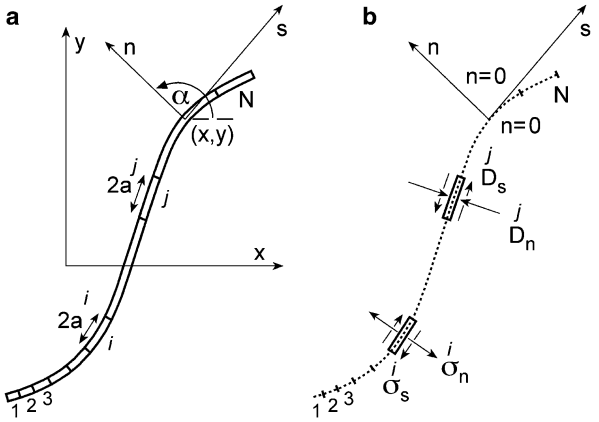


**Fig. 3.2** Representation of a curved crack by N elemental displacement discontinuities

and

$$\begin{aligned}
\sigma_{xx} &= 2GD_x\lfloor +2f_{,xy} + yf_{,xyy}\rfloor + 2GD_y\lfloor f_{,yy} + yf_{,yyy}\rfloor \\
\sigma_{yy} &= 2GD_x\left[-yf_{,xyy}\right] + 2GD_y\left[f_{,yy} + yf_{,yyy}\right] \\
\sigma_{xy} &= 2GD_x\left[f_{,yy} + yf_{,yyy}\right] + 2GD_y\left[-yf_{,xyy}\right]
\end{aligned} \tag{3.3}$$

where $f_{,x}$ represents the derivative of function $f(x,y)$ against x, similarly as for $f_{,y}$, $f_{,xy}, f_{,xxy}$ etc. Function $f(x,y)$ in these equations is given by:

$$\begin{aligned}
f(x,\ y) = \frac{-1}{4\pi(1-\nu)}\Bigg[ & y\left(\arctan\frac{y}{x-a} - \arctan\frac{y}{x+a}\right) \\
& - (x-a)\ln\sqrt{[(x-a)^2+y^2]} + (x+a)\ln\sqrt{[(x+a)^2+y^2]}\Bigg]
\end{aligned} \tag{3.4}$$

### *3.1.2 Numerical Procedure*

For any crack shape, including curves, we assume the shape can be represented with sufficient accuracy by N straight segments, joined end by end. The positions of the segments are specified with reference to the x, y coordinate system shown in Fig. 3.2. If the surfaces of the crack are subjected to stress (for example, a uniform fluid pressure), they will displace relative to one another. The displacement discontinuity method gives a discrete approximation to the smooth distribution

of relative displacement that exits in reality. The discrete approximation is found with reference to the N subdivisions of the crack depicted in Fig. 3.2a. Each of the subdivisions is a boundary element and represents an elemental displacement discontinuity.

The elemental displacement discontinuities are defined with respect to the local coordinates $s$ and $n$ indicated in Fig. 3.2.

Figure 3.2b depicts a single elemental displacement discontinuity at $j$th segment of the crack. The components of discontinuity in the $s$ and $n$ directions at this segment are designated as $\overset{j}{D}_s$ and $\overset{j}{D}_n$ and are defined as follows:

$$\begin{aligned} \overset{j}{D}_s &= \overset{j}{u}_s^- - \overset{j}{u}_s^+ \\ \overset{j}{D}_n &= \overset{j}{u}_n^- - \overset{j}{u}_n^+ \end{aligned} \tag{3.5}$$

In these definitions, $\overset{j}{u}_s$ and $\overset{j}{u}_n$ refer to the shear ($s$) and normal ($n$) displacement of the $j$th segment of the crack. The superscripts '+' and '−' denote the positive and negative surfaces of the crack with respect to local coordinate $n$.

The local displacements $\overset{j}{u}_s$ and $\overset{j}{u}_n$ form the two components of a vector. They are positive in the positive direction of $s$ and $n$, irrespective of whether we are considering the positive or negative surface of the crack. As a consequence, it follows from Eq. (3.5) that the normal component of displacement discontinuity $\overset{j}{D}_n$ is positive if the two surfaces of the crack displace toward one another. Similarly, the shear component $\overset{j}{D}_s$ is positive if the positive surface of the crack moves to the left with respect to the negative surface.

The effects of a single elemental displacement discontinuity on the displacements and stresses at an arbitrary point in the infinite solid can be computed from the results for Sect. 3.1.1, provided we transform the equations to suit the position and orientation of the line segment in question. In particular, the shear and normal stresses at the midpoint of the $i$th element in Fig. 3.2b can be expressed in terms of the displacement discontinuity components at the $j$th element as follows:

$$\left.\begin{aligned} \overset{i}{\sigma}_s &= \overset{ij}{A}_{ss}\,\overset{j}{D}_s + \overset{ij}{A}_{sn}\,\overset{j}{D}_n \\ \overset{i}{\sigma}_n &= \overset{ij}{A}_{ns}\,\overset{j}{D}_s + \overset{ij}{A}_{nn}\,\overset{j}{D}_n \end{aligned}\right\} i = 1 \ to \ N \tag{3.6}$$

Where $\overset{ij}{A}_{ss}$, etc., are the boundary influence coefficients for the stresses. For example, the coefficient $\overset{ij}{A}_{ns}$ gives the normal stress at the midpoint of the $i$th element (i.e. $\sigma_n^i$) due to a constant unit shear displacement discontinuity over the $j$th element (i.e. $\overset{j}{D}_s = 1$).

Returning to the crack problem depicted in Fig. 3.2b, we locate an elemental displacement discontinuity at each of the N segments along the curved crack and write, from Eq. (3.6):

$$\left.\begin{aligned} \overset{i}{\sigma}_s &= \sum_{j=1}^{N} \overset{ij}{A}_{ss}\, \overset{j}{D}_s + \sum_{j=1}^{N} \overset{ij}{A}_{sn}\, \overset{j}{D}_n \\ \overset{i}{\sigma}_n &= \sum_{j=1}^{N} \overset{ij}{A}_{ns}\, \overset{j}{D}_s + \sum_{j=1}^{N} \overset{ij}{A}_{nn}\, \overset{j}{D}_n \end{aligned}\right\} \; i = 1 \; to \; N \tag{3.7}$$

If we specify the values of the stress $\overset{j}{\sigma}_s$ and $\overset{j}{\sigma}_n$ for each element of the crack, then Eq. (3.7) is a system of $2N$ simultaneous linear equations with $2N$ unknowns, namely the elemental displacement discontinuity components $\overset{j}{D}_s$ and $\overset{j}{D}_n$. We can find the displacements and stresses at designated points in the body by using the principle of superposition. In particular, the displacements along the crack in Fig. 3.2a are given as:

$$\left.\begin{aligned} \overset{i}{u}_s &= \sum_{j=1}^{N} \overset{ij}{B}_{ss}\, \overset{j}{D}_s + \sum_{j=1}^{N} \overset{ij}{B}_{sn}\, \overset{j}{D}_n \\ \overset{i}{u}_n &= \sum_{j=1}^{N} \overset{ij}{B}_{ns}\, \overset{j}{D}_s + \sum_{j=1}^{N} \overset{ij}{B}_{nn}\, \overset{j}{D}_n \end{aligned}\right\} \; i = 1 \; to \; N \tag{3.8}$$

where $\overset{ij}{B}_{ss}$, etc., are the boundary influence coefficients for the displacements. The displacements are discontinuous when passing from one side of the $j$th element to the other, so we must distinguish between these two sides when computing the influence coefficients in Eq. (3.8). The diagonal terms of the influence coefficients in these equations have the values:

$$\begin{aligned} \overset{ij}{B}_{sn} &= \overset{ij}{B}_{ns} = 0 \\ \overset{ij}{B}_{ss} &= \overset{ij}{B}_{nn} = -\frac{1}{2}(n \to 0_+); + \frac{1}{2}(n \to 0_-); \end{aligned} \tag{3.9}$$

The remaining coefficients (i.e. the ones for which $i \neq j$) are continuous and they can be obtained by using Eqs. (3.1, 3.2 and 3.3) in Sect. 3.1.1.

Displacements $\overset{i}{u}_s$ and $\overset{i}{u}_n$ in Eq. (3.8) will exhibit constant discontinuities $\overset{i}{D}_s$ and $\overset{i}{D}_n$, as required.

## 3.2 Simulation of Rock Discontinuities

For a rock discontinuity (crack, joint, etc.) in an infinite elastic rock mass, the system of governing Eq. (3.7) can be written as:

$$\left.\begin{aligned} \overset{i}{\sigma}_s &= \sum_{j=1}^{N} \overset{ij}{A}_{ss}\, \overset{j}{D}_s + \sum_{j=1}^{N} \overset{ij}{A}_{sn}\, \overset{j}{D}_n - \left(\overset{i}{\sigma}_s\right)_0 \\ \overset{i}{\sigma}_n &= \sum_{j=1}^{N} \overset{ij}{A}_{ns}\, \overset{j}{D}_s + \sum_{j=1}^{N} \overset{ij}{A}_{nn}\, \overset{j}{D}_n - \left(\overset{i}{\sigma}_n\right)_0 \end{aligned}\right\} \; i = 1 \; to \; N \tag{3.10}$$

where $\overset{i}{\sigma}_s$ and $\overset{i}{\sigma}_n$ represent the shear and normal stresses of the $i$th element respectively; $\left(\overset{i}{\sigma}_s\right)_0$ and $\left(\overset{i}{\sigma}_n\right)_0$ are the far-field stresses transformed in the crack shear and normal directions. $\overset{ij}{A}_{ss}, \ldots, \overset{ij}{A}_{nn}$ are the influence coefficients, and $\overset{j}{D}_s$, $\overset{j}{D}_n$ represent displacement discontinuities of $j$th element which are unknowns in the system of equations.

A rock discontinuity has three states: open, in elastic contact or sliding. The system of governing Eq. (3.10) developed for an open crack can be easily extended to the case for cracks in contact and sliding. For different crack states, their systems of governing equations can be rewritten in the following ways, depending on the shear and normal stresses ($\overset{i}{\sigma}_s$ and $\overset{i}{\sigma}_n$) of the crack.

For an open crack we have $\overset{i}{\sigma}_s = \overset{i}{\sigma}_n = 0$, therefore the system of governing Eq. (3.10) can be rewritten as:

$$\left.\begin{aligned} \overset{i}{\sigma}_s = 0 &= \sum_{j=1}^{N} \overset{ij}{A}_{ss}\, \overset{j}{D}_s + \sum_{j=1}^{N} \overset{ij}{A}_{sn}\, \overset{j}{D}_n - \left(\overset{i}{\sigma}_s\right)_0 \\ \overset{i}{\sigma}_n = 0 &= \sum_{j=1}^{N} \overset{ij}{A}_{ns}\, \overset{j}{D}_s + \sum_{j=1}^{N} \overset{ij}{A}_{nn}\, \overset{j}{D}_n - \left(\overset{i}{\sigma}_n\right)_0 \end{aligned}\right\} \; i = 1 \; to \; N \tag{3.11}$$

When the two crack surfaces are in elastic contact, the magnitude of $\overset{i}{\sigma}_s$ and $\overset{i}{\sigma}_n$ will depend on the crack stiffness ($K_s$, $K_n$) and the displacement discontinuities ($\overset{j}{D}_s$, $\overset{j}{D}_n$)

$$\begin{aligned} \overset{i}{\sigma}_s &= K_s\, \overset{i}{D}_s \\ \overset{i}{\sigma}_n &= K_n\, \overset{i}{D}_n \end{aligned} \tag{3.12}$$

where $K_s$ and $K_n$ are the crack shear and normal stiffness, respectively. Substituting Eq. (3.12) into Eq. (3.10) and carrying out simple mathematical manipulation, the system of governing equations then becomes:

$$\left.\begin{aligned} 0 &= \sum_{j=1}^{N} \overset{ij}{A}_{ss} \overset{j}{D}_s + \sum_{j=1}^{N} \overset{ij}{A}_{sn} \overset{j}{D}_n - \left(\overset{i}{\sigma}_s\right)_0 - K_s \overset{i}{D}_s \\ 0 &= \sum_{j=1}^{N} \overset{ij}{A}_{ns} \overset{j}{D}_s + \sum_{j=1}^{N} \overset{ij}{A}_{nn} \overset{j}{D}_n - \left(\overset{i}{\sigma}_n\right)_0 - K_n \overset{i}{D}_n \end{aligned}\right\} \; i = 1 \; to \; N \tag{3.13}$$

For a crack with its surfaces sliding

$$\begin{aligned} \overset{i}{\sigma}_n &= K_n \overset{i}{D}_n \\ \overset{i}{\sigma}_s &= \pm \overset{i}{\sigma}_n \tan\phi = \pm K_n \overset{i}{D}_n \tan\phi \end{aligned} \tag{3.14}$$

where $\phi$ is the friction angle of the crack surfaces. The sign of $\overset{i}{\sigma}_s$ depends on the sliding direction. Consequently, the system of Eq. (3.10) can be presented as:

$$\left.\begin{aligned} 0 &= \sum_{j=1}^{N} \overset{ij}{A}_{ss} \overset{j}{D}_s + \sum_{j=1}^{N} \overset{ij}{A}_{sn} \overset{j}{D}_n - \left(\overset{i}{\sigma}_s\right)_0 \pm K_n \overset{i}{D}_n \tan\phi \\ 0 &= \sum_{j=1}^{N} \overset{ij}{A}_{ns} \overset{j}{D}_s + \sum_{j=1}^{N} \overset{ij}{A}_{nn} \overset{j}{D}_n - \left(\overset{i}{\sigma}_n\right)_0 - K_n \overset{i}{D}_n \end{aligned}\right\} \; i = 1 \; to \; N \tag{3.15}$$

The displacement discontinuities ($\overset{j}{D}_s$, $\overset{j}{D}_n$) of the crack are obtained by solving the system of governing equations using conventional numerical techniques, e.g. Gauss elimination method. If the crack is open, the stresses ($\overset{i}{\sigma}_s$, $\overset{i}{\sigma}_n$) on the crack surfaces are zero. If the crack surfaces are in contact or sliding, they can be calculated by Eq. (3.12) or Eq. (3.14).

The state of each crack (joint) element can be determined using the Mohr-Coulomb failure criterion:

1. Open joint: $\sigma_n > 0$
2. Elastic joint: $\sigma_n < 0, \; |\sigma_s| < c + |\sigma_n| \, tan\,\phi$
3. Sliding joint: $\sigma_n < 0, \; |\sigma_s| \geq c + |\sigma_n| \, tan\,\phi$

where a compressive stress is taken to be negative and $c$ is cohesion. If the joint has experienced sliding, then cohesion is zero, $c = 0$.

Most joints have dilation during shear movement. As a result, the joint tends to open during shearing if there is no restriction in joint normal displacement.

However, with confinement in normal direction, the tendency of open movement will be absorbed by the normal stiffness of the joint, leading to a high normal stress but very little change in normal displacement.

When the dilation angle of a joint ($\phi_d$) is considered, the additional normal stress caused by the dilation is calculated by $\Delta \overset{i}{\sigma}_n = K_n \overset{i}{D}_s \tan\phi_d$

For dilation joints, Eq. (3.15) becomes

$$\left.\begin{aligned} 0 &= \sum_{j=1}^{N} \overset{ij}{A}_{ss} \overset{j}{D}_s + \sum_{j=1}^{N} \overset{ij}{A}_{sn} \overset{j}{D}_n - \left(\overset{i}{\sigma}_s\right)_0 \pm K_n \overset{i}{D}_n \tan\phi \\ 0 &= \sum_{j=1}^{N} \overset{ij}{A}_{ns} \overset{j}{D}_s + \sum_{j=1}^{N} \overset{ij}{A}_{nn} \overset{j}{D}_n - \left(\overset{i}{\sigma}_n\right)_0 - K_n \overset{i}{D}_n - K_n \overset{i}{D}_s \tan\phi_d \end{aligned}\right\} \cdot i = 1 \cdot to \cdot N \tag{3.16}$$

A joint with higher dilation angle is more difficult to shear because any shear movement will be transformed into higher joint normal stress and hence high friction resistance.

## 3.3 Fracture Propagation Criterion

In modelling fracture propagation in rock masses where both tensile and shear failure are common, a fracture criterion is needed for predicting both Mode I and Mode II fracture propagation. Existing fracture criteria in the macro-scale approach to fracture propagation can be classified into two groups: the principal stress (strain)-based criteria and the energy-based criteria. The first group consists of the Maximum Principal Stress Criterion and the Maximum Principal Strain Criterion. The second group includes the Maximum Strain Energy Release Rate Criterion (G-criterion) and the Minimum Strain Energy Density Criterion (S-criterion). The principal stress (strain)-based criteria are only applicable to the Mode I fracture propagation that relies on the principal tensile stress (strain). To be applied for the Mode II propagation, a fracture criterion has to consider not only the principal stress (strain) but also the shear stress (strain). From this point of view, the energy-based criteria seem to be applicable for both Mode I and II propagation because the strain energy in the vicinity of a fracture tip is related to all the components of stress and strain.

Both the G-criterion and the S-criterion have been examined for application to Mode I and Mode II propagation (Shen and Stephansson 1993b), and neither of them is directly suitable. In a study by Shen and Stephansson (1993b) the original G-criterion has been improved and extended. The original G-criterion states that when the strain energy release rate in the direction of the maximum G-value reaches the critical value $G_c$, the fracture tip will propagate in that direction. It does not distinguish between Mode I and Mode II fracture toughness of energy ($G_{Ic}$ and $G_{IIc}$).

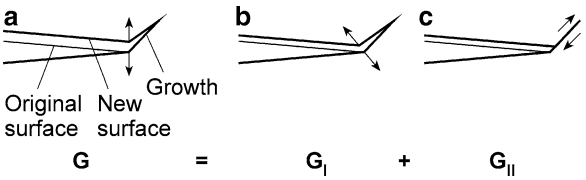


**Fig. 3.3** Definition of strain energy release rate $G_I$ and $G_{II}$ for fracture growth. (**a**) $G$, growth has both open and shear displacement; (**b**) $G_I$, growth has only open displacement; (**c**) $G_{II}$, growth has only shear displacement

In fact, for most engineering materials, the Mode II fracture toughness is much higher than the Mode I toughness due to differences in the failure mechanism. In rocks, for instance, $G_{IIc}$ is found in laboratory scale to be at least twice as high as $G_{Ic}$ considering the effect of confinement (Backers 2005). Applied to Mixed Mode I and Mode II fracture propagation, the G-criterion is difficult to use since the critical value $G_c$ must be carefully chosen between $G_{Ic}$ and $G_{IIc}$.

A modified G-criterion, namely the F-criterion, was proposed (Shen and Stephansson, 1993b). Using the F-criterion the resultant strain energy release rate ($G$) at a fracture tip is divided into two parts, one due to Mode I deformation ($G_I$) and the other due to Mode II deformation ($G_{II}$). The sum of their normalized values is then used to determine the failure load and its direction. $G_I$ and $G_{II}$ can be expressed as follows (Fig. 3.3): if a fracture grows a unit length in an arbitrary direction and the new fracture opens without any surface shear dislocation, the strain energy loss in the surrounding body due to the fracture growth is $G_I$. Similarly, if the new fracture has only a surface shear dislocation, the strain energy loss is $G_{II}$. The principles of the F-criterion can be stated as follows, (Fig. 3.3):

1. In an arbitrary direction (θ) at a fracture tip, an F-value exists which is calculated:

$$F(\theta) = \frac{G_I(\theta)}{G_{Ic}} + \frac{G_{II}(\theta)}{G_{IIc}} \tag{3.17}$$

2. The possible direction of propagation of the fracture tip is the direction ($\theta = \theta_0$) for which the F-value reaches its maximum:

$$F(\theta)\,|_{\theta=\theta_0} = \max. \tag{3.18}$$

3. When the maximum F-value reaches 1.0, the fracture tip will propagate:

$$F(\theta)\,|_{\theta=\theta_0} = 1.0 \tag{3.19}$$

The F-criterion is actually a more general form of the G-criterion and allows simultaneous consideration of Mode I and Mode II propagation. In most cases, the F-value reaches its peak either in the direction of maximum tension ($G_{Ic} =$ maximum while $G_{IIc} = 0$) or in the direction of maximum shearing

($G_{IIc}$ = maximum while $G_{Ic} = 0$). This means that a fracture propagation of a finite length (the length of an element, for instance) is either pure Mode I or pure Mode II. However, the fracture growth may alternate between Mode I and Mode II during an ongoing process of propagation, and hence form a path that generally exhibits mixed-mode failure.

## 3.4 Fracture Propagation Using DDM

The key step in modelling fracture propagation using the F-criterion is determining the strain energy release rates of Mode I ($G_I$), and Mode II ($G_{II}$) at a given fracture tip. As $G_I$ and $G_{II}$ are only the special cases of $G$, the next question is how to use DDM to calculate the strain energy release rate $G$.

The G-value, by definition, is the change of the strain energy in a linearly elastic body when the crack has grown one unit length. Therefore, to obtain the G-value the strain energy must first be estimated.

By definition, the strain energy, $W$, in a linearly elastic body is

$$W = \int\int\int_{\mathrm{v}} \frac{1}{2}\sigma_{ij}\,\varepsilon_{ij}\,dV \tag{3.20}$$

where $\sigma_{ij}$ and $\varepsilon_{ij}$ are the stress and strain tensors, and $V$ is the body's volume. The strain energy can also be calculated from the stresses and displacements along its boundary:

$$W = \frac{1}{2}\int_{\mathrm{s}} (\sigma_s u_s + \sigma_n u_n) ds \tag{3.21}$$

where $\sigma_s$,$\sigma_n$, $u_s$, $u_n$ are the stresses and displacements in shear and normal direction of the boundary of an elastic body. Applying Eq. (3.21) to the crack system in an infinite body with far-field stresses $(\sigma_s)_0$ and $(\sigma_n)_0$ in the shear and normal direction relative to the crack, the strain energy, $W$, in the infinite elastic body is calculated:

$$W = \frac{1}{2}\int_0^a [(\sigma_s - (\sigma_s)_0)D_s + (\sigma_n - (\sigma_n)_0)D_n]\,da \tag{3.22}$$

where $a$ is the crack length, $D_s$ is the shear displacement discontinuity and $D_n$ is the normal displacement discontinuity of the crack. When DDM is used to calculate the stresses and displacement discontinuities of the crack, the strain energy can also be written in terms of the element length ($a^i$) and the stresses and displacement discontinuities of the $i$th element of the crack.

$$W \approx \frac{1}{2}\sum_i \left(\overset{i}{a}\left(\overset{i}{\sigma}_s - \left(\overset{i}{\sigma}_s\right)_0\right)\overset{i}{D}_s + \overset{i}{a}\left(\overset{i}{\sigma}_n - \left(\overset{i}{\sigma}_n\right)_0\right)\overset{i}{D}_n\right) \tag{3.23}$$

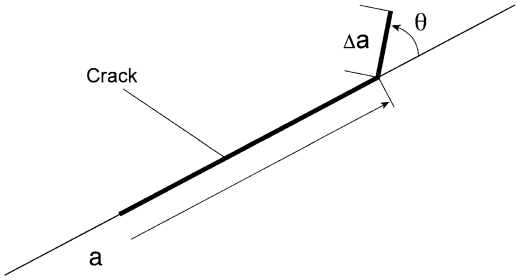


**Fig. 3.4** Fictitious crack increment $\Delta a$ in direction $\theta$ with respect to the initial crack orientation and initial crack length $a$

The G-value can be estimated as:

$$G(\theta) = \frac{\partial W}{\partial a} \approx \frac{[W(a + \Delta a) - W(a)]}{\Delta a} \tag{3.24}$$

where $W(a)$ is the strain energy governed by the original crack, whereas $W(a + \Delta a)$ is the strain energy governed by both the original crack, $a$, and its small extension, $a$ (Fig. 3.4) where a 'fictitious' element is introduced to the tip of the original crack with the length $a$ in the direction $\theta$. Both $W(a)$ and $W(a + \Delta a)$ can be determined easily by directly using DDM and Eq. (3.24).

In the above calculation, if we limit the shear displacement of the "fictitious" element to zero, the result obtained using Eq. (3.24) will be $G_I(\theta)$. Similarly, if we restrict the normal displacement of the "fictitious" element to zero, the result obtained will be $G_{II}(\theta)$. After obtaining both $G_I(\theta)$ and $G_{II}(\theta)$, the F-value in Eq. (3.17) can be calculated using the fracture toughness values $G_{Ic}$ and $G_{IIc}$ of a given rock type.

## 3.5 Fracture Initiation Criterion in FRACOD

In addition to the propagation of existing fractures, new fractures (cracks) may initiate at boundaries or inside an intact rock. This section describes the criteria used to detect fracture initiation and presents the probability of new crack formation.

### *3.5.1 Fracture Initiation Criterion*

Fracture initiation is a complex process. Often it starts with micro-crack formation. These micro-cracks coalesce and finally form macro-fractures. Because FRACOD is designed to simulate the fracturing process in macro-scale, we ignore the process

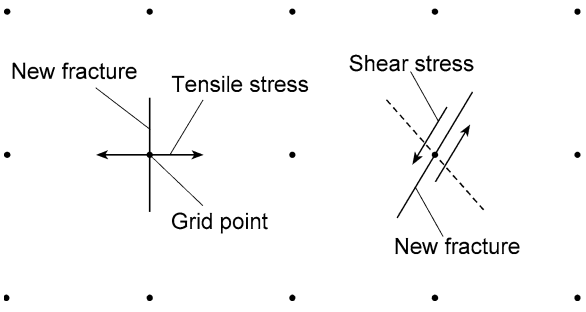


**Fig. 3.5** Fracture initiation in tension or shear in intact rock

of micro-crack formation. Instead, we will focus on when and whether a macro-fracture will form at a given location with a given stress state.

The FRACOD code considers the intact rock as a flawless, homogeneous, and linearly elastic medium. Therefore, any fracture initiation from such a medium represents a localized failure of the intact rock. This localized failure can be predicted by an existing failure criterion, e.g. the Mohr-Coulomb criterion. Other criteria widely used in rock mechanics and rock engineering can also be used, such as the Hoek-Brown criterion.

A rock failure can be caused by tension or shear. Hence, a fracture initiation can also be formed due to tension or shear. For tensile fracture initiation, the tensile failure criterion is used in FRACOD, i.e. when the tensile stress at a given point in an intact rock exceeds the tensile strength of the intact rock a new rock fracture will be generated in the direction perpendicular to the tensile stress (Fig. 3.5).

The critical stress of fracture initiation in tension is given by:

$$\sigma_{tensile} \geq \sigma_t \tag{3.25}$$

The direction of fracture initiation in tension is given by:

$$\theta_{it} = \theta(\sigma_{tensile}) + \pi/2 \tag{3.26}$$

where $\sigma_{tensile}$ is the principal tensile stress at a given point, $\sigma_t$ is the tensile strength of the intact rock, $\theta_{it}$ is the direction of the fracture initiation in tension, and $\theta(\sigma_{tensile})$ is the direction of the principal tensile stress.

The actual length of the newly generated fracture depends on many factors and may not be easily determined. In the numerical method, we assume it is determined by the spacing of the grid points used in the intact rock. In FRACOD, the fracture initiation length is assumed to be equal to the grid point spacing in the initiation direction. The smaller the grid point spacing, the shorter the new fracture. However, the closer the grid points, the less different the stresses at the adjacent grid points, and hence the more likely a fracture initiation occurs in the adjacent grid points simultaneously. The newly formed short fractures may link with each other to form a longer fracture. This mechanism reduces the sensitivity of the modelling results to the grid point spacing.

For a shear fracture initiation, the Mohr-Coulomb failure criterion is used in FRACOD, i.e. when the shear stress at a given point of the intact rock exceeds the shear strength of the intact rock, a new rock fracture will be generated (Fig. 3.5).

The critical stress of fracture initiation in shear is:

$$\sigma_{shear} \geq \sigma_n tan(\phi) + c \tag{3.27}$$

Direction of fracture initiation in shear is governed by:

$$\theta_{is} = \phi/2 + \pi/4 \tag{3.28}$$

where $\sigma_{shear}$ is the shear stress in the direction of $\theta_{is}$, $\sigma_n$ is the normal stress to the shear failure plane, $\phi$ is the internal friction angle of intact rock, $c$ is the cohesion, and $\theta_{is}$ is the direction of potential shear failure, which is measured from the direction of the minimum principal stress.

Like the tensile fracture initiation, the length of the shear fracture initiation depends on the spacing of the grid points, as discussed above.

### 3.5.2 Probability of New Crack Formation

Crack initiation can start at a stress level far below the ultimate short-term strength of the rock based on the Acoustic Emission monitoring results during laboratory compression strength tests. Usually the intensity of crack initiation (AE counting) increases with stress. To consider this phenomenon, FRACOD uses a probabilistic approach to simulate new crack formation. It is assumed that, at a candidate location for fracture initiation, the probability of a fracture initiation depends upon the stress/strength ratio ($\sigma/\sigma_m$):

$$p = 0; \qquad \text{if } \left(0 \leq \frac{\sigma}{\sigma_m} \leq \beta\right) \tag{3.29}$$

$$p = \frac{1}{(1-\beta)^2}\left[\frac{\sigma}{\sigma_m} - \beta\right]^2; \text{ if } \left(\beta \leq \frac{\sigma}{\sigma_m} \leq 1.0\right) \tag{3.30}$$

$$p = 1.0; \qquad \text{if } \left(\frac{\sigma}{\sigma_m} > 1.0\right) \tag{3.31}$$

where $p$ is the probability of fracture initiation, $\sigma/\sigma_m$ is the ratio of the stress to strength and $\beta$ is fracture initiation threshold level. An example of the probability of new crack formation as a function of the stress/strength ratio is presented in Fig. 3.6. This figure illustrates how the new cracks are modelled in a rock specimen loaded under uniaxial compression. The probability of new crack formation can

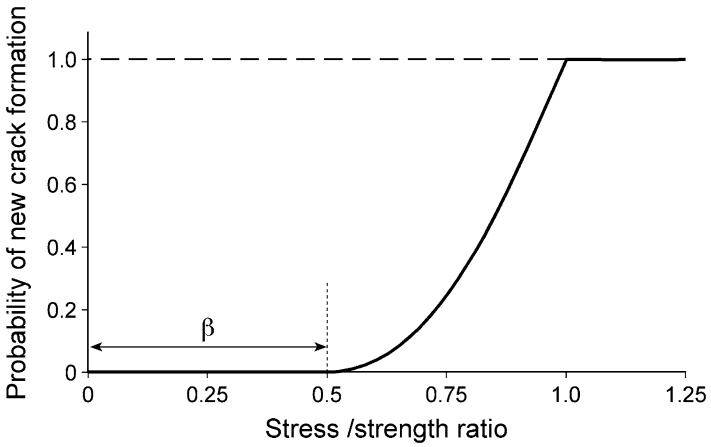


**Fig. 3.6** Probability of new crack formation as a function of the stress and strength ratio. The probability of fracture propagation is plotted for $\beta = 0.5$

be considered as a consequence of the inhomogeneity of rock with weaker and stronger minerals or mineral grain boundaries. The form of the probability curve (Eq. (3.30)) can be adapted when the actual crack initiation behaviour is known, e.g. from registration of acoustic emissions during rock testing.

## References

Backers T (2005) Fracture toughness determination and micromechanics of rock under mode I and mode II loading. Doctoral thesis, University of Potsdam, p 95

Crouch SL (1976) Solution of plane elasticity problems by the displacement discontinuity method. Int J Num Methods Eng 10:301–343

Crouch SL, Starfield AM (1983) Boundary element methods in solid mechanics. George Allen & Unwin, London

Shen B, Stephansson O (1993a) Modification of the G-criterion of crack propagation in compression. Int J Eng Fract Mech 47(2):177–189

Shen B, Stephansson O (1993b) Numerical analysis of mixed mode I and mode II fracture propagation. Special issue for the 34th US symposium of rock mechanics. Int J Rock Mech Min Sci 30:861–867

# Chapter 4
# Iteration Process in FRACOD

**Abstract** This chapter describe the iteration process used in FRACOD. Boundary element methods (including DDM) are implicit numerical methods. This means that the numerical calculation will only provide a final solution at given stress or displacement boundary conditions, ignoring the linearity of the process that reaches the final solution. For elastic problems, the implicit method is the most efficient and straightforward way to get the final solution because of the linear stress–strain relation. However, for plasticity problems caused by joint sliding and fracture propagation, the implicit method can give false results if the process to reach the final solution is non-linear. Final solutions will then depend on the path of loading. Iteration process is an effective method to consider the path dependent problem.

## 4.1 Iteration for Joint Sliding

Let us consider a joint element simulated by FRACOD (Fig. 4.1). The joint element is initially loaded in shear up to the maximum shear strength $(\sigma_s)_{max}$, then slides at the same shear stress to a specified maximum displacement $(D_s)_{max}$, then is unloaded. Let us also assume that the loading process is displacement-controlled.

To model this complex process in FRACOD, we can subdivide the total maximum shear displacement into many small increments such as $(\Delta D_s)^i$ and $(\Delta D_s)^j$. The corresponding increments in shear stress $(\Delta\sigma_s)^i$ and $(\Delta\sigma_s)^j$ can be calculated using different equations depending upon the state of the joint element. If the joint element is still elastic such as at increment $i$, then the shear stress increment is:

$$(\Delta\sigma_s)^i = K_s(\Delta D_s)^i \tag{4.1}$$

If the joint element is sliding such as at increment $j$, then the shear stress increment is:

$$(\Delta\sigma_s)^i = 0 \tag{4.2}$$

B. Shen et al., *Modelling Rock Fracturing Processes: A Fracture Mechanics Approach Using FRACOD*, DOI 10.1007/978-94-007-6904-5_4,

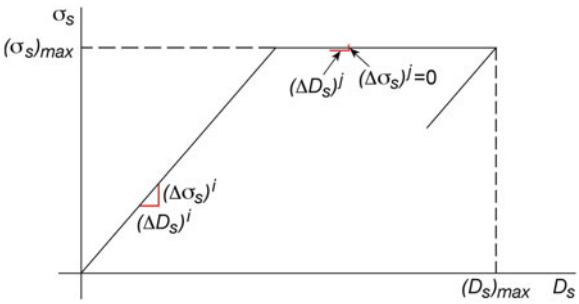


**Fig. 4.1** Iteration process in FRACOD to simulate complex loading path

The state of the joint element is determined by the total shear stress: a sum of the individual stress increments during the previous loading path. For instance:

$$(\sigma_s)^i = \sum_{n=1,i} (\Delta\sigma_s)^n$$
$$(\sigma_s)^j = \sum_{n=1,j} (\Delta\sigma_s)^n \tag{4.3}$$

At the *i*th increment, $(\sigma_s)^i < (\sigma_s)_{max}$, therefore the joint element is elastic. At the *j*th increment, $(\sigma_s)^j = (\sigma_s)_{max}$, hence the joint element is sliding.

In actual modelling, the joint element is assumed to be elastic initially, i.e. in the first increment. When the resultant total shear stress is higher than the shear strength at any given increment cycle, the joint element is identified as sliding. In the next increment cycle, the incremental joint shear stress will be recalculated using the sliding joint conditions.

For a complex joint system modelled by FRACOD, the following steps are used:

**Step 1:** Divide the final boundary stresses and/or displacement into *n* small equal increments. Only the incremental boundary values are used in subsequent calculations.

**Step 2:** Calculate the incremental shear and normal stresses for all joint elements using the incremental boundary values. If this is the first increment, all joint elements are assumed to be elastic. Otherwise, the joint states are those determined from the previous increment. In this step, the normal numerical process such as setting up and solving a matrix system as described in Chap. 3 is used.

**Step 3:** Calculate the total element shear and normal stresses at each joint element by accumulating their incremental values from the previous increments.

(continued)

(continued)

**Step 4:** Determine if the resultant total shear stress exceeds the shear strength for each joint element. If so, the joint element is considered to be sliding, and sliding conditions will be used for this joint element in the next increment.

**Step 5:** Go to the next increment and repeat Steps 2–4 using the last determined joint states.

Steps 2–5 are repeated until the designed boundary values are reached. The incremental shear and normal displacement discontinuities of each joint element and boundary element are recorded and accumulated in each increment cycle. Their final values will be the problem solution using the iteration method. After knowing the displacement discontinuities, the stresses and displacement at any internal point of a rock mass can be calculated.

## 4.2 Iteration for Fracture Propagation

The above iteration process cannot be directly applied to the cases with fracture propagation. During the process of detecting the possibility and the direction of a potential propagation using the F-criterion, a fictitious crack element is added to the candidate crack tip in different directions to simulate possible crack growth. For each possible fracture propagation direction, a complete iteration process from the beginning of loading is required to obtain the necessary stress/displacement values of the fracture elements and boundary elements to determine the F-value. This would be extremely time consuming and practically impossible. In addition, the above treatment implies that the fictitious element existed at the beginning of the loading and this is theoretically incorrect. An alternative approach is developed to simulate the fracture propagation using iteration process. This approach is described below.

Let us consider a single crack tip in a finite body under external Mode I stress σ. The crack has grown by one element length in a given direction. This problem can be decomposed into two stages, as shown in Fig. 4.2.

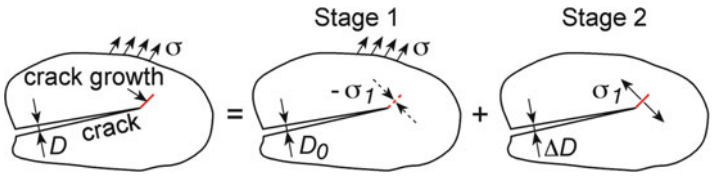


**Fig. 4.2** Decomposition of crack growth modelling using Mode I crack growth iteration

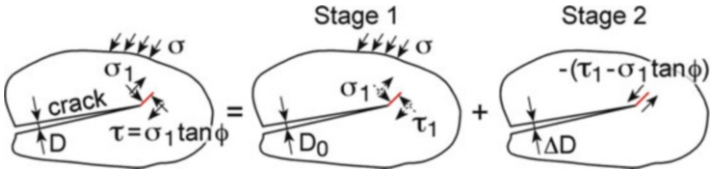


**Fig. 4.3** Decomposition of crack growth modelling using Mode II crack growth iteration

***Stage 1*** The existing crack and its growth element are subject to external stress σ. The growth element is applied with a high stress $-\sigma_1$ so that the displacement discontinuities at the element are zero. Here $\sigma_1$ should be equal to the stress at the element centre calculated by considering the pre-existing crack only. This stage is equivalent to the case where the growth element does not exist.

***Stage 2*** The existing crack and its growth element are free of external stress. Only the growth element is subject to internal stress $\sigma_1$.

In this treatment, the total resultant stress at the growth element is the sum of $-\sigma_1$ (Stage 1) and $\sigma_1$ (Stage 2), i.e. zero. This is expected for Mode I fracture growth. For Mode II fracture growth (Fig. 4.3), the surfaces of the growth element are in contact, therefore no "bonding" stress is required at Stage 1. At Stage 2, additional shear stress is applied to the growth element to composite the difference between the total resultant shear stress at Stage 1 and the shear strength.

In the cases shown in Figs. 4.2 and 4.3 the crack geometry of the real problem is kept the same in the decomposed stages, and only the stresses are decomposed. This is essential when using the decomposition theory.

In both cases, Stage 1 is equivalent to the case without crack growth. Therefore it can be modelled by the normal iteration method described in the previous section. When crack growth occurs, only one additional iteration step is needed to model Stage 2, i.e. adding the growth element to the existing fracture system and applying the specified stresses to this element.

The detailed process of modelling in FRACOD is outlined below:

**Step 1:** Use the iteration process to solve for the existing fracture system without fracture growth. Record the stresses and displacement discontinuities of the joint elements. Calculate the stresses at the centre of the potential growth element near the crack tip for use in the next step.

**Step 2:** Add a growth element to the crack tip in a given direction. Apply the stresses determined from Step 1 to the growth element and solve for the new fracture system with the growth element. Record the resultant stresses and displacement discontinuities of the joint elements.

(continued)

(continued)

**Step 3:** Obtain the total stresses and displacement discontinuities of the joint elements by adding those from Steps 1 and 2. Calculate the F-value using the final stresses and displacement discontinuities.

**Step 4:** Repeat Steps 2 and 3 using the growth element in a different direction. After all the desired directions are calculated, find the maximum F-value and its direction. If F-value is greater than 1.0, a real fracture growth is determined. Otherwise, the growth element is disregarded.

# Chapter 5
# Modelling Time Dependency

**Abstract** This chapter describes the theories of sub-critical crack growth and numerical procedures implemented in FRACOD. Classical fracture mechanics postulates that a fracture tip with a stress intensity equal to the material's critical fracture toughness will accelerate to speeds approaching the elastic wave speed in a medium. However, in cases of long-term loading, fractures can grow at stress intensities significantly lower than the critical values. This process is called subcritical fracture growth (SCG); SCG and propagation velocities can vary over many orders of magnitude as a function of stress intensity. In FRACOD the subcritical crack growth is modelled by considering the crack length as a function of time. Using the subcritical crack growth function, the time-dependent stability of fractured rock masses can be modelled.

## 5.1 Subcritical Fracture Model for a Mode I Fracture Under Pure Tension

Let us consider a crack under tensional loading. When this fracture (in elastic and isotropic medium) is under a biaxial far-field tension ($\sigma$) as shown in Fig. 5.1, the stress $\sigma_y$ in front of the crack tip ($\theta = 0$) is given by:

$$\sigma_y = \frac{K_I}{\sqrt{2\pi \times r}} \tag{5.1}$$

Stress $\sigma_y$ varies with the distance $r$ from the crack tip and becomes infinite at the fracture tip.

B. Shen et al., *Modelling Rock Fracturing Processes: A Fracture Mechanics Approach Using FRACOD*, DOI 10.1007/978-94-007-6904-5_5,

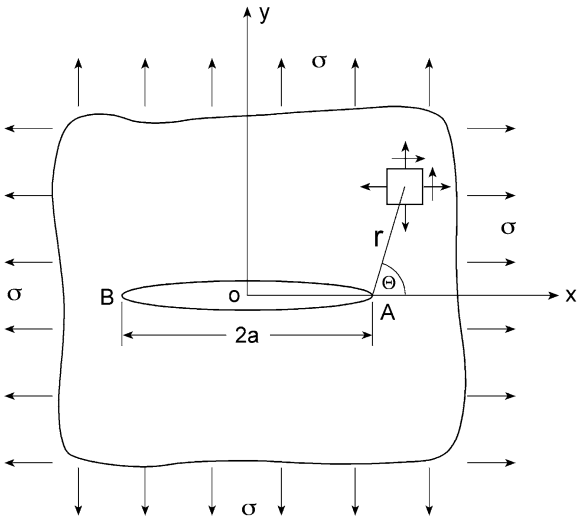


**Fig. 5.1** An infinite plate containing a crack under biaxial loading

The stress intensity factor $K_I$ determines the stress singularity at the fracture tip and its magnitude depends on the far-field stress ($\sigma$) and the crack length ($2a$):

$$K_I = \sigma\sqrt{\pi \times a} \tag{5.2}$$

In classical fracture mechanics the fracture initiation from the crack tip occurs when:

$$K_I = K_{Ic}, \tag{5.3}$$

where $K_{Ic}$ is the Mode I fracture toughness, a material constant, determinable by laboratory testing.

In subcritical crack growth theory, the slow crack extending occurs when:

$$K_I < K_{Ic}, \tag{5.4}$$

The modelling approach presented here for subcritical crack growth consists of a mathematical relationship between crack growth rate and stress intensity. Various mathematical functions can be fitted to the laboratory data. Charles (1958) stated that most experimental data can be fitted with an expression for subcritical velocity:

$$v_1 = AK^{n_1} \tag{5.5}$$

where $v_1$ is the crack velocity, $A$ is a constant, $K$ is the stress intensity factor and $n_1$ is the stress corrosion or crack propagation factor. The subscript "1" indicates Mode I subcritical growth.

## 5.2 Subcritical Fracture Model for Shear and Compression

In the previous section the simplest case was presented: a crack under pure Mode I loading with the fracture extension in the direction of the crack tip in Mode I. In practice, shear or compressive or mixed mode loading is more common.

For pure Mode II loading as shown in Fig. 5.2 the fracture stress intensity factor is:

$$K_{II} = \tau \sqrt{\pi \times a} \tag{5.6}$$

It can be seen that Eq. (5.6) has the same shape as Mode I, Eq. (5.2) except on the subject of shear stress ($\tau$) instead of normal stress ($\sigma$). However, the stress conditions are much more complicated in compression and shear than under tension. This is due to friction effects along the fracture surface.

Classical stress criteria do not account for the friction effect in front of the fracture tip. In FRACOD the friction on the existing fracture surface is considered by DDM. The F-criterion based on stress energy release uses a fictitious element to model the tip part of a growing fracture and its friction is also included in the energy change.

Even though Eq. (5.5) for fracture velocity is mainly used in Mode I problems, its use for Mode II problems is discussed in Kemeny (1993, 2002). Most likely the constants $A$ and $n$ greatly differ for Mode II loading conditions. Laboratory results in compression and shear suggest a completely different mathematical relation for the crack velocity. It is also argued that because cracking is not restricted to a single major crack in compression, the term crack velocity is not appropriate (Lajtai and

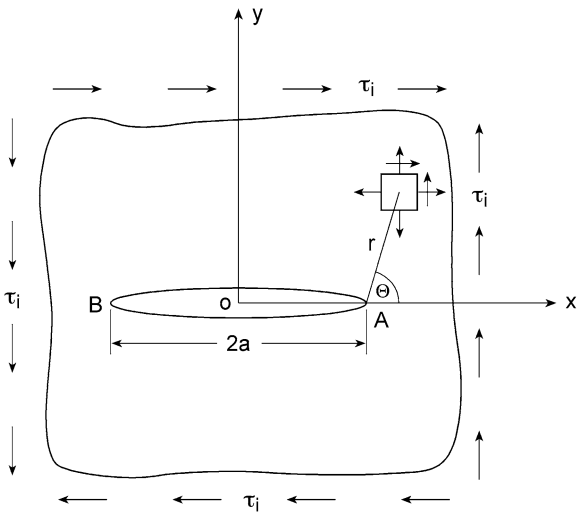


**Fig. 5.2** An infinite plate containing a crack under in-plane shear. $\tau_i$ is remote in-plane shear stress

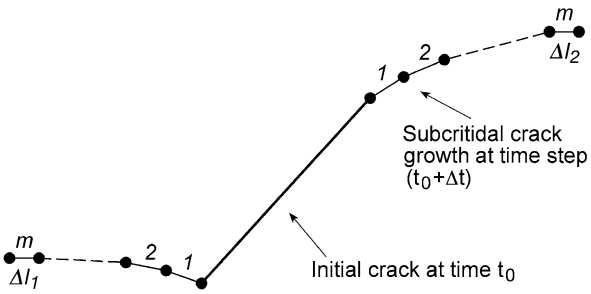


**Fig. 5.3** Simulation of SCG in FRACOD for length ($\Delta l$) at the $m$th time step ($t = t_0 + m\Delta t$) (After Shen and Rinne 2007)

Bielus 1986). Nevertheless, as a first attempt, the subcritical crack extension for a Mode II fracture will be handled in FRACOD in the same manner as presented for a tensile fracture.

## 5.3 Simulation of Subcritical Crack Growth

Because FRACOD takes into account distinct fractures and explicitly models fracture propagation, it is suitable for studying the time-dependent SCG of rock. A time step $\Delta t$ is used in the iteration procedure. Figure 5.3 shows the principles of the SCG simulation process.

The following calculation steps are performed to simulate subcritical crack growth in FRACOD:

**Step 1:** The stress intensity factors $K_I$ and $K_{II}$ are calculated at any given crack tip for the given loading condition and fracture configuration. The factors are calculated from strain energy release rates using the relationship between $K$ and $G$, as discussed in Chap. 3. Subcritical crack velocities $v_1$ and $v_2$ are determined for the time $t_0$. First the code determines which failure mode will occur at any given time, then it calculates the SCG velocity in the direction consistent with the failure mode.

**Step 2:** The length of SCG for a time step $\Delta t$ is calculated for every crack tip using the relation:

$$\Delta l = v_1 \cdot \Delta t; \text{ or } \Delta l = v_2 \cdot \Delta t$$

**Step 3:** If the SCG length is equal to or greater than an element length, a new tip element is added to the crack. Otherwise, the length is temporarily stored in memory and accumulated in the subsequent time steps until it reaches one element length. Similar crack elements are used for SCG as

(continued)

(continued)

described for (stable and unstable) fracture propagation. The length of the tip element is defined in the model set-up and depends on the model accuracy requirements and the calculation capacity.

**Step 4:** Steps 1–3 are repeated using a new time step ($t_0 + N\Delta t$) until the specified end time is reached. $N$ is the number of simulation cycles. If only one mode occurs, the total accumulated SCG length is for this mode only. If mixed-mode occurs, the accumulated length is a mix of Mode I SCG and Mode II SCG. When the direct distance between the starting point (crack tip) and the finishing point is greater than the element length, a new element is then added. Hence, the direct distance is not necessarily the total SCG length because the path of a mixed mode crack growth can zigzag.

The size of each time step is defined based on the ratios $K_I/K_{IC}$ or $K_{II}/K_{IIC}$ to minimise the iteration cycles required to reach the specified end time. When the ratio is low ($K_I/K_{IC}$ or $K_{II}/K_{IIC} << 1.0$), the SCG speed is low; hence the time step can be larger. When the ratio is close to 1.0, the SCG speed is high; hence higher accuracy is needed and the time step must be smaller. The minimum and maximum lengths for a time step ($\Delta t$) and the total time (time span, $T_{tot}$) are given as input values. In addition to the parameters needed for non-time-dependent calculations, the time-dependent calculations require the SCG parameters $n_1$, $n_2$, *etc.*

A more detailed description of the SCG function is presented in Rinne 2008.

## References

Charles RJ (1958) Static fatigue of glass. J Appl Phys 29:1549–1560

Kemeny JM (1993) The Micromechanics of deformation and failure in rocks. In: Proceedings of the international symposium on assessment and prevention of failure phenomena in rock engineering, Istanbul, A.A. Balkema, Rotterdam, pp 23–33

Kemeny JM (2002) The time-dependent reduction of sliding cohesion due to rock bridges along discontinuities: a fracture mechanics approach. Rock Mech Rock Eng 36(1):27–38

Lajtai E, Bielus L (1986) Stress corrosion cracking of Lac du Bonnet granite in tension and compression. Rock Mech Rock Eng 19:71–87

Rinne M (2008) Fracture mechanics and subcritical crack growth approach to model time-dependent failure in brittle rock. Doctoral dissertation, Helsinki University of Technology, Rock Engineering. ISBN 978-951-22-9434-3. http://lib.tkk.fi/Diss/2008/isbn9789512294350/

Shen B, Rinne M (2007) A fracture mechanics code for modelling sub-critical crack growth and time dependency. In: Proceedings of the 1st Canada-US rock mechanics symposium. Ed. Eberhardt, Stead and Morrison, Vancouver B.C, p. 591–598

# Chapter 6
# Simulation of Multiple Region System

**Abstract** Rock mass may have different properties in different regions of its structure. An example is a shaft where three different regions (concrete lining, Excavation Disturbed Zone (EDZ), and in situ rock mass) must be considered.

For application in this case, FRACOD needs to simulate the multiple regions with different material properties. Because FRACOD is a boundary element code based on the mathematical solutions in an elastic, homogeneous, isotropic medium, it is not a trivial task to extend FRACOD to handle multiple region problems. New approaches must be found. This chapter presents the mathematical formulations and their implementation in FRACOD for multiple region problems.

## 6.1 Theoretical Formulation for Multi-Region Function

The Displacement Discontinuity Method (DDM) discussed in Chap. 3 is for homogenous rock, and the solutions in Eqs. (3.1, 3.2, 3.3 and 3.4) are based on this assumption. If the structure is inhomogeneous as with Fig. 6.1, these basic solutions are no longer valid. Naturally, one may think that the basic solutions can be extended for multi-region problems, but finding mathematical solutions for all geometric cases of an unspecified number of regions is very difficult, if not impossible. Other more feasible approaches are required.

A simple way to model a multi-region problem is to separate the problem into several individual regions, each being a homogeneous region with the same rock properties (Fig. 6.2). For each homogeneous region, the basic solutions discussed in Chap. 3 apply, and systematic equations can be set up for each region to solve for stress and displacement at the internal point and on the boundary. The interfaces between two regions now become boundaries of both regions. However, the boundary stress/displacement values at the interface boundaries must meet certain conditions to ensure the continuity of two regions at the interface. This approach is being adapted in FRACOD for multi-region problems, as discussed below.

B. Shen et al., *Modelling Rock Fracturing Processes: A Fracture Mechanics Approach Using FRACOD*, DOI 10.1007/978-94-007-6904-5_6,

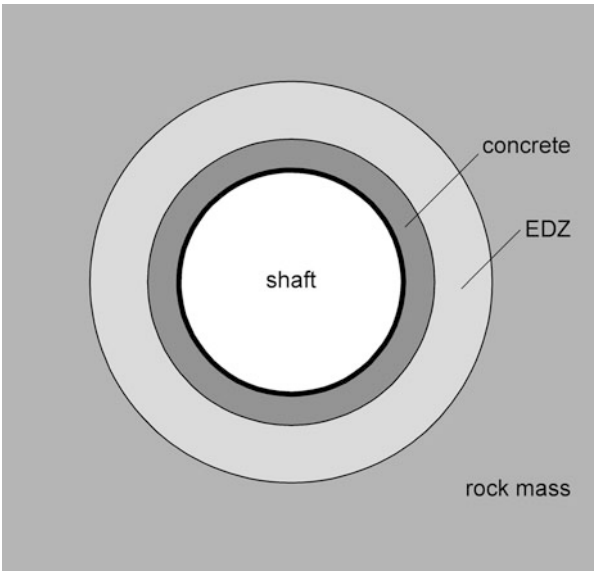


**Fig. 6.1** A multiple region problem: a shaft with concrete lining and EDZ in a fractured rock mass

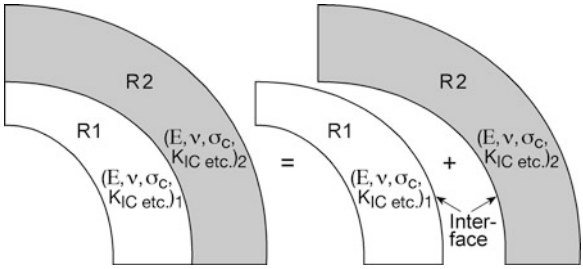


**Fig. 6.2** Treatment of multi-regions in FRACOD by modelling the two regions separately

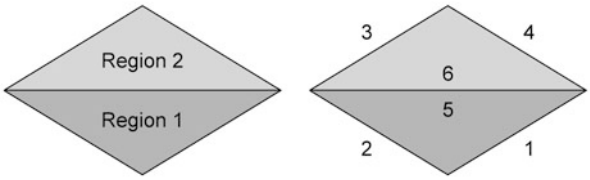


**Fig. 6.3** A simple problem with two different regions

To aid the comprehension of this approach and formulation, let us first consider a very simple problem as shown in Fig. 6.3. The problem has two triangular regions with two different properties. The two regions are joined at a straight interface.

To model this problem, we now separate the two regions and describe each region using three DD elements. The elements used here are:

Region 1: DD elements No. 1, 2, 5
Region 2: DD elements No. 3, 4, 6

Note that elements No. 5 and No. 6 both represent the interface but are in different regions. We call them the "twin" interface elements.

For the problem with 6 DD elements, the systematic equations described by Eq. 3.7 can be written in full:

$$
\begin{aligned}
&A_{ss}^{11}D_s^1 + A_{sn}^{11}D_n^1 + A_{ss}^{12}D_s^2 + A_{sn}^{12}D_n^2 + A_{ss}^{13}D_s^3 + A_{sn}^{13}D_n^3 + A_{ss}^{14}D_s^4 + A_{sn}^{14}D_n^4 + \\
&\quad A_{ss}^{15}D_n^5 + A_{sn}^{15}D_n^5 + A_{ss}^{16}D_s^6 + A_{sn}^{16}D_n^6 = b_s^1 \\
&A_{ns}^{11}D_s^1 + A_{nn}^{11}D_n^1 + A_{ns}^{12}D_s^2 + A_{nn}^{12}D_n^2 + A_{ns}^{13}D_s^3 + A_{nn}^{13}D_n^3 + A_{ns}^{14}D_s^4 + A_{nn}^{14}D_n^4 + \\
&\quad A_{ns}^{15}D_n^5 + A_{nn}^{15}D_n^5 + A_{ns}^{16}D_s^6 + A_{nn}^{16}D_n^6 = b_n^1 \\
&A_{ss}^{21}D_s^1 + A_{sn}^{21}D_n^1 + A_{ss}^{22}D_s^2 + A_{sn}^{22}D_n^2 + A_{ss}^{23}D_s^3 + A_{sn}^{23}D_n^3 + A_{ss}^{24}D_s^4 + A_{sn}^{24}D_n^4 + \\
&\quad A_{ss}^{25}D_n^5 + A_{sn}^{25}D_n^5 + A_{ss}^{26}D_s^6 + A_{sn}^{26}D_n^6 = b_s^2 \\
&A_{ns}^{21}D_s^1 + A_{nn}^{21}D_n^1 + A_{ns}^{22}D_s^2 + A_{nn}^{22}D_n^2 + A_{ns}^{23}D_s^3 + A_{nn}^{23}D_n^3 + A_{ns}^{24}D_s^4 + A_{nn}^{24}D_n^4 + \\
&\quad A_{ns}^{25}D_n^5 + A_{nn}^{25}D_n^5 + A_{ns}^{26}D_s^6 + A_{nn}^{26}D_n^6 = b_n^2 \\
&A_{ss}^{31}D_s^1 + A_{sn}^{31}D_n^1 + A_{ss}^{32}D_s^2 + A_{sn}^{32}D_n^2 + A_{ss}^{33}D_s^3 + A_{sn}^{33}D_n^3 + A_{ss}^{34}D_s^4 + A_{sn}^{34}D_n^4 + \\
&\quad A_{ss}^{35}D_n^5 + A_{sn}^{35}D_n^5 + A_{ss}^{36}D_s^6 + A_{sn}^{36}D_n^6 = b_s^3 \\
&A_{ns}^{31}D_s^1 + A_{nn}^{31}D_n^1 + A_{ns}^{32}D_s^2 + A_{nn}^{32}D_n^2 + A_{ns}^{33}D_s^3 + A_{nn}^{33}D_n^3 + A_{ns}^{34}D_s^4 + A_{nn}^{34}D_n^4 + \\
&\quad A_{ns}^{35}D_n^5 + A_{nn}^{35}D_n^5 + A_{ns}^{36}D_s^6 + A_{nn}^{36}D_n^6 = b_n^3 \\
&A_{ss}^{41}D_s^1 + A_{sn}^{41}D_n^1 + A_{ss}^{42}D_s^2 + A_{sn}^{42}D_n^2 + A_{ss}^{43}D_s^3 + A_{sn}^{43}D_n^3 + A_{ss}^{44}D_s^4 + A_{sn}^{44}D_n^4 + \\
&\quad A_{ss}^{45}D_n^5 + A_{sn}^{45}D_n^5 + A_{ss}^{46}D_s^6 + A_{sn}^{46}D_n^6 = b_s^4 \\
&A_{ns}^{41}D_s^1 + A_{nn}^{41}D_n^1 + A_{ns}^{42}D_s^2 + A_{nn}^{42}D_n^2 + A_{ns}^{43}D_s^3 + A_{nn}^{43}D_n^3 + A_{ns}^{44}D_s^4 + A_{nn}^{44}D_n^4 + \\
&\quad A_{ns}^{45}D_n^5 + A_{nn}^{45}D_n^5 + A_{ns}^{46}D_s^6 + A_{nn}^{46}D_n^6 = b_n^4 \\
&A_{ss}^{51}D_s^1 + A_{sn}^{51}D_n^1 + A_{ss}^{52}D_s^2 + A_{sn}^{52}D_n^2 + A_{ss}^{53}D_s^3 + A_{sn}^{53}D_n^3 + A_{ss}^{54}D_s^4 + A_{sn}^{54}D_n^4 + \\
&\quad A_{ss}^{55}D_n^5 + A_{sn}^{55}D_n^5 + A_{ss}^{56}D_s^6 + A_{sn}^{56}D_n^6 = b_s^5 \\
&A_{ns}^{51}D_s^1 + A_{nn}^{51}D_n^1 + A_{ns}^{52}D_s^2 + A_{nn}^{52}D_n^2 + A_{ns}^{53}D_s^3 + A_{nn}^{53}D_n^3 + A_{ns}^{54}D_s^4 + A_{nn}^{54}D_n^4 + \\
&\quad A_{ns}^{55}D_n^5 + A_{nn}^{55}D_n^5 + A_{ns}^{56}D_s^6 + A_{nn}^{56}D_n^6 = b_n^5
\end{aligned}
$$

$$
\begin{aligned}
&A_{ss}^{61}D_s^1 + A_{sn}^{61}D_n^1 + A_{ss}^{62}D_s^2 + A_{sn}^{62}D_n^2 + A_{ss}^{63}D_s^3 + A_{sn}^{63}D_n^3 + A_{ss}^{64}D_s^4 + A_{sn}^{64}D_n^4 + \\
&\quad A_{ss}^{65}D_n^5 + A_{sn}^{65}D_n^5 + A_{ss}^{66}D_s^6 + A_{sn}^{66}D_n^6 = b_s^6 \\
&A_{ns}^{61}D_s^1 + A_{nn}^{61}D_n^1 + A_{ns}^{62}D_s^2 + A_{nn}^{62}D_n^2 + A_{ns}^{63}D_s^3 + A_{nn}^{63}D_n^3 + A_{ns}^{64}D_s^4 + A_{nn}^{64}D_n^4 + \\
&\quad A_{ns}^{65}D_n^5 + A_{nn}^{65}D_n^5 + A_{ns}^{66}D_s^6 + A_{nn}^{66}D_n^6 = b_n^6
\end{aligned} \tag{6.1}
$$

where $A_{sn}^{12}$ is the influence coefficient, representing the resultant shear stress at the centre point of element 1 due to a unit normal displacement discontinuity of element 2. $b_s^1$ is the boundary value (stress or displacement) at element 1.

Because elements (1, 2, 5) and elements (3, 4, 6) are in separate regions, there will be no cross influence between them except at the "twin" interface elements. Hence, the influence coefficients e.g. $A_{ss}^{14}$, $A_{ss}^{62}$ etc. are zero. Equation (6.1) is then simplified as below:

$$
\begin{aligned}
&A_{ss}^{11}D_s^1 + A_{sn}^{11}D_n^1 + A_{ss}^{12}D_s^2 + A_{sn}^{12}D_n^2 + A_{ss}^{15}D_s^5 + A_{sn}^{15}D_n^5 = b_s^1 \\
&A_{ns}^{11}D_s^1 + A_{nn}^{11}D_n^1 + A_{ns}^{12}D_s^2 + A_{nn}^{12}D_n^2 + A_{ns}^{15}D_s^5 + A_{nn}^{15}D_n^5 = b_n^1 \\
&A_{ss}^{21}D_s^1 + A_{sn}^{21}D_n^1 + A_{ss}^{22}D_s^2 + A_{sn}^{22}D_n^2 + A_{ss}^{25}D_s^5 + A_{sn}^{25}D_n^5 = b_s^2 \\
&A_{ns}^{21}D_s^1 + A_{nn}^{21}D_n^1 + A_{ns}^{22}D_s^2 + A_{nn}^{22}D_n^2 + A_{ns}^{25}D_s^5 + A_{nn}^{25}D_n^5 = b_n^2 \\
&A_{ss}^{33}D_s^3 + A_{sn}^{33}D_n^3 + A_{ss}^{34}D_s^4 + A_{sn}^{34}D_n^4 + A_{ss}^{36}D_s^6 + A_{sn}^{36}D_n^6 = b_s^3 \\
&A_{ns}^{33}D_s^3 + A_{nn}^{33}D_n^3 + A_{ns}^{34}D_s^4 + A_{nn}^{34}D_n^4 + A_{ns}^{36}D_s^6 + A_{nn}^{36}D_n^6 = b_n^3 \\
&A_{ss}^{43}D_s^3 + A_{sn}^{43}D_n^3 + A_{ss}^{44}D_s^4 + A_{sn}^{44}D_n^4 + A_{ss}^{46}D_s^6 + A_{sn}^{46}D_n^6 = b_s^4 \\
&A_{ns}^{43}D_s^3 + A_{nn}^{43}D_n^3 + A_{ns}^{44}D_s^4 + A_{nn}^{44}D_n^4 + A_{ns}^{46}D_s^6 + A_{nn}^{46}D_n^6 = b_n^4 \\
&A_{ss}^{51}D_s^1 + A_{sn}^{51}D_n^1 + A_{ss}^{52}D_s^2 + A_{sn}^{52}D_n^2 + A_{ss}^{55}D_s^5 + A_{sn}^{55}D_n^5 = b_s^5 \\
&A_{ns}^{51}D_s^1 + A_{nn}^{51}D_n^1 + A_{ns}^{52}D_s^2 + A_{nn}^{52}D_n^2 + A_{ns}^{55}D_s^5 + A_{nn}^{55}D_n^5 = b_n^5 \\
&A_{ss}^{63}D_s^3 + A_{sn}^{63}D_n^3 + A_{ss}^{64}D_s^4 + A_{sn}^{64}D_n^4 + A_{ss}^{66}D_s^6 + A_{sn}^{66}D_n^6 = b_s^6 \\
&A_{ns}^{63}D_s^3 + A_{nn}^{63}D_n^3 + A_{ns}^{64}D_s^4 + A_{nn}^{64}D_n^4 + A_{ns}^{66}D_s^6 + A_{nn}^{66}D_n^6 = b_n^6
\end{aligned} \tag{6.2}
$$

The boundary values $b_s^1, \ldots, b_n^4$ of elements No. 1–4 are known since they are the real boundaries. The boundary values $b_s^5, \ldots, b_n^6$ of the interface elements 5 and 6 are unknown. Hence, in Eq. (6.2) there are 16 unknowns (including 12 for element DD values and 4 for interface values), and it cannot be solved by the available 12 equations. We need to construct more equations using the interface continuity conditions.

Let us consider the stress condition at the twin interface elements 5 and 6. If we assume the stresses at the interface elements 5 and 6 are $\sigma_s^5$, $\sigma_n^5$, $\sigma_s^6$ and $\sigma_n^6$, the last four equations in Eq. (6.2) can be rewritten as follows:

$$
\begin{aligned}
A_{ss}^{51} D_s^1 + A_{sn}^{51} D_n^1 + A_{ss}^{52} D_s^2 + A_{sn}^{52} D_n^2 + A_{ss}^{55} D_s^5 + A_{sn}^{55} D_n^5 &= \sigma_s^5 \\
A_{ns}^{51} D_s^1 + A_{nn}^{51} D_n^1 + A_{ns}^{52} D_s^2 + A_{nn}^{52} D_n^2 + A_{ns}^{55} D_s^5 + A_{nn}^{55} D_n^5 &= \sigma_n^5 \\
A_{ss}^{63} D_s^3 + A_{sn}^{63} D_n^3 + A_{ss}^{64} D_s^4 + A_{sn}^{64} D_n^4 + A_{ss}^{66} D_s^6 + A_{sn}^{66} D_n^6 &= \sigma_s^6 \\
A_{ns}^{63} D_s^3 + A_{nn}^{63} D_n^3 + A_{ns}^{64} D_s^4 + A_{nn}^{64} D_n^4 + A_{ns}^{66} D_s^6 + A_{nn}^{66} D_n^6 &= \sigma_n^6
\end{aligned} \tag{6.3}
$$

If the interface is bonded, the shear and normal stresses at the two sides of the interface should be the same. Hence we have the following stress relations:

$$
\begin{aligned}
\sigma_s^5 &= \sigma_s^6 \\
\sigma_n^5 &= \sigma_n^6
\end{aligned} \tag{6.4}
$$

Using Eq. (6.4) to simplify Eq. (6.3) and after simple re-arrangement we obtain the following equation:

$$
\begin{aligned}
&A_{ss}^{51} D_s^1 + A_{sn}^{51} D_n^1 + A_{ss}^{52} D_s^2 + A_{sn}^{52} D_n^2 - A_{ss}^{63} D_s^3 - A_{sn}^{63} D_n^3 - A_{ss}^{64} D_s^4 - A_{sn}^{64} D_n^4 + \\
&\quad A_{ss}^{55} D_s^5 + A_{sn}^{55} D_n^5 - A_{ss}^{66} D_s^6 - A_{sn}^{66} D_n^6 = 0 \\
&A_{ns}^{51} D_s^1 + A_{nn}^{51} D_n^1 + A_{ns}^{52} D_s^2 + A_{nn}^{52} D_n^2 - A_{ns}^{63} D_s^3 - A_{nn}^{63} D_n^3 - A_{ns}^{64} D_s^4 - A_{nn}^{64} D_n^4 + \\
&\quad A_{ns}^{55} D_s^5 + A_{nn}^{55} D_n^5 - A_{ns}^{66} D_s^6 - A_{nn}^{66} D_n^6 = 0
\end{aligned} \tag{6.5}
$$

Similar to the above process, if we consider the displacements of the interface elements 5 and 6 ($d_s^5$, $d_n^5$, $d_s^6$ and $d_n^6$), we obtain the following equations for the displacement boundary conditions.

$$
\begin{aligned}
B_{ss}^{51} D_s^1 + B_{sn}^{51} D_n^1 + B_{ss}^{52} D_s^2 + B_{sn}^{52} D_n^2 + B_{ss}^{55} D_s^5 + B_{sn}^{55} D_n^5 &= d_s^5 \\
B_{ns}^{51} D_s^1 + B_{nn}^{51} D_n^1 + B_{ns}^{52} D_s^2 + B_{nn}^{52} D_n^2 + B_{ns}^{55} D_s^5 + B_{nn}^{55} D_n^5 &= d_n^5 \\
B_{ss}^{63} D_s^3 + B_{sn}^{63} D_n^3 + B_{ss}^{64} D_s^4 + B_{sn}^{64} D_n^4 + B_{ss}^{66} D_s^6 + B_{sn}^{66} D_n^6 &= d_s^6 \\
B_{ns}^{63} D_s^3 + B_{nn}^{63} D_n^3 + B_{ns}^{64} D_s^4 + B_{nn}^{64} D_n^4 + B_{ns}^{66} D_s^6 + B_{nn}^{66} D_n^6 &= d_n^6
\end{aligned} \tag{6.6}
$$

where $B_{ss}^{51}$ etc. are the influence coefficients for displacement and $d_n^6$ etc. are the displacements of the interface elements.

If the interface is perfectly bonded, the shear and normal displacements at both sides of the interface should be the same, i.e.

$$
\begin{aligned}
d_s^5 &= d_s^6 \\
d_n^5 &= d_n^6
\end{aligned} \tag{6.7}
$$

Substituting the above displacement relations in Eq. (6.6), we obtain the following:

$$
\begin{aligned}
&- B_{ss}^{51} D_s^1 - B_{sn}^{51} D_n^1 - B_{ss}^{52} D_s^2 - B_{sn}^{52} D_n^2 + B_{ss}^{63} D_s^3 + B_{sn}^{63} D_n^3 + B_{ss}^{64} D_s^4 + B_{sn}^{64} D_n^4 \\
&\quad - B_{ss}^{55} D_s^5 - B_{sn}^{55} D_n^5 + B_{ss}^{66} D_s^6 + B_{sn}^{66} D_n^6 = 0 \\
&- B_{ns}^{51} D_s^1 - B_{nn}^{51} D_n^1 - B_{ns}^{52} D_s^2 - B_{nn}^{52} D_n^2 + B_{ns}^{63} D_s^3 + B_{nn}^{63} D_n^3 + B_{ns}^{64} D_s^4 + B_{nn}^{64} D_n^4 \\
&\quad - B_{ns}^{55} D_s^5 - B_{nn}^{55} D_n^5 + B_{ns}^{66} D_s^6 + B_{nn}^{66} D_n^6 = 0
\end{aligned} \tag{6.8}
$$

Using Eqs. (6.5) and (6.8) to replace the last four equations in Eq. (6.2), we have the following complete systematic equations for the multi-region problem shown in Fig. 6.3.

$$
\begin{aligned}
&A_{ss}^{11} D_s^1 + A_{sn}^{11} D_n^1 + A_{ss}^{12} D_s^2 + A_{sn}^{12} D_n^2 + A_{ss}^{15} D_s^5 + A_{sn}^{15} D_n^5 = b_s^1 \\
&A_{ns}^{11} D_s^1 + A_{nn}^{11} D_n^1 + A_{ns}^{12} D_s^2 + A_{nn}^{12} D_n^2 + A_{ns}^{15} D_s^5 + A_{nn}^{15} D_n^5 = b_n^1 \\
&A_{ss}^{21} D_s^1 + A_{sn}^{21} D_n^1 + A_{ss}^{22} D_s^2 + A_{sn}^{22} D_n^2 + A_{ss}^{25} D_s^5 + A_{sn}^{25} D_n^5 = b_s^2 \\
&A_{ns}^{21} D_s^1 + A_{nn}^{21} D_n^1 + A_{ns}^{22} D_s^2 + A_{nn}^{22} D_n^2 + A_{ns}^{25} D_s^5 + A_{nn}^{25} D_n^5 = b_n^2 \\
&A_{ss}^{33} D_s^3 + A_{sn}^{33} D_n^3 + A_{ss}^{34} D_s^4 + A_{sn}^{34} D_n^4 + A_{ss}^{36} D_s^6 + A_{sn}^{36} D_n^6 = b_s^3 \\
&A_{ns}^{33} D_s^3 + A_{nn}^{33} D_n^3 + A_{ns}^{34} D_s^4 + A_{nn}^{34} D_n^4 + A_{ns}^{36} D_s^6 + A_{nn}^{36} D_n^6 = b_n^3 \\
&A_{ss}^{43} D_s^3 + A_{sn}^{43} D_n^3 + A_{ss}^{44} D_s^4 + A_{sn}^{44} D_n^4 + A_{ss}^{46} D_s^6 + A_{sn}^{46} D_n^6 = b_s^4 \\
&A_{ns}^{43} D_s^3 + A_{nn}^{43} D_n^3 + A_{ns}^{44} D_s^4 + A_{nn}^{44} D_n^4 + A_{ns}^{46} D_s^6 + A_{nn}^{46} D_n^6 = b_n^4 \\
&A_{ss}^{51} D_s^1 + A_{sn}^{51} D_n^1 + A_{ss}^{52} D_s^2 + A_{sn}^{52} D_n^2 - A_{ss}^{63} D_s^3 - A_{sn}^{63} D_n^3 - A_{ss}^{64} D_s^4 - A_{sn}^{64} D_n^4 + \\
&\quad A_{ss}^{55} D_s^5 + A_{sn}^{55} D_n^5 - A_{ss}^{66} D_s^6 - A_{sn}^{66} D_n^6 = 0 \\
&A_{ns}^{51} D_s^1 + A_{nn}^{51} D_n^1 + A_{ns}^{52} D_s^2 + A_{nn}^{52} D_n^2 - A_{ns}^{63} D_s^3 - A_{nn}^{63} D_n^3 - A_{ns}^{64} D_s^4 - A_{nn}^{64} D_n^4 + \\
&\quad A_{ns}^{55} D_s^5 + A_{nn}^{55} D_n^5 - A_{ns}^{66} D_s^6 - A_{nn}^{66} D_n^6 = 0 \\
&- B_{ss}^{51} D_s^1 - B_{sn}^{51} D_n^1 - B_{ss}^{52} D_s^2 - B_{sn}^{52} D_n^2 + B_{ss}^{63} D_s^3 + B_{sn}^{63} D_n^3 + B_{ss}^{64} D_s^4 + B_{sn}^{64} D_n^4 \\
&\quad - B_{ss}^{55} D_s^5 - B_{sn}^{55} D_n^5 + B_{ss}^{66} D_s^6 + B_{sn}^{66} D_n^6 = 0 \\
&- B_{ns}^{51} D_s^1 - B_{nn}^{51} D_n^1 - B_{ns}^{52} D_s^2 - B_{nn}^{52} D_n^2 + B_{ns}^{63} D_s^3 + B_{nn}^{63} D_n^3 + B_{ns}^{64} D_s^4 + B_{nn}^{64} D_n^4 \\
&\quad - B_{ns}^{55} D_s^5 - B_{nn}^{55} D_n^5 + B_{ns}^{66} D_s^6 + B_{nn}^{66} D_n^6 = 0
\end{aligned} \tag{6.9}
$$

In Eq. (6.9) there are 12 unknowns and 12 equations, hence the problem is deterministic and solvable. Equation (6.9) can be rewritten in the form of the matrix:

$$
\begin{bmatrix}
A_{ss}^{11} & A_{sn}^{11} & A_{ss}^{12} & A_{sn}^{12} & 0 & 0 & 0 & 0 & A_{ss}^{15} & A_{sn}^{15} & 0 & 0 \\
A_{ns}^{11} & A_{nn}^{11} & A_{ns}^{12} & A_{nn}^{12} & 0 & 0 & 0 & 0 & A_{ns}^{15} & A_{nn}^{15} & 0 & 0 \\
A_{ss}^{21} & A_{sn}^{21} & A_{ss}^{22} & A_{sn}^{22} & 0 & 0 & 0 & 0 & A_{ss}^{25} & A_{sn}^{25} & 0 & 0 \\
A_{ns}^{21} & A_{nn}^{21} & A_{ns}^{22} & A_{nn}^{22} & 0 & 0 & 0 & 0 & A_{ns}^{25} & A_{nn}^{25} & 0 & 0 \\
0 & 0 & 0 & 0 & A_{ss}^{33} & A_{sn}^{33} & A_{ss}^{34} & A_{sn}^{34} & 0 & 0 & A_{ss}^{36} & A_{sn}^{36} \\
0 & 0 & 0 & 0 & A_{ns}^{33} & A_{nn}^{33} & A_{ns}^{34} & A_{nn}^{34} & 0 & 0 & A_{ns}^{36} & A_{nn}^{36} \\
0 & 0 & 0 & 0 & A_{ss}^{43} & A_{sn}^{43} & A_{ss}^{44} & A_{sn}^{44} & 0 & 0 & A_{ss}^{46} & A_{sn}^{46} \\
0 & 0 & 0 & 0 & A_{ns}^{43} & A_{nn}^{43} & A_{ns}^{44} & A_{nn}^{44} & 0 & 0 & A_{ns}^{46} & A_{nn}^{46} \\
A_{ss}^{51} & A_{sn}^{51} & A_{ss}^{52} & A_{sn}^{52} & -A_{ss}^{63} & -A_{sn}^{63} & -A_{ss}^{64} & -A_{sn}^{64} & A_{ss}^{55} & A_{sn}^{55} & -A_{ss}^{66} & -A_{sn}^{66} \\
A_{ns}^{51} & A_{nn}^{51} & A_{ns}^{52} & A_{nn}^{52} & -A_{ns}^{63} & -A_{nn}^{63} & -A_{ns}^{64} & -A_{nn}^{64} & A_{ns}^{55} & A_{nn}^{55} & -A_{ns}^{66} & -A_{nn}^{66} \\
-B_{ss}^{51} & -B_{sn}^{51} & -B_{ss}^{52} & -B_{sn}^{52} & B_{ss}^{63} & B_{sn}^{63} & B_{ss}^{64} & B_{sn}^{64} & -B_{ss}^{55} & -B_{sn}^{55} & B_{ss}^{66} & B_{sn}^{66} \\
-B_{ns}^{51} & -B_{nn}^{51} & -B_{ns}^{52} & -B_{nn}^{52} & B_{ns}^{63} & B_{nn}^{63} & B_{ns}^{64} & B_{nn}^{64} & -B_{ns}^{55} & -B_{nn}^{55} & B_{ns}^{66} & B_{nn}^{66}
\end{bmatrix}
\bullet
\begin{bmatrix}
D_s^1 \\ D_2^1 \\ D_s^2 \\ D_n^2 \\ D_s^3 \\ D_n^3 \\ D_s^4 \\ D_n^4 \\ D_s^5 \\ D_n^5 \\ D_s^6 \\ D_n^6
\end{bmatrix}
=
\begin{bmatrix}
b_s^1 \\ b_2^1 \\ b_s^2 \\ b_n^2 \\ b_s^3 \\ b_n^3 \\ b_s^4 \\ b_n^4 \\ 0 \\ 0 \\ 0 \\ 0
\end{bmatrix}
\tag{6.10}
$$

Equation (6.10) is the final matrix for the multi-region problem shown in Fig. 6.3. The matrix Eq. (6.10) can be solved using the simple Gauss elimination method.

After determining the displacement discontinuities of all boundary and interface elements, the stress and displacement at any internal point can be calculated. Note that since the two regions are considered to be separate, for an internal point in, say, region 1, only the contributions from elements 1, 2 and 5 are used. Elements 3, 4 and 6 of region 2 will not contribute to the stress and displacement of an internal point in Region 1.

When using the above formulations to consider the concrete lining in an infinite rock mass, careful attention must be paid to in situ stresses in the rock mass. Because concrete linings are normally not pre-stressed, there will be no in situ stress components in the boundary element of a concrete lining. For the problem shown in

Fig. 6.3, if we assume Region 1 is the concrete lining and Region 2 is the rock mass with in situ stresses, the final matrix equation for this case will be the following:

$$
\begin{bmatrix}
A_{ss}^{11} & A_{sn}^{11} & A_{ss}^{12} & A_{sn}^{12} & 0 & 0 & 0 & 0 & A_{ss}^{15} & A_{sn}^{15} & 0 & 0 \\
A_{ns}^{11} & A_{nn}^{11} & A_{ns}^{12} & A_{nn}^{12} & 0 & 0 & 0 & 0 & A_{ns}^{15} & A_{nn}^{15} & 0 & 0 \\
A_{ss}^{21} & A_{sn}^{21} & A_{ss}^{22} & A_{sn}^{22} & 0 & 0 & 0 & 0 & A_{ss}^{25} & A_{sn}^{25} & 0 & 0 \\
A_{ns}^{21} & A_{nn}^{21} & A_{ns}^{22} & A_{nn}^{22} & 0 & 0 & 0 & 0 & A_{ns}^{25} & A_{nn}^{25} & 0 & 0 \\
0 & 0 & 0 & 0 & A_{ss}^{33} & A_{sn}^{33} & A_{ss}^{34} & A_{sn}^{34} & 0 & 0 & A_{ss}^{36} & A_{sn}^{36} \\
0 & 0 & 0 & 0 & A_{ns}^{33} & A_{nn}^{33} & A_{ns}^{34} & A_{nn}^{34} & 0 & 0 & A_{ns}^{36} & A_{nn}^{36} \\
0 & 0 & 0 & 0 & A_{ss}^{43} & A_{sn}^{43} & A_{ss}^{44} & A_{sn}^{44} & 0 & 0 & A_{ss}^{46} & A_{sn}^{46} \\
0 & 0 & 0 & 0 & A_{ns}^{43} & A_{nn}^{43} & A_{ns}^{44} & A_{nn}^{44} & 0 & 0 & A_{ns}^{46} & A_{nn}^{46} \\
A_{ss}^{51} & A_{sn}^{51} & A_{ss}^{52} & A_{sn}^{52} & -A_{ss}^{63} & -A_{sn}^{63} & -A_{ss}^{64} & -A_{sn}^{64} & A_{ss}^{55} & A_{sn}^{55} & -A_{ss}^{66} & -A_{sn}^{66} \\
A_{ns}^{51} & A_{nn}^{51} & A_{ns}^{52} & A_{nn}^{52} & -A_{ns}^{63} & -A_{nn}^{63} & -A_{ns}^{64} & -A_{nn}^{64} & A_{ns}^{55} & A_{nn}^{55} & -A_{ns}^{66} & -A_{nn}^{66} \\
-B_{ss}^{51} & -B_{sn}^{51} & -B_{ss}^{52} & -B_{sn}^{52} & B_{ss}^{63} & B_{sn}^{63} & B_{ss}^{64} & B_{sn}^{64} & -B_{ss}^{55} & -B_{sn}^{55} & B_{ss}^{66} & B_{sn}^{66} \\
-B_{ns}^{51} & -B_{nn}^{51} & -B_{ns}^{52} & -B_{nn}^{52} & B_{ns}^{63} & B_{nn}^{63} & B_{ns}^{64} & B_{nn}^{64} & -B_{ns}^{55} & -B_{nn}^{55} & B_{ns}^{66} & B_{nn}^{66}
\end{bmatrix}
\bullet
\begin{bmatrix} D_s^1 \\ D_2^1 \\ D_s^2 \\ D_n^2 \\ D_s^3 \\ D_n^3 \\ D_s^4 \\ D_n^4 \\ D_s^5 \\ D_n^5 \\ D_s^6 \\ D_n^6 \end{bmatrix}
=
\begin{bmatrix} b_s^1 \\ b_2^1 \\ b_s^2 \\ b_n^2 \\ b_s^3 - (b_s^3)_0 \\ b_n^3 - (b_n^3)_0 \\ b_s^4 - (b_s^4)_0 \\ b_n^4 - (b_n^4)_0 \\ (b_s^6)_0 \\ (b_n^6)_0 \\ 0 \\ 0 \end{bmatrix}
\tag{6.11}
$$

where $\left(\sigma_s^3\right)_0$ etc. are the in situ stress components in Region 2. The above discussion is based on a simple problem with six elements and two regions. The same principles and formulations apply to a more complicated problem with many regions and elements. They are implemented in FRACOD in the next section for generalised cases with multiple region problems.

## 6.2 Numerical Implementation

The following functions for multiple regions are available in FRACOD:

1. Interface element option for each region;
2. Different mechanical properties for different regions;
3. Concrete lining option (no in situ stresses);
4. Special graphic option for multiple region code.

With these new multiple region functions, FRACOD can model up to ten regions with different mechanical properties. Although the number of regions is theoretically unlimited in the code, we noticed that the calculation speed reduces significantly with increasing number of regions modelled. This is because each interface between regions requires at least two DD elements, one at each side of the interface. This results in twice as many elements as for a normal boundary or fracture.

# Chapter 7
# Solving Gravitational Problems

**Abstract** Many practical rock-engineering problems involve gravitational stresses. Rock slope stability and shallow tunnel stability are two examples where the gravity stresses cannot simply be ignored or simplified as far-field in situ stresses. In such cases, uneven gravitational stresses at different depths of the rock mass must be explicitly considered.

Modelling gravitational stresses with boundary element (BE) methods is not as straightforward as in finite element (FE) method where the mass and weight of the rock are distributed into each element. Because the elements in BE methods are only located at the boundaries, they are not able to directly represent the gravitational force inside the rock body. To effectively represent this gravitational force, we need to: (1) account for the uneven gravitational stresses at the centre of all boundary elements; (2) superposition the gravitational stresses at any point inside the rock. This chapter provides the formulations to consider the effect of gravitational forces.

## 7.1 Theoretical Background

Let us consider a simple case where an underground cavern is located in shallow ground, see Fig. 7.1. The boundary of the cavern is discretised into $N$ elements. The centre of each element is at a different depth, say, $d_i$ for the $i$th element.

The system of governing equations for this problem can be written:

$$\left.\begin{aligned} \overset{i}{\sigma}_s &= \sum_{j=1}^{N} \overset{ij}{A}_{ss}\, \overset{j}{D}_s + \sum_{j=1}^{N} \overset{ij}{A}_{sn}\, \overset{j}{D}_n - \left(\overset{i}{\sigma}_s\right)_g \\ \overset{i}{\sigma}_n &= \sum_{j=1}^{N} \overset{ij}{A}_{ns}\, \overset{j}{D}_s + \sum_{j=1}^{N} \overset{ij}{A}_{nn}\, \overset{j}{D}_n - \left(\overset{i}{\sigma}_n\right)_g \end{aligned}\right\} \cdot i = 1 \cdot to \cdot N \qquad (7.1)$$

B. Shen et al., *Modelling Rock Fracturing Processes: A Fracture Mechanics Approach Using FRACOD*, DOI 10.1007/978-94-007-6904-5_7,

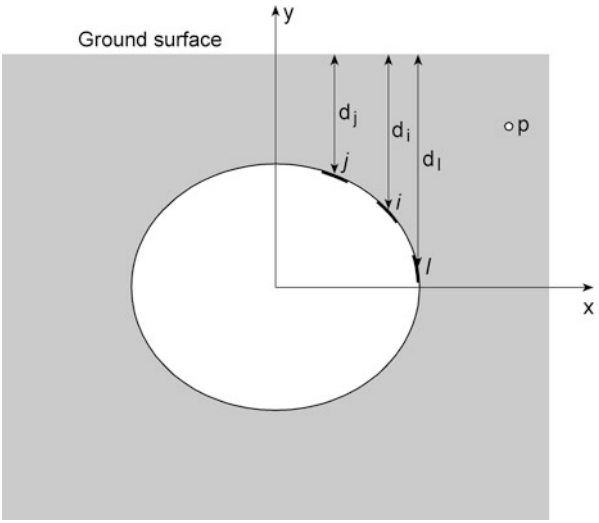


**Fig. 7.1** A shallow underground excavation to demonstrate the gravity effect from the rock mass

where $\left(\overset{i}{\sigma}_s\right)_g$ and $\left(\overset{i}{\sigma}_n\right)_g$ represent the initial gravitational stresses in shear and normal directions of the *i*th element before the excavation was made.

$\left(\overset{i}{\sigma}_s\right)_g$ and $\left(\overset{i}{\sigma}_n\right)_g$ can be calculated from the stresses in x- and y-directions $\left(\overset{i}{\sigma}_{xx}\right)_g$ and $\left(\overset{i}{\sigma}_{yy}\right)_g$ and the element orientation angle.

The gravitational stresses in the x-y coordinates are

$$\begin{aligned}\left(\overset{i}{\sigma}_{yy}\right)_g &= \rho g d_i \\ \left(\sigma^{i}_{xx}\right)_g &= k\rho g d_i\end{aligned} \tag{7.2}$$

where $\rho$ = rock density;

$g$ = gravitational acceleration;

$k$ = ratio of horizontal stress to vertical stress.

After solving the system of governing Eq. (7.1), the displacement discontinuities $D_s$ and $D_n$ of each element are known. To calculate the stresses at a given point $p$ inside the rock, the following equations can be applied:

$$\left.\begin{aligned}
\overset{p}{\sigma}_{xx} &= \sum_{j=1}^{N} \overset{pj}{A}_{xxs} \overset{j}{D}_s + \sum_{j=1}^{N} \overset{pj}{A}_{xxn} \overset{j}{D}_n - \left(\sigma^{p}_{xx}\right)_g \\
\overset{p}{\sigma}_{xy} &= \sum_{j=1}^{N} \overset{pj}{A}_{xys} \overset{j}{D}_s + \sum_{j=1}^{N} \overset{pj}{A}_{xyn} \overset{j}{D}_n \\
\overset{p}{\sigma}_{yy} &= \sum_{j=1}^{N} \overset{pj}{A}_{yys} \overset{j}{D}_s + \sum_{j=1}^{N} \overset{pj}{A}_{yyn} \overset{j}{D}_n - \left(\sigma^{p}_{yy}\right)_g
\end{aligned}\right\} \cdot i = 1 \cdot to \cdot N \qquad (7.3)$$

where $\overset{pj}{A}_{xxs}$ etc. are the influence coefficients of a unit discontinuity on the stresses at point $p$.

## 7.2 Code Implementation

Implementing the gravitational stresses in FRACOD is not as straightforward as one might think. An exterior problem[1] (such as an excavation in a rock mass where unbalanced gravitational forces act on the excavation boundaries) can cause numerical difficulties.

During calculation, the code not only calculates the exterior region (the rock mass), but also the interior region (the fictitious rock block inside the tunnel) although the latter has no meaning in our analysis. This is an inherent and unavoidable feature in DDM. The same stresses are applied to the exterior and interior regions at their common boundary. Because the unbalanced force on the interior block will lead to a large rigid displacement and consequently very large displacement discontinuities $D_s$ and $D_n$ at the boundary elements, significant numerical errors occur.

To overcome the rigid movement problem, Crouch and Starfield (1983) posited a minimum of two boundary elements in the interior region with zero displacement in two different directions. However, this method was not found to be particularly effective.

This issue was solved using the following method: the elements at the boundaries of an internal excavation are considered to be "constrained"[2] elements where the

[1] Exterior problem means that the primary concern is the rock mass outside an enclosed boundary region, e.g. an excavation in an infinite body. Interior problem is the opposite, e.g. a rock disk with finite size and volume.

[2] "Constrained" element means that the element does not have free shear and normal movement even if stresses on the element are zero.

displacement discontinuities $D_s$ and $D_n$ of these elements will cause shear and normal stresses, i.e.

$$\begin{aligned} \overset{i}{\sigma_s} &= K_s \overset{i}{D_s} \\ \overset{i}{\sigma_n} &= K_n \overset{i}{D_n} \end{aligned} \tag{7.4}$$

where $K_s$ and $K_n$ are the shear and normal stiffness of the "constrained" elements. If there is a small rigid movement of the interior block, stresses will develop at the boundaries that resist the rigid movement.

It should be emphasized that the joint stiffness used for the "constrained" elements must be relatively small compared with the stiffness of the rock mass. Otherwise, high additional boundary stresses may occur and modelling results will not be accurate.

Based on many trials, it was found that the optimal stiffness values of the "constrained" elements are:

$$K_s = K_n = E/1 \times 10^4$$

where E is the Young's modulus of the host rock.

## Reference

Crouch SL, Starfield AM (1983) Boundary element methods in solid mechanics. George Allen & Unwin, London

# Chapter 8
# Sequential Excavation Function

**Abstract** FRACOD as a boundary element code works best for problems with predefined boundaries. If the model boundary is not completely fixed at the beginning, this creates difficulties for boundary element modelling. An example of such a case is the sequential excavation of two adjacent boreholes in a rock mass. One borehole is excavated first, resulting in deformation and failure (fracturing) in the borehole wall. The second borehole is then excavated in an already disturbed stress field, and it may create new fractures and/or further propagate existing fractures in the surrounding rock mass. Because of the problem encountered above, a method to manage sequential excavation has been developed in FRACOD. This chapter describes the principles and numerical procedures of this method.

FRACOD as a boundary element code works best for problems with predefined boundaries. If the model boundary is not completely fixed at the beginning, this creates difficulties for boundary element modelling. An example of such a case is the sequential excavation of two adjacent boreholes in a rock mass, see Fig. 8.1. One borehole is excavated first, resulting in deformation and failure (fracturing) in the borehole wall. The second borehole is then excavated in an already disturbed stress field, and it may create new fractures and/or further propagate existing fractures in the surrounding rock mass.

Without any modification in the BE method, such a problem has to be considered by predefining the boundaries of both boreholes in the numerical model. When modelling the excavation of the first borehole, the second predefined borehole has to be specially treated by either fixing its boundary (no deformation) or applying constant stresses (e.g. in situ rock stresses) on the boundary. However, these treatments can seriously distort the reality because the "imagery" boundary of the second borehole is neither fixed in displacement nor fixed in stresses during the excavation of the first borehole, particularly if the two boreholes are in close proximity.

B. Shen et al., *Modelling Rock Fracturing Processes: A Fracture Mechanics Approach Using FRACOD*, DOI 10.1007/978-94-007-6904-5_8,

Because of the problem encountered above, a method to manage sequential excavation has been developed in FRACOD. This chapter describes the principles and numerical procedures of this method.

## 8.1 Theoretical Considerations

In order to clearly demonstrate the theoretical steps of subsequent excavations using DDM, let us consider the case with two boreholes excavated sequentially, Fig. 8.1. For the benefit of illustration, we assume both boreholes are loaded with internal stress on the boundary after excavation. For excavation in pre-stressed rock mass, FRACOD treats the in situ stresses as equivalent to boundary stress.

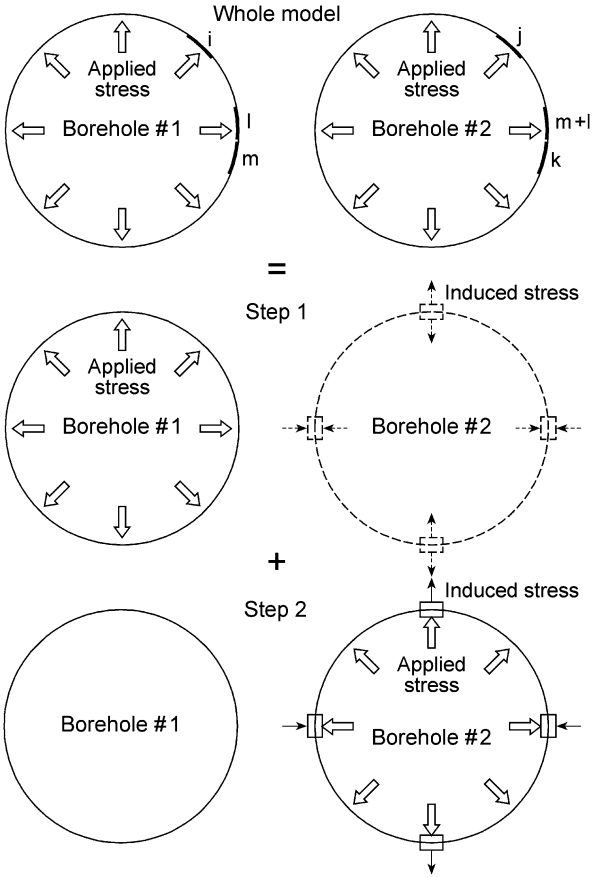


**Fig. 8.1** Decomposition of problem into excavation steps for modelling sequential excavation. The whole model describes the final state after excavation

To make the simulation possible with a boundary element, we now decompose the problem into two steps as shown in Fig. 8.1. The first step only considers excavation of the first borehole. The second step considers both boreholes but the applied stress in the first borehole will be zero and in the second borehole it will be the resultant stress from the first step. The final stress and displacement results in the rock mass and on the borehole boundaries will be the sum of those obtained from the two steps. Note that the conventional decomposition method of simply applying the actual stresses at different steps does not apply to this case, because the model geometry changes in different steps.

To illustrate this process in numerical language, we revisit the formulation for a single borehole in an infinite rock medium with predefined boundaries. The borehole boundary has been divided into $m$ elements. In the case with the predefined borehole, the matrix is:

$$\begin{bmatrix} A_{ss}^{11} & A_{sn}^{11} & \dots & A_{ss}^{1m} & A_{sn}^{1m} \\ A_{ns}^{11} & A_{nn}^{11} & \dots & A_{ns}^{1m} & A_{nn}^{1m} \\ \dots & \dots & \dots & \dots & \dots \\ A_{ss}^{m1} & A_{sn}^{m1} & \dots & A_{ss}^{mm} & A_{sn}^{mm} \\ A_{ns}^{m1} & A_{nn}^{m1} & \dots & A_{ns}^{mm} & A_{nn}^{mm} \end{bmatrix} \times \begin{bmatrix} D_s^1 \\ D_n^1 \\ \dots \\ D_s^m \\ D_n^m \end{bmatrix} = \begin{bmatrix} B_s^1 \\ B_s^1 \\ \dots \\ B_s^m \\ B_n^m \end{bmatrix} \tag{8.1}$$

where $A_{sn}$, $A_{nn}$, $A_{ss}$, $A_{ns}$ are influence coefficients; $D_s$, $D_n$ are displacement discontinuities; $B_s$, $B_n$ are boundary stresses or displacement.

By solving the matrix Eq. (8.1), the displacement discontinuities ($D_s$, $D_n$) at all boundary elements of the single borehole boundary are known. Consequently the stresses and displacement in the rock mass and borehole boundary can be obtained by using the displacement discontinuity values of each element.

Above is the numerical procedure involved in the first step of calculation. For the second step, let us now consider the subsequent excavation of the second borehole. The boundary of this second borehole is divided into ($k$−$m$) elements, making the total element number for both boreholes $k$. In this step, both boreholes have to be modelled. The matrix for the two-hole model is given:

$$\begin{bmatrix} A_{ss}^{11} & A_{sn}^{11} & \dots & A_{ss}^{1m} & A_{sn}^{1m} & \dots & A_{ss}^{1k} & A_{sk}^{1k} \\ A_{ns}^{11} & A_{nn}^{11} & \dots & A_{ns}^{1m} & A_{nn}^{1m} & \dots & A_{ns}^{11} & A_{nn}^{11} \\ \dots & \dots & \dots & \dots & \dots & \dots & \dots & \dots \\ A_{ss}^{m1} & A_{sn}^{m1} & \dots & A_{ss}^{mm} & A_{sn}^{mm} & \dots & A_{ss}^{mk} & A_{sn}^{mk} \\ A_{sn}^{m1} & A_{nn}^{m1} & \dots & A_{sn}^{mm} & A_{nn}^{mm} & \dots & A_{sn}^{mk} & A_{nn}^{mk} \\ \dots & \dots & \dots & \dots & \dots & \dots & \dots & \dots \\ A_{ss}^{k1} & A_{sn}^{k1} & \dots & A_{ss}^{mk} & A_{ns}^{mk} & \dots & A_{ss}^{kk} & A_{sn}^{kk} \\ A_{sn}^{k1} & A_{nn}^{k1} & \dots & A_{sn}^{mk} & A_{nn}^{mk} & \dots & A_{sn}^{11} & A_{nn}^{kk} \end{bmatrix} \times \begin{bmatrix} \Delta D_s^1 \\ \Delta D_n^1 \\ \dots \\ \Delta D_s^m \\ \Delta D_n^m \\ \dots \\ \Delta D_s^k \\ \Delta D_n^k \end{bmatrix} = \begin{bmatrix} 0 \\ 0 \\ \dots \\ 0 \\ 0 \\ \dots \\ B_s^k \\ B_n^k \end{bmatrix} \tag{8.2}$$

where $\Delta D_s$, $\Delta D_n$ are increments of displacement discontinuities.

Based on the decomposition method discussed above, the boundary condition used in the two-hole model has to be specially treated. The stresses applied to the

first borehole boundary are set to be zero in the second step, whereas the stresses applied to the second borehole boundary are the resultant stresses in the first step at the location of the "future" boundary of the second borehole (i.e. $B_s^i$, $B_n^i$. $i = m, k$). They are the sum of the in situ stresses and induced stresses from the excavation of borehole 1.

The solution of Eq. (8.2) will provide the "additional" DD values of all the elements (i.e. $\Delta D_s$, $\Delta D_n$). The final solution of the problem will then be the sum of the DD values from Steps 1 and 2:

$$\begin{aligned} \left(D_s^i\right)_{final} &= D_s^i + \Delta D_s^i \quad (i = 1, m) \\ \left(D_n^i\right)_{final} &= D_n^i + \Delta D_n^i \quad (i = 1, m) \end{aligned} \tag{8.3}$$

For the elements along the second borehole boundary, there were no DD values produced from Step 1 because this borehole was not considered. Therefore, the final DD values are those obtained from the second step, i.e.

$$\begin{aligned} \left(D_s^i\right)_{final} &= \Delta D_s^i \quad (i = m + 1, k) \\ \left(D_n^i\right)_{final} &= \Delta D_n^i \quad (i = m + 1, k) \end{aligned} \tag{8.4}$$

## 8.2 Numerical Implementation in FRACOD

The above decomposition process has been implemented in FRACOD. For sequential excavation problems with $n$ excavation steps, an equal number of calculation steps are used in the simulation. The model boundary is updated in each calculation step. The results (i.e. DD values) from this and previous steps are stored and used in the next step.

There is no limit in the number of excavation steps that can be used in the FRACOD modelling. However, the numerical accuracy tends to reduce as the number of excavation steps increases. This is because the sequential excavation function uses the calculated stresses at the future excavation boundary as the boundary condition for the calculation in the next steps. Hence, any numerical error will be accumulated and propagated step-by-step into the final results. In contrast, the normal "all-in-one" excavation only uses the in situ stresses and applied boundary stresses in the calculation, thereby eliminating the possibility of the above numerical errors.

There is a limitation in the current code version that the new excavation geometry should not have any overlap with the old excavation geometry, and no fractures exist in the area prior to the new excavation. This limitation occurs because FRACOD allows one to add new elements, but not to delete elements.

# Chapter 9
# Thermo-Mechanical Coupling

**Abstract** This chapter provide the theoretical formulations and numerical procedures involved in thermo-mechanical coupling function in FRACOD. Coupling between thermal loading and mechanical process can occur either when the temperature change in rock mass causes thermal stresses or when stress change in the rock mass causes a temperature change. Although heat transfer can result in significant changes in volumetric stress, influences of rock matrix deformation on the temperature field are usually negligible. This means that thermal flux and temperature can be calculated separately without the consideration of mechanical stresses. In this discussion, thermo-mechanical coupling refers only to cases where the heating of rock increases volumetric stresses.

Due to the time dependency of heat conduction, the changes of thermal stress fields are transient processes. It should be noted that for rocks with low permeability, heat conduction dominates the heat transfer process. Heat convection can usually be neglected because of the extremely low heat flow velocity in rocks. This chapter is concerned with low permeability rocks like shale and granite, so effects of heat transported by convection are neglected, and linear thermal conductive behaviour is assumed in the thermo-elastic analysis.

## 9.1 Governing Equations for Thermo-Elasticity

The governing equations for thermo-elasticity can be found in the works of Timoshenko and Goodier (1970). The following is a brief review of the equations, which consist of constitutive equations, transport laws and balance laws.

B. Shen et al., *Modelling Rock Fracturing Processes: A Fracture Mechanics Approach Using FRACOD*, DOI 10.1007/978-94-007-6904-5_9,

### 9.1.1 Constitutive Equations

In isotropic thermo-elasticity, the constitutive equations can be separated into a deviatoric response and a volumetric response. The latter includes the volumetric response of the solid rock matrix.

Deviatoric response is given by:

$$\varepsilon_{ij} = \frac{\sigma_{ij}}{2G} \ (i \neq j) \tag{9.1}$$

where $\varepsilon_{ij}$ denotes the components of the deviatoric strain tensor, $\sigma_{ij}$ denotes the components of the deviatoric stress tensor, and $G$ is the shear modulus. The subscript indices $i$ and $j$ have values in the range {1,2} and the summation convention is used over repeated indices.

The volumetric response of the solid contains thermal coupling terms:

$$\varepsilon_{kk} = \frac{\sigma_{kk}}{3K} + \alpha T \tag{9.2}$$

where $\varepsilon_{kk}$ is volumetric strain, $\sigma_{kk}/3$ is volumetric stress (mean stress), $T$ is temperature. The constant $K$ is the rock's bulk modulus; α is the volumetric thermal expansion coefficient of the bulk solid under constant stress.

Note that without the temperature term, Eq. (9.2) degenerates to the classical elastic relation of Hooke's Law. Equation (9.2) can also be written as a stress form:

$$\sigma_{ij} = 2G\varepsilon_{ij} + \frac{2G\nu}{1-2\nu}\varepsilon_{ij}\delta_{ij} + K\alpha T\delta_{ij} \tag{9.3}$$

in which ν is Poisson's ratio. $\delta_{ij}$ is Dirac delta function that represents unit concentrated sources.

### 9.1.2 Transport and Balance Laws

The heat flow is governed by Fourier's law, which is written as:

$$q_i^T = -\kappa^T T_i \tag{9.4}$$

where $q_i^T$ is the heat flux, $\kappa^T$ is the thermal conductivity.

For local stress balance, standard considerations of static equilibrium lead to the equilibrium equation used in elasticity:

$$\sigma_{ij,j} = 0 \tag{9.5}$$

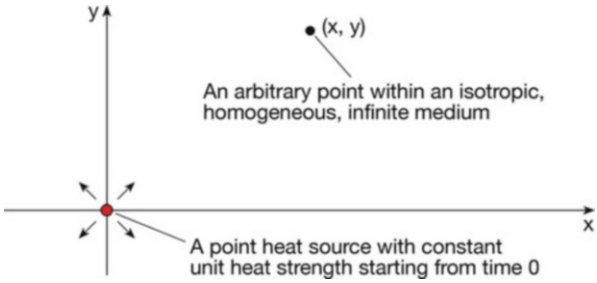


**Fig. 9.1** Ideal case of a point heat source in an infinite isotropic medium

### 9.1.3 Field Equations for Thermo-Elasticity

From the constitutive, balance, and transport laws, the field equations can be derived for temperature $T$, displacement $u_i$ and Navier's Equation:

$$G\nabla^2 u_i \frac{1}{3}(G+3K)\varepsilon_{,i} = K\alpha T_{,i} \tag{9.6}$$

Diffusion equation for temperature *T:*

$$c\nabla^2 T = \frac{\partial T}{\partial t} \tag{9.7}$$

In the above equations, $u_i$ denotes the solid displacement vector, $\varepsilon_{ij}$ is the total strain tensor, and $T$ the temperature. The constant $c$ is thermal diffusivity. As mentioned above, heat transfer is calculated separately because stress changes do not significantly alter the temperature field. Also note that convective heat transport is neglected.

### 9.1.4 Fundamental Solutions in Thermo-Elasticity

The two-dimensional fundamental solutions for temperature and stresses induced by a continuous heat source in thermo-elasticity (Fig. 9.1) are given by the following equations (Berchenko1998; Zhang 2004):

$$T = \frac{1}{4\pi k} Ei(\xi^2) \tag{9.8}$$

$$\sigma_{xx} = \frac{E\alpha}{24\pi k(1-\nu)} \left\{ \left(1 - \frac{2x^2}{r^2}\right) \frac{1-e^{-\xi^2}}{\xi^2} - Ei(\xi^2) \right\} \tag{9.9}$$

$$\sigma_{xy} = \frac{E\alpha}{24\pi k(1-\nu)} \left\{ \left(-\frac{2xy}{r^2}\right) \frac{1-e^{-\xi^2}}{\xi^2} \right\} \tag{9.10}$$

$$\sigma_{yy} = \frac{E\alpha}{24\pi k(1-\nu)} \left\{ \left(1 - \frac{2y^2}{r^2}\right) \frac{1 - e^{-\xi^2}}{\xi^2} - Ei(\xi^2) \right\} \tag{9.11}$$

$$u_x = \frac{\alpha(1+\nu)}{4\pi k(1-\nu)} r \left\{ \frac{x}{r} \frac{\left(1 - e^{-\xi^2}\right)}{2\xi^2} + \frac{1}{2} Ei(\xi^2) \right\} \tag{9.12}$$

$$u_y = \frac{\alpha(1+\nu)}{4\pi k(1-\nu)} r \left\{ \frac{y}{r} \frac{\left(1 - e^{-\xi^2}\right)}{2\xi^2} + \frac{1}{2} Ei(\xi^2) \right\} \tag{9.13}$$

where:

k – thermal conductivity (per metre degree C, W/m·°C)
c – thermal diffusivity (square metres per second or $m^2/s$)
ρ – density ($kg/m^3$)
$c_p$ – specific heat capacity (joules per kilogram degree C, J/kg·°C)

$$c = \frac{k}{\rho c_p}$$

In the above equations: $r = \sqrt{x^2 + y^2}$

$$\xi^2 = \frac{r^2}{4ct}$$

$Ei(u)$ is the exponential integral function, defined as:

$$Ei(u) = \int_u^\infty \frac{e^{-z}}{z} dz$$

Equations (9.8, 9.9, 9.10, 9.11, 9.12 and 9.13) constitute the fundamental equations to be used in all the formulations of numerical process in FRACOD.

## 9.2 Thermo-Mechanical Coupling in FRACOD

Most thermo-elastic problems do not have closed form analytical solutions because the geometry and boundary conditions of real problems are complex. The boundary element method (BEM) has been used extensively for the solution of thermo-elastic problems (e.g., Cheng et al. 2001).

There are two kinds of approaches in BEM: direct and indirect. The direct approach is also called the direct boundary integration method. It uses the reciprocal theorem, and the values (temperature, stresses and displacements) at a given boundary are calculated directly by solving a system of equations. The indirect

approach uses fictitious heat sources with unknown strength over the boundary of the domain. By forcing the solution at a given boundary to meet the specified boundary conditions, the strength of the heat source will be solved. These fictitious heat sources will then be used to obtain the temperature, stress and displacement at any point in the domain.

The indirect method is found to be easier when considering a problem with internal heat sources. Such a heat source can be treated in the same way as the fictitious heat source but with known strength. In the direct approach, a discretisation of the time and spatial domain is required and this makes the numerical process very complex.

An indirect approach, i.e. DDM, has already been used in FRACOD due to its advantage in simulating fracture problems. For the transient thermal flow modelling, an indirect method is also adopted because it is easy to couple with the existing DDM in FRACOD. The fictitious unknown items in the thermal flow modelling are a set of fictitious heat sources at the centre of the boundary elements. They are treated in exactly the same way as the fictitious DD in the mechanical calculation.

Indirect approaches for modeling poroelasticity have been found by Ghassemi et al. (2001) and thermal-poroelasticity by Zhang (2004) using boundary element methods. The thermo-mechanical coupled BEM method used in this book is based on the principle of superposition in solid mechanics.

### *9.2.1 Fictitious Heat Source Method for Thermo-Elasticity*

For an internal problem as shown in Fig. 9.2 the boundary of a finite body has been discretised into $n$ elements. Before any boundary condition is considered, each element is assumed to be in an infinite, isotropic and homogeneous medium. Let us consider that a constant 2D line heat source (plane heat source in 3D) with unit strength is placed along element $j$ at time $t_0 = 0$. At any given time $t$, the temperature, stresses and displacements at the centre point of another element (element $i$) is known based on the fundamental solutions given in Eqs. (9.8, 9.9, 9.10, 9.11, 9.12 and 9.13).

Note that these equations are only for a point source.

For a line source, these equations need to be integrated over the entire length $2a$ of element $j$. They are given below:

$$T\,(j \rightarrow i) = \frac{1}{4\pi k}\int_{-a}^{a} Ei(\xi^2)dx' \tag{9.14}$$

$$\sigma_{x'x'}\,(j \rightarrow i) = \frac{E\alpha}{8\pi k(1-\nu)}\int_{-a}^{a}\left\{\left(1-\frac{2x'^2}{r^2}\right)\frac{1-e^{-\xi^2}}{\xi^2} - Ei(\xi^2)\right\}dx' \tag{9.15}$$

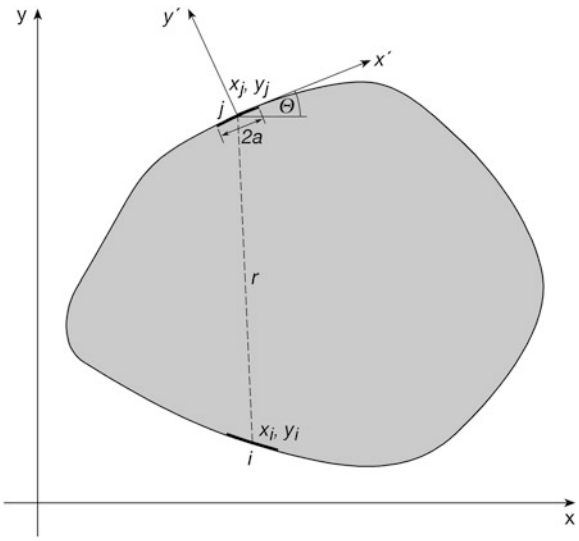


**Fig. 9.2** Elements and coordinates along a solid body boundary

$$\sigma_{x'y'}(j \rightarrow i) = \frac{E\alpha}{8\pi k(1-\nu)} \int_{-a}^{a} \left\{ \left( -\frac{2x'y'}{r^2} \right) \frac{1-e^{-\xi^2}}{\xi^2} \right\} dx' \tag{9.16}$$

$$\sigma_{y'y'}(j \rightarrow i) = \frac{E\alpha}{8\pi k(1-\nu)} \int_{-a}^{a} \left\{ \left( 1 - \frac{2y'^2}{r^2} \right) \frac{1-e^{-\xi^2}}{\xi^2} - Ei(\xi^2) \right\} dx' \tag{9.17}$$

$$u_{x'}(j \rightarrow i) = \frac{\alpha(1+\nu)}{4\pi k(1-\nu)} \int_{-a}^{a} r \left\{ \frac{x'}{r} \frac{\left(1-e^{-\xi^2}\right)}{2\xi^2} + \frac{1}{2} Ei(\xi^2) \right\} dx' \tag{9.18}$$

$$u_{y'}(j \rightarrow i) = \frac{\alpha(1+\nu)}{4\pi k(1-\nu)} \int_{-a}^{a} r \left\{ \frac{y'}{r} \frac{\left(1-e^{-\xi^2}\right)}{2\xi^2} + \frac{1}{2} Ei(\xi^2) \right\} dx' \tag{9.19}$$

The integrations in Eqs. (9.14, 9.15, 9.16, 9.17, 9.18 and 9.19) need to be done numerically since a closed form solution is hard to obtain due to the existence of the exponential integral function $Ei(\xi^2)$.

For numerical integration, element $j$ is divided into 10 equal length segments. For each segment, the line heat source is assumed to have "shrunken" to a point source and the point source has the same total strength as the line source over the segment. Therefore, the entire line source over element $j$ is represented by 10 point sources evenly distributed over the element. For example, the temperature Eq. (9.14) is calculated numerically using

$$T\,(j\ \rightarrow i) = \sum_{k=1}^{10} T\left(x'_{\,k}, y'\right) a/5 \tag{9.20}$$

where $T\ (x'_{\,k},\ y')$ is the temperature at element $i$ calculated from a point source at ($x'_{\,k}$,y') with strength of $a$/5. The coordinates of the ten points are given as:

| | | |
|---|---|---|
| $k=1$ | $x'=-0.9a;$ | $y'=0$ |
| $k=2$ | $x'=-0.7a;$ | $y'=0$ |
| ... | | |
| $k=10$ | $x'=0.9a;$ | $y'=0$ |

The results in the above equations are presented for the local coordinates x′-y′ of the element $j$ as shown in Fig. 9.2. They must be transformed to the global coordinate system. Note that the temperature is not direction dependent and hence is not affected by the coordinate transformation:

$$T = T$$

$$\begin{aligned}
\sigma_{xx}^{ij} &= \sigma_{x'x'}^{ij} \cos^2\theta - 2\sigma_{x'y'}^{ij}\ \sin\theta\ \cos\theta + \sigma_{y'y'}^{ij} \sin^2\theta \\
\sigma_{yy}^{ij} &= \sigma_{x'x'}^{ij} \sin^2\theta + 2\sigma_{x'y'}^{ij}\ \sin\theta\ \cos\theta + \sigma_{y'y'}^{ij} \cos^2\theta \\
\sigma_{xy}^{ij} &= \left(\sigma_{x'x'}^{ij} - \sigma_{y'y'}^{ij}\right)\sin\theta\ \cos\theta + \sigma_{x'y'}^{ij}\,(\cos^2\theta - \sin^2\theta) \\
u_x &= u'_x\ \cos\theta - u'_y\ \sin\theta \\
u_y &= u'_x \sin\theta - u'_y\ \cos\theta
\end{aligned} \tag{9.21}$$

Since the boundary values (stresses and/or displacements) of the boundary element $i$ are often given in its shear and normal directions, the obtained stresses and displacements should be further transformed to the local coordinates of element $i$. After this process, the temperature, shear and normal stresses, and shear and normal displacements of element $i$, caused by a unit line heat source at element $j$ are calculated. The correspondent values are named as "influence coefficients".

In the fictitious heat source method, we assume that a line source has been applied along each boundary element. The strength of these line sources is unknown and needs to be solved.

The total temperature, stresses and displacements at element $i$ due to the fictitious line sources can be calculated by superpositioning the effect of all individual heat sources as shown below:

$$T^i = \sum_{j=1}^{n} T^{ij} H^j\ \ (t = t_0) \tag{9.22}$$

$$\sigma_s^i = \sum_{j=1}^{n} \left( A_{ss}^{ij} D_s^j + A_{sn}^{ij} D_n^j + F_s^{ij} H^j \right) \quad (t = t_0) \tag{9.23}$$

$$\sigma_n^i = \sum_{j=1}^{n} \left( A_{ns}^{ij} D_s^j + A_{nn}^{ij} D_n^j + F_n^{ij} H^j \right) \quad (t = t_0) \tag{9.24}$$

$$u_s^i = \sum_{j=1}^{n} \left( B_{ss}^{ij} D_s^j + B_{sn}^{ij} D_n^j + G_s^{ij} H^j \right) \quad (t = t_0) \tag{9.25}$$

$$u_n^i = \sum_{j=1}^{n} \left( B_{ns}^{ij} D_s^j + B_{nn}^{ij} D_n^j + G_n^{ij} H^j \right) \quad (t = t_0) \tag{9.26}$$

where $H^j$ is the strength of the line heat source at element $j$.

$T^{ij}$, $F_s^{ij}$, $F_n^{ij}$, $G_s^{ij}$, $G_n^{ij}$ are the influence coefficients, representing the temperature, stress and displacement at the centre of the element $i$ due to a unit line source at element $j$. They are calculated based on the Eqs. (9.14, 9.15, 9.16, 9.17, 9.18 and 9.19).

Because the strengths ($H^j$) of the fictitious heat sources are only dependent upon the thermal boundary conditions, they can be solved using Eq. (9.22). If the temperature along the problem boundary is known, using Eq. (9.22) we will have $n$ equations with $n$ unknowns. The fictitious heat source strength along each element can be obtained by solving the system of $n$ equations. Their values can then be used in Eqs. (9.23, 9.24, 9.25 and 9.26) to solve the displacement discontinuities $D_s^j$ and $D_n^j$.

The thermal boundary condition is sometimes defined as heat flux rather than temperature. In this case, we need to use the flux equation below to replace Eq. (9.8) for temperature:

$$Q_{ij} = -k \frac{\partial T}{\partial n} = \frac{(x_i - x_j)\cos\theta_i + (y_i - y_j)\sin\theta_i}{8\pi k t^2} Ei(\xi^2) \tag{9.27}$$

where $Q_{ij}$ is the heat flux in the normal direction of element $i$ due to a unit line source at element $j$. $k$ is the thermal conductivity.

Other numerical processes previously described for temperature boundary conditions are also applicable to flux boundary conditions.

### 9.2.2 *Time Marching Scheme for Transient Heat Flow*

So far in the discussion, time has not been considered. Solutions have been confined to cases where the heat sources and boundary conditions are constant over a period

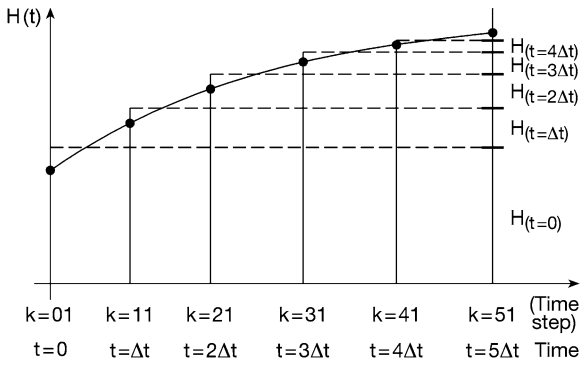


**Fig. 9.3** Time marching scheme for a continuous heat source H($t$)

of time. If either variable changes during this period, the above approach is no longer valid. A time marching scheme must be used in order to simulate the history of heat flow.

There are different approaches for temporal solutions. One approach is solving the problem at the end of a time step and then using the results as the initial condition for the next time step, marching forward in time. The disadvantage of this method is that it requires discretising the spatial domain of the problem. The second approach is dividing the heat source into many sub-sources. The sub-sources start to take effect at different times, thereby allowing the total strength of the heat source to vary with time. The final solution is the accumulated effect of all the sub-sources. This technique eliminates the need for internal discretisation of the spatial domain but has the disadvantage that the coefficient matrix must be retained and used as required. This scheme is illustrated with heat source *H(t)* in Fig. 9.3.

The implementation of this time marching scheme is possible because it is the time interval between thermal loading and receiving that affects the response rather than the absolute times. This is the so-called "time translation" property of fundamental solutions. For example, the stress at a point $\boldsymbol{x}$ and time $\boldsymbol{t}$ due to a heat source occurring at point $\chi$ and at time $\tau$ is equal to the stress at point $\boldsymbol{x}$ and time $t-\tau$ due to a heat source occurring at time zero at the point $\chi$:

$$\sigma_{ij}(\mathbf{x}, t; \chi, \tau) = \sigma_{ij}(\mathbf{x}, t - \tau; \chi, 0)$$

Due to this property of the fundamental solutions, the evaluation time and loading time can be shifted along the time axis without affecting the values of the fundamental solutions. Therefore, the influence coefficient can be calculated only once during the calculation history.

When the time marching scheme is used, Eqs. (9.22, 9.23, 9.24, 9.25 and 9.26) are re-written as:

$$T^i = \sum_{j=1}^{n} \sum_{k=1}^{m} T^{ij}(t_k) H^j(t_k) \quad (t = t_m) \tag{9.28}$$

$$\sigma_s^i = \sum_{j=1}^{n} \left( A_{ss}^{ij} D_s^j + A_{sn}^{ij} D_n^j + \sum_{k=1}^{m} F_s^{ij}(t_k) H^j(t_k) \right) \quad (t = t_m) \tag{9.29}$$

$$\sigma_n^i = \sum_{j=1}^{n} \left( A_{ns}^{ij} D_s^j + A_{nn}^{ij} D_n^j + \sum_{k=1}^{m} F_n^{ij}(t_k) H^j(t_k) \right) \quad (t = t_m) \tag{9.30}$$

$$u_s^i = \sum_{j=1}^{n} \left( B_{ss}^{ij} D_s^j + B_{sn}^{ij} D_n^j + \sum_{k=1}^{m} G_s^{ij}(t_k) H^j(t_k) \right) \quad (t = t_m) \tag{9.31}$$

$$u_n^i = \sum_{j=1}^{n} \left( B_{ns}^{ij} D_s^j + B_{nn}^{ij} D_n^j + \sum_{k=1}^{m} G_n^{ij}(t_k) H^j(t_k) \right) \quad (t = t_m) \tag{9.32}$$

where $t_k$ is the time interval between the evaluation time ($t_m$) and the time when the $k$th sub-source $H^j(t_k)$ takes effect

$$t_k = t_m - k\Delta t \ \ (k = 0, m)$$

In Eqs. (9.28, 9.29, 9.30, 9.31 and 9.32), each $H^j(t_k)$ is a fictitious heat source and needs to be solved using thermal boundary conditions. For a problem with $n$ boundary elements and m time steps there are effectively $(n \times m)$ unknown fictitious heat sources. They can be solved using Eq. (9.28) if the boundary condition is temperature. If the boundary condition is heat flux or mixed temperature and flux, then the correspondent flux equation should be included.

In some cases, real heat sources of known strength and duration are present in the rock mass. This can happen in high-level nuclear waste disposal where the canisters can be regarded as large-scale heat sources. These real heat sources can be considered in the same way as the fictitious heat source except that their strengths are already known. In Eqs. (9.29, 9.30, 9.31 and 9.32), the heat sources $H^j(t_k)$ also include real heat sources if they occur.

To demonstrate the time marching process, let us consider the situation described in Fig. 9.3. The evaluation time domain is divided into five equal time steps, each with an interval of $\Delta t$. The temperature at $i$th element at the end of each time step is given below:

Time step k = 1: $T^i{}_{(t=\Delta t)} = \sum_{j=1}^{n} T^{ij}{}_{(t=\Delta t)} H^j{}_{(t=0)}$

Time step k = 2: $T^i{}_{(t=2\Delta t)} = \sum_{j=1}^{n} \left( T^{ij}{}_{(t=2\Delta t)} H^j{}_{(t=0)} + T^{ij}{}_{(t=\Delta t)} H^j{}_{(t=\Delta t)} \right)$

Time step k = 3:

$T^i{}_{(t=3\Delta t)} = \sum_{j=1}^{n} \left( T^{ij}{}_{(t=3\Delta t)} H^j{}_{(t=0)} + T^{ij}{}_{(t=2\Delta t)} H^j{}_{(t=\Delta t)} + T^{ij}{}_{(t=\Delta t)} H^j{}_{(t=2\Delta t)} \right)$

Time step k = 4:

$$T^{i}{}_{(t=4\Delta t)} = \sum_{j=1}^{n} \begin{pmatrix} T^{ij}{}_{(t=4\Delta t)} H^{j}{}_{(t=0)} + T^{ij}{}_{(t=3\Delta t)} H^{j}{}_{(t=\Delta t)} \\ + T^{ij}{}_{(t=2\Delta t)} H^{j}{}_{(t=2\Delta t)} + T^{ij}{}_{(t=\Delta t)} H^{j}{}_{(t=3\Delta t)} \end{pmatrix}$$

Time step k = 5:

$$T^{i}{}_{(t=5\Delta t)} = \sum_{j=1}^{n} \begin{pmatrix} T^{ij}{}_{(t=5\Delta t)} H^{j}{}_{(t=0)} + T^{ij}{}_{(t=4\Delta t)} H^{j}{}_{(t=\Delta t)} + T^{ij}{}_{(t=3\Delta t)} \\ \times H^{j}{}_{(t=2\Delta t)} + T^{ij}{}_{(t=2\Delta t)} H^{j}{}_{(t=3\Delta t)} + T^{ij}{}_{(t=2\Delta t)} H^{j}{}_{(t=4\Delta t)} \end{pmatrix}$$

To calculate the temperature at the end of a given time step $k$, the fictitious heat source in the previous step is required. If a uniform time step is used, the influence coefficient calculated from previous time steps can be saved and re-used during the calculation of time step $k$, significantly reducing computational time.

In practice, increasing the number of time steps will dramatically increase the size of the system of equations and hence reduce the calculation speed. It is recommended that the number of time steps be uniform and limited to 10.

## 9.3 Implementation of Thermal Mechanical Coupling in FRACOD

The following steps are generally involved in coupling the thermal stresses in FRACOD:

**Step 1:** Solve the thermal problem separately without mechanical calculations, using the fictitious heat source method. Obtain the fictitious heat sources along the boundary. Take into account any real heat sources in the rock mass.

**Step 2:** Calculate the thermal stress at the centre of all boundary elements. The thermal stresses are treated as the negative boundary stress on the elements and they are added into the total boundary stresses for the mechanical calculation. The same principle applies to the displacement boundary conditions.

**Step 3:** Solve the mechanical system of equations for the DDs of each element. The solution has already included the thermal effect.

**Step 4:** Calculate the stresses and displacements at any internal point in the rock mass using the resultant DDs. The thermal stresses and displacements need to be added to their mechanical values and they are calculated using fictitious and real heat sources.

(continued)

(continued)

In FRACOD, the following new functions are added regarding the thermal loading:

- Two types of thermal boundary conditions can be used: temperature or heat flux. The boundary condition can be constant or variable for the duration of problem time;
- Fractures can be treated as an internal thermal boundary. They can have temperature, heat flux or zero thermal resistant (i.e. the derivative of heat flux is constant across the fracture);
- Internal heat sources are allowed, including both point sources and line source in two dimensions. The internal heat sources can have variable strength;
- Equal time steps are used. The maximum number of time steps allowed is 10.

## 9.4 Temperature Dependent Rock Properties

Experimental data shows that many rock properties are temperature dependent. The key rock property parameters known to have significant temperature dependency include:

- Uniaxial compressive strength *decreases* with temperature increases;
- Tensile strength *decreases* with temperature increases;
- Fracture toughness *decreases* with temperature increases;
- Thermal conductivity *decreases* with temperature increases;
- Thermal expansion coefficient *increases* with temperature increases.

To properly model the thermal mechanical behaviour of rock, FRACOD needs to consider this temperature dependency.

FRACOD may easily incorporate the temperature dependency of rock strength parameters, such as compressive and tensile strength and fracture toughness. It is however difficult to consider the temperature dependency of modulus including the thermal conductivity and thermal expansion coefficient. Only the former has been implemented in FRACOD to date.

Implementation of the temperature dependency in FRACOD is relatively straightforward. It involves the following steps:

**Step 1:** Record the strength parameters ($\sigma_t$, c, $\phi$, $K_{IC}$, $K_{IIC}$) for a number of temperature values. For any temperature in between two given values, the strength parameters can be calculated using a linear function.

(continued)

(continued)

**Step 2:** Determine the temperature value at the rock internal points and fracture tips.

**Step 3:** Calculate the strength values at the internal points or fracture tips using the temperature obtained.

**Step 4:** Determine if fracture initiation and/or fracture propagation will occur.

The temperature dependency function will be a user-defined input file. No pre-set function is given in FRACOD. This treatment provides users with the maximum flexibility to use any temperature variation functions.

## References

Berchenko I (1998) Thermal loading of saturated rock mass: field experiment and modelling using thermoporoelastic singular solutions. Ph.D. thesis, University of Minnesota

Cheng AH-D, Ghassemi A, Detournay E (2001) A two-dimensional solution for heat extraction from a fracture in hot dry rock. Int Numl Analyt Meth in Geomech 25:1327–1338

Ghassemi A, Cheng AHD, Diek A, Roegiers JC (2001) A complete plane strain fictitious stress boundary element method for poroelastic media. Eng Anal Bound Elem 25:41–48

Timoshenko SP, Goodier JN (1970) Theory of elasticity, 3rd edn. MacGraw-Hill Book Company, New York

Zhang Q (2004) A boundary element method for thermo-poroelasticity with applications in rock mechanics. M.Sc. thesis, University of North Dakota

# Chapter 10
# Hydro-Mechanical Coupling

**Abstract** This chapter provide the theoretical formulations and numerical procedures involved in hydro-mechanical coupling function in FRACOD.

An explicit iteration approached is used in FRACOD to solve the coupled fracturing – hydraulic flow processes. The mechanical calculation (including rock deformation and fracture propagation) is completed using the Displacement Discontinuity Method (DDM) with an iteration scheme for modelling fracture propagation processes. The fracture fluid flow calculation is conducted through the time-marching iteration based on the Cubic Law.

In fractured hard rock such as granite, fluid flow occurs predominantly through explicit fractures rather than intact rock, due to the intact rock's low permeability. Fluid pressure in rock fractures may cause rock fracture movement, increase fracture aperture or even cause fracture propagation. On the other hand, fracture movement and propagation will change the fracture hydraulic conductivity and create new flow paths. The dynamic interaction between fracture mechanical response and fluid flow is critically important in studying the coupled fracturing–hydraulic flow (F-H) processes.

Two fundamental approaches have been used in modelling the hydro-mechanical coupling in fractured rock medium. The first is the implicit approach, where fluid flow equations are solved together with mechanical equations for rock matrix and fractures. Most of the finite element codes using Darcy's Law and designed for modelling porous flows are based on this approach. The boundary element code used by Zhang et al. (2005) to simulate hydraulic fracturing is also based on this approach.

The second is the explicit approach, where both fluid flow and mechanical response are simulated using a time marching iteration process. The well-known commercial distinct element code UDEC (Itasca 2010) is based on this approach. Compared to the implicit approach, the explicit approach is mathematically simple

B. Shen et al., *Modelling Rock Fracturing Processes: A Fracture Mechanics Approach Using FRACOD*, DOI 10.1007/978-94-007-6904-5_10,

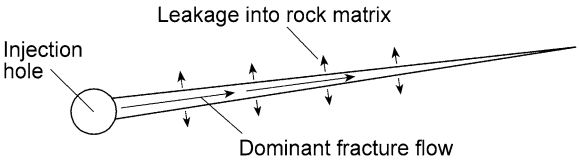


**Fig. 10.1** A flow system with dominant fracture flow and minor leakage into rock matrix from an injection hole

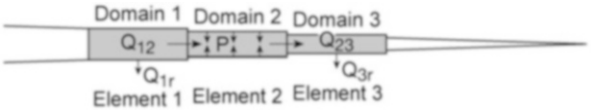


**Fig. 10.2** Domain division for fluid flow simulation in a fracture

and easily adopts complicated boundary conditions and changing model conditions. However, this approach often requires significantly longer computational time, as small time steps are required to achieve convergence for flow solutions.

The explicit approach is used in this book. The mechanical calculation (including rock deformation and fracture propagation) is completed using the Displacement Discontinuity Method (DDM) with an iteration scheme for modelling fracture propagation processes. The fracture fluid flow calculation is conducted through the time-marching iteration based on the Cubic Law.

## 10.1 Numerical Considerations

This chapter focuses on fluid flow predominantly in rock fractures. However, leakages from fracture fluid channels to the rock matrix are also considered, see Fig. 10.1.

During the mechanical numerical simulation using DDM, a fracture is discretised into a number of DD elements. In the flow calculation, each DD element is considered as a hydraulic domain and the adjacent domains are connected hydraulically (see Fig. 10.2). Fluid may flow from one domain to another depending on the pressure difference between the two domains.

## 10.2 Iteration Scheme

The solution of a coupled F-H problem can be achieved numerically using the iteration scheme shown in Fig. 10.3. Iteration steps are described below:

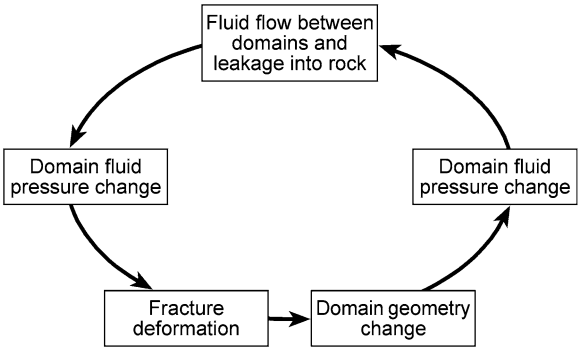


**Fig. 10.3** Iteration process for a coupled F-H process

**Step 1.** Fluid flow occurs between fracture domains and fluid leaks into rock matrix. The fluid flow between fracture domains is calculated using the Cubic Law. The flow rate (Q) between two domains is calculated using Eq. (10.1):

$$Q = \frac{e^3}{12\mu}\frac{\Delta P}{l} \tag{10.1}$$

where: $e$ is fracture hydraulic aperture; $l$ is element length; $\Delta P$ is fluid pressure difference; $\mu$ is fluid viscosity.

The leakage from a fracture domain into the rock matrix ($Q_{leak}$) is calculated using Eq. (10.2).

$$Q_{leak} = \frac{k}{\mu}\frac{P - P_0}{d} \tag{10.2}$$

where: $k$ is rock permeability; $d$ is effective leakage distance; $P$ is domain fluid pressure; $P_0$ is initial pore pressure.

**Step 2.** Fluid flow causes changes in domain fluid pressure. The new domain pressure due to fluid flow during a small time duration $\Delta t$ is calculated using Eq. (10.3):

$$P(t + \Delta t) = P_0 + E_w Q\frac{\Delta t}{V} - E_w Q leak\frac{\Delta t}{V} \tag{10.3}$$

where: $E_w$ is fluid bulk modulus; $V$ is domain volume; $\Delta t$ is time step.

**Step 3.** Change in fluid pressure causes fracture deformation. The fracture deformation is calculated using DDM where the new fluid pressures in

(continued)

(continued)

fracture domains are the input boundary stresses. After considering the fluid pressure in the fracture domains (elements), the system of equations for calculating the element displacement discontinuities is given below in Eq. (10.4):

$$\begin{cases} \left(\overset{i}{\sigma_s}\right)_0 = \sum_{j=1}^{N} \overset{ij}{A_{ss}}\ \overset{i}{D_s} + \sum_{j=1}^{N} \overset{ij}{A_{sn}}\ \overset{i}{D_n} - K_s \overset{i}{D_s} \\ \left(\overset{i}{\sigma_n}\right)_0 = p(t+\Delta t) - p_0 = \sum_{j=1}^{N} \overset{ij}{A_{ns}}\ \overset{i}{D_s} + \sum_{j=1}^{N} \overset{ij}{A_{nn}}\ \overset{i}{D_n} - K_n \overset{i}{D_n} \end{cases} \tag{10.4}$$

where: $(\sigma_s)_0$, $(\sigma_n)_0$ are in situ stresses in fracture shear and normal directions; $D_s$, $D_n$ are displacement discontinuities in shear and normal directions; $A_{ss}$, $A_{sn}$, $A_{ns}$, $A_{nn}$ are influence coefficients; $K_s$, $K_n$ are fracture shear and normal stiffness.

**Step 4.** Fracture deformation alters the domain volume, changing the fluid pressure in domains. The new domain pressure is calculated using Eq. (10.5).

$$P'(t+\Delta t) = P(t+\Delta t) - E_w \frac{\Delta e \cdot l}{V} \tag{10.5}$$

The new domain fluid pressures are then used to calculate the flow rate between domains in Step 1. Steps 1–4 are iterated until the desired fluid time is reached and a stable solution is achieved.

## 10.3 Fluid Time Step

During the fluid flow calculation, a proper time step is needed for the iteration process to converge to a final solution. To determine the optimal time step for fluid flow calculation, we consider a case with two connected fluid domains as shown in Fig. 10.4. The two domains have the same length and aperture, but with an initial fluid pressure difference of $\Delta P$.

The change of fluid pressure in Domain 1 is calculated using Eq. (10.6):

$$\Delta P_1 = \frac{\Delta V}{V} E_w = \frac{Q \Delta t}{l \cdot e} E_w \tag{10.6}$$

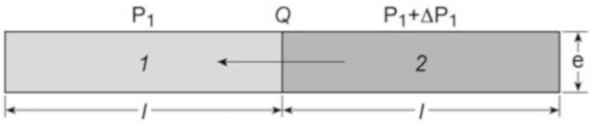


**Fig. 10.4** A two-domain flow system demonstrating the stable time step

where:

$\Delta P_1$ – Fluid pressure change in Domain 1 due to fluid inflow;
$\Delta V$ – Change of fluid volume;
$V$ – Domain volume;
$Q$ – Rate of fluid into the Domain 1;
$l$ – Element length;
$e$ – Domain aperture, related to normal displacement;
$\Delta t$ – Flow time step;
$E_w$ – Fluid bulk modulus.

Based on Eq. (10.1), the pressure difference between the two cells is calculated:

$$\Delta P_{12} = Q \frac{12\mu l}{e^3} \tag{10.7}$$

where: $\Delta P_{12}$ is the fluid pressure difference between Domain 1 and Domain 2.

After one time step, if the domain pressure change $\Delta P_1$ in Domain 1 equals the original pressure difference $\Delta P_{12}$ between the two domains, the resultant pressure difference will again be $\Delta P_{12}$ but with higher pressure in Domain 1 than Domain 2. In the next time step, the flow will be reversed, the flow pressure will revert to the original state as shown in Fig. 10.4. This means that, numerically, the flow will be oscillating between the two domains and never converge.

Hence, to achieve a numerical convergence, it is necessary that the domain pressure change $\Delta P_1$ is less than the original pressure difference $\Delta P_{12}$ between the two domains, i.e.

$$\Delta P_1 = \frac{Q\Delta t}{l \cdot e} E_w < \Delta P_{12} = Q \frac{12\,\mu l}{e^3}$$

With simple mathematical manipulation, the time step required for a converging numerical solution is given in Eq. (10.8)

$$\Delta t < \frac{12\mu \cdot l^2}{E_w \cdot e^2} \tag{10.8}$$

It is noted from Eq. (10.8) that the convergent time step is sensitive to fluid bulk modulus and fracture aperture. High fracture aperture and fluid bulk modulus will require a small time step. For water at room temperature, if the fracture aperture is 50 μ and the element length is 0.1 m, the required time step for fluid calculation will be $2.4 \times 10^{-5}$ s.

The time step determined using Eq. (10.8) is for dynamic fluid calculation. For transient flow or steady state flow problems where the time duration is often days

to months, this time step could be too small to reach a final solution quickly. One way to improve the calculation speed is to use a much lower fluid bulk modulus. Experience indicates that a fluid with a low bulk modulus is also much more stable in the coupled calculation with mechanical deformation.

## References

Itasca (2010) UDEC – Universal Distinct Element Code. Itasca Consulting Group, Minnesota
Zhang X, Jeffrey RG, Detournay E (2005) Propagation of a fluid-driven fracture parallel to the free surface of an elastic half plane. Int J Numer Anal Meth Geomech 29:1317–1340

# Chapter 11
# Anisotropic Rock Strength Function

**Abstract** In rock engineering, anisotropic rock masses are often encountered and cannot be simplified as an isotropic problem in numerical models. Hence an anisotropic function in the numerical model is required.

Rock anisotropy includes strength anisotropy and modulus anisotropy. Developing the anisotropic function in FRACOD requires significantly different complexity for strength anisotropy and modulus anisotropy. The strength anisotropy function alone does not require any alteration in the way FRACOD calculates the rock stress and displacement, and therefore it is relatively straightforward. The modulus anisotropy function, on the other hand, will require the modification of the fundamental equations of stress and displacement, and hence will be much more complex and difficult. In actual rock engineering, the strength anisotropy is often considered to be much more pronounced and important than the modulus anisotropy, and it dominates the stability and failure pattern of the rock mass.

This chapter discusses work related to the development of the strength anisotropy in FRACOD. This function has been developed for modelling the rock fracturing behaviours at the Finnish URL for high-level radioactive waste disposal where the host rock of gneiss is highly foliated and anisotropic.

## 11.1 Fracture Initiation

Fracture initiation occurs in rock when the combination of two principal stresses (in 2D) reaches a critical value. The critical value is the rock fracture initiation strength, often proportional to the rock ultimate strength. In FRACOD, the Mohr-Coulomb criterion is adopted as mentioned in Sect. 3.5.1, and the compressive strength of the rock is given by:

$$\sigma_1 = \frac{2c\ \cos\phi + \sigma_3(1 + \sin\phi)}{1 - \sin\phi} \tag{11.1}$$

B. Shen et al., *Modelling Rock Fracturing Processes: A Fracture Mechanics Approach Using FRACOD*, DOI 10.1007/978-94-007-6904-5_11,

where $\sigma_1$ and $\sigma_3$ are the major and minor principal stresses; $\phi$ is the rock internal friction angle, and $c$ is the cohesion. The direction of the failure plane is at an angle $\beta = \frac{\pi}{2} + \frac{\phi}{2}$ from the direction of $\sigma_3$.

The tensile strength is given by:

$$\sigma_1 = \sigma_t \tag{11.2}$$

where $\sigma_t$ is the tensile strength of intact rock. The failure plane is in the direction of $\sigma_3$.

Equations (11.1) and (11.2) are for isotropic rock only. In an anisotropic rock, the rock strength is direction dependent, and the Mohr-Coulomb strength parameters will also be a function of orientation angle $\beta$, i.e:

$$\begin{aligned} \sigma_t &= \sigma_t(\beta) \\ \phi &= \phi(\beta) \\ c &= c(\beta) \end{aligned}$$

In this case, both the critical principal stress ($\sigma_1$) in Eq. (11.1) and the failure plane direction ($\beta = \frac{\pi}{4} + \frac{\phi}{2}$) are no longer valid. To determine the failure plane direction for anisotropic rock, we need to consider the stresses and strength of an arbitrary plane A-B with an angle β (see Fig. 11.1). For compression failure, the normal and shear stresses on the plane A-B are:

$$\begin{aligned} \sigma_n &= \frac{\sigma_1 + \sigma_3}{2} + \frac{\sigma_1 - \sigma_3}{2} \cos 2\beta \\ \sigma_s &= \frac{\sigma_1 - \sigma_3}{2} \sin 2\beta \end{aligned} \tag{11.3}$$

The shear strength of plane A-B is given below:

$$S = \left[ \frac{\sigma_1 + \sigma_3}{2} + \frac{\sigma_1 - \sigma_3}{2} \cos 2\beta \right] \tan \phi(\beta) + c(\beta) \tag{11.4}$$

Let us define a shear failure indicator ($Fs$) on plane A-B as:

$$Fs = \frac{\sigma_s}{S} = \frac{(\sigma_1 - \sigma_3) \sin 2\beta}{[\sigma_1 + \sigma_3 + (\sigma_1 - \sigma_3) \cos 2\beta] \tan \phi(\beta) + c(\beta)} \tag{11.5}$$

A shear failure will occur in a plane where the failure indicator is the maximum and reaches 1.0, i.e. the shear stress exceeds the shear strength. In mathematical terms, $Fs$ should meet the following conditions:

$$\frac{dFs}{d\beta} = 0$$

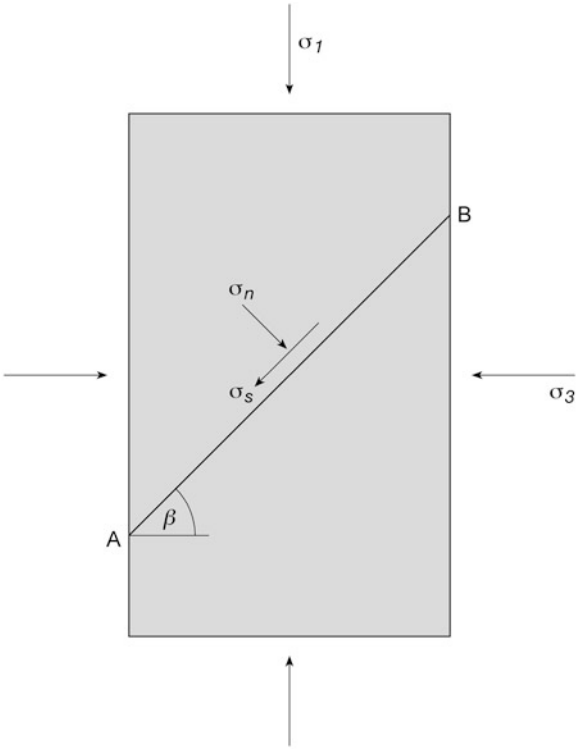


**Fig. 11.1** Shear failure on plane A-B in anisotropic rock

$$\frac{d^2 Fs}{d\beta^2} < 0$$

$$Fs \geq 1.0$$

Over the entire angle range from 0° to 360°, *Fs* often has four peak values in four different directions depending on the anisotropic rock strength parameters (see Fig. 11.2). It is important that all the four peaks are considered and only the maximum ones are selected.

For a tensile failure, the failure factor (*Ft*) is defined using the tensile stress and tensile strength as shown below:

$$Ft = \frac{\sigma_n}{\sigma_t} + \frac{(\sigma_1 + \sigma_3) + (\sigma_1 - \sigma_3)\cos 2\beta}{2\sigma_t} \tag{11.6}$$

Similarly, the actual tensile failure plane will be the one where *Ft* reaches the maximum and is equal to or greater than 1.0.

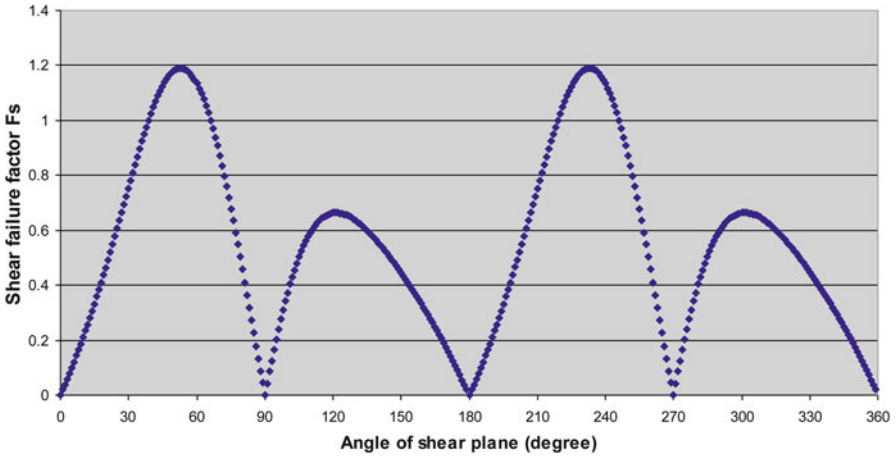


**Fig. 11.2** Four potential shear failure planes at which the failure factor *Fs* reaches a peak. The planes with maximum *Fs* are the actual failure planes

## 11.2 Fracture Propagation

FRACOD uses the F-criterion to determine the likelihood and the direction of fracture propagation,

$$F = \frac{G_I}{G_{Ic}} + \frac{G_{II}}{G_{IIc}} = 1.0 \tag{11.7}$$

where $G_I$ and $G_{II}$ are the strain energy release rate in Mode I and Mode II, and $G_{Ic}$ and $G_{IIc}$ are the critical strain energy release rate in Mode I and Mode II. The direction of fracture propagation is the direction in which $F$ reaches the maximum value.

The F-criterion can also be expressed in terms of fracture stress intensity factors ($K_I$ and $K_{II}$) and fracture toughness ($K_{Ic}$ and $K_{IIc}$) for Mode I and Mode II, as shown below:

$$F = \left(\frac{K_I}{K_{Ic}}\right)^2 + \left(\frac{K_{II}}{K_{IIc}}\right)^2 = 1.0 \tag{11.8}$$

In an anisotropic rock, the fracture toughness will be direction dependent, i.e.

$$K_{Ic} = K_{Ic}(\beta)$$
$$K_{IIc} = K_{IIc}(\beta)$$

In this case, the F-criterion needs to be re-written as:

$$F = \left(\frac{K_I}{K_{Ic}(\beta)}\right)^2 + \left(\frac{K_{II}}{K_{IIc}(\beta)}\right)^2 = 1.0 \tag{11.9}$$

When determining the direction of fracture propagation, we must consider the direction dependency of the fracture toughness. The direction where the F-value is the highest will be the potential direction of fracture propagation.

## 11.3 Numerical Implementation

The strength anisotropy described above has been implemented in FRACOD in the following steps:

**Step 1:** Record the strength parameters ($\sigma_t$, $c$, $\phi$, $K_{IC}$, $K_{IIC}$) for all angles in the range (0, 360°) where angle interval is set at 1°.
**Step 2:** Calculate *Fs* and *Ft* values using Eqs. (11.5) and (11.6) for all angles at the pre-defined grid points in the intact rock, and record the potential fracture initiation angles where *Fs* or *Ft* reaches its maximum value.
**Step 3:** Calculate the F value using Eq. (11.9) for all angles at the fracture tips, and record the potential fracture propagation angle where F reaches the maximum value.
**Step 4:** Determine if fracture initiation and/or fracture propagation will occur at the given potential initiation and propagation directions.

Once fracture initiation or propagation is detected, the normal numerical process will be followed to simulate the fracture growth.

Three functions are available in FRACOD to define the variation of the strength parameters with direction. They are:

1. Linear variation from θ to θ + 90° (where θ can be any angle between 0° and 90°)
2. Elliptical variation from θ to θ + 90° (where θ can be any angle between 0° and 90°)
3. User-defined variation from 0° to 360°

The user can also define any irregular functions of strength anisotropy by simply listing the values at different direction angles.

In FRACOD, anisotropy of intact rock strength and fracture toughness is defined separately. Therefore the users can employ different anisotropic functions for the intact strength and for the fracture toughness.

# Chapter 12
# Rock Properties for FRACOD Modelling

**Abstract** Modelling of rock fracturing problems with FRACOD requires some physical and mechanical rock properties not commonly used in traditional rock mechanics. This chapter gives a short description and references to testing methods and data for properties in the following areas:

- Mechanical properties
  - Intact rock
  - Joint
  - New fracture
- Fracture mechanics properties
- Thermal properties

In modelling fractured rocks and rock masses for a project or a site one sometimes has access to parameters measured in the field or determined in the laboratory. This chapter refers to suggested methods for evaluating rock parameters recorded in the field or in the laboratory. Ulusay and Hudson's (2007) publication of a complete set of the ISRM Suggested Methods for rock characterisation, testing and monitoring during the time period 1974–2006 is highly recommended. In addition, a number of handbooks present rock physical and mechanical data. Well-regarded are handbooks by Clark (1966), Angenheister (1982), Hudson (1993) and Ahrens (1995).

## 12.1 Mechanical Properties of Intact Rock

Strength and deformability are required parameters for analysing most rock engineering problems. The parameters needed in FRACOD modelling are listed in Table 12.1 together with references to ISRM Suggested Methods for performing the rock tests and references to data collection of parameters.

B. Shen et al., *Modelling Rock Fracturing Processes: A Fracture Mechanics Approach Using FRACOD*, DOI 10.1007/978-94-007-6904-5_12,

**Table 12.1** Mechanical properties of intact rock

| | *Symbol* | Parameter | Unit | Reference |
|---|---|---|---|---|
| Rock deformability | $\nu$ | Poisson's ratio | | Ulusay and Hudson (2007, pp. 153–156) |
| | $E$ | Young's modulus | Pa | |
| Intact strength for fracture initiation | $\phi$ | Internal friction angle | Degree | Ulusay and Hudson (2007, pp. 159–164; 177–183) |
| | $c$ | Cohesion | Pa | |
| | $\sigma_t$ | Tensile strength | Pa | |

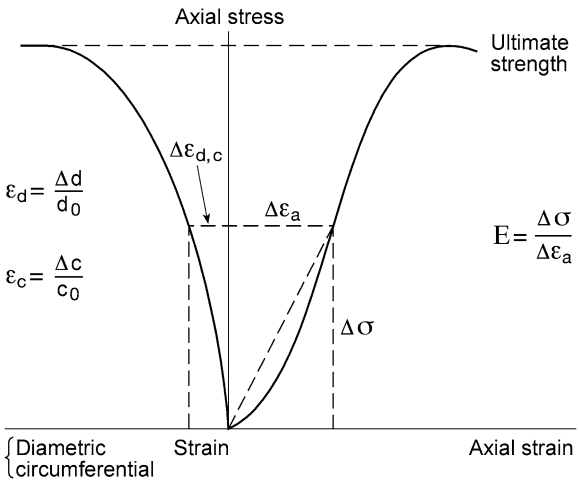


**Fig. 12.1** Method for calculating secant Young's modulus and Poisson's ratio from axial and diametrical stress–strain curve at 50 % of ultimate strength. $\Delta d$ diametric deformation, $\Delta c$ circumferential deformation

Drill cores from diamond drilling are usually used to test intact rock material. Samples typically have a height to diameter ratio of 2 when NX core size (54 mm) is used. A sample is placed between plates in a preferably stiff testing machine and the load is applied at a stress rate of 0.5–1.0 MPa/s. The sample is loaded and the stress versus axial and diametrical/circumferential strain is recorded until failure. Typically five samples of the same rock type are tested and the average value of strength and deformability is calculated.

A typical graphical format for axial and diametrical stress–strain curves up to ultimate strength is presented in Fig. 12.1. Rock deformability can be determined by three different methods: (1) tangent modulus; (2) average modulus and (3) secant modulus of the Young's modulus and Poisson's ratio. Graphical representation the secant modulus is given in Fig. 12.1.

The elastic parameters Young's modulus and Poisson's ratio can also be determined from triaxial compression tests. Here we distinguish between true triaxial compression tests where all three principal stresses are independently controllable and conventional triaxial tests where two of the principal stresses are equal. Due to the confinement generated by the applied compressive intermediate and least

**Table 12.2** Elastic properties of intact rock types. Data provided by Backers (2011, personal communication)

| Rock class | Rock type | Young's modulus (GPa) | Poisson's ratio |
|---|---|---|---|
| Sedimentary rock | Flechtingen sandstone | 21 | 0.12 |
| | Rüdersdorf limestone | 22 | 0.22 |
| | Alum shale | 12 | 0.15 |
| Metamorphic rock | Carrara marble | 49 | 0.23 |
| | Schist | 45 | 0.20 |
| | Migmatitic gneiss | 63 | 0.25 |
| Igneous rock | Granodiorite | 72 | 0.23 |
| | Aue granite | 48 | 0.19 |
| | Gabbro | 75 | 0.27 |

principal stress, the Young's modulus and Poisson's ratio becomes slightly larger than for uniaxial compressive test. Less often, elastic properties of rock are tested in tension.

Elastic properties of different rock types are presented in Table 12.2. Note the increase in elastic properties as alteration, temperature and pressure of the rock-forming processes increase.

In determining the intact rock's internal friction angle, $\phi$, and cohesion, $c$, triaxial rock testing is employed. Tests are typically conducted on a set of drill cores, say five to ten, with two to three samples at different constant confining pressure. Tests are performed until failure and pre-and post-peak stress versus strain is recorded. Following the tests conducted at different confining pressure, the failure stress and confining stress are plotted as a set of Mohr circles and a Mohr failure envelope is constructed. From the intercept of the envelope at zero normal stress the rock cohesion is defined. The angle of internal friction defines the limiting size of the Mohr's circles and corresponds to the frictional sliding of the inclined failure plane in the sample. Any stress condition below the Mohr failure envelope represents stable state for the sample. The principle of Mohr-Coulomb criterion in normal stress – shear stress space is depicted in Fig. 12.2. As rocks are weak in tension, a so-called tension cut-off is usually introduced in the graphical representation of the criterion.

Intact rock tensile strength, $\sigma_t$ can be determined from Brazilian tests or directly by the conventional pull-apart test of drill cores (where the core is glued on both ends to steel chains and where the other ends of the chains are fixed to the grips of the testing machine). The stress is slowly increased until the sample fails and the stress at failure gives the tensile strength. Alternatively, tensile strength can be determined indirectly by the Brazilian test where disc-shaped rock samples are loaded diametrically and the tensile strength is calculated with a formula containing the maximum load and the geometry of the specimen. The ISRM Suggested Method

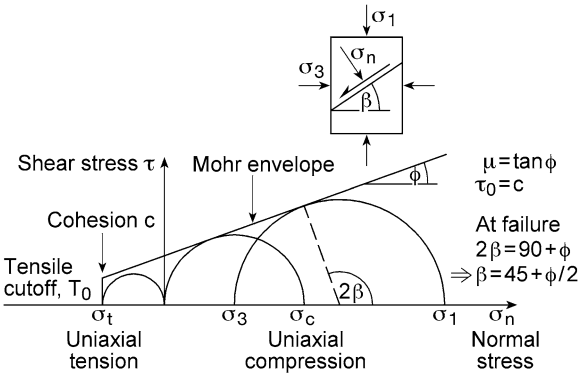


**Fig. 12.2** Graphical representation of Mohr-Coulomb failure criterion of rock from a set of four triaxial tests at different confinements

**Table 12.3** Intact rock strength for fracture initiation

| Rock class | Rock type | Friction angle $\phi$ (degrees) | Cohesion $c$ (MPa) | Tensile strength $\sigma_t$ (MPa) |
|---|---|---|---|---|
| Sedimentary rock | Sandstone | 40 | 7 | 6 |
| | Limestone | 35 | 5 | 4 |
| | Shale | 20 | 2 | 1 |
| Metamorphic rock | Marble | 40 | 6 | 7 |
| | Schist | 35 | 7 | 6 |
| | Gneiss | 45 | 9 | 8 |
| Igneous rock | Granodiorite | 50 | 28 | 13 |
| | Granite | 45 | 23 | 11 |
| | Gabbro | 60 | 30 | 15 |

for determining the tensile strength of rock material is reprinted by Ulusay and Hudson (2007). The following is a set of typical strength data for fracture initiation (Table 12.3).

## 12.2 Mechanical Properties of Fracture Surface Contact

The presence of fractures makes the mechanical behaviour of rock masses different from that of most engineering materials. Fractures or joints often have a controlling influence on mechanical and hydraulic properties. A rock fracture consists of two planar rough surfaces that are in contact at some points and separated at others. The separation between the nominal fracture plane at zero normal stress is known as the aperture. As a fracture is deformed, the undulation of the surface may cause the rock blocks to ride on top of each other and thereby increase the opening of the fracture. This process is called dilation and defined by the fracture dilation angle $\phi_d$ (degree) (Table 12.4).

**Table 12.4** Mechanical properties of fracture surface contact

| Property | Parameter | Unit | Command in FRACOD | ISRM suggested method | Data references |
|---|---|---|---|---|---|
| Fracture surface contact | Shear stiffness | Pa/m | *Ks* | Ulusay and Hudson (2007, pp. 165–176) | Jaeger et al. (2007) |
| | Normal stiffness | Pa/m | *Kn* | | |
| | Fracture friction angle | degree | $\phi$ | | Hudson and Harrison (2000) |
| | Fracture dilation angle | degree | $\phi_d$ | | |
| | Fracture cohesion | Pa | *c* | | |

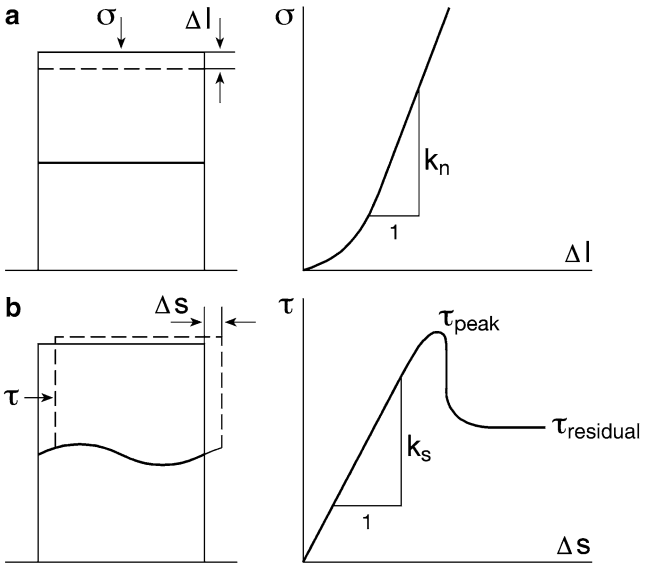


**Fig. 12.3** Definition of linear stiffness of rock fracture and joint; (**a**) normal stiffness, (**b**) shear stiffness

When a fracture or joint located in the rock mass is subjected to a stress, the force acting across the fracture plane can be resolved into one component acting perpendicular to the fracture plane and another component acting along the fracture plane. The force acting normal to the fracture plane will result in normal closure as shown in Fig. 12.3a. The closure of the fracture for a given normal stress is defined as the normal stiffness $K_n$ of the fracture. In testing the normal stiffness of rock material, the deformation of the rock material on both sides of the fracture should be subtracted.

As the shear displacement increases, the shear stress reaches the peak shear strength. This is followed by a drop in stress and subsequent residual shear strength, as illustrated in Fig. 12.3b. Results from all test specimens are plotted on graphs

of peak and residual shear strength versus normal stress. The lines combining the experimental data points define the peak shear strength and residual shear strength. The slope of the lines gives the peak and residual friction angle, respectively. The cohesion is defined by the intercept of the linear part of the data point from the peak shear strength data on the axis of the shear stress.

The shear stiffness and direct shear strength testing of fractures is performed in a shear box in the field or laboratory. The sample with its fracture is cast in two holders and, after hardening, removed to the shear box. A constant normal load is applied to the boxes then the normal displacement across the fracture is recorded and the normal stiffness is calculated (Fig. 12.3a). Thereafter, shear load is applied for the applied normal stress, and normal and shear displacement is recorded as a function of applied shear stress. The linear shear stiffness $K_s$ is defined as shown in Fig. 12.3b.

## 12.3 Fracture Toughness and Critical Strain Energy Release Rate

In Chap. 2, the three basic loading configurations and fracture modes of crack tip deformation, Modes I, II and III were explained and illustrated (see Fig. 12.4). Mode I is the opening (or tensional) mode. Mode II is the edge-sliding mode (or in-plane shearing). Mode III is the tearing (or out-of plane) mode. A combination of any of the three loading modes forms a mixed-mode loading.

Each of the three stress intensity factors ($K_I$, $K_{II}$, $K_{III}$) is associated with a unique stress distribution near the crack tip and is governed by Eqs. (2.9, 2.11 and 2.12). The fracture initiation occurs when the stress intensity factor reaches its critical value called the fracture toughness ($K_{Ic}$, $K_{IIc}$, $K_{IIIc}$) (Table 12.5).

### *12.3.1 Mode I Fracture Toughness*

ISRM Suggested Methods (Ulusay and Hudson 2007) offers three different methods for determinating Mode I fracture toughness:

1. Chevron bend specimen testing
2. Short rod specimen testing
3. Cracked Chevron Notched Brazilian Disc (CCNBD) specimen testing

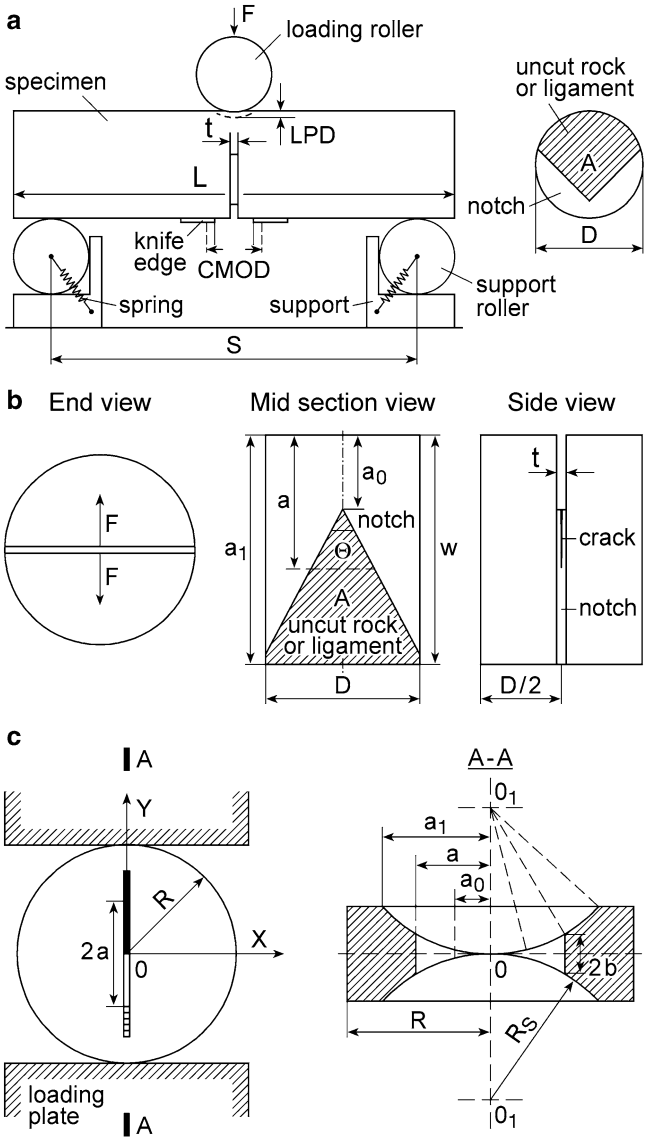


**Fig. 12.4** ISRM Suggested Methods for Mode I fracture toughness testing of rock. (**a**) Method 1, Chevron bend testing, (**b**) Method 2, Short rod testing, and (**c**) Method 3, Cracked chevron notched Brazilian disc testing (Modified after Ulusay and Hudson (2007))

**Table 12.5** Fracture toughness and critical strain energy release rate

| Property | Parameter | Unit | Symbol | ISRM suggested method | Data references |
|---|---|---|---|---|---|
| Fracture toughness | Mode I (tensile) | Pa $m^{1/2}$ | $K_{Ic}$ | Ulusay and Hudson (2007, pp. 231–268) | Backers et al. (2002) |
| | Mode II (shear) | Pa $m^{1/2}$ | $K_{IIc}$ | | |
| Critical energy release rate | Mode I energy release | J $m^{-2}$ | $G_{Ic}$ | Ulusay and Hudson (2007, pp. 238–246) | Backers et al. (2002) |
| | Mode II energy release | J $m^{-2}$ | $G_{IIc}$ | | |

Method 1 uses a bend specimen with a notch cut perpendicular to the axis of the drill core. The specimen rests on two roller supports and is loaded in the centre. The sides of the notches are pressed and the fracture propagates in the ligament as the load is increased. The ligament of the notch section has a V-shape that generates a stable crack growth. Figure 12.4a shows the testing arrangement of this method where LPD is load point deflection, A is ligament and CMOD is crack mouth opening displacement.

Method 2 uses a short section of the drill core with the notch fabricated parallel with the drill core's axis. The tensile load is applied at the edge of the sample by means of a special grip of the loading machine. The pulling force is F as shown in Fig. 12.4b.

Methods 1 and 2 offer two test levels. Level 1 testing is the simpler method, where only the maximum load for failure is needed to calculate the fracture toughness. Level 2 testing prescribes a continuous load and displacement in the post-peak region of the load versus displacement recordings. This approach demands a servo-hydraulic testing machine so that the rate of deformation can be controlled.

Method 3 uses CCNBD specimens in the shape of a disc cut from the drill core. Loading is done as for Brazilian testing. A chevron notch is cut in the centre of the sample with a circular diamond saw. The fracture is allowed to propagate from the centre of the chevron saw cut to the periphery of the disc. The fracture toughness is calculated from a simple formula containing the maximum load, geometry of the disc and the stress intensity for the specimen.

The three different methods allow fracture toughness testing in three different directions of the drill core, thus allowing determination of the anisotropy of toughness for the rock mass.

Influence of relative humidity on Mode I fracture toughness of different rock types and its implications for subcritical crack growth has been studied by Nara et al. (2012) using the double torsion method. For sandstones, andesite and granite the fracture toughness decreases with increasing relative humidity.

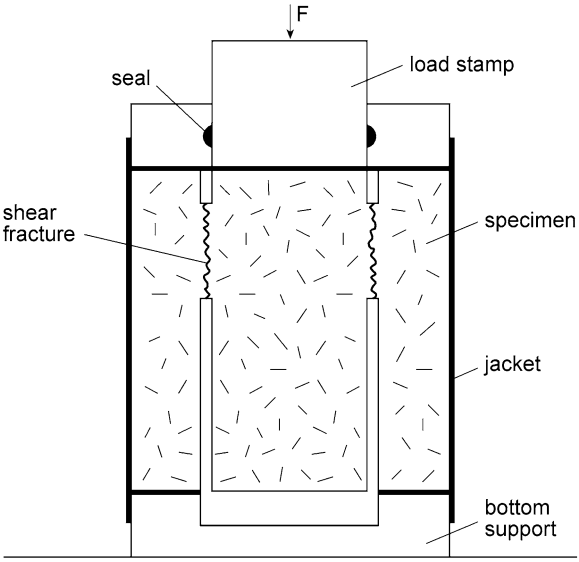


**Fig. 12.5** Set-up of the Punch-Through Shear with Confining Pressure (PTS/CP) for testing Mode II fracture toughness of rock (Modified after Backers et al. 2002)

### *12.3.2 Mode II Fracture Toughness*

The Suggested Method for $K_{IIc}$ fracture toughness determination makes use of the Punch-Through Shear with Confining Pressure (PTS/CP) experiment, where samples from $K_{Ic}$ testing can be used to obtain fracture toughness data for both Mode I and Mode II analysis (Backers et al. 2002; Backers and Stephansson 2012).

The geometry of the test specimen is designed to use standard core materials (NX size or 50 mm diameter) and to deploy the remaining halves from Mode I (tensile) fracture toughness testing by the Chevron Bend method. The experimental set-up allows measuring the Mode II fracture toughness at different levels of confining pressure.

The specimen is placed on top of a bottom support that has a central cut-out, slightly larger than the sample's diameter. The specimen surface with the longest notch faces downwards, Fig. 12.5.

A load stamp assembly is placed on top of the specimen, containing a load piston and a sealing to prevent leakage of confining pressure liquid, and is covered with a jacket that seals the specimen from the confining pressure medium. The assembly consisting of specimen, loading devices and jacket is placed into a loading frame of sufficient capacity and equipped with a system to apply a confining pressure that can be independently controlled. The confining pressure is applied and then kept constant during the time of the test. Axial displacement is increased at a constant rate of 0.2 mm/min and the axial load is recorded. At peak load a fracture propagates

**Table 12.6** Values of Mode I and Mode II fracture toughness of rock (After Backers et al. 2002)

| | | $K_{Ic}$ | $K_{IIc}$ (low P) | $K_{IIc}$ (high P) | $K_{Ic}/K_{IIc}$ |
|---|---|---|---|---|---|
| Äspö granite, medium grained | Sweden | 3.8 | 4.7 | 11.5 | 1.2/3.0 |
| Aue granite, coarse grained | Germany | 1.6 | 4.2 | 10.5 | 2.6/6.6 |
| Mizunami granite, medium grained | Japan | 2.4 | 4.2 | 10.9 | 1.5/3.8 |
| Daejson granite, fine grained | Korea | 1.6 | 4.0 | – | 2.5/– |
| Carrara marble | Italy | 2.4 | 3.1 | 6.7 | 1.3/2.8 |
| Flechtingen sandstone, fine grained | Germany | 1.2 | 2.1 | 5.3 | 1.8/4.4 |
| Bentheim sandstone, fine grained | Germany | 0.9 | – | – | –/– |
| Ruedersdorf limestone, mudstone | Germany | 1.1 | 3.1 | 4.2 | 2.8/3.8 |

between the lower and upper notches. The test is terminated after driving the test to the post-peak stage. The Mode II fracture toughness is evaluated from the maximum load during testing and a set of constants valid for a given geometry of the sample and notches.

Typical values of $K_{IC}$ and $K_{IIC}$ and the ratio $K_{IIC}/K_{IC}$ are presented in Table 13.7. Notice that $K_{IIC}$ is dependent on confinement so that fracture toughness increases as confining pressure increases (Table 12.6).

## 12.4 Thermal Properties of Rock

Rock engineering applications can involve rock mass response for different temperature ranges. Geothermal energy extraction often operates in a reservoir with temperature >150 °C. For underground disposal of high-level nuclear waste and spent fuel, although usually just below 100 °C, the rock temperature in the repository can rise to 400 °C. LNG underground storage in rock caverns normally operate in temperature ranges below −160 °C inside the cavern and −30 °C in the surrounding rock. Also, the mechanical properties of rocks are temperature dependent. This is illustrated by the results of a series of laboratory tests conducted on granites for LNG storage in rock in the Republic of Korea (Fig. 12.6).

The thermal parameters used in FRACOD are presented in Table 12.7.

Change in temperature has varying effects on rock's thermal properties. When temperature increases, thermal conductivity of rock decreases, whereas specific heat increases. Density remains practically constant within the temperature range zero to 100 °C. Therefore, thermal diffusivity shows stronger temperature dependence than conductivity with increasing temperature.

Kukkonen et al. (2011) have measured the temperature dependence of thermal properties for different gneisses from the final repository for spent nuclear fuel at Olkiluoto, Finland. The data and estimated correction for different temperature intervals are presented in Table 12.8. At present FRACOD can consider the temperature dependence of the rock strength. For the other thermal parameters, users are recommended to perform a sensitivity analysis of the influence of temperature dependence on the thermal properties.

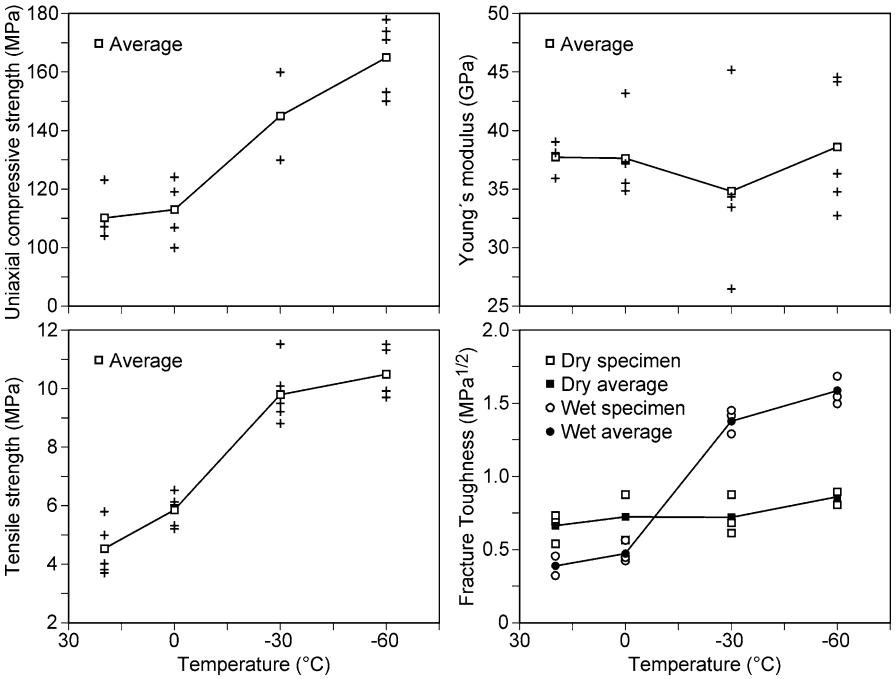


**Fig. 12.6** Temperature dependence of rock mechanical properties illustrated for granites from a pilot underground LNG storage site in Korea (After Kim 2008)

**Table 12.7** Thermal parameters and units used in FRACOD

| Property | Parameter | Unit | ISRM suggested method | Data references |
|---|---|---|---|---|
| Thermal mechanical parameters | Thermal expansion | $10^{-6}$/K | In preparation | Clark (1966) |
| | Thermal conductivity | W/mK | | Angenheister (1982) |
| | Density | kg/m$^3$ | | Kukkonen et al. (2011) |
| | Spec. heat capacity | J/kgK | | |
| | Initial rock temperature | K | | |
| | Rock material number | No. | | |
| | Diffusivity | $10^{-6}$ m$^2$/s | | |

**Table 12.8** Average thermal properties of Olkiluoto gneiss for elevated temperatures. Density values are average values of different gneisses (After Kukkonen et al. 2011)

| Parameter | Unit | Mean value at 25 °C | Correction 25–60 °C % | Value at 60 °C | Correction 25–100 °C % | Value at 100 °C |
|---|---|---|---|---|---|---|
| Conductivity | W/mK | 2.91 | −3.1 | 2.82 | −6.4 | 2.72 |
| Spec. heat capacity | J/kgK | 712 | 7.3 | 764 | 15.8 | 824 |
| Diffusivity | $10^{-6}$ m$^2$/s | 1.47 | −8.5 | 1.34 | −18.1 | 1.20 |
| Density | kg/m$^3$ | 2,743 | 0 | 2,743 | 0 | 2,743 |
| Thermal expansion | $10^{-6}$/K | | 10.6 | | | |

## References

Ahrens TJ (ed) (1995) Rock physics and phase relations: a handbook of physical constants. American Geophysical Union, Washington, DC

Angenheister G (1982) Physical properties of rocks. Landholt-Börnstein numerical data and functional relationships in science and technology, vol 1. Springer, Berlin

Backers T, Stephansson O (2012) ISRM suggested method for determination of Mode II fracture toughness. Rock Mech Rock Eng 45:1011–1022

Backers T, Stephansson O, Rybacki E (2002) Rock fracture toughness testing in mode II- punch-through shear test. Int J Rock Mech Min Sci 39(6):755–769

Clark SP (1966) Handbook of physical constants – Revised edition, vol 97, The Geological Society of America, Memoir. The Geological Society of America, New York

Hudson JA (ed) (1993) Comprehensive rock engineering. Pergamon Press, Oxford

Hudson JA, Harrison JP (2000) Engineering rock mechanics. An introduction to the principles. Elsevier Science Ltd, Oxford

Jaeger JC, Cook NGW, Zimmerman RW (2007) Fundamentals of rock mechanics, 4th edn. Blackwell Publishing, Malden

Kim H-M (2008) Summary of previous laboratory test results of KIGAM. Technical report, Korea Institute of Geoscience & Mineral Resources

Kukkonen I, Kivekäs L, Vuoriainen S, Kääriä M (2011) Thermal properties of rocks in Olkiluoto: results of laboratory measurements 1994–2010. Posiva Oy working report 2011–2017, p 98

Nara Y, Morimoto K, Hiroyoshi N, Yoneda T, Kaneko K, Benson PM (2012) Influence of relative humidity on fracture toughness of rock: implications for subcritical crack growth. Int J Solids Struct 49:2471–2481

Ulusay R, Hudson JA (2007) The complete ISRM Suggested Methods for rock characterization, testing and monitoring: 1974–2006. ISRM Turkish National Group, Ankara

# Chapter 13
# FRACOD Verification Tests

**Abstract** This chapter describe several verification tests using FRACOD to model some simple problems from single fracture propagation to coupled fracturing process. The tests cases are designed to demonstrate the functionality of FRACOD, and they include:

1. Propagation of a single fracture under pure tension;
2. Propagation of a single fracture under pure shear;
3. Multiple region model of a shaft with concrete lining;
4. Subcritical crack growth – Creep – model of a single tensile fracture;
5. Gravitational problems involving a tunnel in shallow ground;
6. Thermo-mechanical coupling – a single heat source in rock mass;
7. Dynamic fluid flow in a single fracture;
8. Hydraulic fracturing in rock mass with pre-existing fractures.

Eight verification test cases are listed in this chapter.

## 13.1 Tensile Fracture Propagation

A 2 m fracture in an infinite rock mass is under uniaxial tensile stress of 50 MPa in the direction perpendicular to the fracture plane. The elastic properties of the rock mass are:

$$E = 40\ GPa$$

$$\nu = 0.25.$$

B. Shen et al., *Modelling Rock Fracturing Processes: A Fracture Mechanics Approach Using FRACOD*, DOI 10.1007/978-94-007-6904-5_13,

The strain energy release rate in Mode I for this problem is calculated by using FRACOD with 30 elements along the fracture.

$$(G_I)_{FRACOD} = 190 \times 10^3 J/m^2$$

The theoretical solution of this problem gives the stress intensity factor ($K_I$) as

$$K_I = \sigma \sqrt{\pi a} = 50 \times \sqrt{3.1416 \times 1} = 88.6\, MPa \sqrt{m}$$

where $a$ = half length of the fracture.

The theoretical strain energy release rate is then calculated as:

$$(G_I)_{theory} = \frac{1 - v^2}{E} (K_I)^2 = \frac{1 - 0.25^2}{40 \times 10^9} \times (88.6 \times 10^6)^2 = 184 \times 10^3\ J/m^2$$

The difference between the numerical result and the theoretical result is approximately 3 %.

In this example, the critical strain energy release rates of fracture propagation are:

$$G_{IC} = 50\ J/m^2$$

$$G_{IIC} = 1000\ J/m^2.$$

As the fracture propagation is pure Mode I along the fracture's original plane, only the critical strain energy release rate in Mode I *($G_{IC}$)* is useful. The F-value obtained from FRACOD is:

$$F(0) = \frac{G_I(0)}{G_{IC}} + \frac{G_{II}(0)}{G_{IIC}} = \frac{190 \times 10^3}{50} + \frac{0}{1000} = 3800$$

The F-value is far greater than the critical value 1.0. Hence fracture propagation is detected (Fig. 13.1).

## 13.2 Shear Fracture Propagation

A 2 m fracture in an infinite rock mass is under pure shear stress of 50 MPa. Elastic properties of the rock mass are the same as in the example in Sect. 13.1.

According to Rao (1999), a fracture in pure shear may propagate in Mode I or Mode II depending on the ratio of the fracture toughness of Mode I and Mode II ($K_{IC}/K_{IIC}$). A Mode II fracture propagation may occur only when $K_{IC}/K_{IIC} > 1.15$. FRACOD is used in this example to compare with the theoretical results.

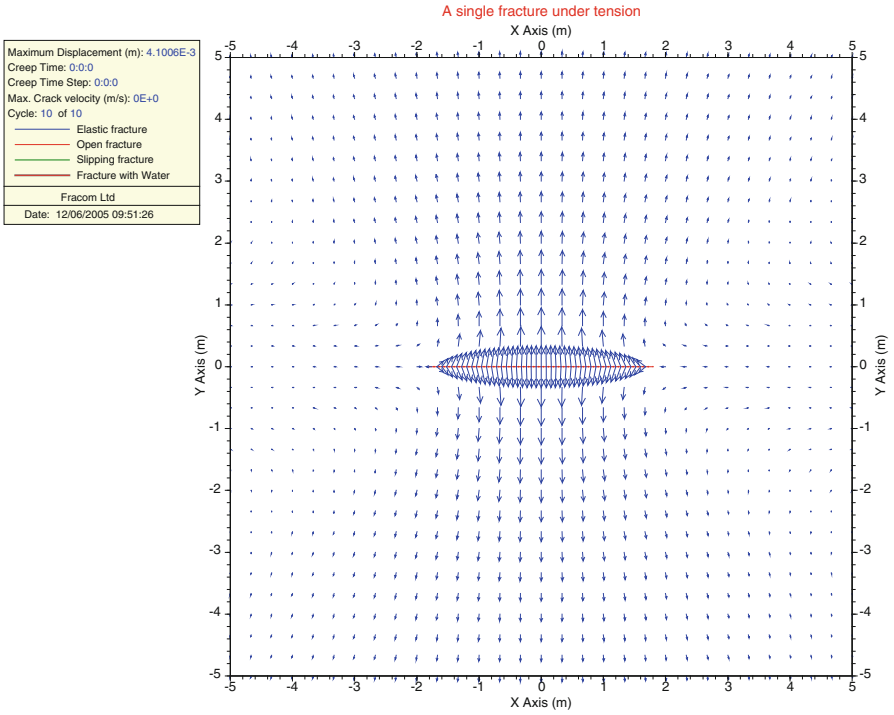


**Fig. 13.1** Modelled fracture propagation under pure tension

A total of 30 elements are used to represent the fracture. The critical Mode II strain energy release rate ($G_{IIC}$) is taken as 1,000 J/m$^2$. The critical Mode I strain energy release rate ($G_{IC}$) is varied to obtain the critical ratio ($G_{IC}/G_{IIC}$) at which the fracture propagation starts to change mode. It was found that when $G_{IC} < 1{,}279$ J/m$^2$, fracture propagates in pure Mode I in the direction of about 70° from the original fracture plane (Fig. 13.2a). When $G_{IC} > 1{,}471$ J/m$^2$ the fracture propagates in pure Mode II (Fig. 13.2b). When $1{,}279$ J/m$^2 < G_{IC} < 1{,}471$ J/m$^2$ the fracture propagates initially in Mode II then in Mode I.

If we take the average of 1,375 J/m$^2$ as the estimated critical value, and use the relation between the critical stress energy release rate and the fracture toughness:

$$\left(\frac{K_{IC}}{K_{II_C}}\right)_{numerical} = \sqrt{\frac{G_{IC}}{G_{IIC}}} = \sqrt{\frac{1375}{1000}} = 1.17$$

The critical toughness ratio for Mode II fracture propagation obtained numerically using FRACOD is 1.17 and in good agreement with the analytical solution of 1.15 reported by Rao (1999).

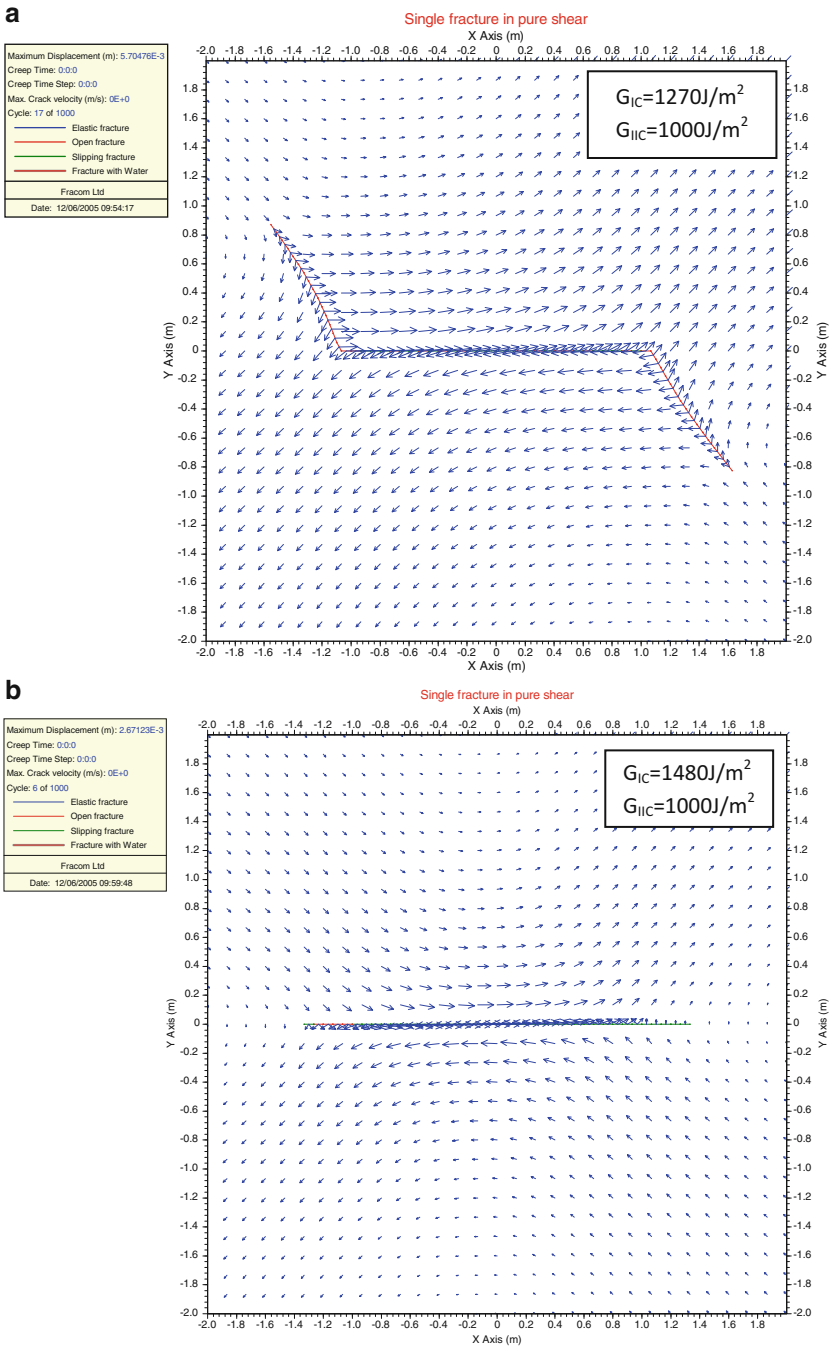


**Fig. 13.2** Fracture propagation in Mode I (*top*) and Mode II (*bottom*) depending on the ratio of $G_{IIC}/G_{IC}$

## 13.3 Multiple Region Model

A simple case of a boundary value problem in an inhomogeneous elastic body is shown in Fig. 13.3. The region of interest consists of an annulus $a \leq r \leq b$ with elastic constants $E_1$ and $\nu_1$ inside a circular hole of radius $r = b$ in a large plate with elastic constants $E_2$ and $\nu_2$. The inside wall of the annulus is subjected to a normal stress $\sigma_{rr} = -p$, and the plate is unstressed at infinity.

The solution to this problem, satisfying continuity of radial stress and displacement at the interface $r = b$, can be constructed from standard formulae for thick-walled cylinders. The radial and tangential stresses are:

$$\sigma_{rr} = \frac{1}{1-(a/b)^2}\left[\left(p(a/b)^2 - p'\right) + (p-p')(a/r)^2\right] \qquad a \leq r \leq b$$

$$\sigma_{\theta\theta} = \frac{1}{1-(a/b)^2}\left[\left(p(a/b)^2 - p'\right) + (p-p')(a/r)^2\right] \qquad a \leq r \leq b$$

$$\sigma_{rr} = -p'(b/r)^2 \qquad r \geq b$$

$$\sigma_{\theta\theta} = -p'(b/r)^2 \qquad r \geq b$$

where:

$$p' = \frac{p(a/b)^2}{1 + \frac{1}{2}\left(\frac{E_1}{E_2} + \frac{1+\nu_2}{1+\nu_1^2} - \frac{1}{1-\nu_1}\right)(1-(a/b)^2)}$$

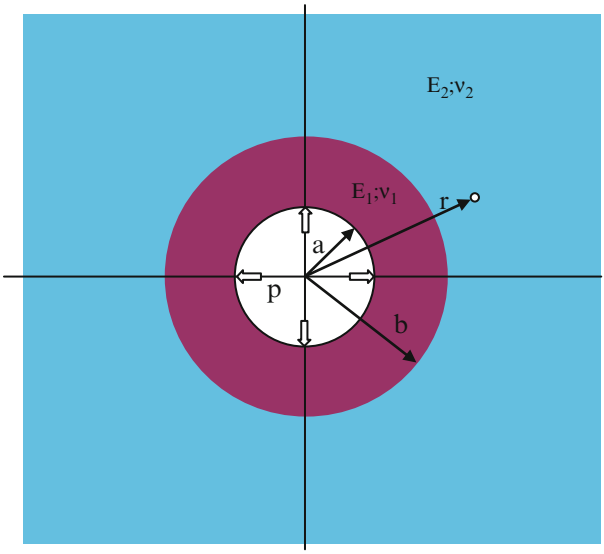


**Fig. 13.3** Annulus inside a circular hole in a plate

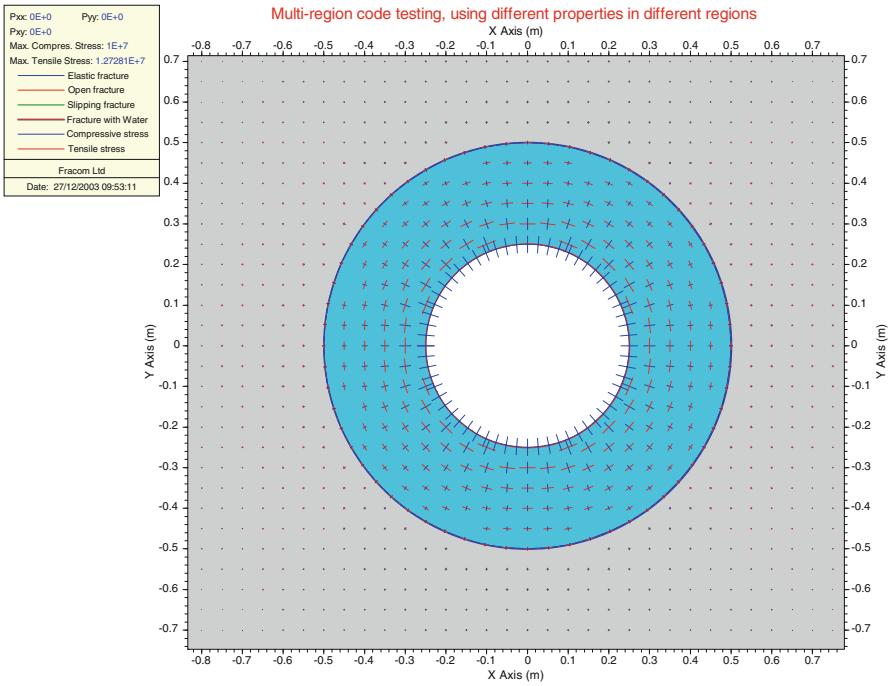


**Fig. 13.4** Modelled stress distribution for the multiple region problem

FRACOD is applied to this problem to compare with analytical results. In this example, the following parameters are used:

$a = 0.5$ m
$b = 1.0$ m
$\nu_1 = \nu_1 = 0.2$
$E_1 = 50$ GPa; $E_2 = 25$ GPa
$p = 10$ MPa

A total of 60 elements are used for the internal circular boundary and 60 elements for each side of the interface. The modelled stress distribution using FRACOD is shown in Fig. 13.4. A comparison of the modelled radial and tangential stresses with the analytical results is shown in Fig. 13.5. Good agreement is obtained, suggesting that FRACOD can accurately simulate a multi-region problem.

## 13.4 Subcritical Crack Growth: Creep

A simple problem as shown in Fig. 13.6 is used to validate the subcritical fracture growth function in FRACOD. Here only Mode I subcritical crack growth is involved.

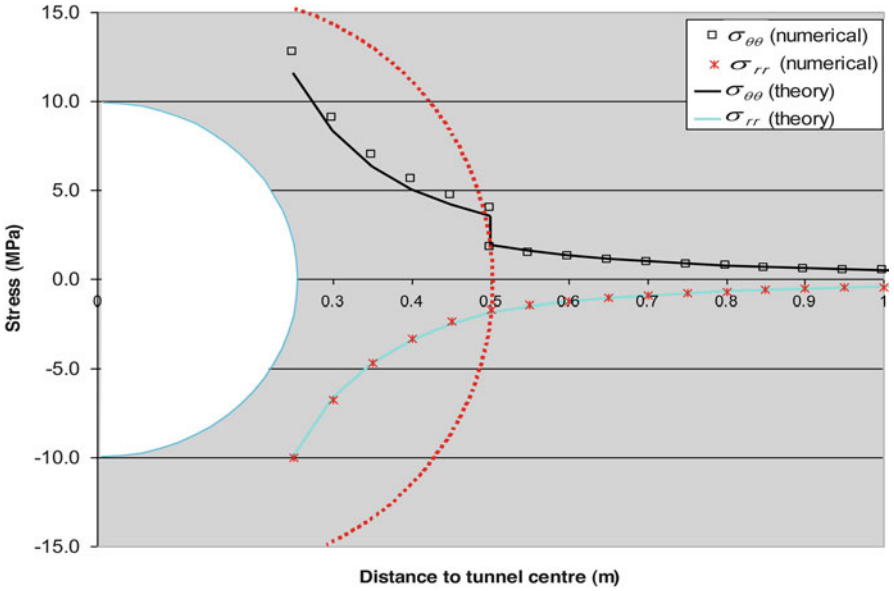


**Fig. 13.5** Comparison between the FRACOD results and analytical results for the multiple region problem

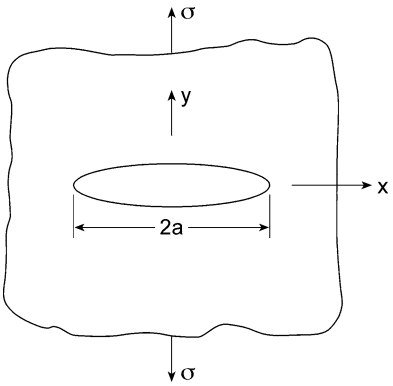


**Fig. 13.6** A single fracture model to test the subcritical crack growth function in FRACOD

The following input properties for FRACOD modeling are assumed in this model:

Far field stresses: $\sigma_x = 0$; $\sigma_y = 10$ MPa,
Initial crack length: $2a = 0.01$ m,
Fracture toughness: $K_{IC} = 3.80$ MPa m$^{1/2}$,
Subcritical crack growth parameters: $(V_{max})_I = 500$ m/s; $n_1 = 30$.

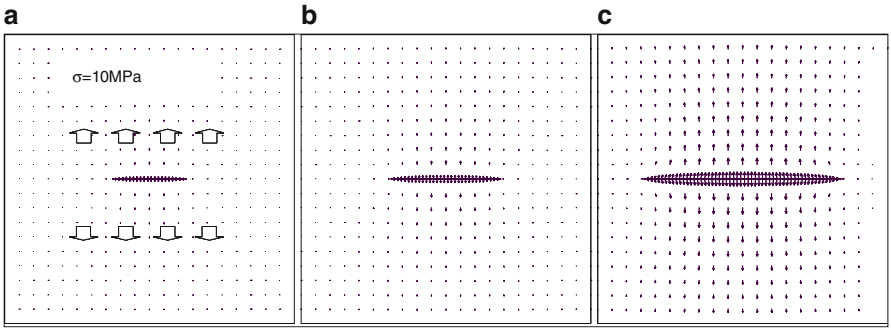


**Fig. 13.7** Subcritical crack growth in tension. (**a**) Initial stage (t = 0) with a pre-existing crack length of 0.010 m. (**b**) After 6.0 years the crack extended by 2 mm. (**c**) After 6.4 years the crack reached the state of unstable fracture propagation when the crack grows rapidly

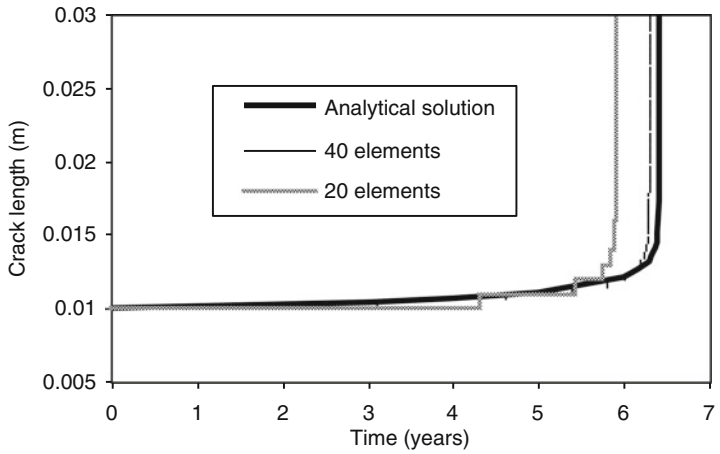


**Fig. 13.8** Theoretical and modelled time versus crack length

An analytical solution exists for this simple problem. At time $t$, the crack half-length can be expressed as (Rasilainen 2006):

$$a = \left\{ {a_0}^{-n/2+1} + (-n/2+1)\left( A \times \left( \frac{\sigma_y \sqrt{\pi}}{K_k} \right)^n \times t \right) \right\}^{\frac{1}{-n/2+1}} \tag{13.1}$$

where $n$ is equivalent to $n_1$ and $A$ is the same as $(V_{max})_1$.

In the beginning, the crack will grow very slowly. After 6 years the crack has extended by only 2 mm. The crack velocity then increases rapidly and after about 6.4 years the stress intensity factor has reached the critical state of unstable facture propagation ($K_I/K_{IC} \geq 1.0$).

FRACOD is used to model the problem. The numerical results are shown in Fig. 13.7. Figure 13.8 shows the modelled crack length at different times compared with the analytical results.

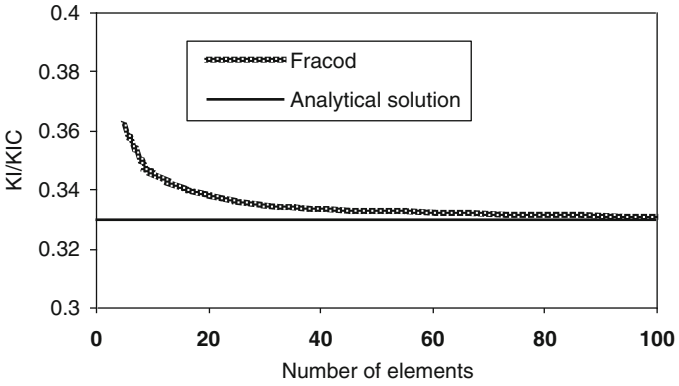


**Fig. 13.9** Number of elements defining the pre-existing fracture at the start of simulation (t = 0) versus $K_I/K_{IC}$

The accuracy of calculated time-to-failure (TTF) (i.e. the time until unstable fracture propagation) has been evaluated. A minor numerical error in the calculated initial stress intensity can lead to a major shift of failure time. Figure 13.9 shows the sensitivity of element number on stress intensity. Applied time steps also affect TTF prediction in the calculation.

## 13.5 Gravity Problems

A circular tunnel with diameter of 2 m is at a depth of 100 m. The key input parameters used are:

Rock density = 2,500 kg/m$^3$
Stress ratio $\sigma_x/\sigma_y = 0.33$

This problem was modelled using the gravity function with "restrained" elements at the tunnel boundary, as discussed in Chap. 7. The predicted displacement distribution is shown in Fig. 13.10.

Because the tunnel is relatively deep, we can also obtain the analytical solution of this problem if we assume the tunnel is under constant far-field stress at this depth ($\sigma_x = 0.83$ MPa; $\sigma_y = 2.5$ MPa), see Brady and Brown (1985, pp. 162–163).

The numerical and analytical results are compared along two monitoring lines shown in Fig. 13.10. The comparison results are shown in Fig. 13.11. Numerical results are nearly identical to analytical results for most stress and displacement components along the two lines. The maximum numerical error is less than 7.8 %.

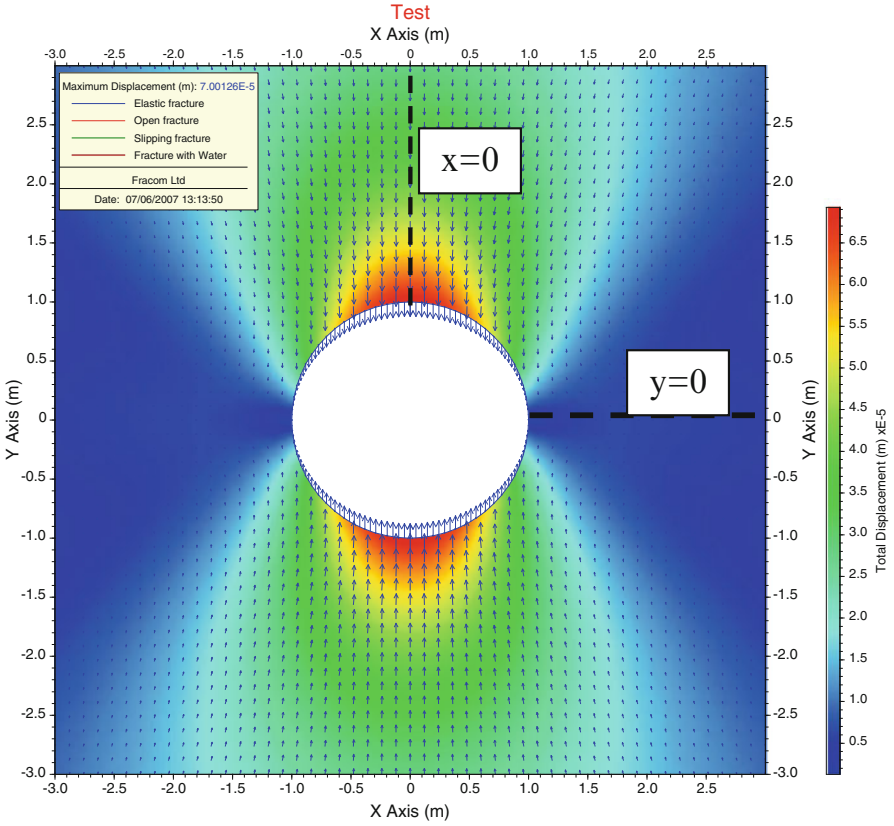


**Fig. 13.10** Predicted displacement field by FRACOD around a circular tunnel from gravity loading

This example demonstrates that the gravity function in FRACOD using the "restrained" elements is effective and accurate enough for engineering problems.

## 13.6 Thermo-Mechanical Coupling

A point heat source with constant heat strength is located in a 2D infinite elastic medium with constant thermal properties. The point source in 2D is equivalent to a line source in 3D. The solution to this problem has already been given in Eqs. (9.8, 9.9, 9.10, 9.11, 9.12 and 9.13) in the Cartesian coordinate system. In a polar system, the solution for the transient values of temperature, radial and tangential stress and radial displacement is provided below:

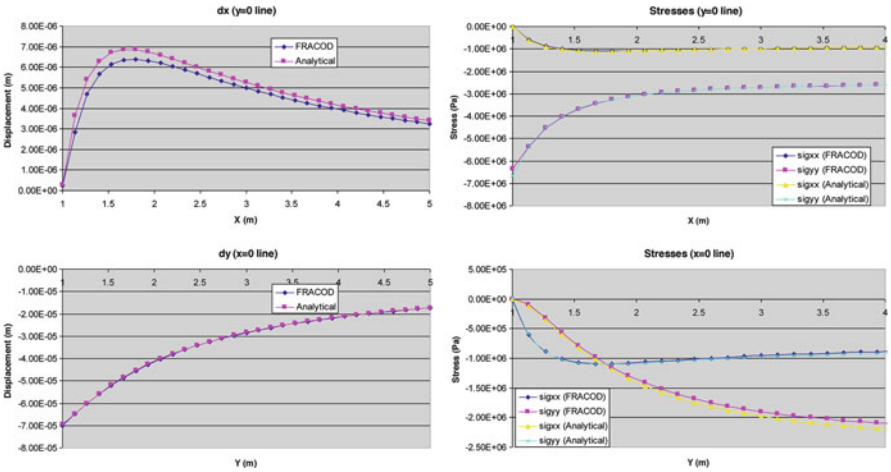


**Fig. 13.11** Comparison between FRACOD results and analytical results for the circular tunnel

$$\frac{T}{a} = \frac{1}{4\pi} E_1(\xi^2)$$

$$\frac{\sigma_r}{bG} = \frac{1}{4\pi} \left[ E_1(\xi^2) + \frac{1 - e^{-\xi^2}}{\xi} \right]$$

$$\frac{\sigma_t}{bG} = \frac{1}{4\pi} \left[ E_1(\xi^2) + \frac{1 - e^{-\xi^2}}{\xi} \right]$$

$$\frac{u_r}{b} = \frac{1}{8\pi} r \left[ E_1(\xi^2) + \frac{1 - e^{-\xi^2}}{\xi} \right]$$

where:

$$\xi^2 = \frac{r^2}{4ct}$$

$$c = \frac{k}{\rho c_p}$$

$$a = \frac{H}{k}$$

$$b = \alpha a \frac{9K}{3K + 4G}$$

$H =$ Heat source strength.

The material properties and initial and boundary conditions for this example are defined as follows:

| | |
|---|---|
| Density ($\rho$) | 2,000 kg/m$^3$ |
| Shear modulus ($G$) | 30 GPa |
| Bulk modulus ($K$) | 50 GPa |
| Specific heat ($Cp$) | 1,000 J/kg °C |
| Thermal conductivity ($k$) | 4 W/m°C |
| Linear thermal expansion coefficient ($\alpha$) | $5 \times 10^{-6}$/°C |
| Initial condition and boundary conditions: | |
| Initial uniform temperature ($t_0$) | 0°C |
| Initial stress state ($\sigma_{ij}$) | 0 (no stresses) |
| Heat source strength ($H$) | 1.0 W |

It is assumed that the material properties are temperature-independent and the thermal output of the source is constant (i.e. no decay).

Two FRACOD models are used to simulate this problem. The first considers the point heat source as acting along a small hole, and a constant heat flux is applied at the inner hole boundary. The hole radius is assumed to be R = 0.1 m, so that the applied flux will be:

$$\text{Flux} = \text{q} = \frac{1.0}{2\pi R} = 1.59 \text{ W/m}^2$$

A symmetry condition is used so that only a quarter section of the model is actually modelled although the results are shown for the whole model. Fifteen boundary elements are used.

The thermally induced temperature, stresses and displacements after 1 year are plotted in Figs. 13.12, 13.13, and 13.14. Comparing the figures with the analytical solutions along a radial line from the model centre, see Fig. 13.15, good agreement is achieved.

Another FRACOD model used to simulate this problem utilises the point source function. The FRACOD model is assumed to be a disc with a radius of 50 m. A point heat source is located at the centre of the model. The outer boundary of the model is assumed to have zero temperature and zero stresses and the material properties are the same as the previous example.

Results using this model are shown in Figs. 13.16, 13.17, 13.18, and 13.19. Again, good agreement is obtained between the modelling results and the analytical results given by Nowacki (1962).

## 13.7 Fluid Flow in Fractures

A simple problem of two boreholes in a rock mass linked by a single fracture is considered. The boreholes have a diameter of 1 m, and the boreholes are 20 m apart. One hole is the injection hole and has a constant fluid pressure of 5 MPa. The other

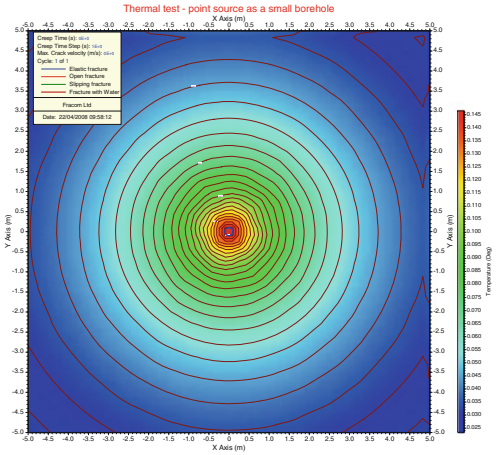


**Fig. 13.12** Thermo-mechanical coupling test case. Temperature distribution after 1 year due to a point heat source simulated as a hole

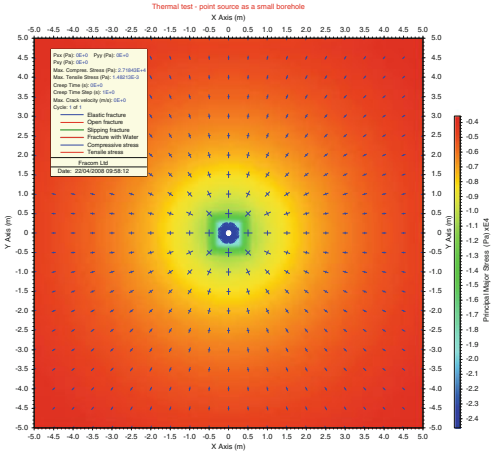


**Fig. 13.13** Principal stress distribution around a hole-like heat source after 1 year

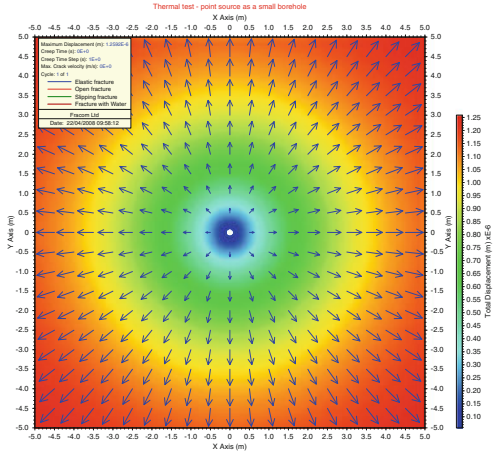


**Fig. 13.14** Displacement distribution around a hole-like heat source after 1 year

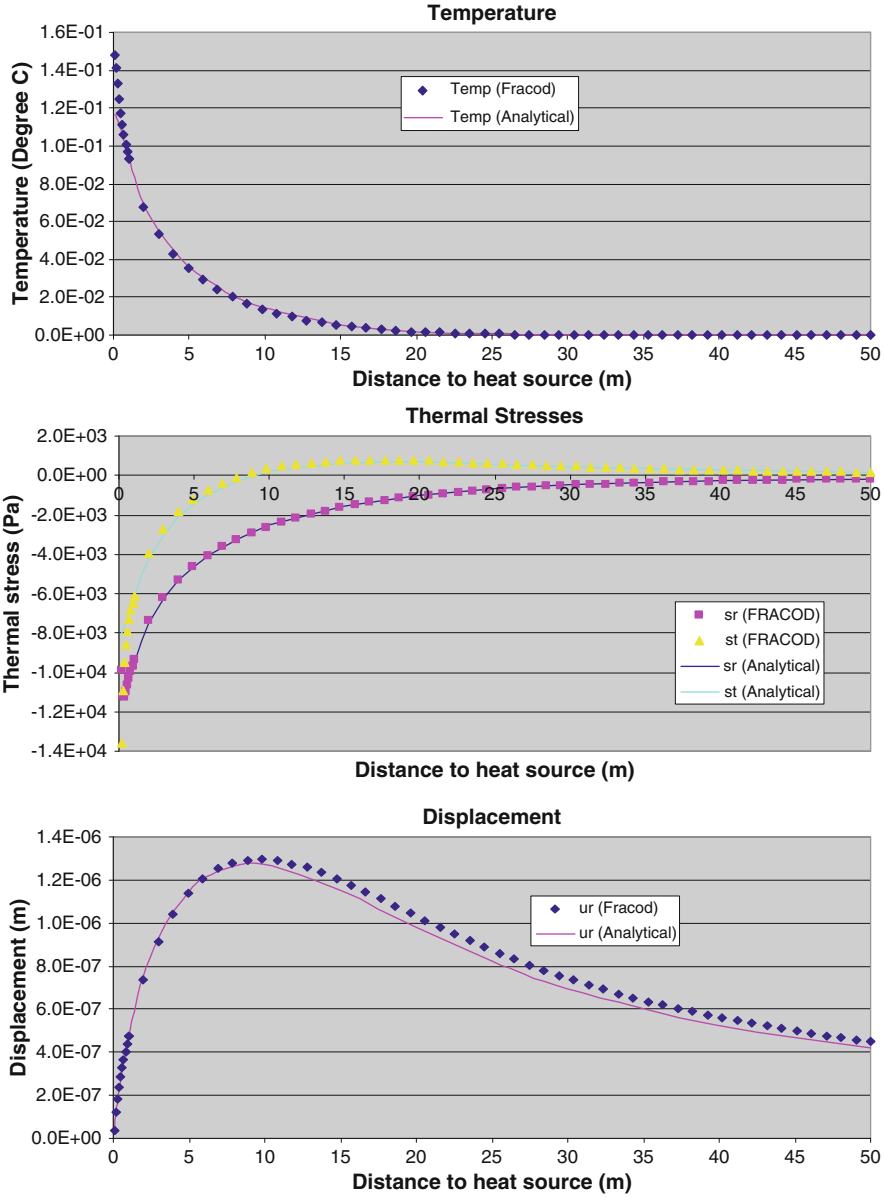


**Fig. 13.15** Comparison between FRACOD and analytical results. Temperature, stresses and displacement along a radial line in a FRACOD model with a hole-like heat source

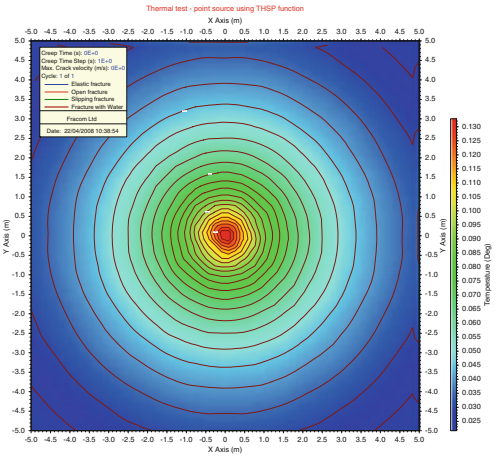


**Fig. 13.16** Temperature distribution around an actual point heat source in a FRACOD model after 1 year of heating

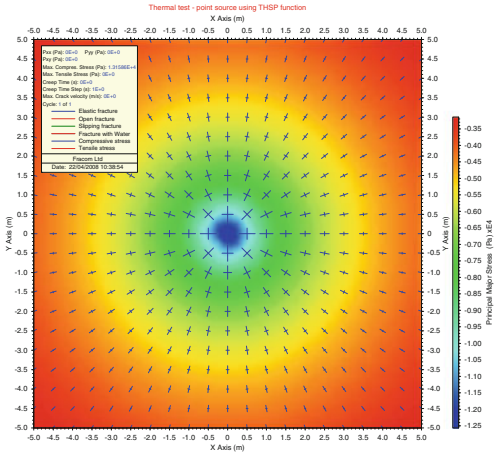


**Fig. 13.17** Stress distribution around an actual point heat source after 1 year of heating

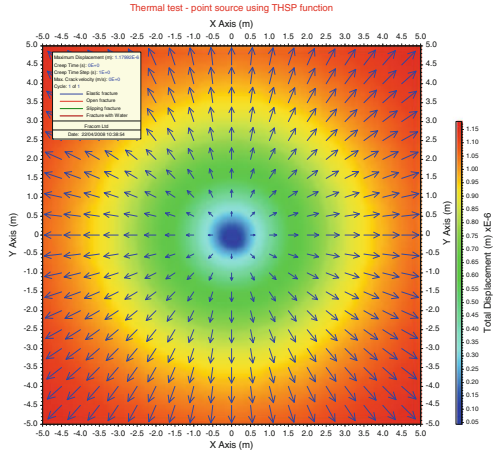


**Fig. 13.18** Displacement distribution around an actual point heat source after 1 year of heating

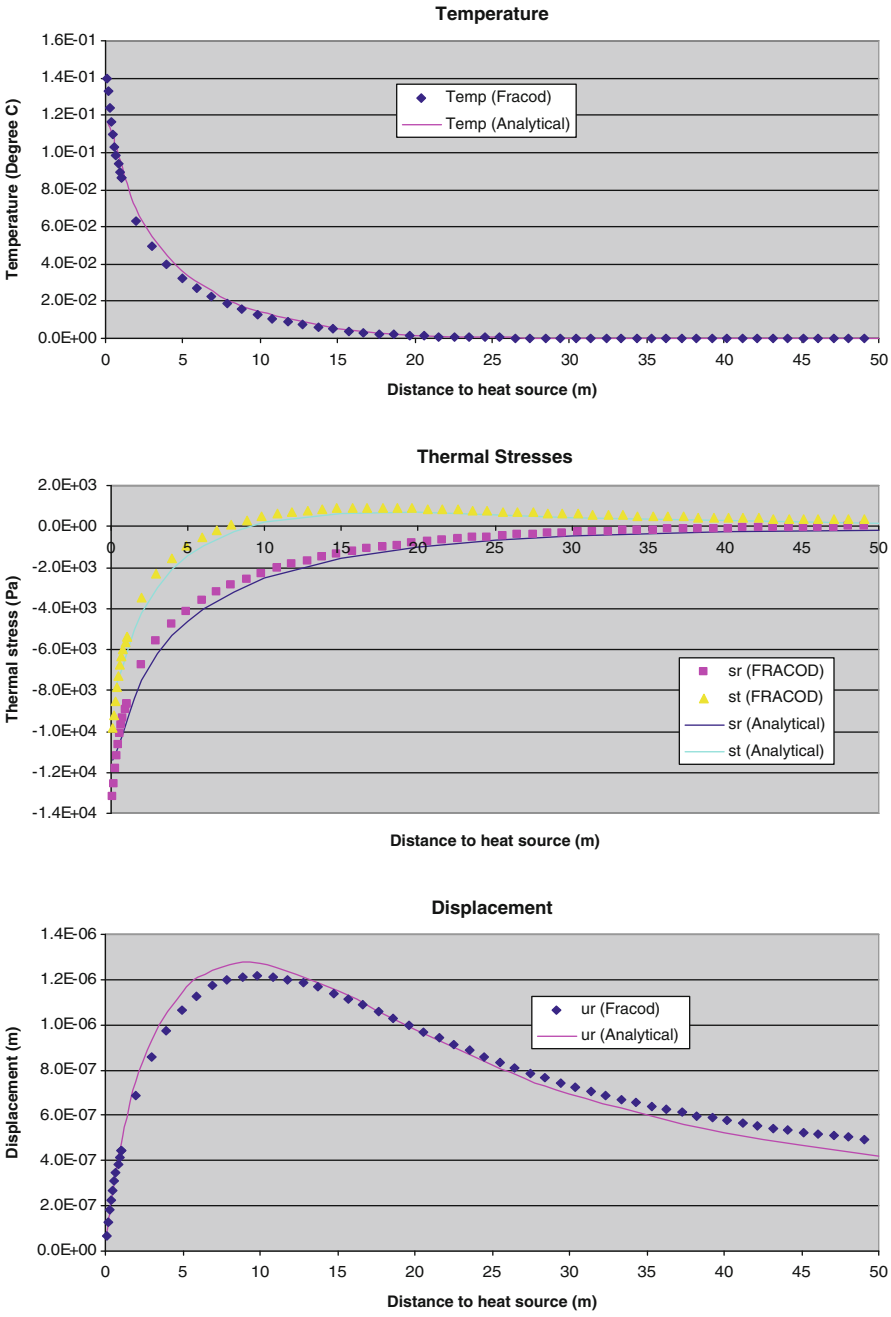


**Fig. 13.19** Comparison between FRACOD and analytical results. Temperature, stresses and displacement along a radial line in a FRACOD model with a point heat source

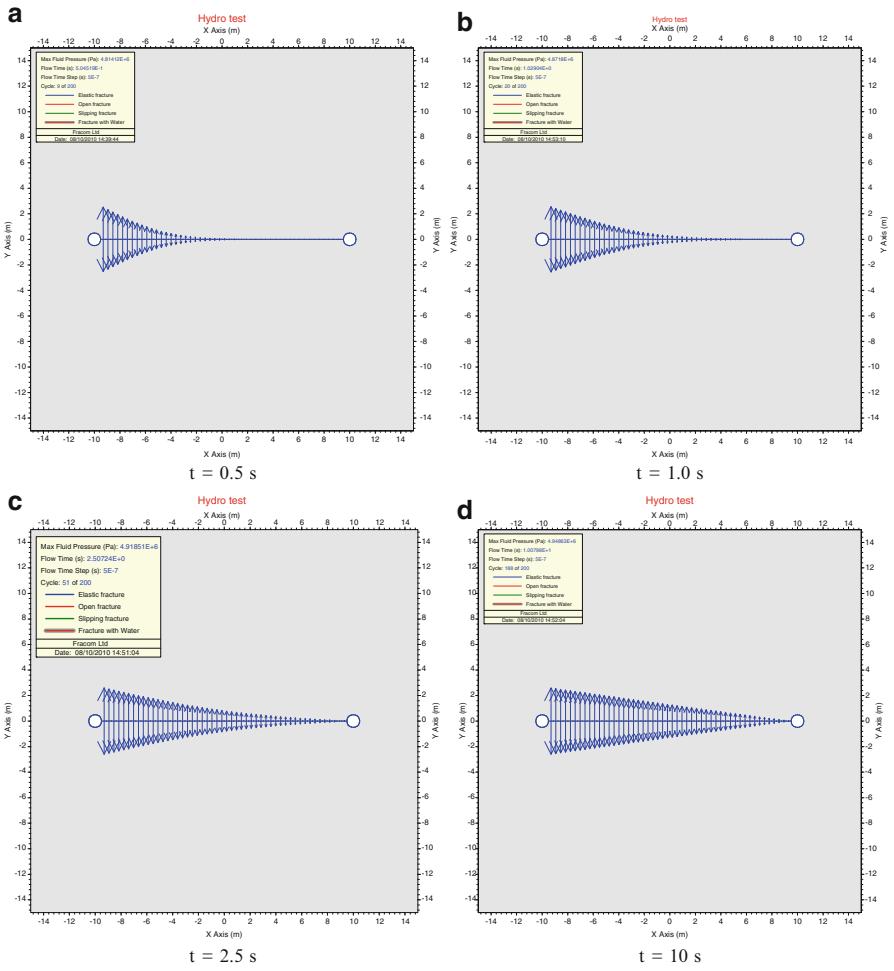


**Fig. 13.20** Fluid pressure distribution as a function of time in a 20 m long fracture between two boreholes

hole is the extraction hole and the fluid pressure remains zero. The fracture linking the two holes has an initial aperture $e_0 = 10$ μm.

In this example, we will only test the fluid flow function without mechanical coupling, i.e. we will assume that the fracture aperture is constant.

Other fluid parameters are listed below:

Fluid bulk modulus $K_w = 2$ GPa;
Fluid viscosity $\mu = 1 \times 10^{-3}$ Pa s
Hydraulic conductivity of intact rock $k = 1 \times 10^{-19}$ m/s.

The modelled fluid pressure distribution with time in the fracture is shown in Figs. 13.20 and 13.21.

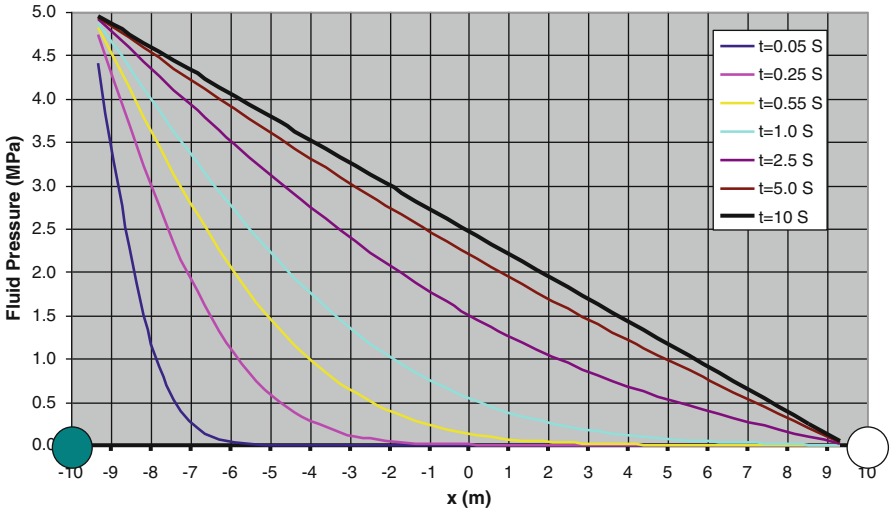


**Fig. 13.21** Fluid pressure variation with time in a single fracture between two boreholes

The results demonstrate a dynamic process of fluid flow from the injection hole to the extraction hole. After a flow time of 0.5 s, the fluid pressure front travelled about 8 m in the fracture and the pressure distribution is nonlinear. The pressure front reached the extraction hole after 2.5 s, with the pressure distribution still being nonlinear. After about 10 s, the pressure in the fracture is linearly distributed, and it has reached a steady state solution.

## 13.8 Hydraulic Fracturing

Hydraulic fracturing is a technique to stimulate production in geological reservoirs. The reservoirs can be used for extraction of oil, gas, water, steam, or for storage of fluid waste like drilling mud and slurries and gas or supercritical gas like $CO_2$. The gas or fluid is injected into the sealed-off section of a well under high pressure until fracture develops in the wall of the well. By maintaining or increasing the pressure, the fracture will continue to propagate in the direction perpendicular to the least principal stress until it stops and stabilises. The generated fracture will enhance gas and fluid flow and thereby increase production in the reservoir. During and sometimes after pressurization, the propagating fracture can generate a tremor or an earthquake.

Hydraulic fracturing is also one of the most common methods to determine the rock stress in geological formations from surface exploration boreholes (Zang and Stephansson 2010). A sealed-off section of about one meter length in the borehole is pressurized until fracture develops and propagates into the formation. The minimum

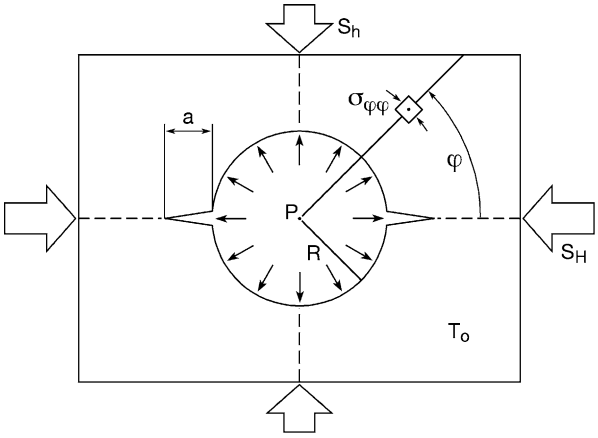


**Fig. 13.22** Hydraulic fracture generated from excess pressure in a borehole subjected to principal stresses (After Zang and Stephansson (2010))

horizontal stress, $S_h$ is inferred from the pressure at which the hydraulic fracture closes in the pressure–time record of the test, Fig. 13.22. For brief estimation of the maximum horizontal stress, the peak fluid pressure $S_H$ and the rock tensile strength $T_o$ are needed.

For an elastic and impermeable rock, we can formulate the Hubbert-Willis elastic hydrofracture criterion as:

$$p_{crit}^{HWS} = 3S_h - S_H + T_0 \tag{13.2}$$

where $p_{crit}{}^{HWS}$ is the critical fluid pressure for fracture initiation at the borehole wall.

A typical case of hydraulic fracturing is simulated to demonstrate the effectiveness of the coupled F-H function in FRACOD. A borehole is drilled in a rock mass with several isolated pre-existing fractures (Fig. 13.23a). A high fluid pressure is then applied in the borehole to propagate the existing fractures.

Key mechanical and fluid properties used in this model are listed:

Fracture Mode I toughness: $K_{IC} = 1.5$ MPa m$^{1/2}$
Young's modulus: $E = 37.5$ GPa
Poisson's ratio: $\nu = 0.25$
Fracture residual aperture: $e_r = 10$ μm
Fracture initial aperture: $e_0 = 10$ μm
Bulk modulus of fluid: $K_w = 2$ GPa
Intact rock hydraulic conductivity $k = 1.0 \times 10^{-19}$ m/s
Borehole fluid pressure: $P = 5$ MPa
Initial pore pressure: $P_0 = 0$ MPa
In situ stresses: $\sigma_{xx} = \sigma_{yy} = 1.0$ MPa.

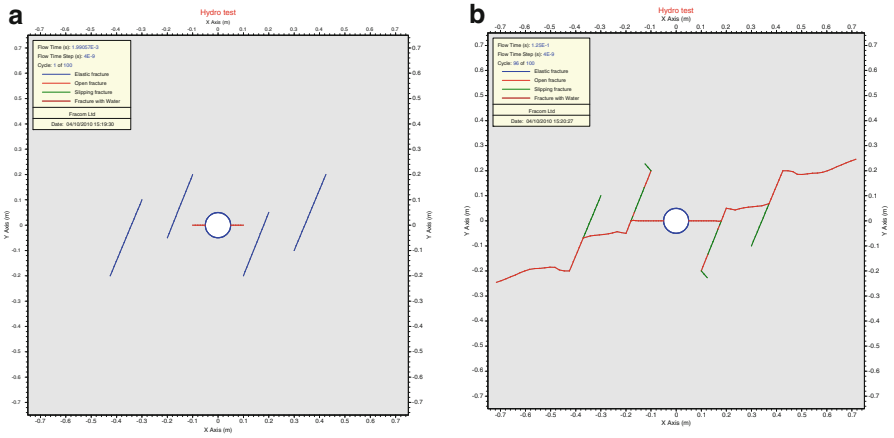


**Fig. 13.23** Simulated rock fracturing process due to high pressure fluid injection in a borehole. (**a**) initial geometry and (**b**) after hydraulic fracturing

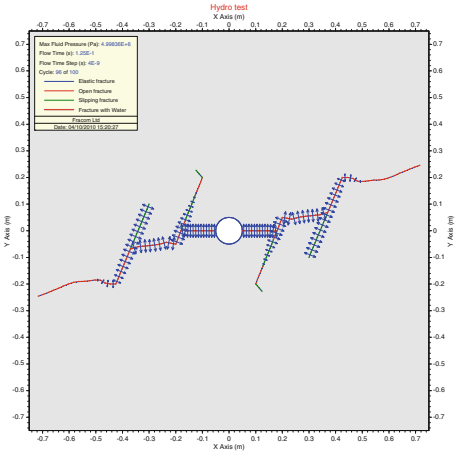


**Fig. 13.24** Fluid pressure distribution in generated fractures after fracture propagation

The simulated fracture propagation pattern after 0.15 s is shown in Fig. 13.23. Fluid pressure distribution in the fractures is shown in Fig. 13.24.

In this model, the fluid pressure drives the initial short tensile fracture at the borehole wall to propagate toward the pre-existing fractures and eventually coalesce with these fractures. The pre-existing fractures then propagate under the high fluid pressure. Note that the tips of the propagating fractures appear to be well ahead of flow fronts in the fracture because the stress wave propagates much faster than the fluid flow.

## References

Brady B, Brown T (1985) Rock mechanics for underground mining. George Allen & Unwin, London

Nowacki W (1962) Thermoelasticity. Addison-Wesley, Reading

Rao Q (1999) Pure shear fracture of brittle rock: a theoretical and laboratory study. Ph.D. thesis 1999:08, Lulea University of Technology

Rasilainen K (2006) The Finnish research programme on nuclear waste management (KYT) 2002–2005. Final report. VTT research notes 2337. Technical Research Centre of Finland, Espoo. ISBN 951-38-6786-2

Zang A, Stephansson O (2010) Stress field of the Earth's crust. Springer Science + Business Media, Dordrecht/Heidelberg/London/New York

# Chapter 14
# Application Case Studies

**Abstract** This chapter provides five representative case studies employing FRACOD, including 1) Borehole Breakout; 2) Tunnel EDZ; 3) LNG Underground Cavern; 4) Pillar Spalling; and 4) UCS and Brazilian Test. These cases cover various aspects of modern rock mechanics and aim to demonstrate the effectiveness of the fracture mechanics approach.

Over the last 20 years, the fracture mechanics approach employing FRACOD has been used by research teams in Sweden, Finland, Australia, Japan, Germany and South Korea to solve various geo-mechanical issues related to nuclear waste disposal, geothermal energy, liquefied natural gas (LNG) underground storage, tunnel stability, rock cutting and indentation, rock sample tests etc. Rinne (2008) used FRACOD to investigate fundamental creep behaviour of rock samples. Shen et al. (2002), Shen (2008), Klee et al. (2011) and Barton (2007) reported several studies using FRACOD to investigate borehole breakouts and tunnel stability. Stephansson et al. (2003) applied the code to stability assessments of large shafts and galleries related to nuclear waste disposal in Japan. Rinne et al. (2003b) completed a detailed study using FRACOD on the Pillar Spalling Experiments conducted at Äspö Hard Rock Laboratory. Tan et al. (1998) applied this fracture mechanics approach to rock breakage during rock indentation tests.

This chapter provides five representative case studies employing FRACOD. These cases cover various aspects of modern rock mechanics and aim to demonstrate the effectiveness of the fracture mechanics approach. The following cases are discussed in detail:

- Borehole Breakout
- EDZ
- LNG Underground Cavern
- Pillar Spalling
- UCS and Brazilian Test

B. Shen et al., *Modelling Rock Fracturing Processes: A Fracture Mechanics Approach Using FRACOD*, DOI 10.1007/978-94-007-6904-5_14,

## 14.1 Borehole Breakout in a Geothermal Reservoir

Geothermal energy is a much favoured clean energy resource. Extracting geothermal energy for electricity generation often requires drilling deep boreholes into high temperature rock formations (or hot rocks). By injecting high-pressure fluid into the rock formation, the hot rocks will fracture, creating a permeable underground heat exchange reservoir. This is a process called reservoir stimulation. The thermal energy can then be extracted by circulating water through the stimulated reservoir via two or more boreholes.

To achieve the best heat extraction, it is desirable to orient the heat exchange reservoir horizontally so that the heat exchange between rock and fluid is confined to the high temperature rocks. A stress regime with horizontal stresses higher than the vertical stress favours the formation of such a reservoir during the simulation process. Therefore, understanding the in situ stress regime is critically important to the geothermal energy operations.

Since the geothermal reservoir is often at a depth greater than several kilometres, direct measurement of the in situ stresses by conventional methods such as hydraulic fracturing is difficult. It is possible, however, to estimate the in situ stresses indirectly, using the borehole breakout data because borehole breakouts occur almost certainly at such depths and the breakout dimension is related to the in situ stress magnitudes.

Borehole breakouts (i.e. failure of the borehole wall due to stress concentrations) result in an elongation of the borehole cross-section in the direction of the minor principal stress. Previous observations and theoretical analyses of borehole breakouts indicated that failure of the borehole wall is often governed by a tensile spalling or shear fracturing mode (Vardoulakis et al. 1988; Guenot 1989). In the case of tensile spalling, the rock breakage starts in the vicinity of a borehole as a result of tensile crack initiation and propagation along the direction of the major principal stress. A series of sub-parallel cracks are formed and the coalescence of these tensile cracks makes up a layer that may fall from the borehole wall. This phenomenon is typical for hard crystalline rocks such as granite under compression with no confinement or with small lateral confinement (Ewy and Cook 1990; Lee and Haimson 1993; Martin et al. 1994; Haimson and Lee 1995; Amadei and Stephansson 1997; Zang and Stephansson 2010). In the case of shear fracturing, shear failure along one or more shear band extends from the borehole wall into the rock. The shear fractures (or shear bands) can cause breakout when they intersect one another. This type of failure is often observed in softer porous rocks, such as dolomite, limestone and sandstone (Zoback et al. 1985; Guenot 1989). Both failure modes can result in so-called “dog ear” shaped breakouts.

Theoretical studies have been conducted to understand and predict these two breakout mechanisms. The breakout by shear was assumed to follow the Mohr-Coulomb failure criterion (Zoback et al. 1985). Although this can explain the wide and shallow breakout shapes sometimes observed in the field, it cannot produce the sharp-edged breakouts corresponding to the “dog ear” type.

Extensile cracking has been observed in laboratory uniaxial or biaxial borehole tests. Extensile cracking is attributed to the structural instability of the borehole wall. Vardoulakis et al. (1988) and Zheng et al. (1989) implemented a compressive failure criterion in a numerical method and predicted a breakout of "dog ear" shape as a result of gradual failure. Their results provided a close representation of the phenomenon but could not explain the physical mechanism of extensile cracking.

A fracture mechanics approach to borehole breakouts was used by Shen et al. (2002) and later by Shen (2008) to predict the breakouts formed by fracturing with the aim of estimating the magnitude of the in situ stresses. This study focused on the Habanero No. 1 Well drilled by Geodynamics Ltd at Cooper Basin. It was the first deep well drilled for developing hot fractured rock (HFR) geothermal resource in Australia. This well was drilled to a depth of 4,421 m with bottom hole temperature of 240 °C. Extensive borehole breakouts occurred in the granite section (depth = 3,650–4,421 m) of Habanero No. 1 Well after drilling. The direction and dimension of borehole breakouts were measured using borehole geophysical logging.

The study was conducted in the following steps:

- Establish a quantitative relation between breakout dimensions and in situ stresses in granitic rock using FRACOD.
- Back-calculate the in situ stresses using the measured borehole breakout data at Habanero No. 1 Well at various depths.
- Evaluate the overall stress state and stress ratios in Habanero No. 1 Well granite.

### *14.1.1 Input Properties*

The mechanical properties required in this study include intact rock strength, fracture contact properties and fracture toughness. Due to the lack of directly measured data of the Habanero No. 1 granite, the mechanical properties used in this study are mostly based on previous modelling experience for granitic rock (Stephansson et al. 2003). Some data were modified to reproduce the breakout shape observed in the AECL experimental tunnel (Martin et al. 1997). The values of the mechanical properties used in this study are listed below (Table 14.1).

The fracture properties are found to have minor effects on results once they have fallen within a certain range (i.e. the stiffness values are high enough and the friction angle is low enough). The chosen values above are considered to be reasonable based on previous modelling experience with granite at Tono Mine in Japan and with diorite at Äspö Hard Rock Laboratory in Sweden. Discussion and sensitivity analyses of material parameters used in FRACOD is presented in Rinne (2000) and Rinne (2008).

**Table 14.1** Summary of mechanical properties used in the FRACOD model of in situ stress in Habanero No. 1 Well

| | |
|---|---|
| Intact rock strength | |
| Young's modulus | 65 GPa |
| Poisson's Ratio | 0.25 |
| Cohesion | 31 MPa |
| Friction angle | 35° |
| Uniaxial Compression Strength ($\sigma_c$) | 120 MPa |
| Fracture toughness | |
| Mode I toughness | 1.35 MPa $m^{1/2}$ |
| Mode II toughness | 3.07 MPa $m^{1/2}$ |
| Joint/fracture properties | |
| Normal stiffness Kn | 50,000 GPa/m |
| Shear stiffness Ks | 12,550 GPa/m |
| Friction | 25.5° |
| Cohesion | 0 |
| Dilation angle | 2° |

### *14.1.2 Modelling Results*

Borehole breakouts are predicted numerically in the following steps:

1. Setting up the numerical model including defining borehole geometry, rock properties and in situ stresses;
2. FRACOD automatically calculates stresses in the borehole walls using solid mechanics principles;
3. FRACOD then determines if any failure (fracture initiation) occurs in the borehole wall based on the stresses obtained and the rock strength;
4. If failure is detected, new fractures will be generated in the model and FRACOD then determines if and how they propagate;
5. Breakouts will be formed when fractures in the borehole wall propagate and coalesce.
6. The dimensions of the final breakouts are obtained when there is no further failure or fracture propagation in the borehole wall.

Fifteen cases with different combinations of the major and minor principal horizontal stresses ($\sigma_{Hmax}$ and $\sigma_{hmin}$) were simulated (Table 14.2). The modelled magnitude of $\sigma_{Hmax}$ and $\sigma_{hmin}$ varies in the range of 50–80 MPa and 10–60 MPa, respectively. The stress ratio $\sigma_{Hmax}/\sigma_{hmin}$ varies in the range of 1.2–8.0. Note that the stresses used in the numerical modelling are effective stresses and at this stage, pore pressure and mud pressure are assumed to be balanced out and hence are not considered.

Figure 14.1 shows a typical set of the modelling results. The breakout angle is defined as the azimuth angle of the breakout at the borehole wall. The breakout depth is defined as the distance from the tip of the breakout to the original borehole wall. Several observations can be made based on the modelling results:

**Table 14.2** Summary of modelling results for Habanero No. 1 Well

| $\sigma_{Hmax}$ (MPa) | $\sigma_{hmin}$ (MPa) | Breakout angle (°) | Normalised breakout depth (% of borehole radius) |
|---|---|---|---|
| 80 | 60 | 117 | 28 |
| 80 | 40 | 90 | 31 |
| 80 | 25 | 81 | 37 |
| 80 | 10 | 72 | 32 |
| 70 | 50 | 86.4 | 24 |
| 70 | 30 | 72 | 24 |
| 70 | 15 | 72 | 26 |
| 60 | 50 | 64.8 | 16 |
| 60 | 40 | 57.6 | 14 |
| 60 | 30 | 57.6 | 26 |
| 60 | 20 | 64.8 | 20 |
| 60 | 11 | 57.6 | 29 |
| 50 | 30 | 14.4 | 5 |
| 50 | 20 | 36 | 20 |
| 50 | 10 | 43.2 | 24 |

- For a given $\sigma_{Hmax}$, a lower $\sigma_{hmin}$ is found to result in a deeper breakout. Since the variation of $\sigma_{hmin}$ affects the stress ratio $\sigma_{Hmax}/\sigma_{hmin}$ much more severely than an overall average stress (e.g. $(\sigma_{Hmax} + \sigma_{hmin})/2$), this implies that the depth of the breakout is very much dependent on the stress ratio $\sigma_{Hmax}/\sigma_{hmin}$, rather than an average stress index.
- For a given $\sigma_{hmin}$, a higher $\sigma_{Hmax}$ will result in a wider breakout, implying that the width (or azimuth angle) of the breakouts depends on the magnitude of the major horizontal principal stress.
- Breakouts are caused by combined tensile and shear fracturing. The initial fracturing starts at the borehole wall and propagates into the rock. Some failures also initiate inside the borehole wall during breakout development.

Note that the results for some cases are off trend due to the randomness in the fracture initiation and propagation processes.

### *14.1.3 Back-Analysis of Horizontal Stress Magnitude*

The modelling results listed in Table 14.2 are analysed to establish the correlations between the stress magnitude and the breakout dimensions. The relations will be used to estimate the stress magnitudes using the measured breakout dimensions.

For a perfect borehole without fracturing, the tangential stress at the borehole wall can be determined using elasticity theory. The azimuth angle within which the

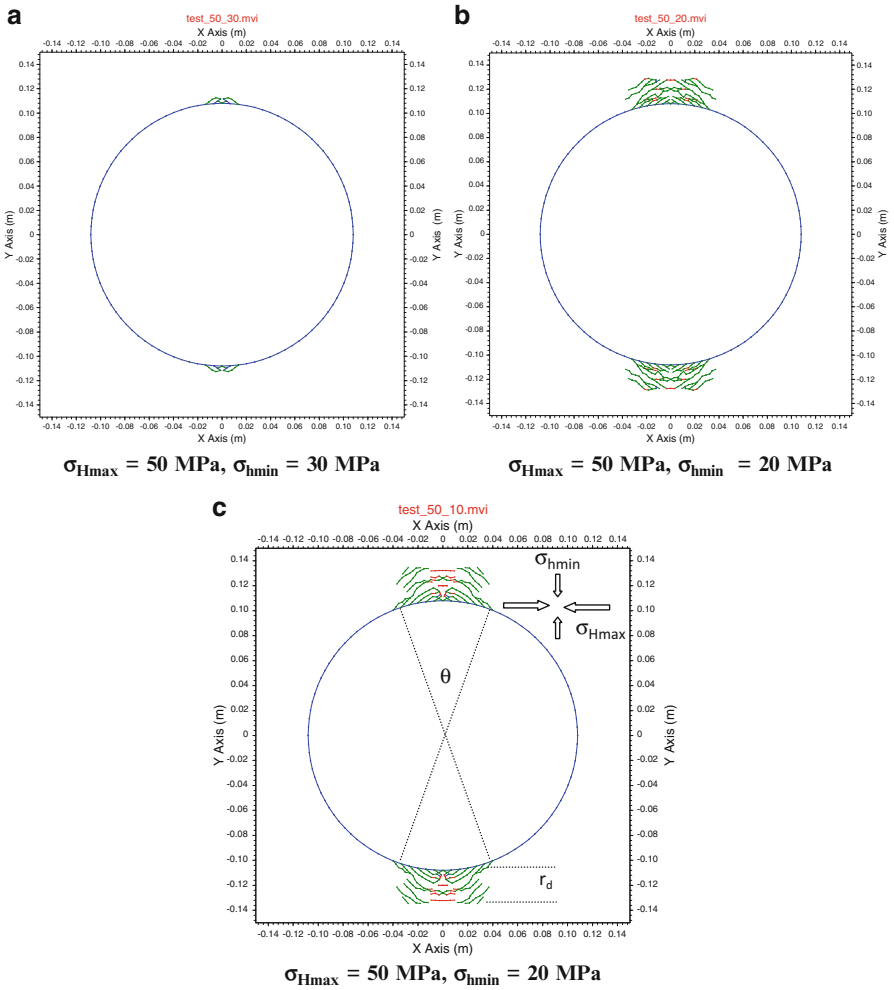


**Fig. 14.1** Predicted borehole breakouts at $\sigma_{Hmax} = 50$ MPa and different $\sigma_{hmin}$. The definition of the breakout angle ($\theta$) and depth ($r_d$) is also shown

tangential stress exceeds the uniaxial compressive strength can be calculated from Eq. (14.1).

$$\frac{1-(\sigma_{H\,\max}+\sigma_{h\,\min})/\sigma_c}{2(\sigma_{H\,\max}-\sigma_{h\,\min})/\sigma_c}=\cos(\theta) \tag{14.1}$$

where:

$\theta =$ breakout angle at the borehole wall (°)
$\sigma_c =$ uniaxial compressive strength of rock (MPa)

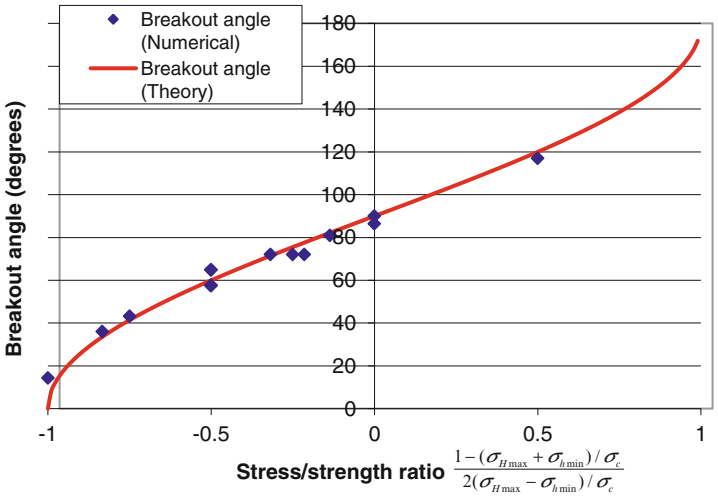


**Fig. 14.2** Predicted relationship between stress/strength ratio and the breakout angle results for Habanero No. 1 Well

The numerical method used in this study takes into account the effect of progressive fracturing—something the analytical method does not consider. FRACOD does not incorporate Eq. (14.1) in its formulation. Rather, it is based on fundamental solid mechanics and fracture mechanics principles. The numerically predicted breakout angles are plotted against the stress/strength factor on the left side of Eq. (14.1), and they are compared with the analytical results, see Fig. 14.2. The numerical results agree well with the analytical results, suggesting that breakout angle is not significantly affected by progressive rock failure processes. Rather it is dominated by the initial stress distribution at the borehole wall.

The normalised depth of the breakout (breakout depth/borehole radius) is found to have a reasonable correlation with the ratio of maximum tangential stress at the borehole and the rock uniaxial compressive strength, see Fig. 14.3. However, there are noticeable variations in the numerical results from the average correlation curve (Fig. 14.3), possibly due to the limitations in the control of the numerical accuracy and the variation due to randomness of fracture initiation and propagation.

To account for these variations, we consider the average as well as the upper and lower limits of the stress ratio/breakout depth relationship, as given in Eq. (14.2).

$$(3\sigma_{H\,\max} - \sigma_{h\,\min})/\sigma_c = 1 + A\left[\frac{r_d}{r}\right]^B \tag{14.2}$$

where:

$r_d$ = depth of breakouts;
$r$ = original radius of the wellbore;
$r_d/r$ = "normalised breakout depth";

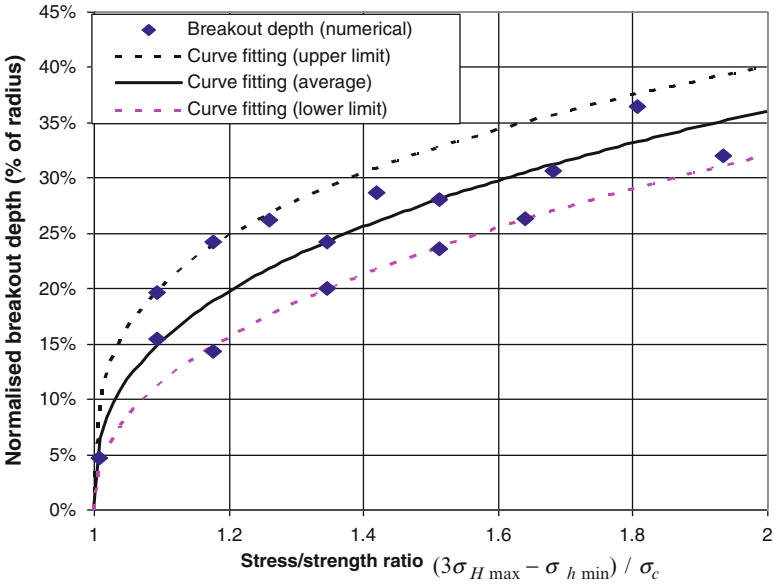


**Fig. 14.3** Predicted relationship between stress/strength ratio and the normalised breakout depths results for Habanero No. 1 Well

$A$, $B$ = the regression parameters. Their values are: A = 15.2, B = 2.67 (Average curve); A = 21.2, B = 3.33 (Upper limit curve); A = 12.6, B = 2.22 (Lower limit curve), respectively.

When the breakout angle and depth are known, the magnitude of the major and minor horizontal principal stresses can be obtained by solving the systematic equations defined by Eqs. (14.1) and (14.2).

$$\sigma_{H\,\max} = \frac{1 + (1 - 2\cos(\theta)) \left(1 + A\left[\frac{r_d}{r}\right]^B\right)}{4(1 - \cos(\theta))} \sigma_c \tag{14.3}$$

$$\sigma_{h\,\min} = 3\,\sigma_{H\,\max} - \left(1 + A\left[\frac{r_d}{r}\right]^B\right) \sigma_c \tag{14.4}$$

These equations can be used to calculate the magnitude of the horizontal stresses in the Habanero No. 1 granite using the measured breakout dimensions. For each cross-section, three stress states will be given: the average, higher, and lower stress state. The uncertainty of the estimated stress states is expressed by lower and upper limit values.

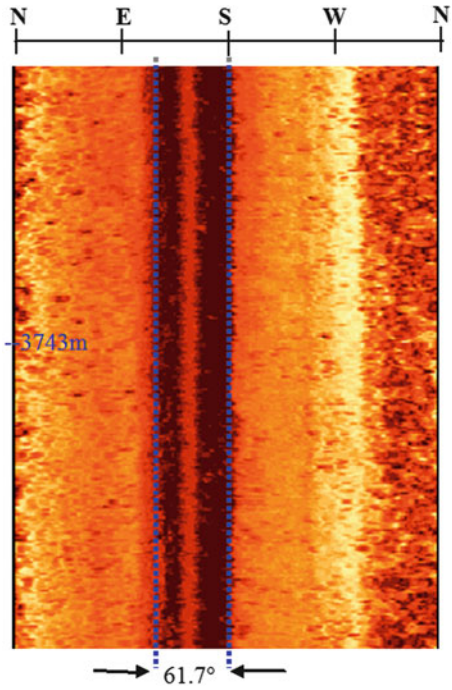


**Fig. 14.4** Image of the geophysical survey of the Habanero No. 1 Well at 3,743 m depth. The breakout angle was measured from the images, whereas the depth of the breakout was obtained from caliper logging results (not shown in this Figure)

### *14.1.4 Stress State in the Habanero No. 1 Well Granite*

Borehole breakouts in the Habanero No. 1 Well granite have been surveyed using geophysical logging tools. The geophysical logging data were used to extract the breakout angle and depth in a number of locations along the wellbore in the granite section. The selected locations are those considered to have a representative borehole breakout angle and depth for a considerable length of the wellbore. They are also intended to cover the whole length of the granite section in the wellbore.

To provide a statistical trend on stress distribution over the entire length of granite section, a reasonable number of cross-sections at different depths require investigation. In this study, a total of 13 cross-sections were selected to back-analyse the stress states. Figure 14.4 shows a typical image of the geophysical survey of the wellbore. For each cross-section, the breakout angle was measured from the images, whereas the depth of the breakout was obtained from the caliper logging results. Table 14.3 lists the measured breakout dimensions of all cross-sections.

After obtaining the breakout angle and depth, Eqs. (14.3) and (14.4) were used to calculate the magnitude of the horizontal stresses. Note that the calculated stresses are the effective stresses only. To calculate the total stresses, it was assumed that pore pressure in granite equals the mud pressure equivalent to a mud density of 1,800 kg/m$^3$ used during drilling below the depth of 4,135 m. This gives a mud pressure of 74.1 MPa at the depth of 4,209 m.

**Table 14.3** Measured borehole breakout dimensions at different depths results for Habanero No. 1 Well

| Depth (m) | Breakout angle (°) | Normalised breakout depth ($r_d$/r) (%) |
|---|---|---|
| 3,728 | 67 | 6 |
| 3,743 | 61.7 | 8 |
| 3,776 | 72 | 13 |
| 3,810 | 61 | 9 |
| 3,885 | 66.8 | 14 |
| 3,923 | 61.7 | 18 |
| 3,968 | 61.7 | 24 |
| 3,996 | 66.9 | 17 |
| 4,033 | 61.7 | 18 |
| 4,109 | 61.7 | 18 |
| 4,121 | 72 | 22 |
| 4,142 | 72 | 15 |

For each case, the average value and upper and lower limits are given to consider the uncertainty. The predicted horizontal stresses and their variations with depth and the stress ratios are given below. Note that all back-analysed stresses presented subsequently are total stresses, i.e. the sum of the effective stress and the pore pressure = mud pressure.

The vertical stress was estimated based on study results by Hill et al. (1997) in this area for the sediments, plus a density of 2,670 kg/m$^3$ for the granite.

$$\sigma_{Hmax}\,(\text{total}) = (0.033 \sim 0.034) \cdot D$$

$$\sigma_{hmin}\,(\text{total}) = (0.028 \sim 0.032) \cdot D$$

$$\sigma_{v}\,(\text{total}) = 0.023 \cdot D$$

$$\sigma_{Hmax}/\sigma_{hmin}/\sigma_{v}\,(\text{total}) = (1.43 \sim 1.48)/(1.22 \sim 1.39)/1.00$$

where D is the depth in metres.

The predicted stress magnitudes are consistent with the actual observations at Habanero No. 1 Well. During the actual reservoir stimulation test conducted afterwards, seismic monitoring indicated that fractures dipping 20° in the East and West directions experienced movement, Fig. 14.5. This is a strong indication that both horizontal principal stresses are higher than the vertical stress, resulting in sub-horizontal failures planes in the heat reservoir.

The predicted stress ratios from this study have been used to model the fracture movement at Habanero No. 1 Well during well stimulation tests (i.e. wellbore injection tests), see a separate study by Shen (2004). It was found that the predicted stress state would lead to the slippage of sub-horizontal fractures dipping to the East or West when high-pressure fluid is injected from the wellbore. The modelling results further demonstrate that the stress state obtained from this study is likely to reflect the true stress state in the granite at the Habanero No. 1 Well area.

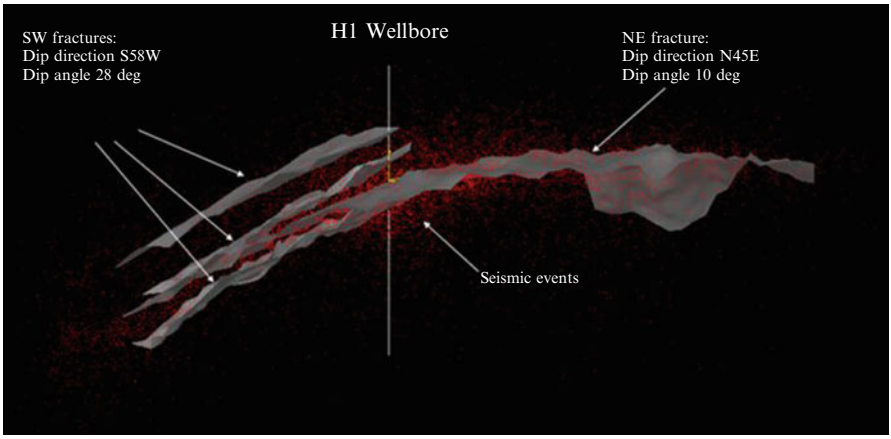


**Fig. 14.5** Seismic cloud and interpreted sub-horizontal fractures from stimulation of Habanero No. 1 Well

This study demonstrates that it is indeed feasible to use the borehole breakout dimension to estimate the magnitude of in situ stress if proper models are used that capture the real breakout mechanisms. However, the results are sensitive to parameters such as rock strength, fracture properties, etc. This method may only give us a likely range of the in situ stress magnitude rather than a definite value, as is often obtained from hydraulic fracturing.

## 14.2 Rock Fracturing and Related Permeability Change in Excavation Damage Zone: EDZ

Whenever rock is excavated, the immediate zone around the excavation is altered. We must distinguish between two types of alterations: (a) an excavation damaged zone EDZ from the surface of the excavation and inwards, (b) an excavation disturbed zone EdZ from the boundary of EDZ and inwards. The excavation damage zone EDZ is characterized by irreversible deformation and fracturing and fracture propagation where new fractures are developed and permeability is changed. The EdZ is a zone where stress distribution occurs and the rock mass deformation behaves elastically and reversibly and the permeability undergoes minor changes. EDZ and EdZ in different rock types are presented by Tsang et al. (2005). The application in this section examines the EDZ.

There are four principal factors that affect the characteristics and extent of the EDZ:

1. Excavation method (drilling and blasting generally cause greater damage than tunnel-boring machines (TBMs));

2. In situ stress and its orientation;
3. Strength and deformability of the rock mass; and
4. Hydraulic pressure in the groundwater surrounding the opening.

Certain rock features (such as porosity, microstructures, and hydraulic conductivity in the EDZ around deposition tunnels) affect long-term safety, particularly for deep geological disposal of radioactive waste. Therefore, it is of the utmost importance to minimize the extent of EDZ and to understand its evolution with time.

In this application we apply FRACOD to determine the extent of EDZ and permeability change around the Drill and Blast and TBM tunnels in the ZEDEX experiment in Äspö Hard Rock Laboratory, Sweden, and in the vicinity of the TSX tunnel of the Underground Research Laboratory in Canada (Stephansson et al. 2008; Shen et al. 2011).

### *14.2.1 Predicting Conductivity in EDZ Using FRACOD*

FRACOD simulates rock mass failure using explicit fracturing processes such as fracture initiation, propagation and coalescence. The normal and shear displacements of existing and new fractures are predicted and recorded during the failure process. FRACOD predicts the fracture aperture change using the normal displacement of the fractures. Each fracture is discretised into a number of Displacement Discontinuity (DD) elements in a FRACOD model. Each element has a calculated constant fracture aperture ($a$), based on its normal displacement. The conductivity of each fracture element is calculated in FRACOD as follows:

$$K_f = \frac{a^3 g \rho}{12 \mu w} \quad \text{(m/s)}$$

where $\mu$ is the dynamic viscosity (for water at room temperature, $\mu = 1.0 \times 10^{-3}$ Pa s); $w$ is the width of the fracture zone, or grid point spacing used for estimation (m); $\rho$ is the water density (kg/m$^3$); and $g$ is the acceleration of gravity (m/s$^2$).

In FRACOD models, a number of grid points are specified in the solid, and the stresses and displacements are calculated at each grid point. These grid points are also used to estimate the rock mass conductivity. As shown in Fig. 14.6, we specified a square window around each grid point for conductivity calculations. Only the fracture elements within the defined window are considered.

For a rock mass with explicit fractures, the hydraulic conductivity is direction dependent. Therefore, for each grid point we need to consider at least two orthogonal directions (i.e. x and y). For problems with circular excavations, we also consider the radial and tangential directions, see Fig. 14.6.

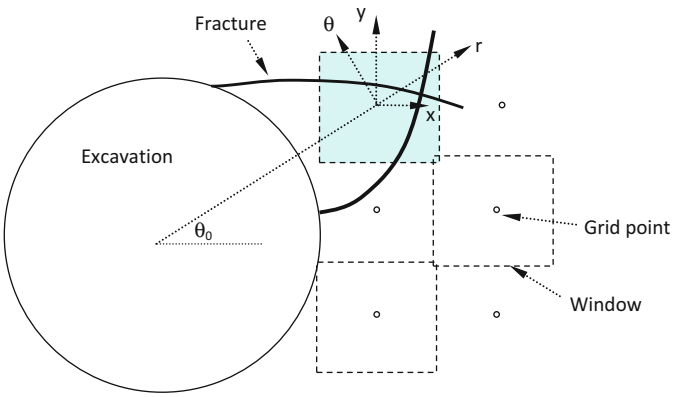


**Fig. 14.6** Grid points and windows used for conductivity estimation in FRACOD

$$K_f = \left[ \frac{\sum\limits_{i=1,n} L_i K_f^{(i)} \cos\,\theta_i}{\sum\limits_{i=1,n} L_i / K_f^{(i)}} \right]^{\frac{1}{2}} \tag{14.5}$$

Where

$K_f$ hydraulic conductivity of the fracture network;
$K_f^{(i)}$ hydraulic conductivity of individual fracture $i$;
$L_i$ length of fracture $i$;
$\theta_i$ angle of fracture $i$.

The total hydraulic conductivity ($K$) of a fractured rock mass is a product of fracture conductivity ($K_f$) and rock matrix conductivity ($K_r$) and is given by:

$$K = \text{integer}\left(\frac{L_f}{L}\right) \cdot K_f + \left(K_f + K_r\right)^{L'_f/L} (K_r)^{(L-L'_f)/L} \tag{14.6}$$

where $L_f$ = effective length of all fractures;

$$L_f = \sum_{i=1,n} L_i \cos\,\theta_i$$

$L$ = length of the rock mass;
$L_f'$ = length of a contained fracture.

If the effective fracture length $L_f$ is greater than $L$, it will be treated as one (or more) through-going fracture with length of $L$ and a contained fracture with a length of $L'_f = L_f - L$.

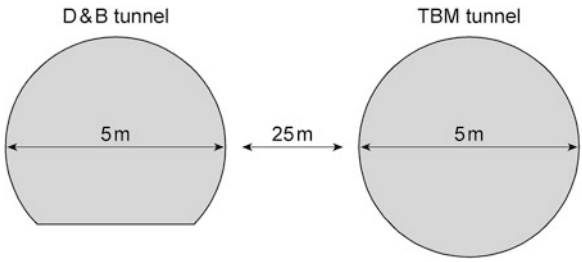


**Fig. 14.7** Geometry of the ZEDEX tunnels in Äspö Hard Rock Laboratory, Sweden

The rock mass conductivity in the x-direction ($K_x$) can be estimated using the Eqs. (14.5) and (14.6) and where $\theta_i$ in these equations is the angle of each fracture element to the x-axis. The rock mass conductivity in the y-direction ($K_y$) is calculated by replacing $cos\theta_i$ with $sin\theta_i$ in the same equations.

### *14.2.2 Comparison of FRACOD Prediction with EDZ Measurements of the ZEDEX Experiment in Äspö Hard Rock Laboratory, Sweden*

ZEDEX was one of the first underground experiments conducted to study the damage and disturbance from excavation by blasting and tunnel boring (Emsley et al.1997). It was conducted at Äspö Hard Rock Laboratory in Sweden at a depth of 420 m. Two parallel experimental tunnels were excavated, one by drill and blast (D&B) and the other by TBM (Fig. 14.7). The D&B tunnel is a semicircular excavation with a flat floor. The TBM tunnel has a circular opening. Both tunnels have diameters of 5 m. The tunnels were driven in the direction of approximately 45° from the maximum horizontal principal stress.

Comprehensive tests were conducted to characterize the EDZs around the two tunnels. These include in situ stress measurements, acoustic emission monitoring, displacement monitoring, in situ and laboratory permeability tests, and seismic mapping. Results from ZEDEX indicate that the EDZ width range in the TBM tunnel is 0–0.35 m depending upon the method used, and in the D&B tunnel the EDZ width range is <1.5 m with the deepest EDZ measured in the floor.

The input parameters for the ZEDEX validation study are listed in Table 14.4 and results from applying fracture initiation stress of $0.12\sigma_c$ are presented in Fig. 14.8.

Modelling results for tunnels with fracture initiation level $0.12\sigma_c$ are shown in Fig. 14.8. The predicted EDZ is predominately in the roof and floor of the tunnels where stress concentration occurs because the horizontal stress is greater than the vertical stress. For the D&B tunnel, the EDZ extends up to 1.3 m into the floor and 0.8 m into the roof and a very limited distance into the sidewalls. For the TBM tunnel, the EDZ extends approximately 0.7 m into both the roof and floor and an insignificant distance into the sidewalls.

**Table 14.4** Input rock parameters for the ZEDEX application

| Input parameter | Value | Source |
|---|---|---|
| Rock type | Äspö Diorite | Emsley et al. (1997) |
| Intact compressive strength ($\sigma_c$) | 165 MPa | Rinne et al. (2003a) |
| Intact tensile strength ($\sigma_t$) | 14.8 MPa | |
| Internal friction angle ($\phi$) | 49° | |
| Intact rock cohesion (c) | 31 MPa | |
| Young's modulus (E) | 68 GPa | |
| Poisson's ratio ($\nu$) | 0.24 | |
| Fracture toughness: $K_{Ic}$ | 2.54 MPa $m^{1/2}$ | Rinne et al. (2003a) |
| Fracture toughness: $K_{IIc}$ | 6.35 MPa $m^{1/2}$ | |
| In-situ stresses: $\sigma_H$ (317.5°N) | −20.7 MPa | Chryssanthakis et al. (2003) |
| $\sigma_v$ | −10.4 MPa | |
| $\sigma_h$ | −9.6 MPa | |
| Fracture initiation level ($\sigma_{ci}$): | $0.3\sigma_c$ and $0.12\sigma_c$ | Emsley et al. (1997) |
| Fracture normal stiffness ($K_n$) | 13,800 GPa/m | Assumed |
| Fracture normal stiffness ($K_s$) | 3,099 GPa/m | |
| Fracture friction angle ($\phi$) | 49° | From intact rock strength |
| Fracture cohesion (c) | 31 MPa | |
| Fracture dilation angle ($\phi_d$) | 5° | Assumed |
| In-situ hydraulic conductivity ($K_{is}$) | $1.5 \times 10^{-13}$ m/s | Emsley et al. (1997) |
| Fracture initial aperture ($e_{initial}$) | $10 \times 10^{-6}$ m | Assumed |
| Fracture residual aperture ($e_{resid}$) | $5 \times 10^{-6}$ m | |

FRACOD predicted hydraulic conductivity in the EDZ ranges from the background value of $1 \times 10^{-13}$ m/s to a maximum value of approximately $1 \times 10^{-9}$ m/s. The maximum value agrees well with the measured hydraulic conductivity in the vertical boreholes of the D&B tunnel, which is approximately $1 \times 10^{-9}$ m/s [or $1 \times 10^{-16}$ $m^2$ in the report by Emsley et al. (1997)]. However, the predicted hydraulic conductivity does not agree with the very low values measured in the roof and floor of the TBM tunnel.

The FRACOD models also predict a maximum convergence of 2.6 mm in the D&B tunnel and 2.8 mm in the TBM tunnel. The measured average value of 2.5 mm agrees well with the FRACOD model predictions.

Overall, the predicted EDZs in the ZEDEX tunnels are in broad agreement with the measurements, taking into account uncertainties in the in situ stresses and fracture system and the local fracture initiation levels.

### *14.2.3 FRACOD Modeling of Permeability Measurements in the Tunnel Sealing Experiment (TSX) of URL, Canada*

Several large-scale underground experiments have been conducted at AECL's URL in Canada to address geo-mechanical issues related to the disposal of nuclear

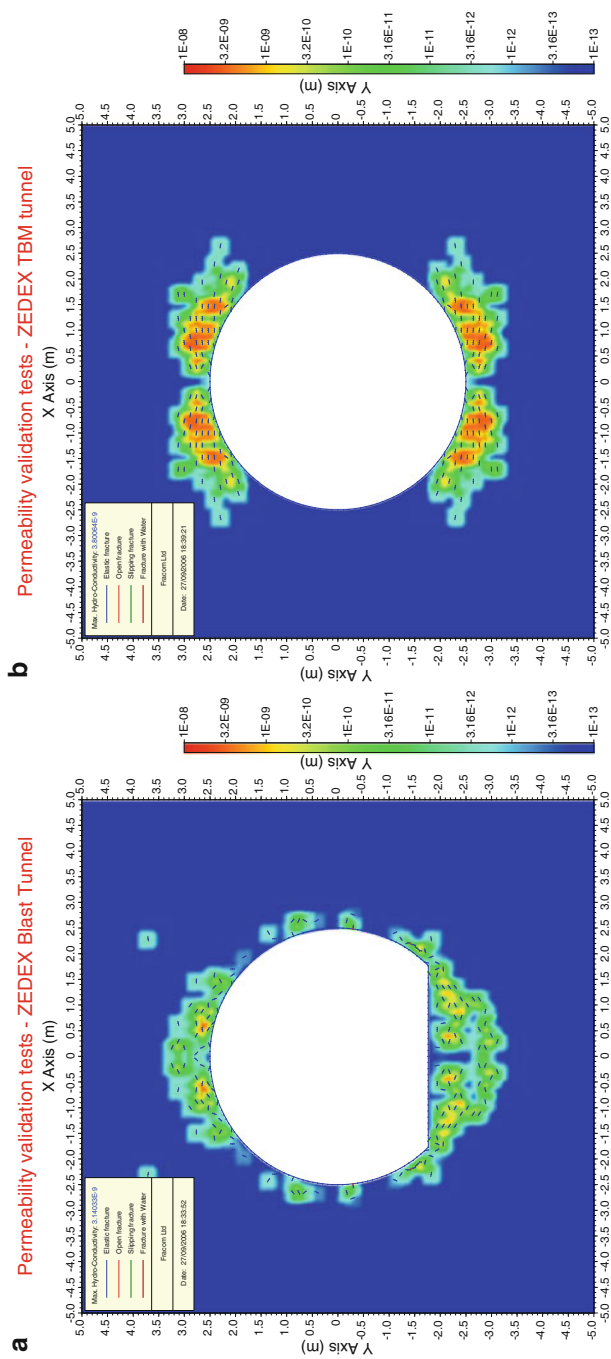


**Fig. 14.8** Predicted EDZ and hydraulic conductivity of (**a**) D&B tunnel; (**b**) TBM tunnel of the ZEDEX experiment at Äspö Hard Rock Laboratory, Sweden

fuel waste. As part of these experiments, hydraulic characterization of EDZ was investigated in Room 425 of the TSX. The tunnel was excavated using the controlled drill and blast (D&B) technique.

In situ hydraulic experiments, including pulse tests, were conducted around Room 425 at a depth of 425 m. The tests were performed using a SEPPI probe in eight short (3–4 m in length) radial boreholes drilled around Room 425. Typical variations of the in situ permeability in the roof and sidewalls of the tunnel are provided by Souley et al. (2001). The rock in the AECL's URL is predominantly Lac du Bonnet granite. Its mechanical properties have been extensively studied and well documented. The rock mass is basically intact, containing no or very few fractures. The in situ stresses in the AECL's URL are well understood. This site is ideal for validation tests because of its simple geology, well understood rock properties and in situ stresses. Room 425 has an elliptical cross-section. The ellipse is approximately 4.4 m along the longer axis and 3.5 m along the shorter axis. The tunnel is aligned to the maximum horizontal stress $\sigma_1$, and its cross-section is in the $\sigma_2$–$\sigma_3$ plane.

Rock mechanical parameters used for the validation study are mostly from the open literature for the AECL's URL, including Souley et al. (2001), Hajiabdolmajid et al. (2002) and Martino and Chandler (2004). Some special fracture mechanics parameters needed for FRACOD modelling are not readily available in the literature. These have been assumed based on past experience. Where possible, sensitivity studies have been conducted to quantify the effect of the assumed parameters. The input parameters for the AECL's URL application study follow (Table 14.5).

The FRACOD models include the elliptical opening of Room 425. The model's x- and y-axes are rotated to align with the intermediate and minor principal stresses in URL.

Blast damage is simulated by the introduction of randomly distributed short fractures within a specified distance from the excavation boundary. Four basic numerical models are used with different blast-damaged zone sizes:

1. No blast-induced fractures in rocks;
2. Random blast-induced fractures within 0.2 m into rocks;
3. Random blast-induced fractures within 0.4 m into rocks; and
4. Random blast-induced fractures within 0.6 m into rocks.

With or without the blast-induced fractures, all four models predict fracture initiations in the roof and floor of the elliptical cavern. The predicted EDZ and permeability of Model 4 are shown in Fig. 14.9. The zones of fracture initiation in the rock are approximately 0.5–0.7 m deep. Newly initiated fractures are not predicted to propagate under the stress conditions applied. Therefore, no extensive spalling or breakout was predicted and this agrees with the observation at Room 425 that the excavation was generally stable. In the sidewalls of the elliptical cavern, no stress-induced fracture initiations were predicted because the stresses from excavation are released rather than increased. Any damage in these zones is probably caused by the excavation process rather than stress concentration.

**Table 14.5** FRACOD input parameters for TSX application in URL, Canada

| Input parameter | Value | Source |
|---|---|---|
| Rock type: | Lac du Bonnet granite | Hajiabdolmajid (2002); Souley et al. (2001) |
| Intact compressive strength ($\sigma_c$) | 224 MPa | Hajiabdolmajid (2002) |
| Intact tensile strength ($\sigma_t$) | 10 MPa | |
| Rock mass strength ($\sigma_{cm}$) | 128 MPa | |
| Internal friction angle ($\varphi$) | 48° | |
| Intact rock cohesion (c) | 43 MPa | Based on $\sigma_c$ and $\varphi$ |
| Young's modulus (E) | 60 GPa | Hajiabdolmajid (2002) |
| Poisson's ratio ($\nu$) | 0.2 | |
| Fracture toughness: $K_{Ic}$ | 0.96 MPa $m^{1/2}$ | Souley et al. (2001) |
| Fracture toughness: $K_{IIc}$ | 2 MPa $m^{1/2}$ | Assumed |
| In-situ stress $\sigma_1$ | −55 MPa | Souley et al. (2001) |
| In-situ stress $\sigma_2$ | −48 MPa | |
| In-situ stress $\sigma_3$ | −12.8 MPa | |
| Fracture initiation level ($\sigma_{ci}$): | $0.3\sigma_c$ or 67 MPa | Emsley et al. (1997) |
| Fracture normal stiffness ($K_n$) | 13,800 GPa/m | Assumed |
| Fracture normal stiffness ($K_s$) | 3,099 GPa/m | |
| Fracture friction angle ($\phi$) | 48° | From intact rock strength |
| Fracture cohesion (c) | 43 MPa | |
| Fracture dilation angle ($\phi_d$) | 5° | Assumed |
| In-situ hydraulic conductivity ($K_{is}$) | $1.5 \times 10^{-14}$ m/s | Souley et al. (2001) |
| Fracture initial aperture ($e_{initial}$) | $10 \times 10^{-6}$ m | Assumed |
| Fracture residual aperture ($e_{residual}$) | $5 \times 10^{-6}$ m | |

Using these four models, the EDZs and the hydraulic conductivities in the roof and sidewalls of the elliptical cavern were simulated. In each model, two hydraulic conductivity values are provided: one in the x-direction (sub-horizontal), the other in the y-direction (sub-vertical). A geometrical mean of these two values is also calculated. In the cavern roof, the predicted hydraulic conductivities of Model 4 agreed reasonably well with the measurement results (Fig. 14.10). The predicted EDZ is approximately 0.5–0.7 m from the excavation boundary. In this EDZ, the modelled hydraulic conductivity is mostly in the range of $1 \times 10^{-12}$ to $1 \times 10^{-9}$ m/s, corresponding well with the measured results.

In the sidewalls, for Model 4 (blast-induced cracks within 0.6 m into rock) the modelled EDZ is approximately 0.7 m, and the hydraulic conductivity is approximately $1 \times 10^{-13}$ to $1 \times 10^{-12}$ m/s, and both are in general agreement with the measured results (Fig. 14.10). The stresses (tensile or compression) in these zones are not large enough to cause fracture initiation.

Because the horizontal stress is much higher than the vertical stress, the stress concentration at the cavern roof is high. This results in more damage in the roof than in the wall, and consequently permeability is higher in the roof. In addition, new cracks in the roof are more likely to be generated in the horizontal direction (major principal stress direction). This will increase the horizontal permeability more than the vertical permeability.

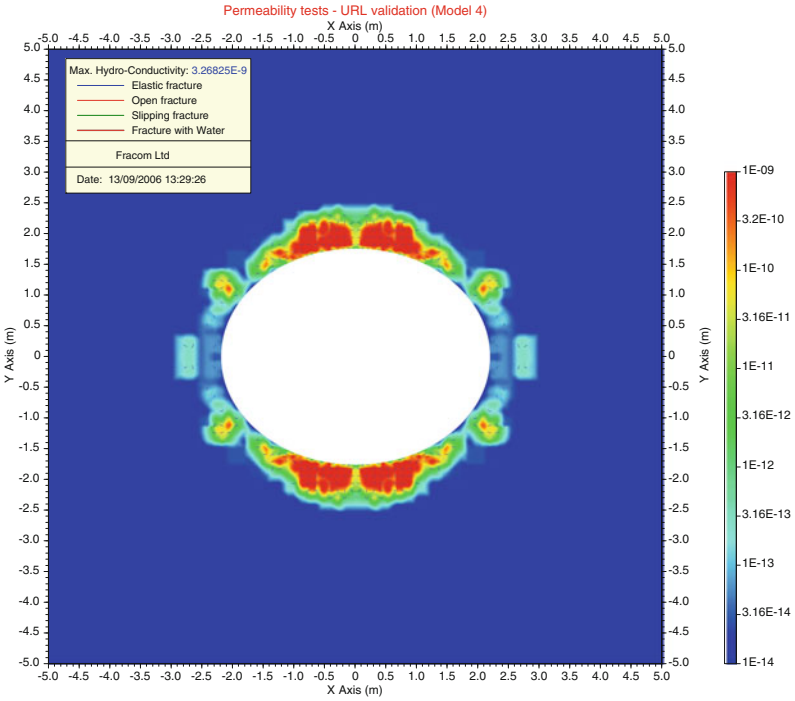


**Fig. 14.9** FRACOD model of the TDX tunnel at URL. Modelled EDZ and permeability $K_x$ in Model 4; the intermediate principal stress ($\sigma_2$) is in the x-direction, whereas the minimum principal stress ($\sigma_3$) is in the y-direction

Overall, the FRACOD modelling results agree well with the permeability measurement data from Room 425, particularly in the cavern roof and floor. The numerical results also indicate that blast damage dominates the EDZs at the sidewalls but has little effect on the EDZs in the roof and floor (where damage is caused by stress concentration). At AECL's URL, a blast damage assessment tunnel was excavated and investigated (Martino and Chandler 2004). It was found that blast damage may extend up to 0.5 m into the walls.

Therefore, the assumption of blast damage zone of 0.4–0.6 m in Models 3 and 4 is considered reasonable.

### *14.2.4 Summary*

Characterization of Excavation Damaged Zone (EDZ) around an underground excavation is a major research topic for deep geological disposal of medium to high-level radioactive waste and spent nuclear fuel. Rock fracturing due to excavation and thermal loading and its resultant rock mass permeability change in the EDZ are important for construction and long-term safety. The functions predicting rock mass

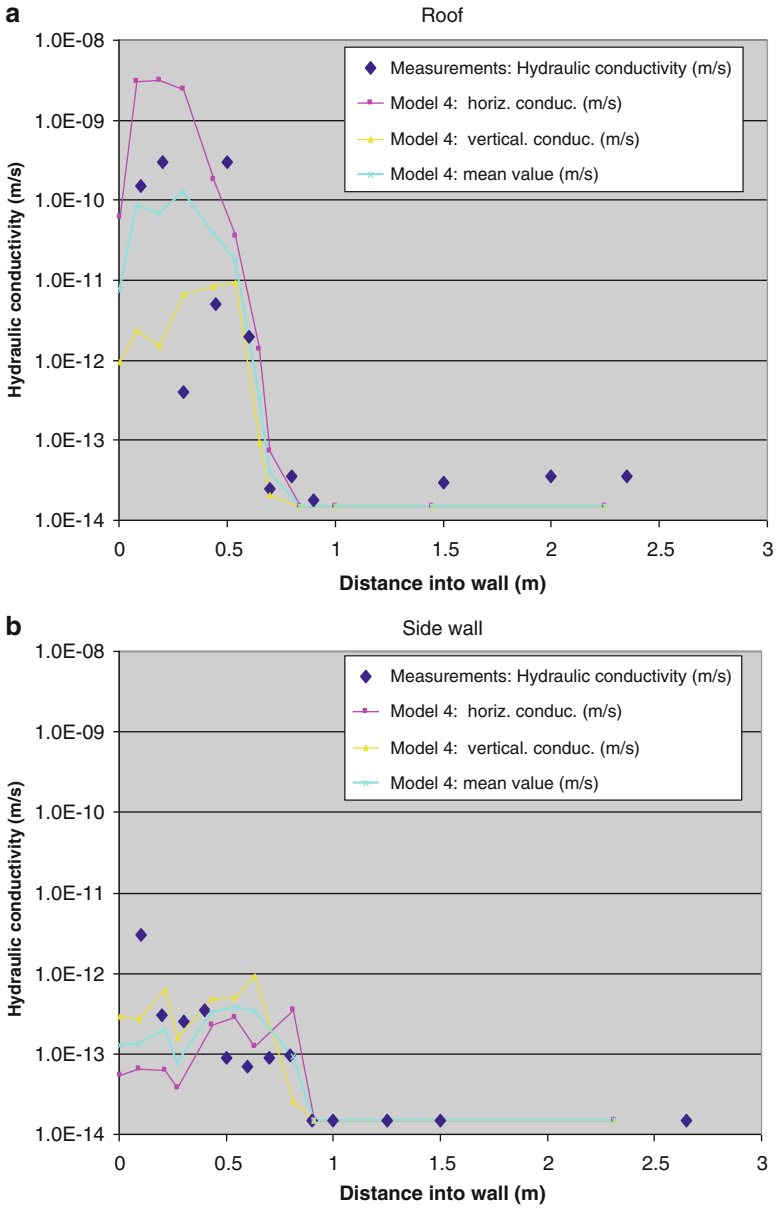


**Fig. 14.10** TDX experiment at URL, Model 4: measured and simulated hydraulic conductivity; (**a**) x-direction (*top*), (**b**) y-direction (*bottom*)

permeability change in EDZ in FRACOD have been applied to predict the extent of EDZ and permeability change in the vicinity of the TSX tunnel of URL (Canada) and the ZEDEX tunnel of the Äspö Hard Rock Laboratory (Sweden). The predicted EDZ and its permeability are consistent with the measured data of the TSX tunnel and ZEDEX tunnel. The results from both tests indicate that FRACOD is capable of realistically predicting the EDZ and permeability change around underground openings.

## 14.3 Underground Lined Rock Cavern for LNG Storage

A real pilot lined cavern tested for underground liquefied natural gas, LNG storage in the Republic of Korea was simulated using FRACOD with multiregion and thermal mechanical coupling modules as described in Chaps. 6 and 9. The underground LNG containment system consists of gas-tight steel liners and insulation panels to protect against failure and damage of surrounding rock by thermal shock caused by the low temperature of liquefied natural gas (Park et al. 2010; Shen et al. 2013). However, in the present example we focus on the comparison between calculation and in situ measurements during the pilot test so as to verify the validity of the developed coupled code. After installing the liners, the inner dimensions of the pilot cavern were 3.5 m × 3.5 m.

Figure 14.11 shows the structural concept of the pilot cavern. During the pilot testing, changes in temperature and displacement in rock mass were monitored and compared with the simulation results obtained using FRACOD.

For practical and safety reasons liquefied nitrogen ($LN_2$) was used to fill the cavern during the operation. $LN_2$ had a measured temperature of −194 °C and the gaseous space in the top of the cavern (due to boiling of $LN_2$) was about −100 °C. Therefore two different regions of thermal boundary conditions were explicitly modelled. The initial rock temperature was 17 °C. Table 14.6 shows the mechanical and thermal parameters of the rock mass used in the simulation. In the simulation

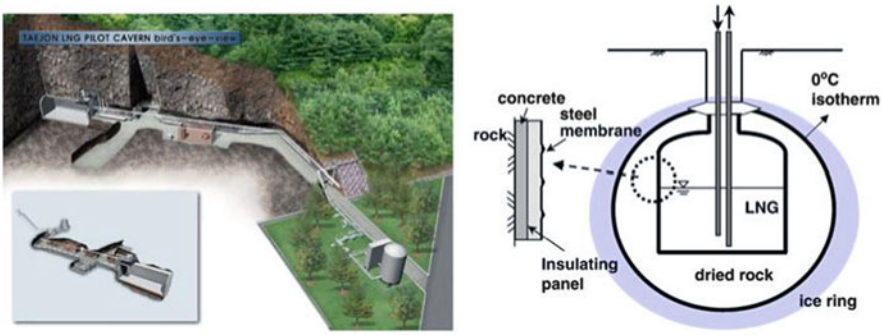


**Fig. 14.11** Location and structure of underground lined rock cavern for underground storage of LNG in Korea. Ice ring will be formed at 0 °C isotherm band

**Table 14.6** Mechanical and thermal rock properties for LNG storage in Korea

| | |
|---|---|
| Tensile strength, $\sigma_t$ (MPa) | 9 |
| Cohesion, $c$ (MPa) | 13 |
| Internal friction angle, $\phi$ (°) | 33 |
| Mode I fracture toughness, $K_{Ic}$ (MPa $m^{0.5}$) | 1.5 |
| Mode II fracture toughness, $K_{IIc}$ (MPa $m^{0.5}$) | 3.3 |
| Density, ρ (kg/$m^3$) | 2,500 |
| Young's modulus, $E$ (GPa) | 43.2 |
| Poisson's ratio, $v$ | 0.25 |
| Specific heat, $C_p$ (J/kg °C) | 710 |
| Thermal conductivity, $k$ (W/m °C) | 2.627 |
| Linear thermal expansion coefficient, α (1/°C) | $6.59 \times 10^{-6}$ |
| In situ stresses, $\sigma_{xx} = \sigma_{yy}$ (MPa) | 0.795 |

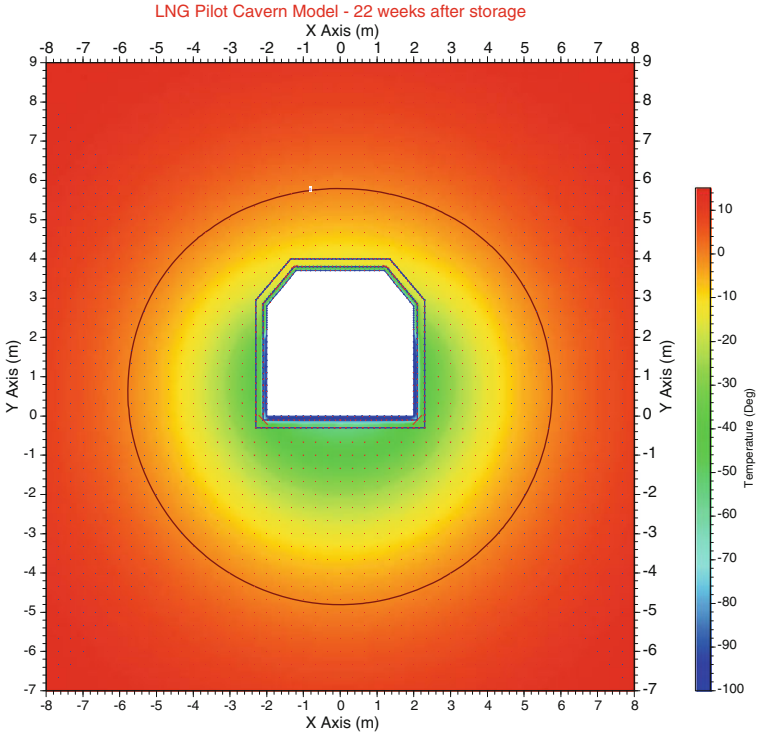


**Fig. 14.12** Modelled temperature distribution around the LNG cavern after 22 weeks of cooling

with FRACOD, we considered only the rock mass stability without pre-existing fractures. An insulation panel of 0.1 m thick polyurethane (PU) foam and a 0.3 m thick concrete wall were assumed to have sufficiently high strengths so as not to fail.

Simulated and measured temperature distribution in the rock mass after 22 weeks of cooling are presented in Figs. 14.12 and 14.13. The calculated temperature

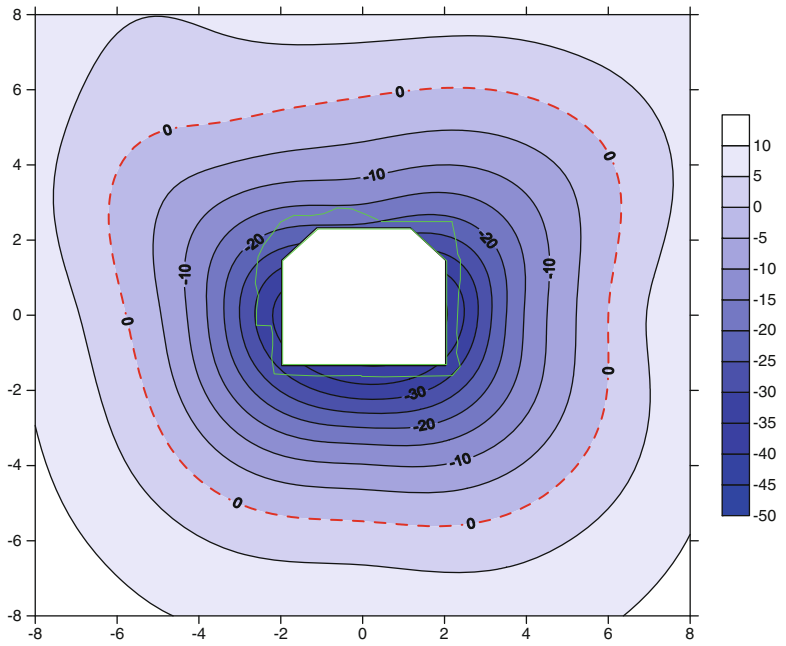


**Fig. 14.13** Measured temperature distribution around the LNG cavern after 22 weeks of cooling. The *light colour line* is the excavation profile

distribution agrees well with the measurement results, even though the site's geological complexity was not considered.

Figure 14.14 compares the simulated and measured temperature evolution during 22 weeks at the floor of the cavern. Reasonably good agreement was obtained.

Figures 14.15 and 14.16 indicate the modelled major and minor principal stresses distribution after 22 weeks of operation. The simulated tensile stresses in the rock were <3 MPa, hence no tensile fracturing was predicted, considering the tensile strength of concrete and rock usually ranges between 5 and 20 MPa.

### *14.3.1 Summary*

Coupled processes in fractured rock mass are important in the performance and safety analysis of many rock engineering projects such as $CO_2$ geosequestration, energy storage and geothermal extraction. These processes are difficult to predict by in situ tests due to many unknown factors affecting the test conditions and results. In view of this, numerical methods generating predictions under many different conditions provide valuable information about the nature of coupled processes. Due to its capacity to model propagation of discrete fractures, FRACOD has potential to realistically predict the complex behaviours of fractured rock mass.

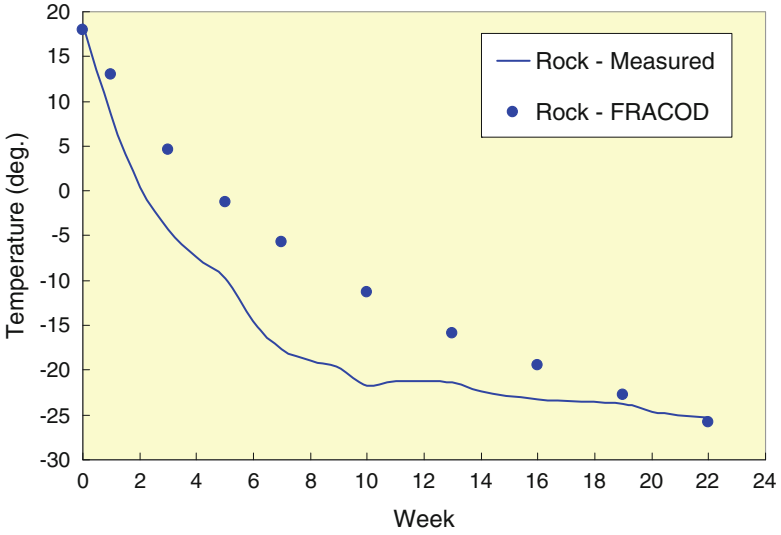


**Fig. 14.14** Measured and modelled temperature versus time in the floor of the LNG cavern

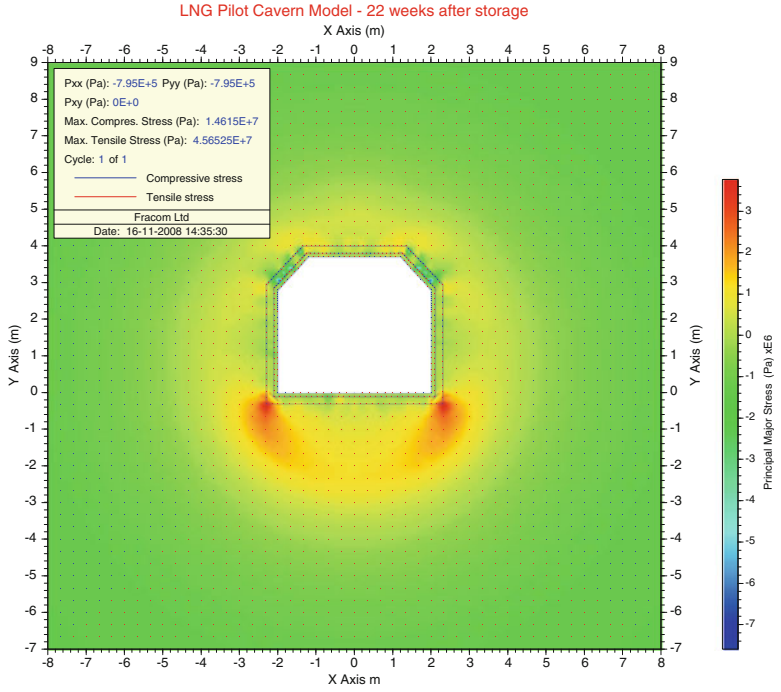


**Fig. 14.15** Major principal stress around pilot cavern after 22 weeks of operation

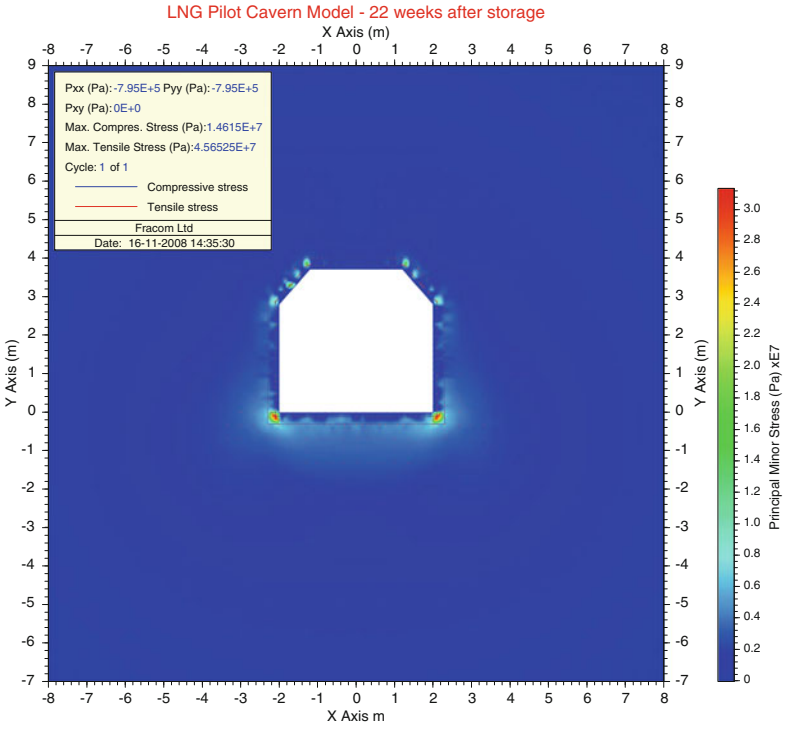


**Fig. 14.16** Minor principal stress around pilot cavern after 22 weeks of operation

The application example of LNG storage in a rock cavern demonstrates good agreement between the simulation results and in situ measurement. Therefore, the developed coupled code can be effectively employed when designing structures that are placed under extreme temperature conditions where thermal fracturing would be a significant concern for long-term stability.

## 14.4 Modelling Fracture Propagation and Failure in a Rock Pillar Under Mechanical and Thermal Loading

The failure process in the wall of an underground opening in brittle rock is often called spalling; the failed zone is generally described as a breakout or a v-shaped notch.

The Äspö Pillar Stability Experiment (APSE) was conducted to examine the spalling in an inhomogeneous and slightly fractured rock mass (Andersson 2007).

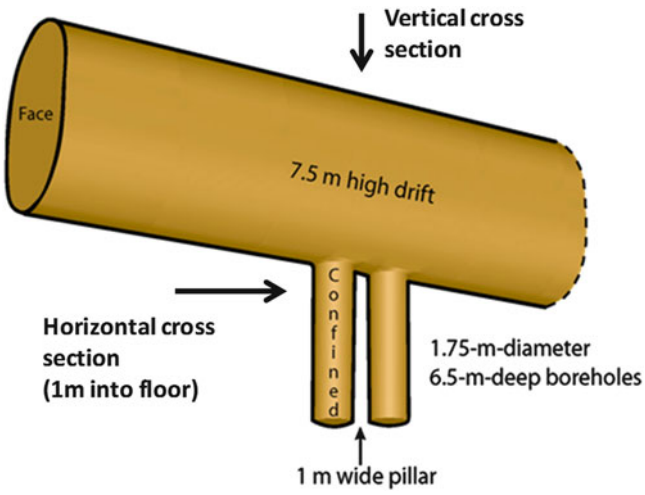


**Fig. 14.17** Geometry of the TASQ Tunnel and APSE boreholes. Locations of modelled cross-sections are indicated (Modified from Andersson et al. 2003)

The experiment's major objectives were to determine the spalling strength of the granitic rock mass of Äspö URL and to investigate how confining pressure suppresses the spalling. To introduce high stresses and spalling of the rock mass, a combination of excavation-induced stresses and thermally-induced stresses were applied in a 1 m wide rock pillar between two large boreholes.

The vertical boreholes (diameter = 1.75 m, depth = 6.5 m) were drilled using a modified Tunnel Boring Machine (Fig. 14.17). One of the boreholes was hydraulically pressurized. After detecting the response of purely mechanical loads in the pillar, the rock mass was slowly heated with electrical heaters to increase stresses and to enhance the failure. The following loading sequences were used in the field experiments:

Step 1 – Excavation of the tunnel (TASQ Tunnel)
Step 2 – Excavation of borehole #1
Step 3 – Application of confining pressure of 0.7 MPa in hole #1
Step 4 – Excavation of borehole #2
Step 5 – Heating of the pillar between the hole #1 and #2 for about 60 days
Step 6 – Stop heating
Step 7 – Release of confining pressure from borehole #1

Acoustic emission, displacement and temperature change were monitored (Fig. 14.18) during the experiment when the failure in the pillar wall occurred as the rock temperature increased. During the heating of the pillar, the failed zone propagated down along the pillar wall, creating a v-shaped notch. The main

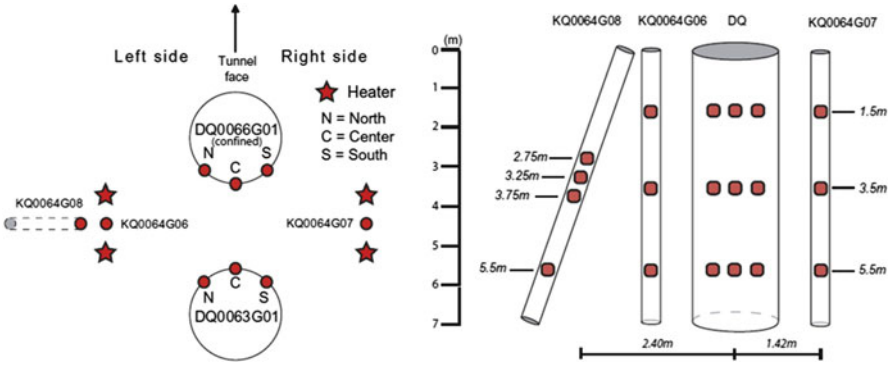


**Fig. 14.18** Plan view of instrumentation of the APSE experiment (*left*) and a vertical section perpendicular to the TASQ Tunnel axis showing the thermocouples and the boreholes (Andersson 2007)

modelling results are presented in the following section. Predictive modelling of the APSE experiment is presented in Andersson et al. (2003), Andersson (2004) and in Rinne et al. (2004).

### *14.4.1 Layout and Parameters*

Figure 14.17 shows the layout of the APSE pillar experiment. The shape and the alignment of 7.5 m high TASQ Tunnel were planned to maximize the induced tangential stresses at the tunnel floor. The large diameter boreholes, mimicking deposition holes of spent nuclear fuel, were excavated from the floor of the TASQ Tunnel. These boreholes were placed in a position maximising the stresses in the pillar to a level that was predict to cause spalling.

A plan and a vertical section of the pillar volume including instrumentation and heaters are shown in Fig. 14.18. FRACOD was used to calculate the pillar spalling in this experiment. The modelling was made in two sections. The vertical section of TASQ Tunnel aims to assess the stresses in the experimental rock volume. Of special interest is the stress distribution at various depths in the tunnel floor, at the stage before the two boreholes were drilled (Fig. 14.19).

The horizontal models (Fig. 14.20) consider cross-sections of the pillar and the boreholes at several depths. They were designed to back-calculate the evolution of the stress in the pillar during the mechanical and thermal loading phases and to assess the failure at different depths of the boreholes.

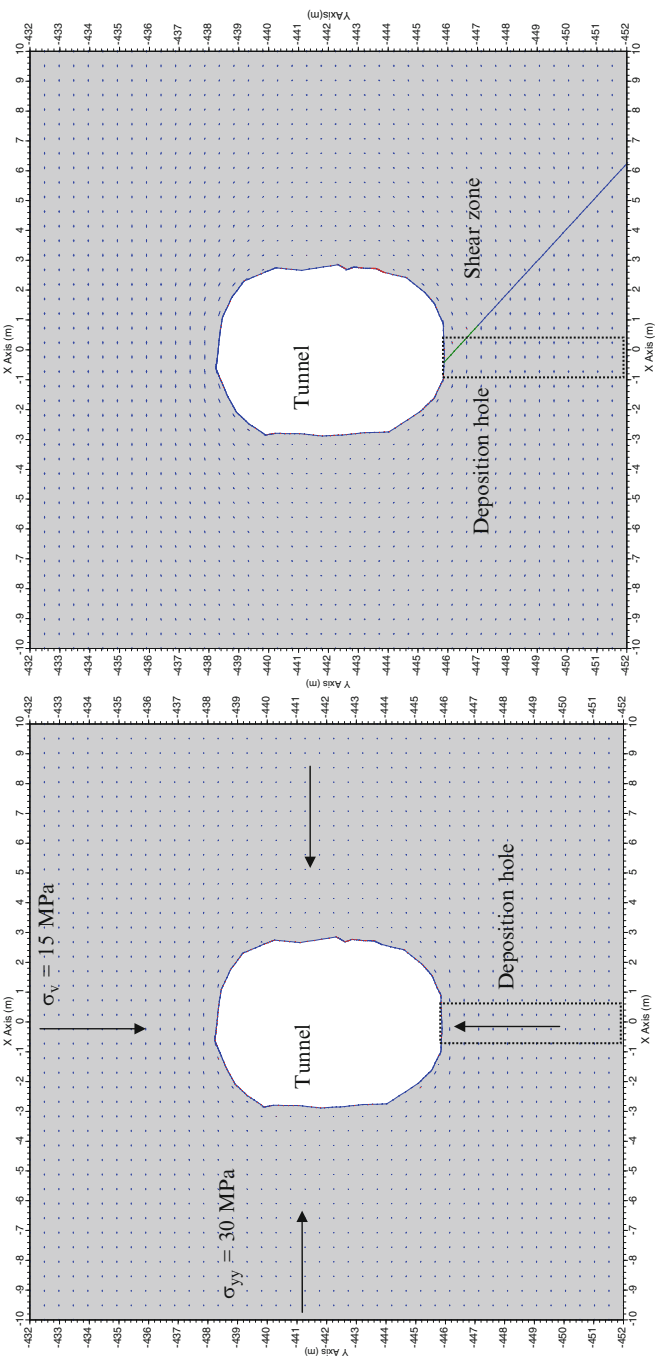


**Fig. 14.19** Vertical section of the TASQ Tunnel: *Left*: without the shear zone; *Right*: with a shear zone in the immediate floor

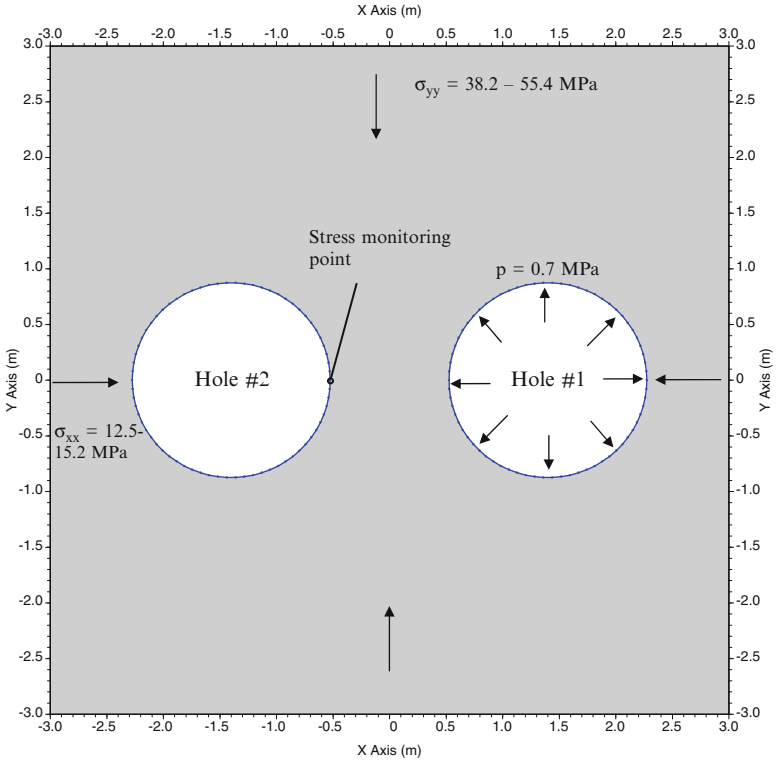


**Fig. 14.20** Model geometry and applied stresses of APSE boreholes. Stresses in a horizontal section 1–2 m below the tunnel floor

**Table 14.7** Stress tensor data for TASQ Tunnel (Andersson 2007)

| | Maximum principal stress | Intermediate principal stress | Minimum principal stress |
|---|---|---|---|
| | S1 | S2 | S3 |
| Magnitude [MPa] | 30 | 15 | 10 |
| Trend [°] | 310 | 090 | 220 |
| Plunge from horizon [°] | 0 | 90 | 0 |

The measured in-situ stresses in the experiment area are listed in Table 14.7. The tunnel axis is perpendicular to the trend of the maximum principal stress. Parameters used for mechanical calculations are listed in Table 14.8.

**Table 14.8** Mechanical parameters used in APSE modelling

| Parameter | Value and unit |
|---|---|
| *Intact rock* | |
| Young's modulus (rock mass) | 55 GPa |
| Poisson's ratio (rock mass) | 0.25 |
| Cohesion | 22.5 MPa −31 MPa |
| Friction angle | 49° |
| Tensile strength | 14.9 MPa |
| *Fractures* | |
| Cohesion | 0 MPa −20 MPa |
| Friction angle | 25–35° |
| Normal stiffness | 20–27,000 GPa/m |
| Shear stiffness | 2–2,700 GPa/m |
| Dilation angle | 2° |
| Fracture toughness – tensile $K_{IC}$ | 3.8 MPa $m^{0.5}$ |
| Fracture toughness – shear $K_{IIC}$ | 4.4 MPa $m^{0.5}$ |
| Fracture initial aperture | $10 \times 10^{-6}$ m |
| Fracture residual aperture | $1 \times 10^{-6}$ m |
| Initial crack element size – laboratory scale test | 0.002 m |
| Initial crack element size – horizontal sections | 0.075 m |
| Initial crack element size – TASQ | 0.25–0.05 m |

## *14.4.2 Back-Calculations of the Excavation Induced Stresses*

### 14.4.2.1 Vertical Section of the TASQ Tunnel

Induced stresses at different depths below the tunnel floor were estimated using the TASQ Tunnel model. Andersson (2007) reported the presence of a shear zone in the immediate tunnel floor where the boreholes were excavated. The shear zone has a dip angle of about 45°. Models with or without this shear zone have been considered (Fig. 14.19). The calculated horizontal and vertical stress components below the tunnel floor are shown in Fig. 14.21.

The mechanical properties of the shear zone are uncertain so several normal and shear stiffness values were used. When the shear zone is not considered, the maximum horizontal stress can reach over 66 MPa. This occurs close to the tunnel floor. However, with the shear zone, the maximum horizontal stress is significantly lower (42 MPa) and occurs at 0.6–1.0 m below the tunnel floor.

The TASQ Tunnel models show very limited fracturing in the sidewalls and roof. The models with or without the shear zone show slightly different results; there are more fractures in the model with the shear zone. Most of the short fractures are probably caused by the high stress concentration created by the roughness of the tunnel surface. The TASQ Tunnel models do not indicate failure in the tunnel floor.

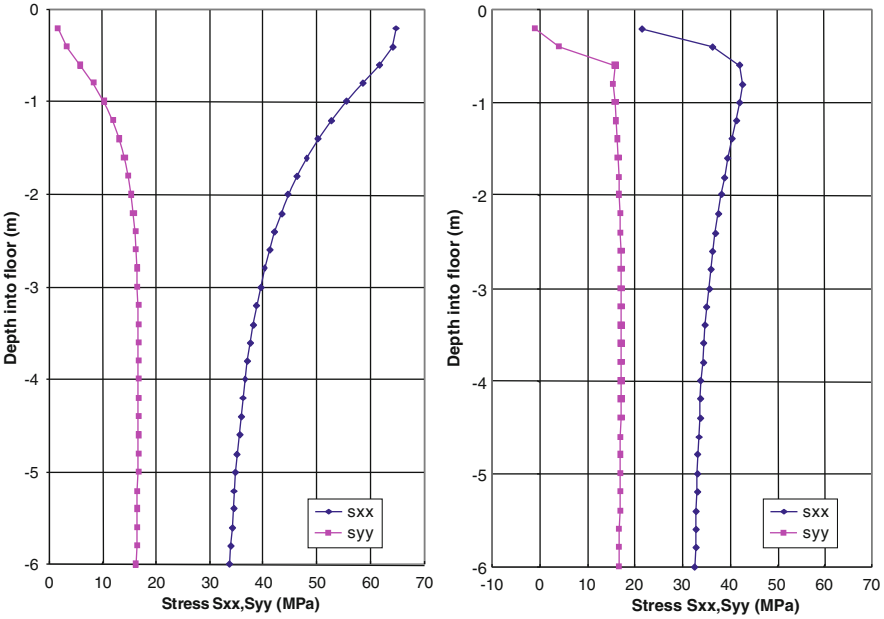


**Fig. 14.21** Plot of the horizontal and vertical stresses along the centre line at the tunnel floor before introducing the pillar. Stresses without (*left*) and with the shear zone (*right*). Fracture normal stiffness of the shear zone is $K_n = 20$ GPa/m

### 14.4.2.2 Horizontal Section of the Boreholes

To model the rock mass response to induced stresses in horizontal cross-section of the APSE pillar, the applied boundary stresses must be defined at different depths. The stress component perpendicular to the TASQ Tunnel axis ($\sigma_{yy}$) is taken from the TASQ Tunnel model. The stress component in the direction parallel to the tunnel axis is calculated using Hooke's law with the assumption of plane strain conditions. To obtain the stresses at the pillar wall, only elastic behaviour is considered, i.e. the effect of fracture initiation and propagation are ignored in the models. The mechanical stress evolution in the rock mass due to drilling of the boreholes in sequence was investigated using the sequential excavation function in FRACOD, as described in Chap. 8.

The location where the stress is higher than strength (spalling) is marked. The upper figure shows the stresses at the wall of borehole #1 due to excavation of the first borehole and after excavation of the second one. The lower figure depicts the stresses at the wall of the borehole #2 after excavation of both boreholes. The compressive strength in the upper figure is higher due to the confinement stress of 0.7 MPa in borehole #1.

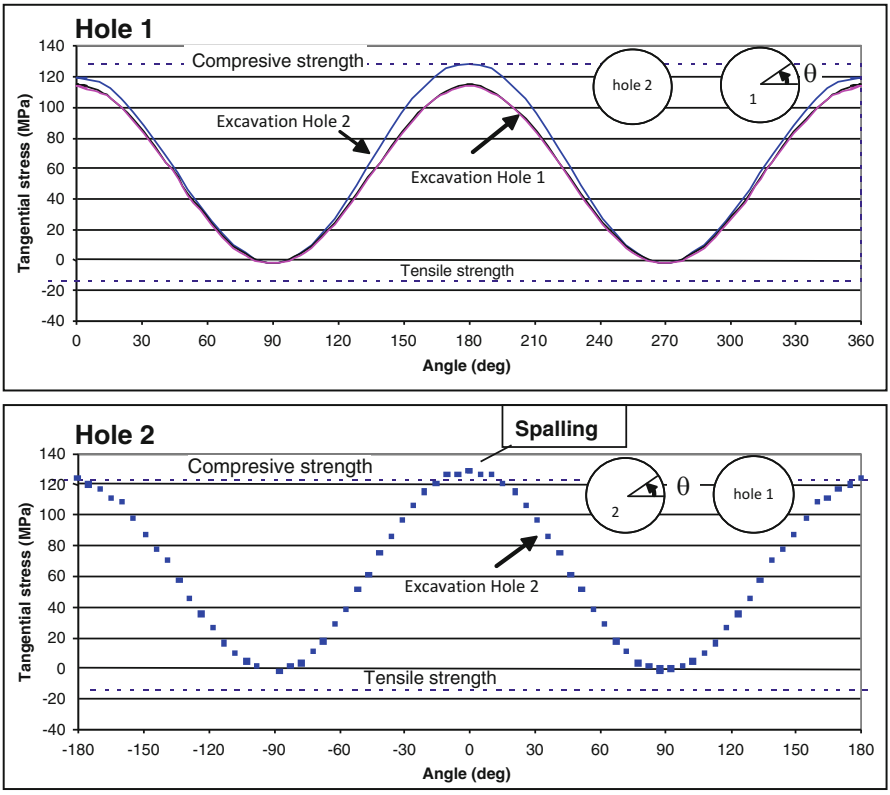


**Fig. 14.22** Tangential stress at the borehole wall 1 m below tunnel floor during excavation of the boreholes

Figure 14.22 shows the predicted tangential stress distribution along the perimeters of the two boreholes at a depth of 1 m. The models indicate that, depending on the rock strength used and whether the shear zone is considered, spalling can occur at the borehole wall due to purely mechanical stresses (i.e. without considering temperature induced stresses). Stress modelling and observations from the field suggests that the spalling strength of the APSE pillar is about 123 MPa. Exceeding this stress level will cause slight fracturing in the pillar wall.

### *14.4.3 Modelling of Thermo-Mechanical Effects*

To model the effects of temperatures change, horizontal cross-sections of the boreholes were used. The workflow for simulation of the temperature evolution, stresses and elastic displacements comprises:

**Table 14.9** Compilation of thermo-mechanical parameters

| Parameter | | Value and unit |
|---|---|---|
| Young's modulus | E | 76 GPa |
| Poisson's ratio | $\nu$ | 0.25 |
| Thermal conductivity | $\lambda$ | 2.6/3.2/4.2 W/mK |
| Coefficient of linear expansion | $\alpha$ | $7.0e^{-6}$ $K^{-1}$ |
| Density | $\rho$ | 2.73 $t/m^3$ |
| Specific heat | $c_t$ | 770 J/kgK |
| Model I fracture toughness | $K_{Ic}$ | 3.8 MPa $m^{1/2}$ |
| Model I fracture toughness | $K_{IIc}$ | 4.4 MPa $m^{1/2}$ |
| Tensile strength | $\sigma_t$ | 14.9 MPa |
| Cohesion | c | 30.9 MPa |
| Angle of internal friction | $\phi$ | 49° |
| Initial fracture length | | 0.075 m |

- Definition of boundary conditions and geometry;
- Calibration of the thermal conductivity for each depth level analysed to meet specific measured temperatures;
- Adjustment of the heater scheme to the time step definition available in the code;
- Adjustment of the thermal flux to optimise the temperature evolution;
- Simulation of the temperature, displacement and stress evolution assuming elastic deformations only;
- Simulation of the fracturing evolution.

The following sections summarise the outcome of the thermo-mechanical (T-M) simulations. Compilation of parameters used in the T-M modelling is listed in Table 14.9. More detailed information can be found in Staub et al. (2004).

#### 14.4.3.1 Temperature Evolution

A typical simulated temperature field is given in Fig. 14.23.

The temperature results from the numerical and physical experiment were calculated for different measurement points and depth levels. A typical numerical and physical comparison is given in Fig. 14.24.

The back-calculated and the measured temperatures agree well. Differences in the temperatures are mostly due to the fact that the numerical heating scheme was bounded to a 5 days interval, whereas the temperature in the physical experiment was changed continuously. The temperature difference after 60 days is usually less than 3 °C.

#### 14.4.3.2 Stress Evolution and Elastic Displacements

The simulation shows an increase of stress with increase in temperature and the stress evolution follows the temperature evolution (Fig. 14.25). The stresses are

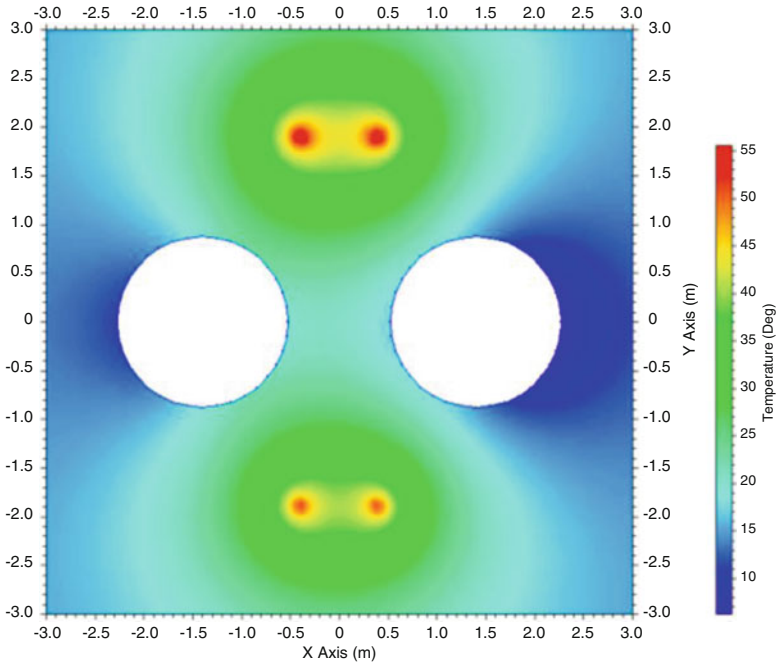


**Fig. 14.23** Temperature field at −3.5 m depth below tunnel floor after 15 days of heating

highest at the tunnel floor and decay with depth. This is due to the distance to the highly stressed tunnel floor. The stress increase from increase of temperatures is about 48 MPa.

The elastic displacements show similar behaviour on the three depth levels with only minor differences in magnitudes. The magnitudes in displacement are in the order of 1/10 mm.

#### 14.4.3.3 Fracture Network Generation

Fracture propagation driven by thermal loading leads to minor spalling. The fractures are initiated at the narrowest point of the pillar at the unconfined borehole. The fracturing then propagates into the pillar and the breakout widens (Fig. 14.26).

Several models were run (using different input data of the Mohr-Coulomb criterion for new crack initiation stress with the aim) to study the effect of the crack initiation level on the extent of pillar failure. Figure 14.27 presents failure patterns when applying 53 % of Mohr-Coulomb strength and 60 days of heating.

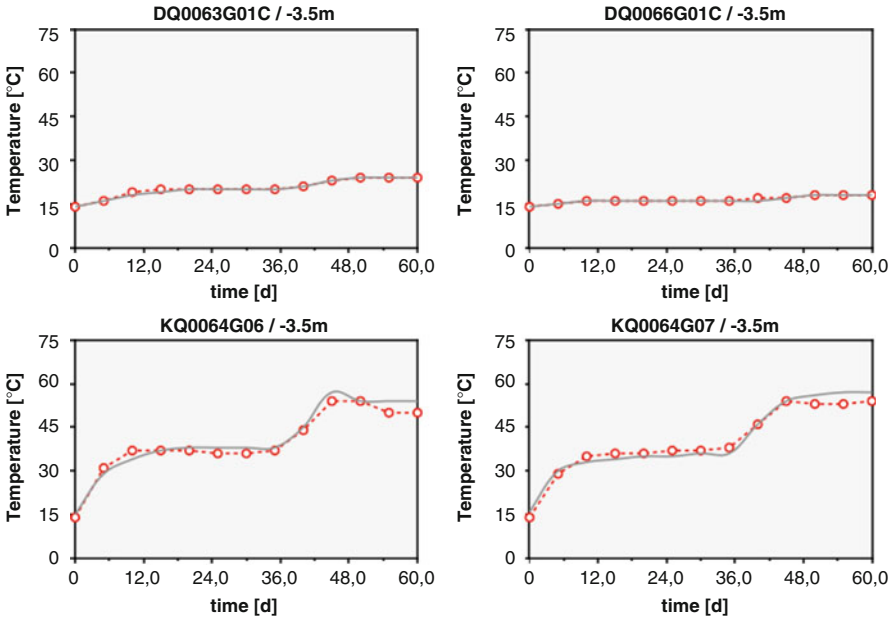


**Fig. 14.24** Temperature as simulated in the numerical experiment (*red dotted line*) compared to the physical experiment (*grey line*) for the measurement points at the borehole walls (63G01C and 66G01C) and between the heaters (64G06 and 64G07) at the −3.5 m depth level below tunnel floor (see instrumentation in Fig. 14.18)

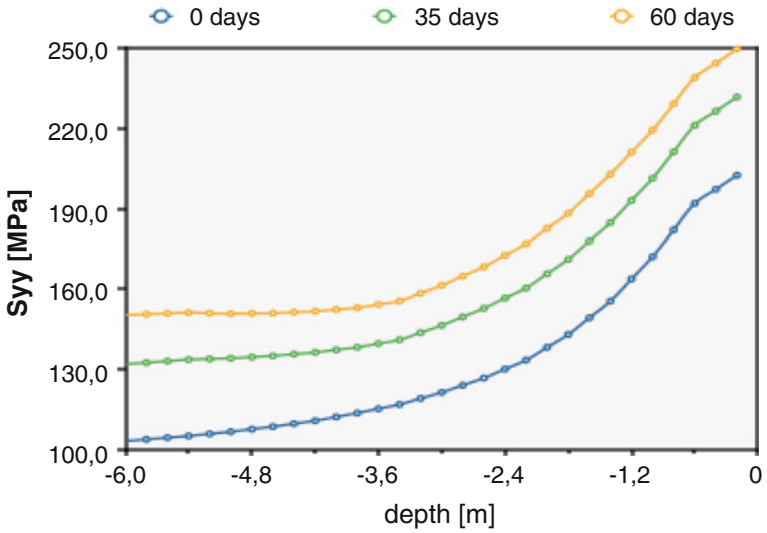


**Fig. 14.25** Tangential stress as a function of depth along hole DQ0063G01 at the narrowest point of the pillar at day 0, 35 and 60 from start of heating

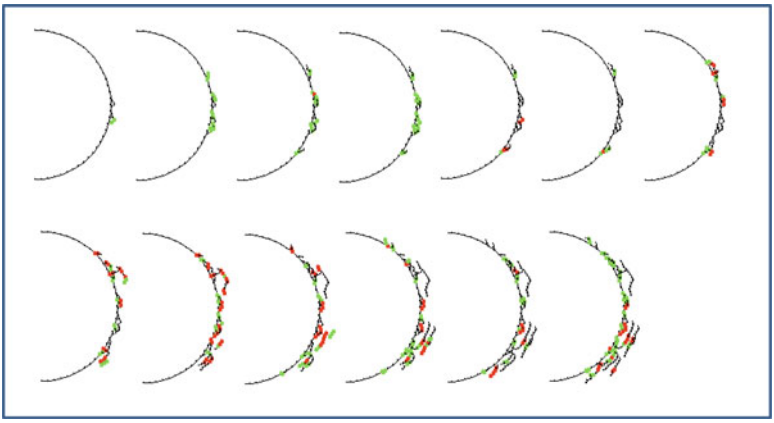

**Fig. 14.26** FRACOD suggested evolution of fracturing under thermal loading

#### 14.4.3.4 Displacements from Fracturing Simulations

The simulation of the fracture network evolution enables one to calculate displacements caused by fracturing and to compare the results with in-situ measurements. Figure 14.28 illustrates a simulation of a model with the crack initiation at 53 % of the Mohr-Coulomb strength.

After moderate outward movement of the wall (negative displacements) at about 40 days, the displacements become larger and the borehole wall moves inward. This is in good agreement with the in situ measurements. The simulated displacements are few millimetres. Some readings from the physical experiment show earlier or larger displacements. These are believed to be governed by the pre-existing fractures and were not considered in the simulation campaign.

### *14.4.4 Summary*

The thermal evolution, elastic behaviour and brittle failure observed experimentally are well reflected by the FRACOD models. The simulated temperature evolution in the pillar volume shows excellent agreement with the in-situ measurements. Small deviations are believed to originate from the two-dimensional model's inability to consider heat transfer in a vertical direction.

Displacements from simulations agree well with the measurements. The simulation of the fracture initiation and propagation resulted in fracture patterns that agree well with the in-situ observations. The breakout angle and breakout depth also show good agreement when the fracture initiation strength as determined in the laboratory (53 % of Mohr-Coulomb strength) is used for the simulations.

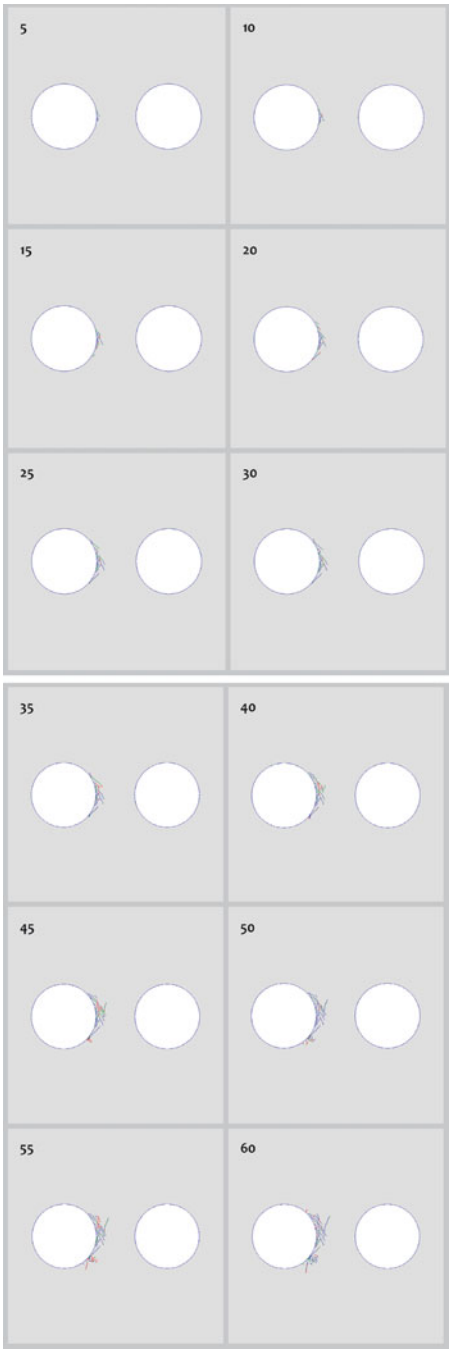


**Fig. 14.27** Simulated fracture network caused by thermal stresses. Snapshots mirror the failure pattern after 5–60 days of heating

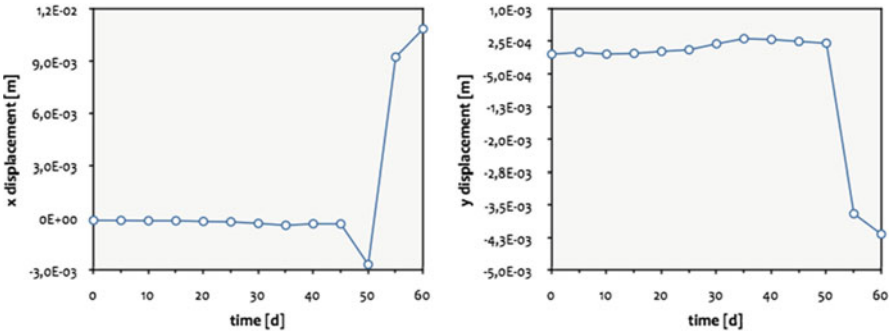


**Fig. 14.28** Simulated displacements from the distinct generation of the fracture network while spalling developed at point DQ0063G01/C. Crack initiation occurs at 53 % of the Mohr-Coulomb uniaxial strength

## 14.5 Modelling Uniaxial and Triaxial Tests

Simulation of uniaxial and triaxial compression strength tests have been reported associated with several FRACOD modelling campaigns (Rinne et al 2004; Rinne et al. 2006, 2007; Rinne and Shen 2007; Rinne 2008).

The main parts of the modelling work described in this chapter have been conducted within the context of the international DECOVALEX Project and the APSE Pillar Stability experiment (Andersson 2007).

In DECOVALEX Task B, short-term compressive strength test models were set up aiming to reproduce the stress–strain behaviour observed in the laboratory for the Äspö diorite. Comparison of laboratory behaviour with the simulation results was the first step to assess the different code's capacity to reproduce the failure. Modelling of failure in well-defined laboratory conditions was believed to help predictions for full-scale pillar failure modelling (see Sect. 14.3. Modelling pillar failure).

### *14.5.1 Brittle Failure Under Compression*

According to laboratory observations the failure process in rocks under compression is complex, involving both stable and unstable crack propagation. Local failure in rocks occurs in the direction of the major applied load and in the shear stress direction. Under uniaxial compression an isolated inclined crack starts to grow in a stable manner towards the major principal stress, forming so-called 'wing cracks'. Successively increased far-field stress is required to maintain wing crack propagation. When the wing crack grows, the angle between the direction of major stress and the wing crack decreases, resulting in decreased stress intensity at the

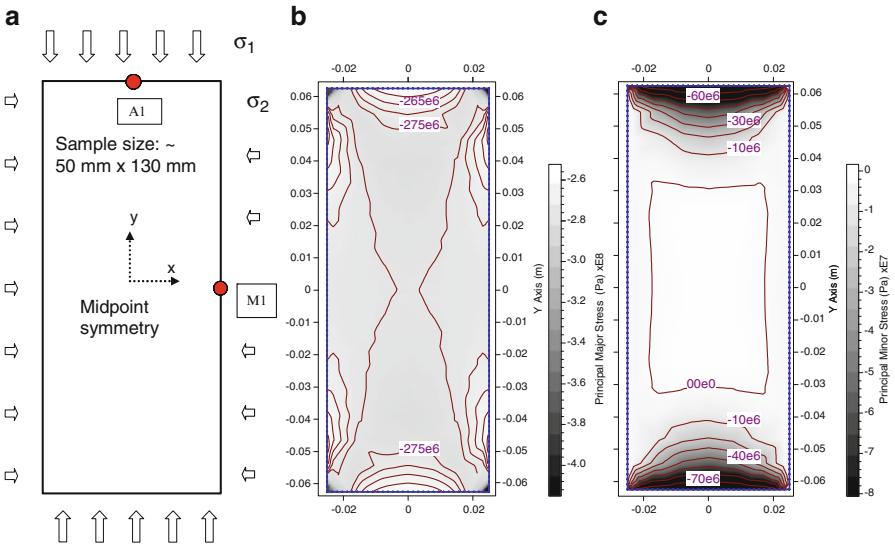


**Fig. 14.29** From *left*: Loading configuration (**a**), major principal stress (**b**) and minor principal stress (**c**) in the UCS model. Elastic conditions are presented for axial stress of $\sigma_1 = 256$ MPa (After Rinne 2008)

crack tip. After the stresses have reached a certain level, failure in the shear stress direction is more favourable from the point of view of the total energy of the system.

Under increasing stress, cracks begin to interact and coalesce. This linkage is often suggested as a possible mechanism for strain softening (Fakhimi and Fairhurst 1994), and it begins long before the uniaxial short-term laboratory peak strength of a rock sample. The final macroscopic failure occurs when cracks begin to coalesce in an unstable manner. A chain of cracks propagates in shear and/or in tensile modes depending on the local inhomogeneity of the rock and the stress state at the crack tip.

### *14.5.2 Model Description*

Figure 14.29 describes the loading configuration of numerical uniaxial and triaxial laboratory tests. This figure also shows the major and minor principal stress in a uniaxially compressed elastic model (with no failure process introduced in the model). Figure 14.30 shows a pattern of fracture initiation and propagation under compression.

Because the compression failure models involve a large number of simultaneously growing fractures, a symmetrical model is used to improve the accuracy and calculation capacity. In this study, symmetry against point $x = 0$ and $y = 0$ is used. All models assume 2D-plane-strain conditions.

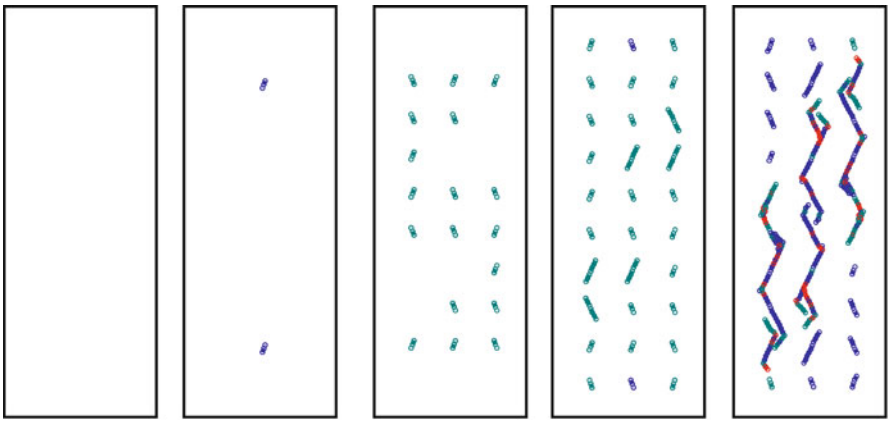

**Fig. 14.30** Initiation of new cracks, fracture propagation and failure in the UCS test according to FRACOD simulation. Failure pattern at different compressive stress states as measured at the monitoring point A1 (see Fig. 14.29). From *left*: 0, 89, 140, 218 MPa and post-peak stress (<226 MPa). *Blue* indicates elastic state of a fracture (no slip), *red* indicates an open fracture and green indicates shear fracture (After Rinne 2008)

The element size at the model boundaries is about 4 mm. The top and bottom boundaries are restricted in shear movement to simulate the stiff contact conditions (i.e. strong friction) in laboratory tests. This is done using displacement boundaries. Boundary conditions at the sidewalls are defined using stress boundaries.

### *14.5.3 Input Parameters and Loading Steps*

UCS and triaxial compression tests have been conducted on Äspö diorite in several studies at different laboratories. The following FRACOD models refer to mechanical properties reported in Staub et al. (2004). The intact rock material between cracks is assumed to be homogeneous, isotropic and linearly elastic. Input parameters for dry rock conditions, as listed in Table 14.10, are used.

During loading of the numerical sample an axial displacement is applied incrementally on the top boundary. The strain is increased in steps with the maximum step size equivalent to about 10 MPa stress increase. Close to the peak strength the step size is reduced to about 1 MPa. After reaching the unstable fracture propagation at the peak, the applied load is alternated between loading and unloading, to sustain controlled failure.

In the stress–strain curves (Fig. 14.33) axial stress in the specimen is detected at the middle of the top boundary of the model (A1 in Fig. 14.29). The lateral displacement mirroring the radial expansion during loading is calculated at the midpoint of the vertical edge (M1).

**Table 14.10** Values of the mechanical parameters of the intact rock and fractures used as input in FRACOD (Modified after Rinne 2008)

| Parameter | Value and unit |
|---|---|
| *Intact rock* | |
| Young's modulus (intact rock) | 73.6–75 GPa |
| Poisson's ratio (intact rock) | 0.21–0.27 |
| Cohesion | 31 MPa |
| Friction angle | 49° |
| Tensile strength | 14.9 MPa |
| *Newly initiated cracks* | |
| Cohesion | 20 MPa |
| Friction angle | 35° |
| Normal stiffness | 27,000 GPa/m |
| Shear stiffness | 2,700 GPa/m |
| Dilation angle | 2° |
| Fracture toughness – tensile $K_{IC}$ | 3.8 MPa $m^{1/2}$ |
| Fracture toughness – shear $K_{IIC}$ | 4.4 MPa $m^{1/2}$ |
| Initial and residual aperture | $10 \times 10^{-6}$ m |

#### 14.5.3.1 Uniaxial Test U626

The model of uniaxial loading refers to the test KQ0064G01 – 6.26, as reported in Staub et al. (2004). The modelled sample length is L = 0.138 m and the diameter is Ø = 0.0509 m. Young's modulus is 73.6 GPa and the Poisson's ratio is 0.27, as defined for the rock sample in the laboratory.

New crack formation depends upon the stress/strength ratio. When the tensile stress at a given point in the model exceeds some predefined portion of the intact rock's tensile strength $\sigma_t$, a potential failure surface will be introduced in the model with a direction perpendicular to the tensile stress. Similarly for shear failure, both the cohesion and the friction angle of the intact rock are used to define the direction of the potential failure plane according to the Mohr-Coulomb criterion. The function describing the new crack formation is explained in Sect. 3.5. In this study the stress level for new crack formation is set to 89.2 MPa as an input value, reflecting the measured Crack Initiation Stress ($\sigma_{ci}$) in the laboratory.

The assigned length of newly formed cracks significantly affects the failure strength (Rinne 2008). The length of newly formed cracks versus the peak strength for UCS models is presented in Fig. 14.31. For sample U626, the initial crack length is set to 2.6 mm to fit with the peak strength of the laboratory sample. Note that for sample U626 dry test conditions are assumed while in the Fig. 14.31 wet conditions are modelled.

The stress field associated with a crack affects any closely positioned cracks in the model. The far-field stress for fracture propagation is reduced when the spacing between the modelled cracks is small with respect to their dimensions (Rinne 2008). In this study the crack density is set to 10 × 10 mm, defined as the crack midpoint distance (Fig. 14.32). According to the results of the sensitivity analysis, the interaction between two cracks becomes significant when the distance is less

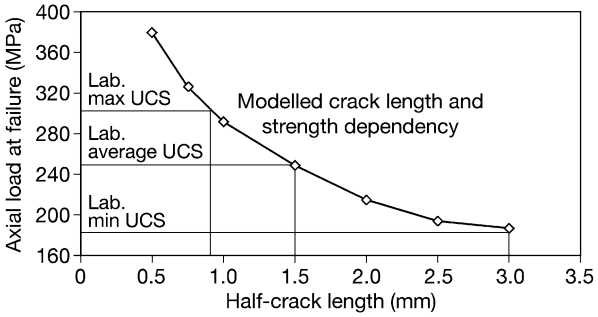


**Fig. 14.31** Initial half-crack length versus peak strength. FRACOD model behaviour as calculated for the Äspö diorite assuming wet test conditions (After Rinne 2008)

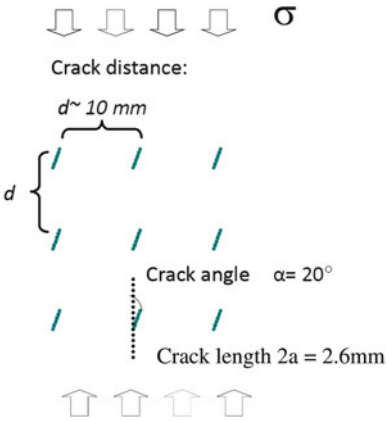


**Fig. 14.32** Crack initiation pattern for FRACOD simulation of UCS test. Using Äspö diorite parameters, an inclination angle of $\alpha \approx 20°$ is suggested for the newly formed shear cracks

than about three times the crack length. Hence, the modelled newly formed cracks do not significantly affect each other prior to fracture propagation.

Stress–strain behaviour of samples U262 from laboratory measurements and from FRACOD modelling is shown in Fig. 14.33.

#### 14.5.3.2 Triaxial Test T544

The triaxial test sample T544 refers to drillcore KQ0064G01 – 5.44, as reported in Staub et al. (2004). Initial crack length is set to 2.45 mm. The crack density is about the same as was set for the UCS model (10 mm). Sample length is L = 0.1389 m and diameter is ∅ = 0.0507 m. The Young's modulus of the intact rock is set to 75 GPa and the Poisson's ratio 0.21 gives the best fit for the lateral response. The applied confining pressure is 1 MPa.

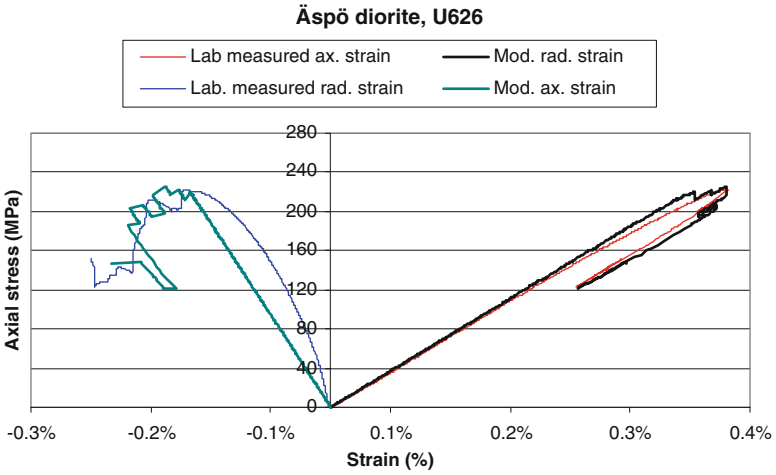


**Fig. 14.33** Stress–strain behaviour of the Äspö diorite during uniaxial loading of sample U626. Laboratory test and FRACOD modelling

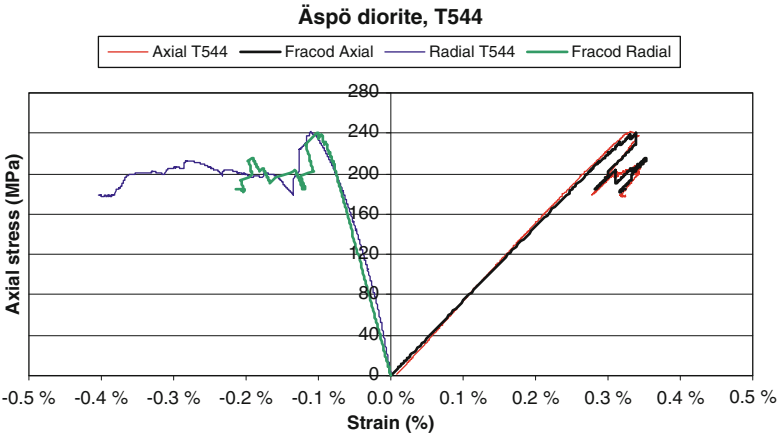


**Fig. 14.34** Stress–strain behaviour of the Äspö diorite. Laboratory test and FRACOD modelling

FRACOD modelling results of the triaxial test T544 are shown in Figs. 14.34 and 14.35. Close to the peak strength the size of the strain steps is reduced and after reaching the unstable fracture propagation at the peak, the applied load is alternated between loading and unloading to sustain controlled failure. Figure 14.36 shows the modelled loading-unloading sequences and the stress reduction caused by fracturing.

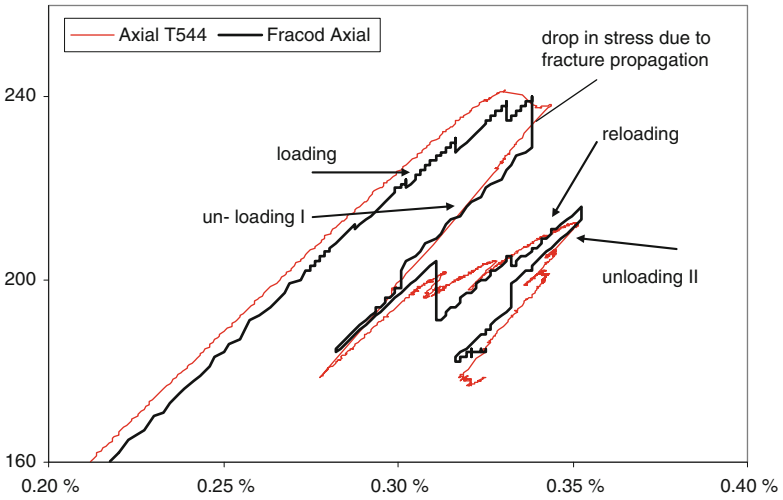


**Fig. 14.35** Detail from Fig. 14.34

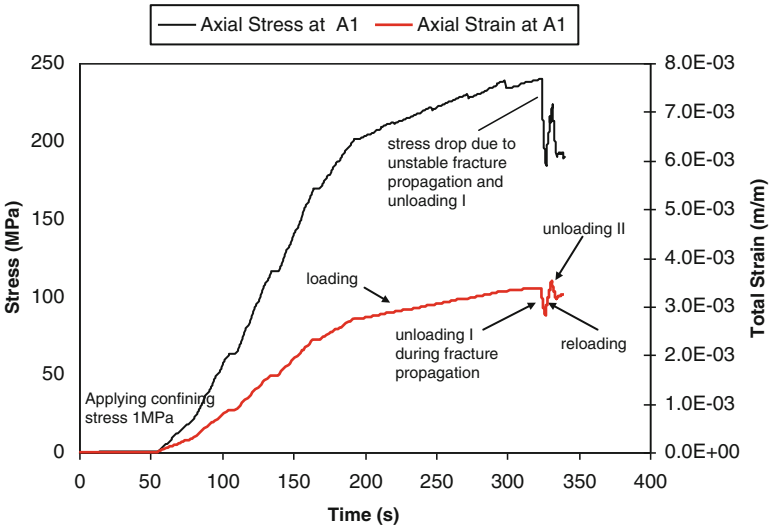


**Fig. 14.36** Loading-unloading-reloading history in the triaxial T544 model. The time-dependent effects and crack velocities are not considered. Time is presented only to illustrate the movement of the modelled piston of the loading machine

### *14.5.4 Summary*

The modelled axial and radial stress–strain curves fit well with the real laboratory results. However, it must be noted that the stress varies greatly in the numerical model from one point to another. The reference point representing the axial stress

in the presented models are taken at the midpoint of the upper boundary suggesting somewhat lower stress compared to the average maximum principal stress in the model. Also, the shape of the radial stress–strain curve varies greatly depending on the location of the monitoring point and propagating fractures (Rinne 2008).

Parameters required for FRACOD analysis can generally be obtained by laboratory testing. However, the maximum crack length of the most critically oriented cracks and the crack density of a certain rock volume cannot be measured with current techniques. In this study the crack length was calibrated to match the laboratory strength. The crack density was chosen so that the cracks do not significantly affect each other prior to fracture propagation. It is not known how much the cracks and other discontinues in the rock sample affect each other during the real test. The modelled crack merely presents a critical stress concentration that is a summary of several discontinuities with different sizes, angles and densities, rather than a distinct isolated crack with a well-defined geometry (length, orientation and density).

The initial crack length in the uniaxial ($l_{crack} = 2.60$ mm) and triaxial ($l_{crack} = 2.45$ mm) models is calibrated to fit the peak strengths of the tests. A shorter crack is assumed in the triaxial model, because the 1 MPa confinement cannot fully explain the increased strength. The higher strength is thought to depend on the slightly different microstructures of these two samples. This is a realistic assumption because the elastic properties also differ. In addition, the sample geometries are not identical and this may affect the peak strength.

Time-dependent effects were not considered in the previous models. The reader is referred to Rinne (2008) where time-effects are considered in UCS and triaxial tests.

## References

Amadei B, Stephansson O (1997) Rock stress and its measurement. Chapman and Hall, London, 490 p

Andersson C (2004) Summary of preparatory work and predictive modelling. Äspö Pillar Stability Experiment. Technical report R-03-02, The Swedish Nuclear Fuel and Waste Management Co (SKB), Stockholm

Andersson C (2007) Rock mass response to coupled mechanical thermal loading. Äspö Pillar Stability Experiment. Doctoral thesis in soil and rock mechanics, Royal Institute of Technology, Stockholm Sweden 2007, TRITA-JOB PHD 1008, ISSN 1650–9501

Andersson C, Rinne M, Staub I, Wanne T (2003) The on-going pillar stability experiment at the Äspö Hard Rock Laboratory, Sweden. In: Stephansson O, Hudson JA, Jing L (eds) The proceedings of GeoProc 2003, International conference on coupled T-H-M-C processes in Geosystems: fundamentals, modelling, experiments & applications, Stockholm, pp 385–390

Barton N (2007) Rock quality, seismic velocity, attenuation and anisotropy. Taylor & Francis, London. ISBN 0-415-39441-4

Chryssanthakis P, Tunbridge L, Christiansson R (2003) Numerical modelling in 3D of the TBM/ZEDEX tunnels at Äspö, Hard Rock Laboratory and comparison with in-situ measurements. In: Proceedings of underground construction conference, London

Emsley S, Olsson O, Stenberg L, Alheid H-J, Falls S (1997) Zedex – a study of damage and disturbance from tunnel excavation by blasting and tunnel boring. SKB technical report 97–30, Swedish Nuclear Fuel and Waste Management Co, Stockholm

Ewy RT, Cook NGW (1990) Deformation and failure around cylindrical openings in rock. Int J Rock Mech Min Sci Geomech Abstr 27:387–427

Fakhimi A, Fairhurst C (1994) A model for the time-dependent behaviour of rock. Int J Rock Mech Min Sci 31:117–126

Guenot A (1989) Borehole breakouts and stress fields. Int J Rock Mech Min Sci Geomech Abstr 26:185–195

Haimson BC, Lee MY (1995). Estimating In Situ stress conditions from borehole breakouts and core disking-experimental results in granite. In: International workshop on rock stress measurement at great depth, September 30, Tokyo, pp 19–24

Hajiabdolmajid V, Kaiser PK, Martin CD (2002) Modelling brittle failure of rock. Int J Rock Mech Min Sci 39:731–741

Hill RR, Meyer JJ, Magee ME (1997) The contemporary stress field of the Nappamerri Trough and its implications for tight gas resources, Report of Department of Geology and Geophysics, University of Adelaide, Australia

Klee G, Bunger A, Meyer G, Rummel F, Shen B (2011) In situ stresses in borehole blanche-1/south Australia derived from breakouts, core discing and hydraulic fracturing to 2 km depth. Rock Mech Rock Eng 44:531–540

Lee MY, Haimson BC (1993) Laboratory study of borehole breakouts in Lac du Bonnet granite: a case of extensile failure mechanism. Int J Rock Mech Min Sci Geomech Abstr 30:1039–1045

Martin CD, Martino JB, Dzik EJ (1994) Comparison of borehole breakouts from laboratory and field tests. In: Proceeding on rock mechanics in petroleum engineering, Balkema, Delft/Rotterdam, pp 183–190

Martin CD, Read RS, Martino JB (1997) Observations of brittle failure around circular test tunnel. Int J Rock Mech Min Sci 34(77):1065–1073

Martino JB, Chandler NA (2004) Excavation-induced damage studies at the Underground Research Laboratory. Int J Rock Mech Min Sci 41:1413–1426

Park ES, Jung YB, Song WK, Lee DH, Chung SK (2010) Pilot study on the underground lined rock cavern for LNG storage. Eng Geol 116:44–52

Rinne M (2000) Propagation of rock fractures in the vicinity of a canister hole for spent nuclear fuel. Licentiate thesis, Royal Institute of Technology, Engineering Geology. Stockholm, ISBN 91-7170-617-8

Rinne M (2008) Fracture mechanics and subcritical crack growth approach to model time-dependent failure in brittle rock. Doctoral dissertation, Helsinki University of Technology, Rock Engineering, ISBN 978-951-22-9434-3. http://lib.tkk.fi/Diss/2008/isbn9789512294350/

Rinne M, Shen B (2007) Numerical simulation of core tests using FRACOD in understanding and characterizing of the Excavation Disturbed Zone (EDZ). DECOVALEX Task B Phase 2 report. In: Hudson JA, Jing L (eds) SKI report 2007:08, Swedish Nuclear Power Inspectorate. www.ski.se

Rinne M, Shen B, Lee H-S (2003a) Modelling of fracture stability by FRACOD. Preliminary results. Äspö Pillar Stability Experiment, R-03-05, The Swedish Nuclear Fuel and Waste Management Co (SKB), Stockholm

Rinne M, Shen B, Lee H-S (2003b) Äspö Hard Rock Laboratory. Äspö pillar stability experiment. Modelling of fracture stability by FRACOD. Preliminary results. SKB IPR-03-05, Swedish Nuclear Fuel and Waste Managing Co, Stockholm

Rinne M, Shen B, Lee H-S (2004) Modelling of fracture development of APSE by FRACOD. Äspö Pillar Stability Experiment, R-04-04, Swedish Nuclear Fuel and Waste Management Co (SKB), Stockholm

Rinne M, Shen B, Stephansson O (2006) Numerical analysis of microstructural breakdown of compressed rock samples. In: EUROCK 2006-multiphysics coupling and long term behaviour in rock mechanics, Taylor & Francis Group, London, ISBN 0 415 41001 0, pp 701–705

Rinne M, Shen B, Backers T (2007) Time and chemical effects on rock sample failure. Results from laboratory tests and numerical modelling. In: GeoProc 2008, international conference on coupled T-H-M-C processes in Geo-systems. Polytech Lille, France

Shen B (2004) Understanding the effects of initial injection pressure on fracture movement at Habanero no. 1 HDR well, CSIRO exploration and mining report 1188C

Shen B (2008) Borehole breakout and in situ stresses. In: SHIRMS 2008, Perth, Australia, September 16–19, 2008, vol 1, pp 407–418

Shen B, Stephansson O, Rinne M (2002) Simulation of borehole breakouts using FRACOD2D. Geomechanics in reservoir simulation. In: International workshop, 5–7 Dec 2001, Oil and Gas Science and Technology. Rev. IFP, vol 57, no 5, pp 579–590

Shen B, Stephansson O, Rinne M, Amemiya K, Yamashi R, Toguri S, Asano H (2011) FRACOD modelling of rock fracturing and permeability change in excavation-damaged zone. Int J Geomech 11:302–31

Shen B, Kim HM, Park ES, Kim TK, Wuttke M, Rinne M, Backers T, Meier T, Stephansson O (2013) Multi-region boundary element analysis for coupled thermal-fracturing processes in geomaterials. Rock Mech Rock Eng 46(1):135–151

Souley M, Homand F, Pepa S, Hoxha R (2001) Damage-induced permeability changes in granite: a case example at the URL in Canada. Int J Rock Mech Min Sci 38:297–310

Staub I, Andersson C, Magnor B (2004) Äspö Pillar Stability Experiment, Geology and mechanical properties of the rock mass in TASQ, R-04-01, The Swedish Nuclear Fuel and Waste Management Co (SKB), Stockholm

Stephansson O, Shen B, Rinne M, Backers T, Koide K, Nakama S, Ishida T, Moro Y, Amemiya K (2003) Geo-mechanical evaluation and analysis of research shafts and galleries in MIU Project, Japan. In: Saito T, Murata S (eds) Proceedings of the 1st Kyoto international symposium on underground environment, Kyoto University, Japan

Stephansson O, Shen B, Rinne M, Amemiya K, Yamashi R, Toguri S (2008) FRACOD modelling of rock fracturing and permeability change in excavation damage zone. In: Proceedings of 12th international conference of international association for computer methods and advances in geomechanics, Goa, India.

Tan XC, Kou SQ, Lindqvist PA (1998) Application of the DDM and fracture mechanics model on the simulation of rock breakage by mechanical tools. Eng Geol 49:277–284

Tsang C-F, Bernier F, Davies C (2005) Geohydromechanical processes in the Excavation Damaged Zone in crystalline rock, rock salt and indurated and plastic clays – in the context of radioactive waste disposal. Int J Rock Mech Min Sci 42:109–125

Vardoulakis J, Sulem J, Guenot A (1988) Borehole instabilities as bifurcation phenomena. Int J Rock Mech Min Sci Geomech Abstr 25:159–170

Zang A, Stephansson O (2010) Stress field of the earth's crust. Springer Science + Business Media, Dordrecht/Heidelberg/London/New York

Zheng Z, Kemeny J, Cook NGW (1989) Analysis of borehole breakouts. J Geophys Res 94(B6):7171–7182

Zoback MD, Mooss D, Mastin L, Anderson R (1985) Wellbore breakout and in situ stress. J Geophys Res 90(B7):5523–5530

# Index




B. Shen et al., *Modelling Rock Fracturing Processes: A Fracture Mechanics Approach Using FRACOD*, DOI 10.1007/978-94-007-6904-5,